Stability of Photo-Electrochemical Interface for Solar Fuels

Thesis by

Weilai Yu

In Partial Fulfillment of the Requirements for the degree of
Doctor of Philosophy

CALIFORNIA INSTITUTE OF TECHNOLOGY
Pasadena, California

2021
(Defended April 12, 2021)

Weilai Yu
ORCID: 0000-0002-9420-0702

To mom and dad

ACKNOWLEDGMENTS

My past five years at Caltech have been life-changing. Graduate school is full of ups and downs, but now when I look back, I will find all those good memories right behind. At the very beginning, I never imagined coming to Caltech for a Ph.D considering the highly competitive application process, while my goal then was to get into UC Berkeley where I thought I might have a better chance. I can still recall my excitement on that morning back in 2016 January, when I woke up and found myself getting an email from Prof. Jim Heath congratulating me on my acceptance into Caltech. Upon my first arrival at Caltech campus, I was attracted not only by the beauty of campus but also the underlying scientific atmosphere and history. After the visit, I followed my heart coming to Caltech and I will never regret such a decision.

First of all, I would like to thank my advisor, Prof. Nate Lewis, for his guidance and care over the years. Nate is such an amazing and unique figure who essentially knows about everything with great insight. Every of my conversations with him is so fruitful that I'm able to constantly learn and grow. I especially appreciate the intellectual freedom that he strongly encourages. Such freedom allows me to explore simply following my pure curiosity, without feeling any external pressure. Nate has his own taste of science with extremely high standards, and by now his attribute towards science has profoundly shaped my vision on how to work out good science. Moreover, his systematic way of thinking and approaching complex scientific questions is crucial for leading me to perform all the works presented in this thesis. I still remembered the very first moments when Nate responded to my first email during my application, as well as when I first met Nate in person in the orange room of Noyes during my campus visit. Afterwards, I was determined to come to Caltech as I felt working with Nate would probably give me an unique experience. It turns out that this experience is not necessarily smooth all the way along, but it definitely feels very rewarding at the end.

Secondly, I would like to thank the chair of my committee, Prof. Harry Gray. Harry is almost like my second advisor as he always cheers me up at those difficult times and encourages me to chase my goals with his strong support. Actually, I first met Harry during my exchange term as an undergraduate at Harvard back in 2015 spring. That night, Harry was giving a lecture introducing a collective efforts by his solar army. It was that talk that later strengthened my wish to pursue a Ph.D on solar fuels, while also making me realize that Caltech, sitting right in sunny southern California, is an almost perfect place for that purpose. After coming to Caltech, I am very fortunate to have worked closely with both Nate and Harry, who have different characters, but share a similar vision for our world. Not many people have such a wonderful opportunity of working for both of them, and I know some of them who have become great scientists later on. Working with Harry offered me quite a scientific journey to explore N_2-to-NH_3 electrochemistry, and I am so proud that we ended up publishing two papers together. My graduate school life at Caltech wouldn't have been so colorful and pleasant without interacting with Harry.

I would like to thank Prof. Hans-Joachim Lewerenz, who taught me the basics of semiconductor photoelectrochemistry during my first year. Joachim is not only a friendly and patient teacher, but also he is a wonderful mentor who cares a lot about his students. Interestingly, after the course, Joachim ended up with a really nice impression of me, as he always described me as a "top-notch" student to other people in the Jorgensen. In his office, we had many insightful discussions on photoelectrochemistry from which I realized that there were still many topics in this field that remain under-explored. I feel sorry that Joachim left us so early and I wish he had a chance to see what I have achieved today with his help.

I would like to thank the rest of my committee, Prof. Mitchio Okumura and Prof. Kimberly See, for always being supportive and giving me much good advice on my proposals, research, and career. Interacting with both of them always reminds me that there are certain things that I can do better and there is always more that I can achieve.

At Caltech, I have worked with and learnt from so many great colleagues who made this thesis possible. Firstly, I would like to thank Dr. Matthias Richter for generously offering me instrumental help in my projects. Matthias is such a technical wizard that he essentially knows how to solve problems of all kinds, making any problem no longer a problem. By large I learnt from him on how to be a capable, efficient, and creative researcher. The necessary workflow of my projects seems very challenging at the beginning, but with his help I was able to streamline the works I never thought myself capable of doing. I would like to thank Dr. Bruce Brunschwig for his strong support of me and his diligent efforts in maintaining all instruments in the MMRC, especially the Kratos XPS that is the key for this thesis. Bruce also cared a lot about me and gave me good advice on my research and life, especially during those difficult times of my life. I always found it a pleasure to chat with him on almost anything. I would like to thank Dr. Nathan Dalleska for patiently guiding me to use his instruments while generously teaching me essentially every aspect of analytical chemistry. Nathan is such a master of all analytical instruments that I ended up learning very much from him. Also he taught me to "change one factor at a time" when doing experiments. I am so proud that we have worked out the new method to quantify $^{15}NH_3$ and efficiently published that paper together. I would like to thank Prof. Katharina Brinker for initiating a wonderful team collaboration with me on the ammonia projects so that I had the chance to interact with Harry. Working with her has been quite memorable as she is always so nice and patient, and she taught me how to do research in an organized fashion. I would like to thank Dr. Kimberly Papadantonakis for helping edit my manuscripts and being a reliable source of support for our group. I would like to thank Pakpoom Buabthong for helping me with all aspects of my projects while also being a fun Jorgensen buddy. Pai and I started working in the Nate's group at almost the same time, and Pai is another instrument wizard who has diligently kept both our sputter and XPS running smoothly. It is always a joy to sit down and chat with him, either in office, conference room or lab. I would like to thank Dr. Ivan Moreno-Hernandez for introducing me into the Jorgensen lab and teaching me how to do electrochemistry at start. I still remembered those old days when we grabbed dinner together after work, and discussed the state-of-art of solar fuels.

Moreover, my life at Caltech wouldn't have been so colorful if I hadn't met the following people. I would like to thank Katherine Rinaldi and Dr. Ethan Simonoff for being two of my best friends in Nate's group. Every time chatting with you has filled my mind with joy and pleasure. Our trip to Washington D.C. with Caltech Y has been one of my best memories in graduate school. During this final year of my Ph.D, special thanks to Kat for instructing me on the gym workout, and also to Ethan for treating me with your tasty tea. I would like to thank Harold Fu for being a loyal Jorgensen and AFM buddy through the whole past five years. Our AFM trip to Stanford and the Bay area is quite a memory! I would like to thank Dr. Ke Sun, a brilliant, dedicated, and warm-hearted scientist, with whom I had many inspiring discussions on semiconductors and solar fuels in my first year. I wish we had overlapped more so that we have a chance to do some real work together. I would like to thank Dr. Xinghao Zhou for being helpful on all aspects of life and research. I cherished the time we spent together working late at night in our G131 office. In addition, I would like to thank Dr. Yi-Rung Lin from the Atwater group for being a loyal buddy hanging around the Jorgensen lab, and offering me critical support during my postdoc search. We always had great time during the JCAP all-hands meetings. I would like to thank Dr. Chengxiang Xiang (CX) for having insightful conversations with me while also supporting me through applications of both postdoc and fellowship. I would like to thank Dr. Josef Schwan from the Gray group for being a good friend of mine. My memory of our trip to the LA Galaxy game was quite vivid. I would like to thank Dr. Teddy Huang, a group alumni who was working at Bruker, for kindly teaching me the SECM-AFM technique during the Christmas of 2018, and treating me to countless delicious dinners upon every one of his visits. I would like to thank Dr. Yuanlong Huang for many pleasant conversations over the Linde Robinson lab at night when I was there running the ICP-MS, and also for helping me finish the CoMo paper. I would like to thank Dr. Burt Simpson and Dr. Renata Balgley for offering me precious advice on my postdoc search.

I would like to thank other fellows from our 2016 cohort, Katie Hamman, Michael Mazza, and Kathleen Kennedy. We joined the group at almost same time and we always supported each other through these years. Also I would like to than other people who spent time in the Jorgensen G131 for keeping our office like a family, including Dr. Stefan Omelchenko, Dr. Paul Nunez, Dr. Sisir Yalamanchili and Dr. Azhar Carim, Katie Chen, Dr. Erik Verlage, and Dr. Jingjing Jiang. It seems like most people in our office have got their Ph.Ds, and now it is my turn. I would like to thank other folks with whom I have overlapped in the Jorgensen lab for keeping me accompanied, including Dr. Paul Kempler, Zach Ifkovits, Jake Evans, Dr. Carlos Read, Sean Byrne, and Dr. Michael Lichterman. Of course, my Ph.D experience in Nate's group wouldn't be complete if I hadn't met Jackie Dowling, Madeline Meier, Maureen Morla, Ellen Yan, Dr. Noah Plymale, Dr. Fadl Saadi, Dr. Jonathan

Thompson, Dr. Dan Torelli, Dr. Josh Wiensch, Dr. Kyra Lee, Dr. Miguel Caban-Acevedo, and Dr. Nick Batara.

I would like to thank all people from the administration across the campus for smoothing my Caltech experience, including Barbara Miralles (Lewis group), Alisson Ross (CCE), Daniel Yoder and Laura Kim (ISP), Natalie Gilmore (grad office), Heidi Rusina (Resnick), and Tiffani Walker, Mabby Howard, and Xenia Amashukeli (JCAP).

Outside Caltech, I would like to thank our wonderful collaborators for supporting some of the important works presented in this thesis. Firstly, I would like to thank Dr. Todd Deutsch and Dr. James Young from the National Renewable Energy Laboratory (NREL) for generously providing us $InGaP_2$ samples of all kinds, and always holding discussions with me in a timely manner. I would like to thank Dr. Zhenhua Pan from Chuo University (Japan) for occasionally having inspiring chats with me, and providing us with photocatalyst samples for AP-XPS experiments. I would also like to thank Prof. Minjoo Lee and Yukun Sun from UIUC, Dr. Siva Karuturi and Dr. Julie Tournet from the Australian National University (ANU), and Prof. Zetian Mi from University of Michigan, Dr. Thomas Mueller from Bruker for their willingness to collaborate with us.

During my five years at Caltech, I have come across many more great friends and I would like to thank them all for making my time at Caltech a memory of life.

Last but not the least, I would like to thank my parents, Dr. Bei Cheng and Dr. Jiaguo Yu, for your deep love and close company during this long journey towards a Ph.D. You fill my life with the sense of love and care at every second. It is your continuous encouragement and support that helped me make it through the hardest times of graduate school to chase my dream.

ABSTRACT

Photoelectrochemical (PEC) water splitting is a promising approach to convert renewable solar energy to clean hydrogen (H_2) fuels in one simple step. Although III-V semiconductors are attractive candidates as light-absorbers in tandem solar-fuel devices, their long-term stability for the hydrogen-evolution reaction (HER) in either acidic or alkaline aqueous electrolytes needs to be established. Chapter 2-5 of this thesis first aims at revealing the underlying corrosion chemistry for a variety of III-V semiconductors specifically under the HER conditions, offering a rational understanding towards the stability of semiconductor photoelectrode.

In Chapter 2, we start from p-InP and reveal its susceptibility to cathodic photocorrosion forming metallic In^0, which however can be completely mitigated by the presence of Pt catalyst due to kinetic stabilization. We also show that the resulting PEC performance of p-InP/Pt electrodes is sensitive to the changes in surface stoichiometry, whereas an InO_x-rich surface developed in KOH caused a substantial degradation in the current density-potential (J-E) behavior. In Chapter 3, we discovered that a non-stoichiometric and As^0-rich surface of p-GaAs, resulting from a galvanic corrosion by Pt, led to mid-gap surface states as well as a complete loss in photoactivity. In Chapter 4-5, we demonstrate similar kinetic stabilization applied to both p-$InGaP_2$/Pt and pn^+-$InGaP_2$/Pt photocathodes for the HER at both pH 0 and pH 14. Additionally, we found that the corrosion of underlying GaAs substrates for the pn^+-$InGaP_2$/Pt photocathodes at positive potentials caused damage of structural integrity as well as instability in electrode performance. Altogether these works underscore the mutual dependence of the physical and electrochemical stability of semiconductor photoelectrodes during the HER, which also need to be considered separately. Moreover, both catalytic kinetics and surface stoichiometry are crucial factors for defining long-term corrosion chemistry for semiconductor photoelectrode.

In Chapter 6-7, we further explore solar fuels beyond H_2, namely electrochemical N_2-to-NH_3 conversion. We first establish a new analytical method to isotopically quantify the concentrations of $^{15}NH_3$ in aqueous solutions with a high sensitivity and a low limit-of-detection of <1 μM. Further we applied this advanced method to rigorously verify the electrocatalytic activity of a CoMo electrode for reducing N_2(g) to NH_3. We show that the additional ammonia detected in electrolyte was instead attributed to the corrosion of N impurities present in the CoMo electrode under cathodic bias, thus giving false positive results. These works emphasize the importance of both rigorous product analysis and experiment design in further catalyst development.

PUBLISHED CONTENT AND CONTRIBUTIONS

1. Yu, W.; Richter, M. H.; Buabthong, P.; Moreno-Hernandez, I.; Read, C. G.; Simonoff, E.; Papadantonakis, K. M.; Brunschwig, B. S.; Lewis, N. S. Investigations of the Stability of Etched or Platinized p-InP(100) Photocathodes for Solar-driven Hydrogen Evolution in Acidic or Alkaline Aqueous Electrolytes. *To be submitted.*

   Contribution: conception and experiment design, data collection, analysis and interpretation, manuscript drafting.

2. Yu, W.; Richter, M. H.; Simonoff, E.; Brunschwig, B. S.; Lewis, N. S. Stability of GaAs for Photoelectrochemical H_2 Evolution in Acidic and Alkaline Aqueous Electrolytes. *To be submitted.*

   Contribution: conception and experiment design, data collection, analysis and interpretation, manuscript drafting.

3. Yu, W.; Young, J. L.; Deutsch, T. G.; Lewis, N. S. Understanding the Stability of p-$InGaP_2$ Photocathode for Solar-driven H_2 Evolution. *In preparation.*

   Contribution: conception and experiment design, data collection, analysis and interpretation, manuscript drafting.

4. Yu, W.; Buabthong, P.; Young, J. L.; Deutsch, T. G.; Lewis, N. S. Failure Modes of Platinized Homojunction pn^+-$InGaP_2$ Photocathode for Solar-driven H_2 Evolution from Aqueous Acidic and Alkaline Electrolytes *In preparation.*

   Contribution: conception and experiment design, data collection, analysis and interpretation, manuscript drafting.

5. Yu, W.; Lewis, N. S.; Gray, H. B.; Dalleska, N. F. Isotopically Selective Quantification by UPLC-MS of Aqueous Ammonia at Submicromolar Concentrations Using Dansyl Chloride Derivatization. *ACS Energy Letters* **2020**, 1532–1536. https://doi.org/10.1021/acsenergylett.0c00496

   Contribution: conception and experiment design, data collection, analysis and interpretation, manuscript drafting and revision.

6. Yu, W.; Buabthong, P.; Read, C. G.; Dalleska, N. F.; Lewis, N. S.; Lewerenz, H.-J.; Gray, H. B.; Brinkert, K. Cathodic NH_4^+ Leaching of Nitrogen Impurities in CoMo Thin-Film Electrodes in Aqueous Acidic Solutions. *Sustainable Energy Fuels* **2020**, *4* (10), 5080–5087. https://doi.org/10.1039/D0SE00674B.

   Contribution: conception and experiment design, data collection, analysis and interpretation, manuscript drafting and revision.

7. Yu, W.; Fu, H. J.; Mueller, T.; Brunschwig, B. S.; Lewis, N. S. Atomic Force Microscopy: Emerging Illuminated and *Operando* Techniques for Solar Fuel Research. *J. Chem. Phys.* **2020**, *153* (2), 020902. https://doi.org/10.1063/5.0009858.

   Contribution: co-conception, literature collection and review, manuscript drafting and revision.

8. Kempler, P. A.; Ifkovits, Z. P.; Yu, W.; Carim, A. I.; Lewis, N. S. Optical and Electrochemical Effects of H_2 and O_2 Bubbles at Upward-Facing Si Photoelectrodes. *Energy & Environmental Science* **2021**. https://doi.org/10.1039/D0EE02796K.

   Contribution: Preparation of ALD TiO_2 thin-film on Si photoelectrodes.

9. Balgley, R.; Morla, M. B.; Yu, W.; Brunschwig, B. S.; Lewis, N. S. Reductant-Activated Electrophilic Functionalization of Hydrogen-Terminated Si(111). *Submitted.*

   Contribution: Electrochemical measurements of redox potentials.

10. Nunez, P.; Caban-Acevedo, M.; Yu, W.; Richter, M. H.; Kennedy, K.; Villarino, A. M.; Brunschwig, B. S.; Lewis, N. S. Origin of the Electrical Barrier in Electrolessly Deposited Platinum Nanoparticles on p-Si Surfaces. *Submitted.*

    Contribution: Photoelectrochemical measurements of p-Si/Pt electrodes.

11. Dong, H.; Yu, W.; Lewis, N. S.; Hoffman, M. R.; Mixed Metal Oxide Electrodes and the Chlorine Evolution Reaction: Fundamental Principles and Practical Applications. *In preparation.*

    Contribution: co-conception, literature collection and review, manuscript drafting.

TABLE OF CONTENTS

LIST OF ILLUSTRATIONS

LIST OF TABLES

Chapter 1

1 INTRODUCTION

1.1 Solar-driven water splitting

Nowadays, a rapidly growing world population together with expanding industrialization accelerates the rate of global energy consumption.[1] Over the past two centuries, fossil fuels have remained the primary energy carrier for our global society owing to their high energy density, powering major advancements of modern civilization. However, fossil fuels are nonrenewable energy sources with a limited supply on earth, meaning that they will be exhausted in the foreseeable future. Moreover, combustion of fossil fuels produces net emission of CO_2, a greenhouse gas, into the earth's atmosphere, causing global warming as well as other serious environmental concerns. These issues have motivated the pursuit of clean, green, and renewable energy platforms, whereas solar and wind are two major alternatives for the conventional energy sources. Promoting large-scale electricity generation from these renewable energy sources is beneficial for a successful transition of our global society into a net-zero emission energy system (Figure 1.1).[2]

Nevertheless, both solar and wind energy are intermittent in nature and their supply depend on the time of day, weather, and geo-diversity.[3] To address their uncertainty, converting the energy from these renewable sources into chemical fuels is a promising route to achieve both long-term storage and on-demand delivery of energy.[4,5] Compared with other hydrocarbon fuels, molecular hydrogen (H_2) is a preferred zero-emission fuel with much higher specific energy density, only liberating water upon consumption. Notably, hydrogen is also an important industrial chemical for producing ammonia by the Haber-Bosch process, which is critical to meet the rising demands of agriculture.[2,6,7] Moreover, H_2 can be used to produce green electricity in fuel cell which is a promising technology for the next generation clean vehicles.[8] Currently, industrial H_2-production relies on the steam-methane reforming process, which involves using natural gas and high temperatures. Hence, developing electrochemical or photo-electrochemical processes under ambient conditions can enable H_2-production from water in a more clean and renewable fashion.[9]

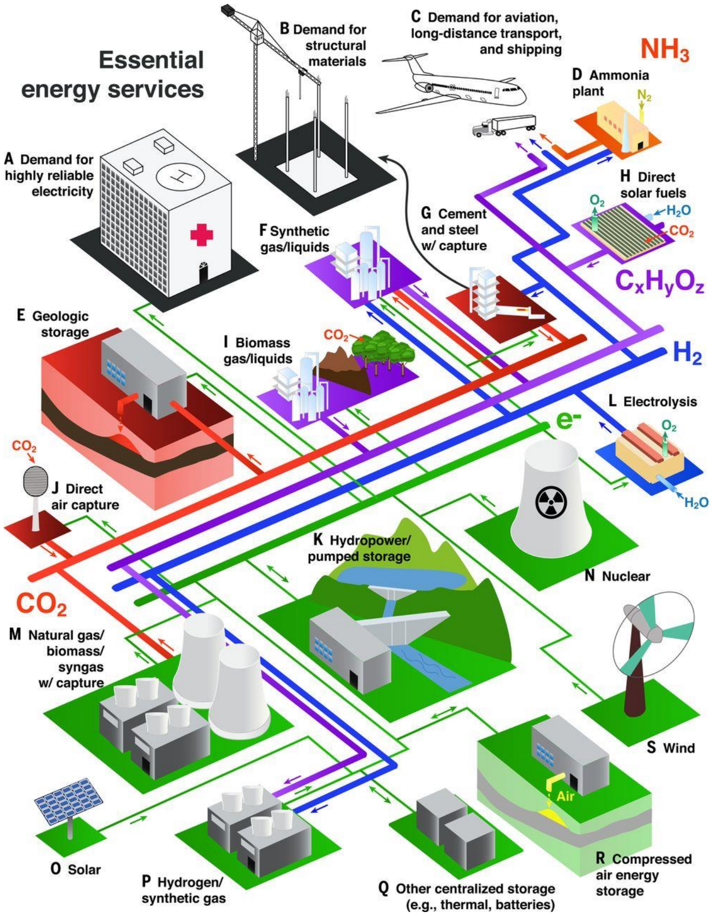

Figure 1.1 An integrated sustainable system powered by renewable energy without adding any CO_2 to the atmosphere. Reprinted with permission from ref [2].

Photoelectrochemical (PEC) water splitting is a promising approach to achieve conversion of solar energy into H_2 in one step, also known as “artificial photosynthesis”.[1] An integrated PEC device consists of a photocathode and a photoanode that are either monolithic or electrically wired to realize the reductive and oxidative half reactions, respectively (Figure 1.2). Each photoelectrode usually consists of a semiconductor generating excited photocarriers by light absorption, as well as an active electrocatalyst promoting fuel-forming reactions. For water-splitting reaction, the thermodynamic standard potentials for the hydrogen-evolution reaction (HER) and oxygen-evolution reaction (OER) are 0 V and 1.23 V versus the reversible hydrogen electrode (RHE), respectively.[10] Operating at a high current density (J) of 10 mA cm^{-2}, water splitting reaction is favored in strongly acidic or alkaline electrolytes to avoid the formation of pH gradient between cathode and anode. At pH=0, the cathodic and anodic half reactions of PEC water splitting are written as:[11]

$$\text{HER: } 2\mathrm{H}^+(\mathrm{aq}) + 2e^- \rightarrow \mathrm{H}_2(\mathrm{g}) \quad E^o = 0 \text{ V vs. RHE}$$

$$\text{OER: } \mathrm{H}_2\mathrm{O}(\mathrm{l}) \rightarrow 2\mathrm{H}^+(\mathrm{aq}) + 2e^- + 1/2\mathrm{O}_2(\mathrm{g}) \quad E^o = 1.23 \text{ V vs. RHE}$$

$$\text{Overall: } \mathrm{H}_2\mathrm{O}(\mathrm{l}) \rightarrow \mathrm{H}_2(\mathrm{g}) + 1/2\mathrm{O}_2(\mathrm{g}) \quad \Delta E^o_{cell} = 1.23 \text{ V}$$

Hence, water-splitting reaction is a thermodynamically uphill process ($\Delta E^o_{cell} > 0$ V), demanding external energy inputs such as solar energy and electricity. The solar-to-hydrogen conversion efficiency (η_{STH}) of a PEC device is primarily determined by its photocurrent density at operation (J_{op}), as given by (under standard conditions):[12]

$$\eta_{\mathrm{STH}} = \frac{1.23V \times J_{\mathrm{op}}}{P_{in}}$$

where J_{op} also represents the rate of hydrogen production converted from a photocurrent density (mA cm^{-2}), and P_{in} is the incident solar irradiance (mW cm^{-2}).

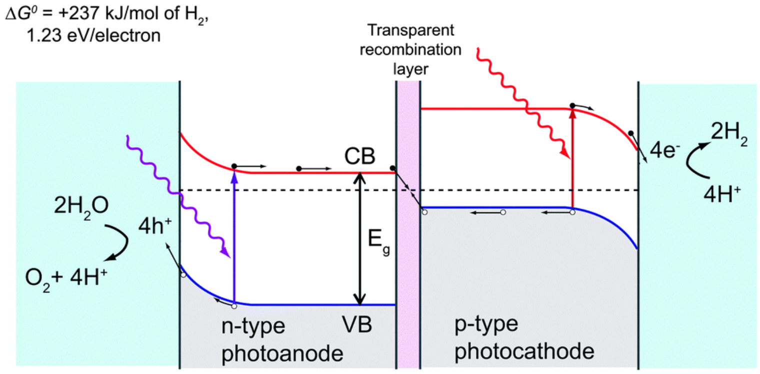

Figure 1.2 an idealized tandem solar-fuel generator under operation of water splitting, composed of a n-type photoanode and a p-type photocathode for the OER and HER, respectively. Reprinted with permission from ref. [12]

Active electrocatalysts are required to accelerate the chemical kinetics of both HER and OER at heterogenous electrode/electrolyte interfaces. The intrinsic catalytic activity at each reaction site depends on the adsorption free energy of reactants at electrode surface, formulating the so-called volcano plot. The optimal adsorption energy of reactant leads to the highest catalytic activity as well as the highest turn-over frequency (TOF). Recent years have witnessed a surge in discovery of new earth-abundant electrocatalytic materials for both HER and OER.

For long, Pt has been the best-performing HER catalyst, requiring only an over-potential (η) of <100 mV to produce an operationally relevant J of -10 mA cm^{-2}. However, the scarcity and high cost of Pt limits its widespread application. Over the past decade, many earth-abundant materials comprised of transition metals are identified exhibiting comparable HER activities as Pt, including metal phosphides, metal selenides, and metal sulfides.[8,11,13–17] For example, Lewis and coworkers have successfully synthesized nanostructured nickel phosphide catalyst with a low η=130 mV at J=-20 mA cm^{-2} in acidic electrolyte, as well as a nearly unity faradaic yield for the HER over extended periods.[13]

Compared with the HER, the OER is a kinetically more sluggish process that requires 4-electron transfer, resulting in a larger η limiting the overall efficiency of water electrolysis.[18] Boettcher and coworkers have demonstrated that a variety of transition metal (TM=Ni/Fe/Co) oxides as active OER catalysts in alkaline electrolytes, which anodically convert into the electrically conductive phase of oxyhydroxides.[19–23] Among these oxides, nickel-iron oxyhydroxide ($Ni_xFe_{1-x}OOH$) displays the best OER activity so far, with η~350 mV at J=10 mA cm^{-2}.[22] Mechanistically, it has been stablished that Fe offers the catalytic activity for the OER, whereas Ni provides a robust lattice with electrical conductivity.[19,24,25] Therefore, for a water-splitting reactor with the state-of-art catalysts operating at J=10 mA cm^{-2}, the cathode and anode are expected to be biased at <-0.1 V and >+1.58 V vs. RHE, respectively, increasing the overall voltage demand to ~1.7 V.[10] The developments of these new earth-abundant HER and OER catalysts also offer further opportunities of lowering the material cost of membrane electrode assembly (MEA) for commercial water electrolyzers.[26–28]

Despite the above promising achievements, further challenges still remain when integrating the HER and OER catalysts for a complete water-electrolysis system under the same electrolytes.[10] For instance, most earth-abundant HER catalysts are active in acidic electrolyte, while most transition-metal OER catalysts only work in basic media. While there are several examples of active HER catalysts (NiMo etc.) in alkaline electrolyte,[29–31] most oxides tend to dissolve and are thus unstable in acidic electrolyte under anodic OER conditions. Only until recently, Lewis and coworkers discovered a nickel manganese antimonate ($NiMnSbO_x$) catalyst displaying remarkable stability for the OER in 1.0 M H_2SO_4(aq), despite its high $\eta > 700$ mV.[32] Further efforts in electrocatalysis should look for new versatile and active materials that can bridge the gap of working environments between the HER and OER for an integrated water-electrolysis system.

The first demonstration of solar-driven full water splitting dates back to 1970s.[12,33] In 1972, Honda and Fujishima from Japan successfully realized spontaneous water splitting into H_2(g) and O_2(g) by illuminating a single-crystal TiO_2 electrode with UV light that is electrically wired to a Pt counter electrode.[33,34] This seminal work has inspired worldwide interests in developing efficient artificial photosynthetic systems based on semiconductors for converting solar energy into chemical fuels. Later on, other large band-gap semiconductors such as $SrTiO_3$ and $KTaO_3$ are also identified as capable of full water splitting, despite their limited efficiencies.[35] However, the energy-conversion efficiencies of these large band-gap semiconductor photoelectrodes are low owing to their insufficient light absorption. Instead, to increase the energy efficiency of photoelectrode requires the use of smaller band-gap semiconductors to obtain a higher photocurrent under 1-sun illumination. In 1998, Turner and coworkers from the National Renewable Energy Laboratory (NREL) demonstrated a multi-junction GaAs/$InGaP_2$ photocathode exhibiting an energy efficiency of > 9% for the HER.[36] Nevertheless, in this monolithic device, the stability of p-type $InGaP_2$ epilayer in contact with strongly acidic electrolyte still remains a topic of debate from then, which will be investigated in details in this thesis.[37–39] Following these earlier works, there are significant efforts of improving the efficiency of full water splitting by using high-efficiency multi-junction photovoltaic (PV) devices based on Si or III-V semiconductors.[40–43] However, prospective widespread applications of these solar-fuel devices demonstrated in laboratory are compromised by either high cost or limited stability.

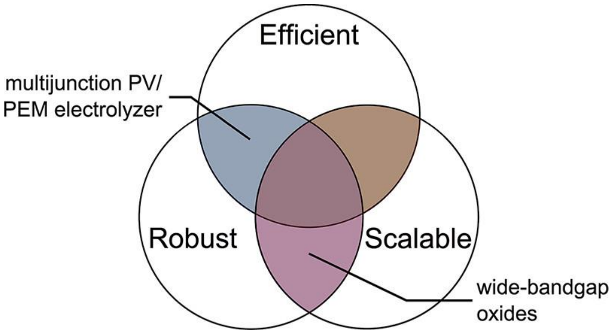

Figure 1.3 Venn diagram depicting the three key requirements for viable solar-driven water-splitting devices, highlighting material sets that satisfy two out of the three. Reprinted with permission from ref [10].

The main constraint of developing PEC devices for practical applications is to fulfill three key requirements simultaneously, namely efficiency, stability, and scalability (Figure 1.3). For example, the PEC devices based on the above-mentioned multi-junction PV cells may afford high efficiency and stability, but may not be scalable due to their high cost; many cheap oxide semiconductors (TiO_2, Fe_2O_3 and $BiVO_4$ etc.) mainly comprised of earth-abundant elements, can be scaled up for stable solar-fuel generation, but their efficiencies are limited by their relatively poor electronic properties and light absorption; furthermore, many small band-gap semiconductors (Si, InP and GaAs) can produce high photocurrents, while undergoing rapid photocorrosion under anodic conditions. Hence, it is possible for a solar-fuel device to fulfill two of the three requirements, but meeting these three demands at the same time still remains challenging and requires further research efforts.

1.2 III-V semiconductors for high-efficient water-splitting

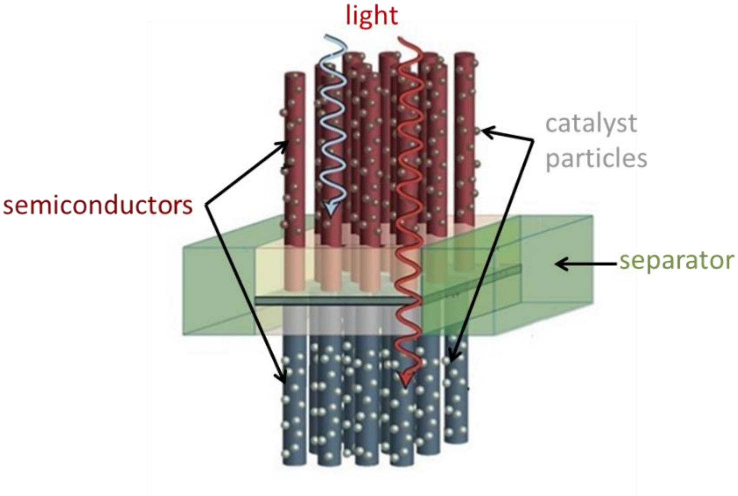

Figure 1.4 A blueprint of an integrated sola-fuel generator consisting of two nanostructured semiconductors with a small and large band gap, electrocatalysts for the HER and OER and a separator to avoid mixing of the $H_2(g)$ and $O_2(g)$ products.

Realizing spontaneous water splitting requires a minimum photovoltage output of 1.7 V by light-absorbing semiconductors. The Shockley–Queisser limits predict the maximum attainable photovoltage of a semiconductor based on its band gap.[44] As a result, a semiconductor with too small and too big a band gap leads to compromised photovoltage and photocurrent, respectively. Therefore, optimizing the efficiency of a solar water-splitting device necessitates a rational assembly of two semiconductors with different band gaps, to achieve both high photovoltage and photocurrent simultaneously. The two different semiconductors in such a tandem configuration can selectively absorb different portions of the solar spectrum, to attain optimal utilization of irradiated photons. Based on these considerations, an analysis presented by Lewis and coworkers have revealed that pairing semiconductors with a band gap of 1.1 and 1.7 eV can realize a η_{STH} >25 %.[44] Another sensitivity analysis suggests that the performances of state-of-art electrocatalysts and membranes are sufficient to support such high efficient solar-fuel device, pointing out that further increase in device efficiency should focus on improving the properties of light absorption and charge separation in semiconductors.[45] A blueprint for a tandem integrated solar-fuel generator has also been proposed and pursued by the Lewis research group at Caltech over the past decade (Figure 1.4).

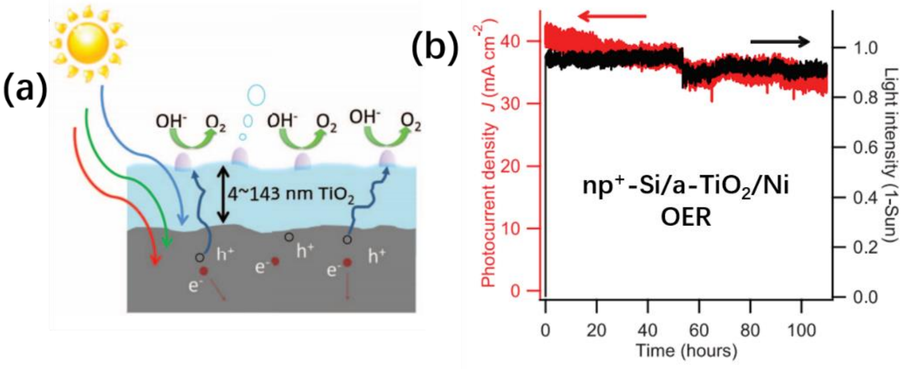

Figure 1.5 (a) Cross-sectional schematic of a Si photoanode stabilized against corrosion in a 1.0 M KOH(aq) by a hole-conductive TiO_2 deposited by ALD. (b) Chronoamperometry of >100 h OER operation by an n-p$^+$-Si photoanode coated with a TiO_2 film and a Ni catalyst for in 1.0 M KOH(aq). Reprinted with permission from ref.[46].

Si is a small band-gap (1.1 eV) semiconductor whose electrochemical behavior in aqueous electrolytes are well established. Si can operate as a stable photocathode for the HER in acidic electrolyte, while its use in alkaline electrolyte (KOH) leads to anisotropic etching.[47,48] When used as a photoanode for the OER, Si undergoes photocorrosion and self-passivates with an insulating SiO_x layer, preventing further charge transfer from Si to electrolyte.[49] Not until 2014 was an amorphous TiO_2 (a-TiO_2) protection layer produced by atomic-layer deposition (ALD) demonstrated for enabling a stable operation (>100 h) of Si photoanode for the OER (Figure 1.5).[46] Later on, other coatings such as NiO_x and CoO_x thin-films were also developed for protection of Si photoanodes against photocorrosion in alkaline electrolytes.[49–53] These recent advancements offer new opportunities for the design of tandem solar-fuel devices, as now Si is useful both as a stable photocathode and photoanode.

In this regard, another semiconductor with a larger band gap (1.8 eV) is required to pair up with Si. Alloying different III-V or II-VI elements with proper ratios is an effective pathway to obtain semiconductors with the desired band gap. For example, alloyed $In_xGa_{1-x}P$ and $GaAs_xP_{1-x}$ with a 1.8-eV band gap are promising candidates for use in tandem solar fuel generators, which has led to successful fabrication of high-efficiency multi-junction solar cells.[54,55] More importantly, the electronic qualities of III-V semiconductors are usually high enough for effective charge separation within depletion region, whereas the strategy of nano-structuring is useful for further increasing photocurrents.[56–58] However, photoanodes based on III-V semiconductors such as GaAs and InP suffer from anodic photocorrosion, as the self-oxidation of anions (As^{3-} and P^{3-}) is both thermodynamically and kinetically more favorable compared with the OER.[46,59,60] A recent demonstration of a tandem photoanode for the OER based on III-V semiconductors again required protection by the a-TiO_2 layer.[61] Nevertheless, nano-sized pinholes are typically inherent in the a-TiO_2 thin-film produced from ALD, allowing electrolytes to penetrate through and thus reach the underlying semiconductors. Unlike Si and CdTe exhibiting self-passivation,[50,62] GaAs and InP photoanodes undergo continuous dissolution in contact with aqueous electrolytes, leading to catastrophic device failure within limited periods.[59–61] Hence, improving the ALD fabrication procedure to decrease the pinhole density is necessary to enable an effective long-term protection of III-V semiconductors for photoanodic OER.

In contrast, applying these III-V semiconductors as photocathodes for the HER has the advantage of mitigating the above anodic corrosion, whereas the impact of cathodic decomposition becomes more significant. As early as 1980s, Heller and coworkers extensively investigated p-type InP (p-InP) photocathodes for both the HER and the reduction of vanadium redox couple (V^{3+}/V^{2+}) in acidic electrolytes, which displayed both high efficiency and considerable stability.[63–66] Notably, some degree of degradation in the PEC performance of p-InP was observed, which could be recovered when electrically disconnected for short periods or brough into air. For long, this mysterious observation was attributed to the presence of an surface oxide over p-InP. However, due to the limitations of analytical tools available at the time, no definitive physical data were obtained regarding the dissolution and the surface changes of p-InP during the long-term stability tests. Similarly, p-$InGaP_2$ is another important photocathode attracting much research interests, due to its suitable band gap (1.8 eV) as the top light-absorber in a tandem solar-fuel device.[36,37,39] In 1998, Turner and coworkers successfully demonstrated spontaneous water-splitting using a dual-junction pn^+-GaAs/p-$InGaP_2$ solar cell.[36] This device exhibited a stability of >20 h for continuous operation at high current density of >100 mA cm^{-2} (11 sun) in strong acidic electrolyte (3 M H_2SO_4), whereas the p-$InGaP_2$ epi-layer decorated with Pt particles was directly in contact with electrolyte performing the HER. However, follow-up studies suggested that the p-$InGaP_2$ layer is neither electrochemically nor chemically stable in both acidic and alkaline electrolytes.[37,39] In this regard, these complicated experimental observations call for a fundamental investigation on the stability of III-V semiconductor photoelectrodes (especially p-InP and p-$InGaP_2$) to scientifically establish their corrosion mechanism under the HER conditions. More recently, multiple research efforts were made to enhance the stability of these semiconductors by applying various protective or catalytic layers, only resulting in limited successes.[58,67–70] Therefore, such a fundamental understanding over the semiconductor stability is urgently necessary to benefit further rational strategies for photoelectrode stabilization.

1.3 Understanding the stability of semiconductor photoelectrodes

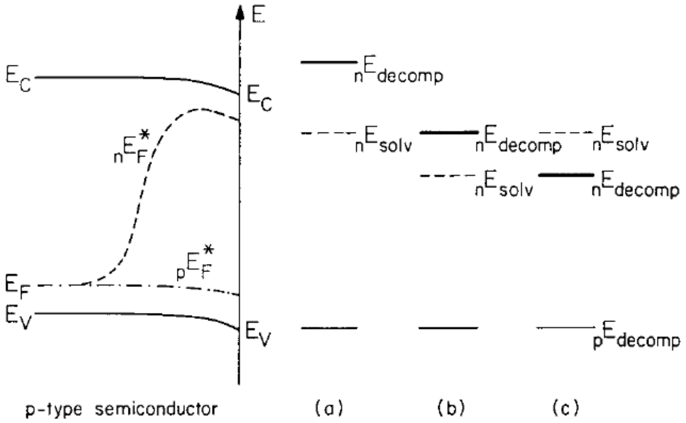

Figure 1.6 Susceptibility of p-type semiconductors towards cathodic decomposition by photogenerated electrons, proposed by Gerischer, based on the relative positions of conduction band edge and the potentials of cathodic decomposition and solvent reduction (HER). (a-c) represent different interfacial energetics for (a) stable, (b) quasi-stable and (c) unstable semiconductors, respectively. Reprinted with permission from ref [71].

In 1978, Prof. Heinz Gerischer, a pioneer in the field of semiconductor electrochemistry, put forward a general theoretical framework for understanding the stability of semiconductor photoelectrodes.[71] It was pointed out that the redox potentials of corrosion reaction and electro-active species in electrolyte (or solvent reduction, like the HER) together with the energy level of band edges, can offer an apparent indication of the susceptibility of semiconductor photoelectrodes towards electrolytic decomposition.

Specifically for a photocathode, three different situations exist based on this consideration (Figure 1.6):

(a) Stable: If the conduction band (CB) edge is below (less negative) the potential of cathodic decomposition but above the potential of solvent reduction, semiconductors will be stable against photodecomposition as the photogenerated electrons coming from the CB will not be energetic to initiate cathodic corrosion. It is also likely that the position of CB edge and the potential of cathodic decomposition are mutually correlated, as the CB of a compound semiconductor typically consists of the states from cations.

If the CB edge is above both potentials of cathodic decomposition and solvent reduction, a competition for photogenerated electrons may be expected between these two different reaction pathways:

(b) Quasi-stable: If the potential of solvent reduction is below that of cathodic decomposition, the photoelectrode is considered as "quasi-stable" due to the thermodynamic preference of solvent reduction against self-reduction; in this case, the key of electrode stabilization is to leverage control over the position of quasi Fermi level (E_{qF}) of minority carriers, which describes the average Gibbs free energy of photogenerated electrons (e^-) under a photo-stationary state; If the position of E_{qf} can be controlled below the potential of cathodic corrosion, the photoelectrode may be kinetically stabilized whereas the photogenerated electrons will perform solvent reduction. As will be demonstrated in this thesis, p-InP photocathode is a good example of the "quasi-stable" case in this model.

(c) Unstable: In contrast to (b), if the potential of cathodic corrosion is below that of solvent reduction, the corrosion pathway is preferred thermodynamically leading to an intrinsic instability of semiconductor photoelectrode. However, the situation may be different by modifying the surface kinetics and/or physically inhibit the cathodic corrosion by protective layers. P-type cuprous oxide (p-Cu_2O) photocathode is an example of the "unstable" case, where the reduction of Cu^+ cations into metallic Cu^0 is favored compared with the HER.[72]

Therefore, while comparing the interfacial energetics is important, analyzing, understanding and controlling the surface chemical kinetics also plays a vital role in defining the stability of semiconductors under practical operation conditions.

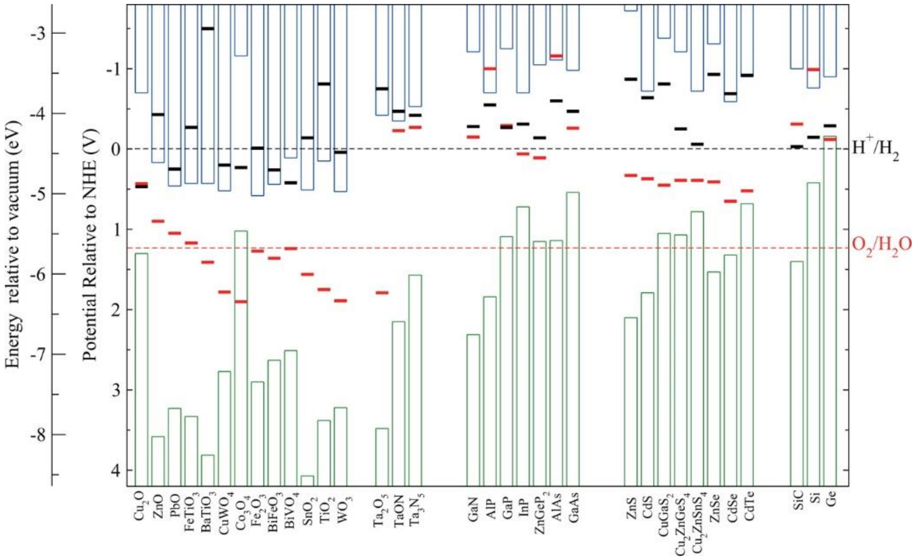

Figure 1.7 Comparison of calculated potentials of anodic corrosion (red bars) and cathodic corrosion (black bars) for a series of semiconductors, relative to their conduction band (blue bar) and valence band (green bar) edges and the potentials of the HER/OER (dashed lines). Reprinted with permission from ref [73].

In 2013, Wang and coworkers presented a systematic investigation over the band edge positions and the potentials of cathodic/anodic decomposition, relative to the HER/OER potentials, for a variety semiconductors of interest in photocatalysis (Figure 1.7).[73] The potentials of anodic decomposition sit above the OER potential for most of non-oxide materials, suggesting that they are all susceptible to anodic corrosion by self-oxidation. This explains why most non-oxide semiconductors are unstable when used as photoanode for the OER. In contrast, the potentials of cathodic corrosion sit above the HER potential for many non-oxide semiconductors, including InP, GaAs, CdS etc, indicating their potential resistance towards self-reduction. Moreover, additional corrosion or dissolution pathway may emerge when simply immersing the semiconductor in electrolyte in the dark without application of any electric potential. Such chemical dissolution may involve redox reaction of semiconductors with water, but its dissolution kinetics needs to be measured experimentally. Furthermore, while the above analyses can facilitate understanding of the electrochemical stability of semiconductors, dynamic surface transformations by corrosion chemistry need to be determined by experiment under various conditions of electrolytes and potentials.

1.4 Semiconductor photoelectrochemistry (PEC)

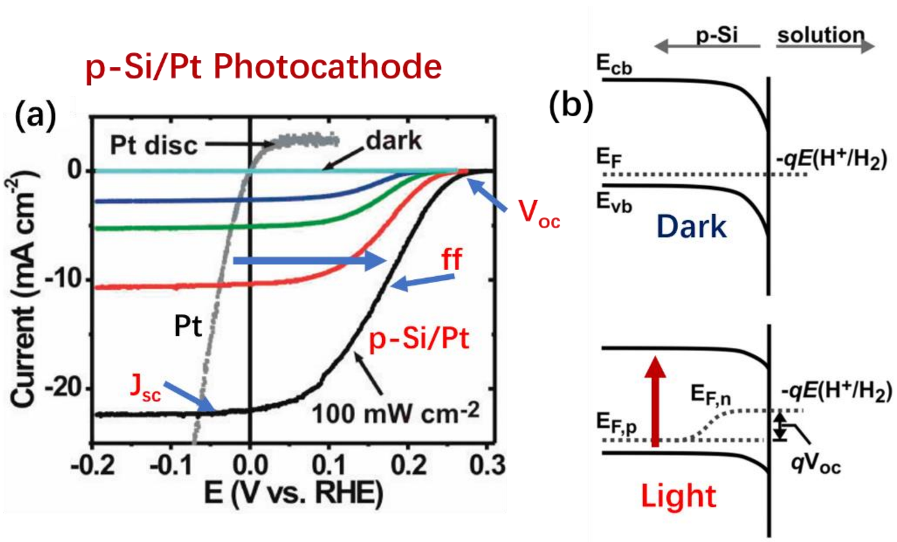

Figure 1.8 (a) Comparison of the J-E behaviors of a p-Si/Pt photocathode and a Pt dark cathode measured in 0.5 M H_2SO_4(aq); RHE refers to the reversible hydrogen electrode; V_{oc}, ff and J_{sc} represent the open-circuit voltage, fill factor and light-limited current density in the J-E behavior of the p-Si/Pt photocathode. (b) Comparison of interfacial energetics of a p-Si/Pt electrode in the dark and under illumination. Under illumination, the quasi Fermi level ($E_{F,n}$) of photogenerated minority carriers of p-Si deviate from that of majority carriers ($E_{F,p}$), leading to the V_{oc} of p-Si/Pt photocathode. Adapted with permission from ref [74].

To understand some basic principles of semiconductor photoelectrochemistry, a typical current density-potential (J-E) behavior of a p-Si/Pt photocathode for the HER in acidic electrolyte is shown in Figure 1.8. Three characters of the J-E behaviors are important for evaluating the PEC performance of an integrated photoelectrode, namely open-circuit voltage (V_{oc}), fill factor (ff) and light-limited current density (J_{sc}).

Firstly, V_{oc} reflects the barrier height at the junction of a photoelectrode, whereas a larger barrier height leads to a higher V_{oc}. The V_{oc} can originate from either a semiconductor/liquid junction or a buried homojunction (pn^+ for a photocathode) or heterojunction. The barrier height is determined by the difference in Fermi level between semiconductor and electrolyte, or two contacted semiconductors with different doping density. A planar p-Si/Pt photocathode yielded a V_{oc}~300 mV which is assigned to the barrier height of the p-Si/H_2O junction. In comparison, a planar pn^+-Si/Pt yielded a higher V_{oc}~560 mV which is attributed to the buried junction formed by a n^+-emitter layer. In comparison, the lower V_{oc} of a p-Si/Pt photocathode is due to an unfavorable band alignment between the valence band (Fermi level) of p-Si and the solution potential.

Compared with a Pt dark electrode, the J-E behavior of a p-Si/Pt photocathode substantially shifted cathodically by the magnitude of V_{oc}. As the J of both electrodes are assigned to the HER, this dramatic shift implies that the p-Si/Pt electrode operate at a potential that is away from the thermodynamic equilibrium potential of the HER (0 V vs. RHE). Physically, this is due to the deviation of the quasi Fermi level of photogenerated electrons ($E_{F,n}$) from that of majority carriers ($E_{F,p}$), resulting in a surface potential that is more negative than the back-contact potential. As a consequence, photogenerated electrons at the p-Si/H_2O interface are energetic enough to perform the HER, despite the more positive potential applied at back contact. The energy level of quasi Fermi levels at the surface of photoelectrodes under active operation can be directly measured by an advanced dual-working electrode (DWE) technique.[75,76] Moreover, the area of the J-E curve that is more positive to 0 V vs. RHE is also considered as the power-producing region of a p-Si/Pt photocathode. V_{oc} is a crucial metric for photoelectrochemistry, as a spontaneous solar-driven water-splitting requires a minimum voltage input of 1.7 V. Also, it should be noted that without favorable interfacial energetics, directly combining a high-performance semiconductor with a high active electrocatalyst may not necessarily construct a high efficient photoelectrode.[77,78]

Intuitively, a ff measures the curvy degree of the J-E behavior of a photoelectrode and how sharply J increases to J_{sc}. A higher ff means a higher maximum attainable power of a photoelectrode, divided by V_{oc} and J_{sc}. A ff usually reflects an integral of several properties of a photoelectrode, including catalytic kinetics and charge transport and recombination at interface.

Light-limited current density (J_{sc}) describes the maximum amount of charge carriers that can be extracted from the semiconductor, which is primarily determined by light absorption (band gap). Based on the effective medium theory, a polished planar Si usually reflects ~30 % of incident light at interface with air/water. By creating gradient interface, nano-structuring is shown as an effective strategy to promote anti-reflection and enhance light absorption,[56,79–81] which however may increase the rate of charge recombination due to a higher surface area.[82,83] Moreover, most electrocatalysts are optically opaque, causing parasitic absorption of incident light, thus decreasing J_{sc}. Nano-structuring the semiconductor photoelectrode into three dimension also offers additional space for depositing electrocatalysts without compromising the J_{sc}.[82,84–86] It also reduces the length of charge migration to reach surface catalytic sites, minimizes charge recombination, and increases J_{sc}.

1.5 Importance of surface chemistry for PEC

The surface chemistry of semiconductor electrode is crucial for determining its resulting J-E behavior, as all photocarriers need to initially travel across the surface and then perform fuel-forming reactions in electrolyte.[87–89] Combining surface analysis with PEC measurements under various conditions offer insights into how the changes in surface conditions of photoelectrodes influence the PEC performance. In 1990s, Lewerenz and coworkers pioneered an advanced experimental setup combining the capability of both electrochemistry and ultra-high vacuum (UHV) measurements. In the works presented in this thesis, we extensively applied an air-free transfer technique to transfer sample from glovebox to the X-ray photoelectron spectroscopy (XPS) without air exposure, with the purpose of preserving pristine nature of sample surface. Both of these protocols share the same goal of understanding the correlation between the applied electrochemistry and the surface chemistry of semiconductors.

Overall, the surface of semiconductor electrodes can influence the electrochemical behaviors through the following aspects:

(a) Surface states: Different from atoms in the bulk, atoms sitting at the surface of a crystal may not be considered as fully coordinated, which may lead to additional states within the band gap of semiconductors. Due to these surface states, photogenerated carriers may first charge these surface states instead of directly transferring from band edges into electrolyte. This will lead to Fermi level pinning as well as increased charge recombination, thus limiting the PEC performance of a semiconductor photoelectrode. However, the presence of surface states may be challenging to directly visualize experimentally, requiring systematic studies. For example, the surface states of hematite photoanode for the OER have been extensively investigated by different groups using various techniques, such as intensity modulated impedance spectroscopy (IMIS).[90–92] These detrimental surface states may be removable by depositing catalysts or tailoring material synthesis conditions. Identifying the chemical origins of surface states may benefit rational approaches for enhancing the device efficiency.

(b) Surface dipole: Covalent functionalization of semiconductor surface by organic functional groups can produce surface dipoles and shift band edges, by a magnitude based on groups' electronegativity.[93] The shifts in band edges may favorably optimize the interfacial energetics in contact with solution potentials to increase the maximum obtainable V_{oc} of photoelectrode.[94] In addition, these surface functional groups may also passivate surface states, decrease surface recombination and improve chemical stability.[95,96] For example, methyl-terminated Si produced a surface dipole of -0.4 eV relative to Si, while substantially increasing both chemical and electrochemical stability of Si .[97]

(c) Surface stoichiometry: For compound semiconductors, surface stoichiometry can also influence the resulting J-E behavior of photoelectrodes, which is one of the major findings in this thesis. The surface stoichiometry of electrodes may be altered by in-situ surface reaction in aqueous electrolytes. To correlate such surface changes with the changes in electrochemical behavior requires careful surface analysis. Very recently, Choi and coworkers showed that a Bi-rich surface of $BiVO_4$ photoanode can produce a favorable shift in band edges, resulting in improved PEC performance compared with that with a stoichiometric surface.[98] As early as 1980s, Spicer and coworkers also proposed an unified defect model to for various III-V semiconductors based on UHV measurements.[99] Their results revealed that non-stoichiometric surfaces of InP and GaAs produce mid-gap surface states at specific energy levels. An In- and P-rich surface of InP can produce surface states located below the conduction band minimum by ~0.1 eV and 0.4 eV respectively. A Ga- and As-rich surface of GaAs can produce surface states located above the valence band maximum by ~0.5 eV and 0.75 eV respectively. In this thesis, following this classic unified defect model, we will demonstrate how the surface non-stoichiometry of p-InP and p-GaAs electrodes changes their PEC behaviors.

(d) Interfacial layer: In-situ chemical or electrochemical formation of surface layers over semiconductor photoelectrodes may potentially improve the resulting PEC performance. Back in 1980s, Lewerenz and coworkers demonstrated a surface transformation of n-type $CuInSe_2$ photoanode into p-type $CuISe_3$-Se^0, when in contact with acidic electrolytes containing I_2/I^- redox couple.[88] Such a surface transformation favorably improved the electrode's PEC performance, due to in-situ construction of heterostructure.[100] Later in 2002, Lewerenz and coworkers showed a similar conversion of p-InP by an in-situ incorporation of chloride ions following surface corrosion in hydrochloric acid, into an efficient photocathode in contact with V^{3+}/V^{2+} redox couple.[101,102] More recently, Lewerenz and coworkers again successfully realized a surface conversion of the top AlInP layer into passivating oxide for a high efficient tandem solar fuel device. However, the stability of this in-situ transformed layer under operational conditions remains unknown. Furthermore, the formation of thin SiO_x layer on Si surface by the RCA cleaning is also crucial for realizing high-performance Si photoanodes for the OER.[51,52,103] All these examples demonstrated the significant impact of surface conversion in electrolyte towards the resulting PEC performance, which will also be a focus of this thesis. However, leveraging such interfacial layers to improve PEC performance requires an electrochemical or chemical capability to optimize its formation and composition by systematically tuning electrolyte and potential.

1.6 Solar fuels beyond H_2: N_2-to-NH_3 conversion

In this last two chapters of this thesis, we will explore solar fuels beyond H_2, which is electrochemical reduction of N_2 into NH_3 under ambient conditions.

Ammonia is an essential chemical for agriculture industry, whose demands rise with the increasing world population.[6,104] At present, industrial production of ammonia relies on the Haber-Bosch process that requires both high temperature and pressure.[105] As a result, the ammonia production through this process alone accounts for ~1.6 % of the total annual energy consumption worldwide, due to the extreme reaction conditions. Moreover, ammonia production requires centralized facilities, whereas a large portion of energy supply may come from nonrenewable energy sources. Developing alternative approaches that can be carried out under ambient conditions is beneficial for enabling a carbon-neutral economy. Therefore, electrochemical reduction of $N_2(g)$ directly into NH_3 has drawn tremendous research attention in recent years, owing to its great potential of being powered by renewable energy. Successful development of such a electrochemical technique will also allow on-site generation of NH_3 using abundant N_2 from air as feedstock. However, the triple-bond nature of molecular nitrogen makes the 6-electron N_2-to-NH_3 conversion kinetically much more challenging, especially compared with the 2-electron HER in aqueous electrolyte.[106] Recently, a promising electrochemical system have been demonstrated by using electroplated Li^0 metal as a mediator, which chemically forms lithium nitride (Li_3N) upon exposure to $N_2(g)$.[107–111] Ammonia can be then released from the obtained Li_3N by either hydrolysis or hydrogenation.

Despite many laboratory demonstrations of electrochemical N_2-reduciton reaction (EC-NRR), an increasing amount of efforts has been devoted to identifying the sources of ammonia contamination in experiment, which can readily lead to false positive results.[112–115] Typically, conclusions of NRR activity are drawn simply based on observations of increased ammonia concentration in electrolyte after electrochemical tests. However, the additional ammonia is likely attributed to contamination instead of reduction of $N_2(g)$, whereas ammonia contamination can originate from nitrogen gas, atmosphere or electrode material itself.[104,116,117] As a consequence, a rigorous protocol of performing robust control experiments as well as isotope-labelled experiments by purging $^{15}N_2(g)$ are urgently necessary (Figure 1.9). In this thesis, we also showed that even commercial $^{15}N_2$ gas contained molecular contaminants of both $^{14}NH_3$ and $^{15}NH_3$, which requires firm removal by using a scrubber containing acidic electrolyte.[116] Moreover, although there are many theoretical predictions of active catalysts for EC-NRR, how they can benefit real electrode design in experiment merits further discussion and exploration. In this thesis, we explored use of a CoMo alloy electrode for EC-NRR, which was predicted by theory to be a promising candidate for active NRR.

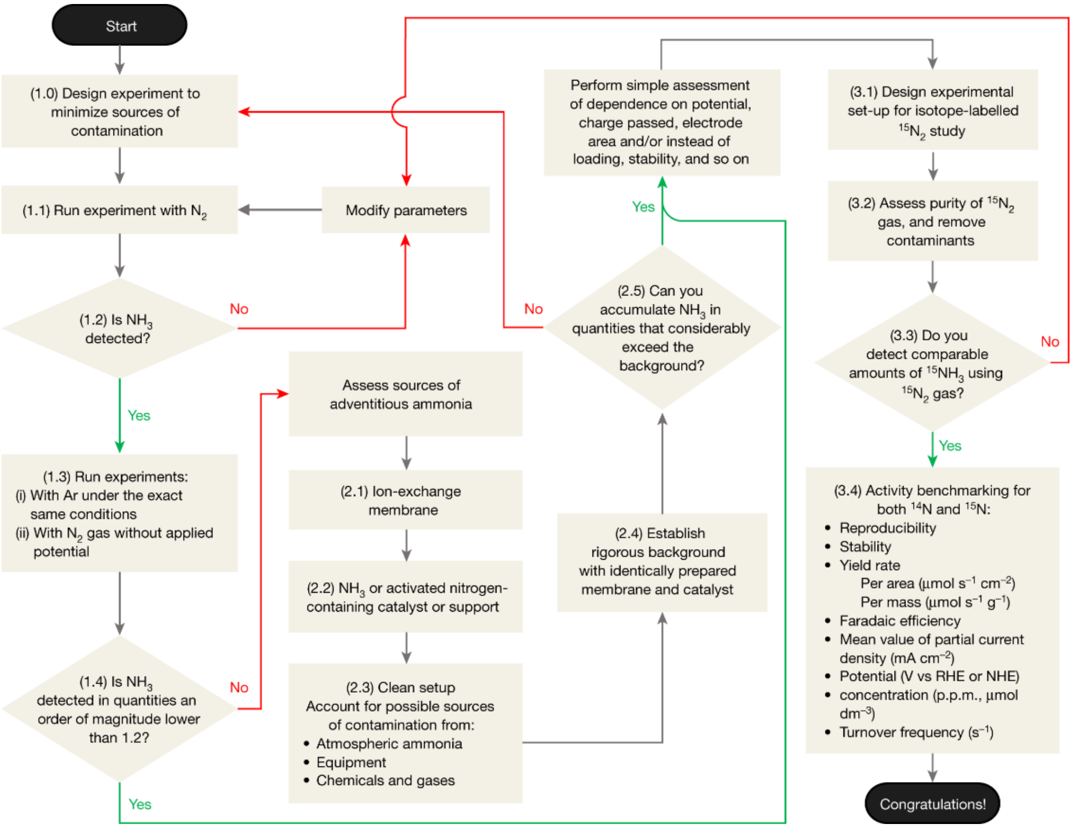

Figure 1.9 A rigorous experimental protocol for the benchmarking of electrochemical nitrogen reduction.

Besides performing the isotope experiments, developing an user-friendly analytical method is also crucial for isotopically quantifying $^{15}NH_3$ products, which is now considered as a necessary step for verifying the catalytic NRR activity. Currently, there are three different methods employed in the literature to quantify ammonia concentration in solution. Firstly, UV-vis spectroscopy followed by ammonia derivatization by the Berthelot method, is the most popular method to quantify ammonia concentration, which however is not able to distinguish between $^{14}NH_3$ and $^{15}NH_3$. Moreover, this colorimetric method is sensitive to changes in electrolyte and reaction conditions, stability of ammonia derivates and interference from other species, and also requires long reaction time. Ion chromatography (IC) is another technique that can quantify ammonium ions (NH_4^+) with both high sensitivity and low limit-of-detection (LOD) of μM, while it is still incapable of assigning isotope identity. Recently, nuclear magnetic resonance (NMR) has been demonstrated as a versatile method for isotopic quantification of ammonium ions, based on the different chemical shifts in the ^1H NMR spectrum between $^{14}NH_4^+$ and $^{15}NH_4^+$.[112,118,119] However, this method can only achieve a detection limit of ~10 μM under normal analytical conditions, which also requires long data collection time (> 10 min). In this regard, all these three methods have their pros and cons, and a complementary use of these methods can offer more robust analytical results. Importantly, the capability of assigning isotope identity while realizing quantification with high sensitivity and low LOD are equally important. Advancing the present analytical protocols of quantifying $^{15}NH_3$ is another focus of this thesis.

1.7 Thesis organization

This thesis aims at mechanistically understanding the interfacial stability of both photoelectrochemical and electrochemical systems for solar-fuel applications, which can be divided into two parts by the HER and NRR. In the first part, the stability of various III-V semiconductors used as photocathodes performing the HER have been evaluated in both acidic and alkaline electrolytes. In the second part, we developed an advanced analytical method to quantify the concentration of $^{15}NH_3$ with both high sensitivity and low LOD. Then we applied this method to rigorously verify the catalytic activity of a CoMo electrode for the NRR.

Chapter 2 first reveals the importance of catalytic kinetics at electrode surface for defining the long-term stability of p-InP photocathodes, by comparing the corrosion chemistry of etched and platinized electrodes. Then it shows that the surface stoichiometry of p-InP/Pt electrode is crucial for determining its J-E behavior as well as its operational stability, due to the different solubility of surface oxide (InO_x) at pH=0 and pH=14. Altogether these results showed that the electrochemical stability and physical stability of p-InP/Pt electrodes need to be considered separately.

Chapter 3 investigates the stability of p-GaAs photocathodes for the HER in both acidic and basic media. We revealed that the etched p-GaAs electrodes maintained both stoichiometric surface and photoactivity under the HER conditions, which is consistent with predictions by the Pourbaix diagram. However, either electrodeposited or sputtered Pt at the surface of p-GaAs induced the formation of excessive As^0, which further caused a shunting type behavior as well as a loss in photoactivity. In comparison, we further studied the surface conversion of p-GaAs/CoP electrodes under the HER conditions, which showed no excessive As^0 formation.

Chapter 4 extends our investigation into the stability of p-$InGaP_2$ electrodes with a band gap of 1.8 eV at both pH=0 and pH=14. Our results showed etched p-$InGaP_2$ electrodes corroded cathodically under illumination, while such a corrosion pathway was mitigated by the presence of Pt catalyst. We further found that the p-$InGaP_2$/Pt electrodes exhibited a slow and stoichiometric dissolution in acidic electrolyte, while a similar surface passivation by an InO_x layer occurred in alkaline electrolyte.

Chapter 5 presents a systematic investigation over the long-term stability as well as failure modes of pn^+-$InGaP_2$/Pt photoelectrode for the HER. We focus on correlating the changes in the J-E behaviors with the electrode dissolution. We discovered that the corrosion of underlying GaAs substrates caused damage to the structural integrity of the whole photoelectrode, which was not emphasized in previous works.

Chapter 6 develops a new analytical method of isotopically quantifying ammonia in aqueous electrolytes, using chemical derivatization followed by UPLC-MS analysis. We established the derivatization reaction between dansyl chloride and ammonia readily occurred at room temperature at an optimal pH=9.5. Moreover, we demonstrated that this method can achieve sensitive detection ammonia at a low LOD < 1 uM, which can be applied to gauge the impact of ambient ammonia under different environments.

Chapter 7 applies the new analytical method developed in Chapter 5 to rigorously verify the catalytic activity of a CoMo electrode prepared by sputtering. Although increases of ammonia concentrations were observed after electrochemical tests, we showed that these additional ammonia in electrolyte were assigned to $^{14}NH_3$ regardless of purging $^{15}N_2$, $^{14}N_2$, or Ar gas. These results suggested the presence of N impurities originally incorporated into the CoMo thin-film during the fabrication process, which leached out into electrolytes as NH_4^+ ions under cathodic bias.

Chapter 8 concludes this thesis and offers future directions for rationally building stable interfaces for solar fuel applications.

Chapter 2

2 INVESTIGATIONS OF THE STABILITY OF ETCHED OR PLATINIZED P-INP(100) PHOTOCATHODES FOR SOLAR-DRIVEN HYDROGEN EVOLUTION IN ACIDIC OR ALKALINE AQUEOUS ELECTROLYTES

2.1 Abstract

The stability of p-InP photocathodes performing the hydrogen-evolution reaction (HER) has been evaluated in contact with either 1.0 M H_2SO_4(aq) or 1.0 M KOH(aq), with a focus on identifying corrosion mechanisms. Stability for the solar-driven HER was evaluated using p-InP electrodes that were either etched or coated with an electrodeposited Pt catalyst (p-InP/Pt). Variables such as trace O_2 were systematically controlled during the measurements. Changes in surface characteristics after exposure to electrochemical conditions as well as electrode dissolution processes were monitored using X-ray photoelectron spectroscopy (XPS) and inductively coupled plasma mass spectrometry (ICP-MS).

In either H_2SO_4 or KOH, etched p-InP photoelectrodes corroded cathodically under illumination, forming metallic In^0 at the electrode surface. In contrast, electrodeposition of Pt kinetically stabilized illuminated p-InP photocathodes in either H_2SO_4 or KOH by inhibiting the cathodic corrosion pathway. Notably, when held at 0 V vs the reversible hydrogen electrode (RHE) in 1.0 M H_2SO_4(aq), p-InP/Pt exhibited a current density, J, of ~-18 mA cm^{-2} for >285 h under simulated 1-sun illumination. The long-term current density vs potential (J-E) behavior at pH 0 and pH 14 of p-InP/Pt photocathodes correlated with changes in the surface chemistry as well as the dissolution of p-InP. In acidic media, the J-E behavior of p-InP/Pt photocathodes remained nearly constant with time, but the surface of p-InP/Pt electrodes gradually turned P-rich via a slow and continuous leaching of In ions. In alkaline electrolyte, the surface of p-InP/Pt electrodes was passivated by formation of an InO_x layer that exhibited negligible dissolution but led to a substantial

degradation in the *J-E* characteristics. Consequently, changes in the catalytic kinetics and surface stoichiometry are both important considerations for determining the corrosion chemistry and the long-term operational stability of InP photoelectrodes.

2.2 Introduction

Stability is the most persistent materials challenge, limiting the development of operational, efficient integrated solar-driven water-splitting cells. Although a solar-to-hydrogen energy-conversion efficiency $\eta_{STH} \geq 10\%$ was reported over twenty years ago,[36] and cell efficiencies have improved gradually to $\geq 15\%$,[40,41,120–122] such efficiencies are rarely, if ever, maintained for more than a few days in the laboratory.

Maximizing the theoretically achievable efficiency of a water-splitting cell requires the use of a highly acidic or highly alkaline electrolytes, to limit pH gradients in the cell and to provide high ionic conductivities without a loss of energy associated with electrodialysis of the electrolyte buffer species.[123,124] However, the aggressive electrochemical environment required for maximum operational efficiency presents challenges to the stability of the materials in the device. For example, known semiconductors with band gaps ($\mathbf{E}_g$) useful for absorbing a substantial portion of the solar spectrum ($\mathbf{E}_g \leq 2.2$ eV)[44] are thermodynamically unstable in strongly acidic or alkaline aqueous electrolytes as photoanodes operated at potentials needed to effect the water-oxidation half-reaction.[73,125–128] In contrast, thermodynamic calculations suggest that many semiconductors, including GaP, InP, GaAs, and Si, are predicted to be electrochemically stable when used as hydrogen-evolving cathodes in aqueous electrolytes.

Group III-V semiconductors, such as InP, GaP, and GaAs, are attractive candidates for use in efficient tandem solar-driven water-splitting cells, because high-efficiency multijunction photovoltaic cells can be made using epitaxial growth and lift-off techniques.[129] Alloying within the Group III-V materials allows band-gap tuning of the light absorbers to optimal values for a solar-driven water-splitting cell.[130] Furthermore, the conduction-band edges of III-V materials are located favorably relative to the water-reduction potential. Group III-V materials have been the foundation of nearly all solar water-splitting cells that have resulted in $\eta_{STH} \geq 10\%$.[36,40,41,61,122]

P-type InP (p-InP) has been explored as a photocathode in hydrogen-evolving cells with acidic electrolytes, including water-splitting and hydrohalic acid-splitting cells, but has rarely been examined as a photocathode in hydrogen-evolving cells with alkaline electrolytes.[63,65,131–135]

Differential electrochemical mass spectrometry (DEMS) of illuminated etched p-InP(111) photocathodes in contact with 0.5 M H_2SO_4(aq) has revealed a photocorrosion process involving evolution of PH_3(g).[136] A more recent study using on-line electrochemical mass spectrometry (OLEMS) has shown that PH_3 evolution accompanies hydrogen evolution on illuminated etched p-InP(100) photocathodes.[137] p-InP has been reported to act as a stable photocathode for the reduction of VCl_3 to VCl_2 in HCl.[64,65] However with hydrogen-evolution reaction (HER) catalysts of metallic Ru, Rh, or Pt, p-InP photocathodes displayed stable photocurrents in 1 M HCl (in the absence of O_2) only when the electrode was electrically disconnected every 20 min.[63,66] Electrodeposition of Pt onto the p-InP surface suppresses such photocorrosion by accelerating the kinetics of the HER.

Typically, experimental investigations of photoelectrode stability are not conducted for more than a few hours, and do not measure the electrode dissolution at a sensitivity level of nm. For evaluation of multi-year use in solar water-splitting devices, the long-term dissolution rate of semiconductors needs to be defined quantitatively, in conjunction with a detailed assessment of the changes in the electrode surface as a result of sustained photoelectrode operation. Combined with the thermodynamic Pourbiax diagram, such experimental studies can provide a comprehensive understanding of the corrosion mechanism.

Theoretical predictions of thermodynamic materials stability generally do not consider reactions involving O_2. Additional corrosion pathways may result from the sensitivity of III-V materials to O_2, such as dissolution induced by surface oxidation.[63] Phenomenological investigations of electrode stability generally do not rigorously control the concentration of dissolved O_2 in the catholyte. Possible oxidation of the electrode surface by ambient O_2(g) after electrochemical measurements may further convolute the analysis of the conditions of a pristine electrode surface. Based on these considerations, a comparison between theoretical expectations and experimental observations would benefit from careful control over possible reactions between the electrode surface and O_2.

Herein we systematically evaluate the stability of InP for use as a photocathode for the HER in both 1.0 M H_2SO_4(aq) or 1.0 M KOH(aq). We focus on establishing both the mechanisms and rates of corrosion reactions observed under hydrogen-evolving conditions. Electrochemical experiments and XPS measurements were performed without exposing the electrodes to O_2, and were performed for both etched p-InP and for p-InP with an electrodeposited Pt catalyst. The surface conditions of InP electrodes were compared by XPS before and after exposure to electrochemical conditions. Quantitative analyses by ICP-MS of electrode dissolution into the electrolyte were performed throughout the electrochemical tests. Considering the thermodynamic Pourbaix diagram, the corrosion pathways of p-InP were determined at both pH 0 and pH 14, with and without a Pt catalyst on the electrode surface. The long-term evolution of the *J*-*E* behavior of these photoelectrodes was monitored during the stability tests. Consequently, the changes in photoelectrochemical (PEC) performance were correlated with dissolution as well as with changes in the surface composition and morphology of the semiconductor photoelectrodes.

2.3 Results

2.3.1 Stability of illuminated etched p-InP electrode for HER.

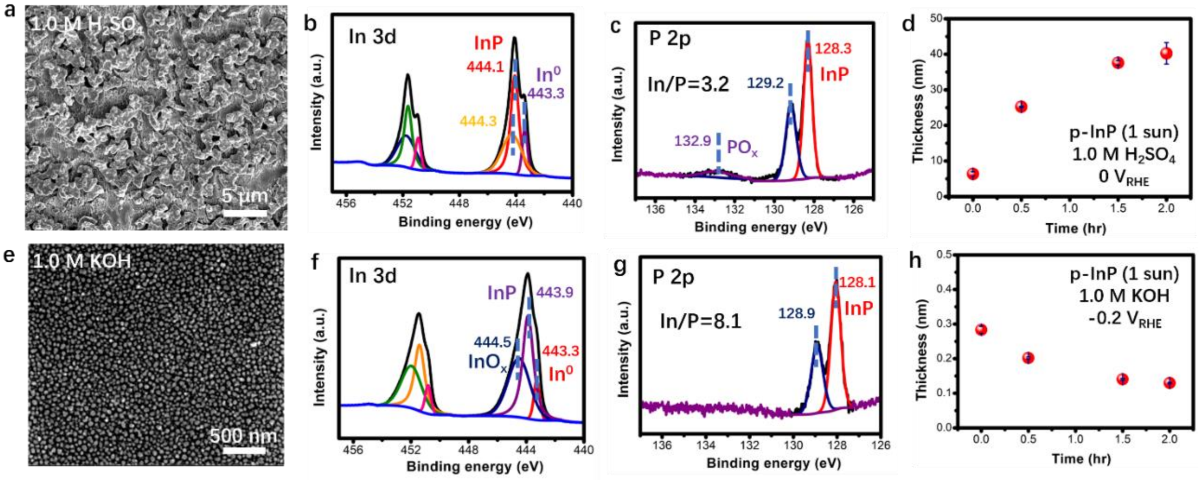

Figure 2.1 Surface analyses of illuminated etched p-InP electrodes (1-sun) after 2 h of chronoamperometry (CA) at (a-d) $E = 0$ V vs RHE in contact with 1.0 M H_2SO_4(aq), and (e-h) $E = -0.2$ V vs RHE in contact with 1.0 M KOH(aq). (a,e) SEM images showing the morphology of electrode surfaces. (b,c,f,g) XPS data of the (b,f) In 3d and (c,g) P 2p regions. (d,h) Total amount of dissolved In ions in the electrolyte during the 2 h CA, calculated as the equivalent depth of InP dissolved from the electrode surface.

Figure 2.1 presents surface analyses of after 2-h of chronoamperometry (CA) to assess the cathodic stability of illuminated etched p-InP electrodes (1 sun) in contact with either 1.0 M H_2SO_4(aq) or 1.0 M KOH(aq). During CA at *E* = 0 V vs. RHE in 1.0 M H_2SO_4(aq), within the first 20 min the current density (|*J*|) of an illuminated etched p-InP electrode decreased from ~9 mA cm^{-2} to 1 mA cm^{-2} (Figure S 2.3). After 2 h, the electrode surface was covered by a whitish film, and the SEM image showed a fibrous morphology on the surface (Figure 2.1a). XPS analysis of the In $3d_{5/2}$ spectral region revealed a large peak for the In^{3+} cations of InP (BE=444.1 eV), accompanied by a peak at lower binding energy, BE = 443.3 eV, ascribable to metallic In^0 (Figure 2.1b). The P 2p XPS data showed the P anions of InP (BE=128.3/129.2 eV) with minimal surface phosphates (BE≈133 eV) (Figure 2.1c). Before CA, a fresh p-InP sample displayed an In/P atomic ratio of 1.3 at the surface (Figure S 2.4), whereas after the CA in H_2SO_4, the In/P atomic ratio increased to 3.2, indicating enrichment of In at the surface. The concentration of dissolved In ions in the acidic electrolyte increased over the 2 h experiment, indicating dissolution of >40 nm in depth of InP (Figure 2.1d).

During CA at *E* = -0.2 V vs RHE in 1.0 M KOH(aq), in the first 10 min |*J*| of illuminated etched p-InP decreased from ~6 mA cm^{-2} to 0.5 mA cm^{-2} (Figure S 2.6). After the 2-h CA, the surface of the p-InP electrode was covered uniformly by densely packed nanoparticles (Figure 2.1e). Similar to the behavior of the etched p-InP electrode at *E* = -0.0 V vs RHE in acid, after CA of p-InP at -0.2 V vs RHE in 1.0 M KOH(aq), a peak at BE = 443.3 eV, corresponding to metallic In^0, was observed in the In 3d XPS region (Figure 2.1f). The peak at higher BE = 444.5 eV is attributable to the presence of surface oxide (InO_x), consistent with the peak in the O 1s XPS region at BE = 529.6 eV (Figure S 2.5).[138] The P 2p XPS region only showed peaks ascribable to P^{3-} anions, whereas after CA the 8.1:1 In/P ratio indicated a substantial enrichment of In relative to P (Figure 2.1g). However, the concentration of dissolved In ions in the alkaline electrolyte remained negligible and did not increase with time (Figure 2.1h).

Collectively, these results clearly show the formation of metallic In^0 on the surface of illuminated etched p-InP electrodes under cathodic conditions in both 1.0 M H_2SO_4(aq) and 1.0 M KOH(aq).

The stripping behavior of plated In^0 metal on the surfaces of n-InP electrodes was explored in the dark and p-InP under 1-sun illumination, at both pH 0 and pH 14. A series of 30-min CAs were performed for n-InP electrodes in the dark and for p-InP electrodes under illumination as a function of the electrode potential, E, followed by CV scans from the originally applied E towards more positive E values. The CA initiated the cathodic corrosion of InP to In^0 metal, whereas the CV was used to observe the onset potential of In^0 oxidation on the InP surface.

Initially, a series of CAs at E between -0.4 to -0.9 V vs RHE was performed for n-InP electrodes in the dark (Figure 2.2a-b and Figure S 2.7). Figure 2.2a-b shows the first CV sweeps of the respective electrodes after CA. In 1.0 M H_2SO_4(aq), an anodic wave with an onset E (E_{on}) of ~ -0.4 V vs RHE was observed during the first CV sweep for n-InP electrodes that had been initially held at $E \leq -0.6$ V vs RHE (Figure 2.2a and Figure S 2.7). The value of J during the anodic wave increased as the electrodes were held at increasingly negative potentials during the CA. Typically, the anodic waves disappeared after the second CV cycle (Figure S 2.8). For comparison, E_{oc} of anodic current for an In metal foil electrode in 1.0 M H_2SO_4(aq) was ~-0.36 V vs RHE (Figure S 2.9). The observed anodic waves of n-InP electrodes held at $E \leq -0.6$ V vs RHE in the dark thus correspond to the stripping of In^0 metal plated onto the InP surface during the prior 30 min CAs (Eq 1):

$$\mathrm{In} \rightleftarrows \mathrm{In}^{3+} + 3e^- \qquad E^0 = -0.342 + 0.0197 \log{[\mathrm{In}^{3+}]}\ \mathrm{V\ vs.NHE} \qquad (1)$$

In 1.0 M KOH(aq), two anodic waves, one with E_{on}~-0.2 V vs RHE and the other with E_{on}~-0.15 V vs RHE were observed during the positive scan of the first CV for n-InP electrodes that had been held at $E \leq -0.4$ V vs RHE (Figure 2.2b and Figure S 2.6). A single reductive peak was observed at E ~ -0.25 V vs RHE in the return scan. Similar to the behavior in acid, electrodes that had been initially held at more negative potentials exhibited larger peaks in J. Similarly positioned anodic and cathodic waves were observed in the CVs of an In metal foil electrode in 1.0 M KOH(aq) (Figure S 2.10). The peak J depended linearly on scan rate, consistent with a redox process confined to a single monolayer of In atoms (Figure S 2.9b). Thus, the anodic waves observed after the CAs are consistent with the oxidation of metallic In^0 plated on the electrode surface to anhydrous and hydrated In(III) oxide (Eq 2a-b):

$$\mathrm{In} + 3\mathrm{OH}^- \rightleftarrows \mathrm{In(OH)_3} + 3e^- \qquad E^0 = -0.172\ \mathrm{V\ versus\ RHE} \qquad \text{(2a)}^{10}$$

$$2\mathrm{In} + 6\mathrm{OH}^- \rightleftarrows \mathrm{In_2O_3} + 3\mathrm{H_2O} + 6e^- \qquad E^0 = -0.190\ \mathrm{V\ versus\ RHE} \qquad \text{(2b)}^{10}$$

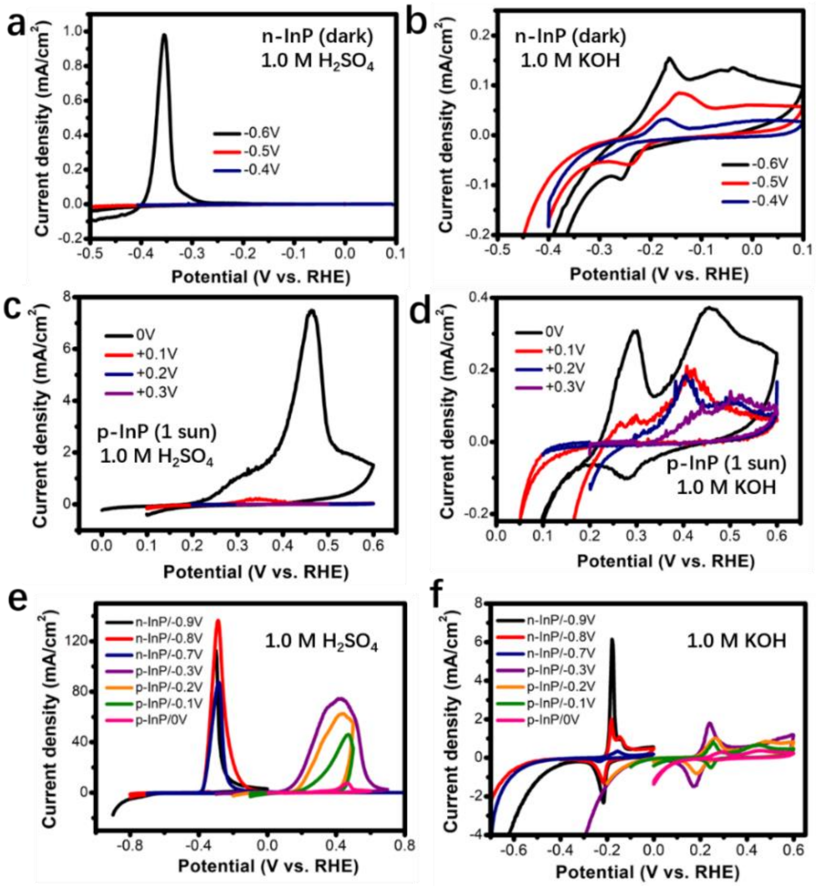

Figure 2.2 (a-b) Comparison of the 1st CV obtained after the 30-min CAs of n-InP electrodes at *E* from -0.6 to -0.4 V vs RHE in the dark in (a) 1.0 M H_2SO_4(aq) and (b) 1.0 M KOH(aq); (c-d) Comparison of the first CV obtained after the 30-min CAs of p-InP electrodes under 1-sun illumination at *E* = 0.3 V vs RHE in (c) 1.0 M H_2SO_4(aq) or (d) 1.0 M KOH(aq). (e-f) Comparison of the CVs of n-InP dark electrodes and illuminated p-InP electrodes, respectively, after 30-min CAs at various potentials, in (e) 1.0 M H_2SO_4(aq) and (f) 1.0 M KOH(aq). All CVs were scanned in the positive direction from the initially applied potential (scan rate: 20 mV s^{-1}).

In parallel, a series of 30-min CAs was performed for p-InP electrodes under 1-sun illumination between *E* = 0.3 and -0.3 V vs RHE, in both 1.0 M H_2SO_4(aq) and 1.0 M KOH(aq) (Figure 2.2c-d and Figure S 2.11). In the post-CA CVs, anodic waves similar to those exhibited by n-InP were observed in both electrolytes. However, the potentials of the waves were offset positively for the p-InP electrodes held at $E \leq +0.2$ V vs RHE in 1.0 M H_2SO_4(aq), and for all p-InP electrodes tested in 1.0 M KOH(aq). p-InP electrodes that had been held at negative E exhibited large peaks in J. These anodic waves are consistent with the deposition of metallic In^0 on the surface of illuminated p-InP electrodes during the prior 30-min CAs.[101,102] As shown in Figure 2.2e-f, comparisons between In^0 stripping waves in the CVs reveals positive shifts from n-InP (dark) to p-InP (light) by >550 mV and >400 mV in 1.0 M H_2SO_4(aq) and 1.0 M KOH(aq), respectively.

2.3.2 Stability of illuminated p-InP/Pt electrode for HER.

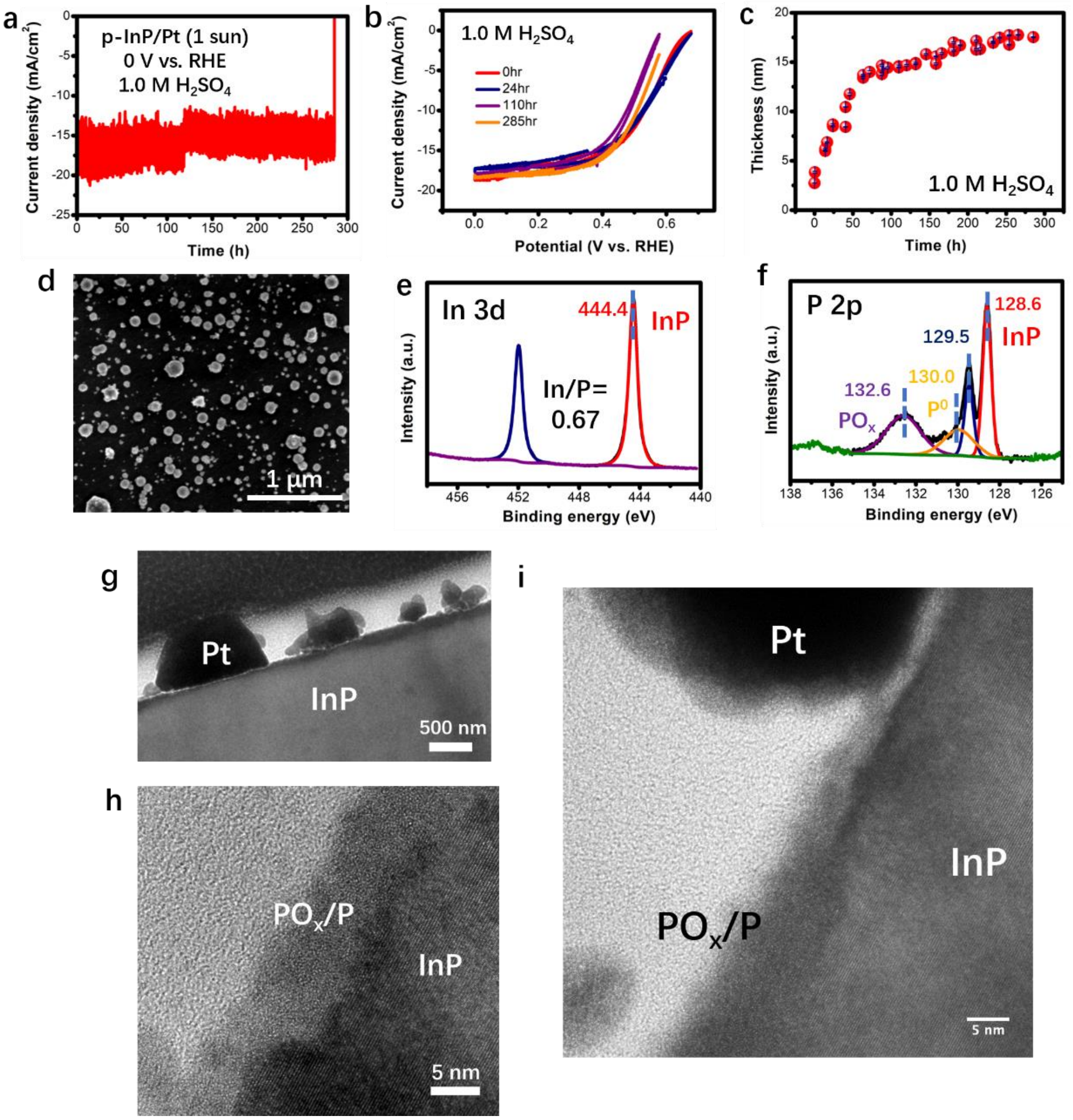

Figure 2.3 (a) CA of a p-InP/Pt photoelectrode at 0 V vs RHE in 1.0 M H_2SO_4(aq) under 1-sun illumination. (b) Comparison of *J-E* behaviors of a p-InP/Pt electrode (scan rate: 50 mV s^{-1}) and (c) the corrosion thickness of InP over time measured during the CA in (a). (d) SEM image and (e-f) XP spectra in the (e) In 3d and (f) P 2p regions, and (g-i) cross-sectional TEM images of the p-InP/Pt electrode after the 285 h of CA in (a).

The behavior of etched InP electrodes was also compared to the behavior of InP electrodes that had a layer of Pt electrodeposited onto the surface. Pt was electrodeposited over the surface of illuminated p-InP electrode (1 sun) at J = -0.2 mA cm^{-2} in a Pt plating solution, and the resulting p-InP/Pt electrodes were subsequently evaluated by CA at 0 V vs RHE in either 1.0 M H_2SO_4(aq) or 1.0 M KOH(aq). XPS analysis of the as-prepared p-InP/Pt electrode revealed a nearly stoichiometric InP surface (In/P=1.1) with minimal PO_x (Figure S 2.12). The SEM image showed that the electrodeposited Pt was present as sparsely distributed particles on the electrode surface (Figure S 2.13).

Prior to CA, the p-InP/Pt electrode yielded an open-circuit potential (E_{oc}) of 0.71±0.01 V vs RHE in contact with 1.0 M H_2SO_4(aq) under 1-sun illumination (Figure S 2.14). During CA at E = 0 V vs RHE in 1.0 M H_2SO_4(aq), the illuminated p-InP/Pt electrode exhibited a stable $|J|$ of 17.9±1.4 mA cm^{-2} for >285 h (Figure 2.3a). A gradual decrease of E_{oc} to ~0.55 V vs RHE was observed in the first 150 h and then towards the end of the experiment E_{oc} slightly increased to ~0.62 V vs RHE (Figure S 2.14). Despite the slight changes in E_{oc}, the J-E behavior of p-InP/Pt electrodes that was periodically measured during the CA remained nearly unchanged (Figure 2.3b). Within the first 50 h of CA, the leaching rate of In ions from p-InP into the electrolyte was ~0.15 nm h^{-1}, and after 150 h the leaching rate decreased to 0.03 nm h^{-1} (Figure 2.3c). After the 285 h CA, SEM imaging showed that the electrodeposited Pt particles remained on the surface (Figure 2.3d).

After CA, the XPS data in the In 3d region only showed a single peak ascribable to the In^{3+} cations of InP, whereas no peak attributable to metallic In^0 was observed (Figure 2.3e). The XPS data in the P 2p region revealed a pronounced peak at 132.7 eV, attributable to oxidized phosphorous (PO_x) at the electrode surface (Figure 2.3f). A new peak attributable to elemental P^0 emerged at BE =130.0 eV. The In/P atomic ratio decreased to ~0.67, indicating an enrichment of P over In at the electrode surface.

Consistent with the SEM image of p-InP/Pt after CA, electrodeposited Pt was visible as discrete micron-sized particles in the cross-sectional TEM image of the p-InP substrate (Figure 2.3g). Close examination of the p-InP surface reveals the presence of an amorphous overlayer with a maximum thickness of 8 nm in the regions of p-InP that had been exposed to the electrolyte. This layer is attributable to the oxidized phosphorous and elemental P^0 species observed in the XPS data (Figure

2.3h-i). In contrast, the amorphous layer was much thinner (~2 nm) in the regions directly beneath the Pt particles.

To better understand the formation of a P-rich surface of p-InP/Pt after long-term CA, two other p-InP/Pt electrodes were tested at *E* = 0 V vs RHE under 1-sun illumination, for 1 h and for 25 h, respectively, without intermediate CV experiments. XPS analysis indicated that the surfaces of both two electrodes remained nearly stoichiometric (In/P=1.2) with minimal oxidized phosphorus (Figure S 2.15). These results suggest that the observed P-enrichment of the electrode surface developed over long (>25 h) time periods of CA.

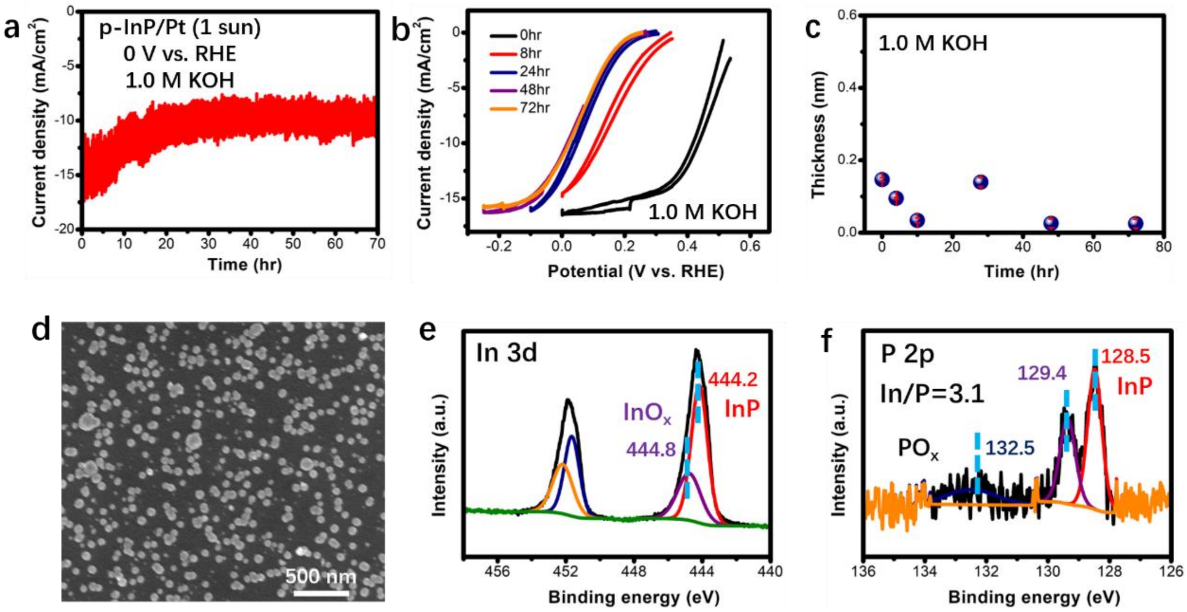

Figure 2.4 (a) CA for a p-InP/Pt electrode held at 0 V vs RHE in 1.0 M KOH(aq) under 1-sun illumination. (b) Comparison of the *J-E* behavior of a p-InP/Pt electrode (scan rate: 50 mV s^{-1}) and (c) the corrosion thickness of InP over time measured during the test in (a). (d) SEM image of p-InP/Pt electrode surface after the 72 h test. (e-f) XP spectra of the (e) In 3d and (f) P 2p regions of a p-InP/Pt electrode after 72 h of operation in (a).

In 1.0 M KOH(aq), the initial E_{oc} of the illuminated p-InP/Pt electrode (1 sun) was *E* = 0.63±0.03 V vs RHE, ~80 mV lower than the initial E_{oc} measured in 1.0 M H_2SO(aq). Within the first 24 h at $E = 0$ V vs RHE under 1-sun illumination, $|J|$ for the p-InP/Pt electrode in 1.0 M KOH(aq) gradually decreased from ~17 mA cm^{-2} to ~12 mA cm^{-2}, and subsequently remained nearly unchanged (Figure 2.4a). The decrease in $|J|$ is attributable to a substantial shift of the *J-E* behavior towards negative potentials during the first 24 h of CA (Figure 2.4b). In contrast, the *J-E* behavior of p-InP/Pt electrode remained nearly unchanged between 24 and 72 h of operation. Notably, the light-limited current density (J_{ph}) in the measured *J-E* behavior remained at ~ -17 mA cm^{-2} from the starting time to 72 h of operating time. Measurements of the concentrations of dissolved In ions in the electrolyte indicted negligible dissolution (<0.2 nm) of InP over the 72-h CA (Figure 2.4c). SEM images showed that discrete Pt particles remained on the p-InP surface after CA (Figure 2.4d). The atomic-force microscopy (AFM) image in the region of the p-InP that had been exposed to the 1.0 M KOH(aq) electrolyte showed aggregated nanoparticles, with a surface roughness (R_q) of 1.7 nm (Figure S 2.16).

After the 72-h of CA, the XPS data of the In 3d region (Figure 2.4e) displayed a distinct peak at higher BE = 444.8 eV ascribable to InO_x,[139–141] in addition to the peak at lower BE = 444.2 eV assigned to the In^{3+} cations in InP. Consistently, the XPS data in the O 1s region displayed a pronounced peak at 529.9 eV attributable to InO_x (Figure S 2.17).[138,142,143] The XPS data in the P 2p region showed peaks at BE <130 eV that are ascribable to the P^{3-} anions in InP, as well as a small peak at BE ~132 eV indicative of PO_x (Figure 2.4f). Notably, the increased atomic ratio of In/P (~3.1) after 72 h of operation indicated a substantial enrichment of In at electrode surface. Such In enrichment was not observed for the same p-InP/Pt electrode that however underwent only 3 cycles of CV in 1.0 M KOH(aq), with the surface In/P ratio remaining at ~1.3 (Figure S 2.18-19) for such electrodes.

Cross-sectional TEM images were obtained for a p-InP/Pt electrode after 72 h of CA in 1.0 M KOH (aq) (Figure 2.5a-c). A conformal overlayer attributable to the InO_x observed in the XPS data was evident on the exposed InP surface (Figure 2.5a). A higher magnification TEM image of the InP/InO_x interface revealed that this overlayer was amorphous and had a maximum thickness of 7 nm (Figure 2.5b). This amorphous layer was not observed at the InP/Pt interface (Figure 2.5c). An energy-dispersive X-ray spectroscopy (EDS) line scan showed that the atomic fraction of P gradually decreased from 50% to 0% within the 5 nm region beyond InP (In/P~1), accompanied by a rapid increase in the number of O atoms (Figure 2.5d). Collectively, these data suggest a gradient InP/$InPO_x$/InO_x interfacial region, consistent with the XPS analyses. The EDS mapping also confirmed the enrichment of In and O relative to P in the region beyond InP. Pt and Fe (~20 at.%) were observed in addition to the amorphous $InPO_x$/InO_x layer. The Pt was located closer to the InP substrate than Fe, implying that these small Pt particles resulted from the prior electrodeposition. Consistent with the EDS mapping, the XPS of Fe 2p (Figure S 2.20) revealed weak but observable signals attributable to trace FeO_x species (BE~711 eV), which may have deposited from the electrolyte during the long-term CA.

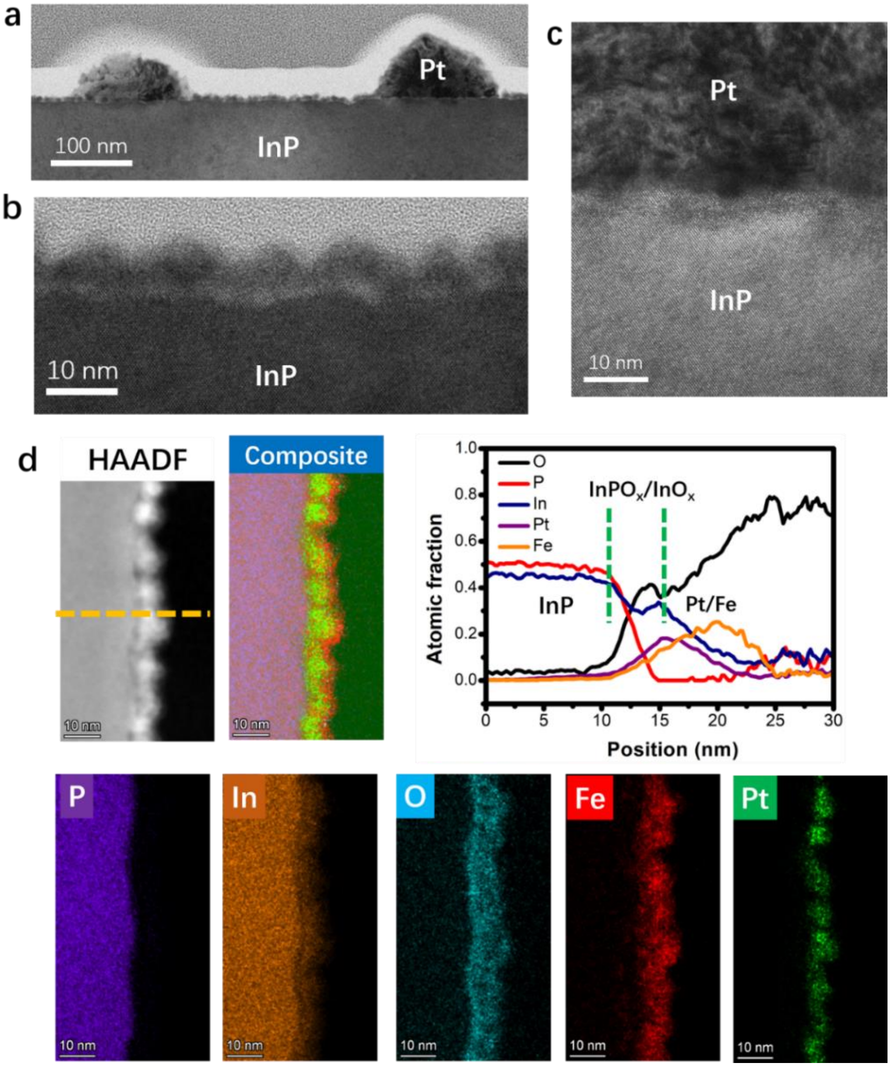

Figure 2.5 (a-c) Cross-sectional TEM images and (d) high-angle annular dark-field (HAADF) image, EDS maps and EDS line scan of the p-InP/Pt photoelectrode after 72 h at 0 V vs RHE in 1.0 M KOH(aq) under 1-sun illumination.

To robustly attribute the degradation in the *J*-*E* behavior to formation of interfacial InO_x, the illuminated p-InP/Pt electrode was first held in 1.0 M KOH(aq) at $E = 0$ V vs RHE for 15 h and was then immersed in 1.0 M H_2SO_4(aq). After the 15-h CA in KOH, the *J*-*E* behavior shifted towards negative potentials, and E_{oc} decreased from 0.62 to 0.34 V vs RHE (Figure 2.6). However, when the degraded p-InP/Pt electrode was further immersed in 1.0 M H_2SO_4(aq), the *J*-*E* behavior was immediately restored to its original shape before CA, accompanied by an increase in E_{oc} to 0.66 V vs RHE. The XPS data (Figure S 2.21) confirmed that after exposure to 1.0 M H_2SO_4(aq), the electrode surface was restored to nearly stoichiometric InP (In/P=1.2) and no peak ascribable to InO_x was observed in either the O 1s and In 3d XPS regions.

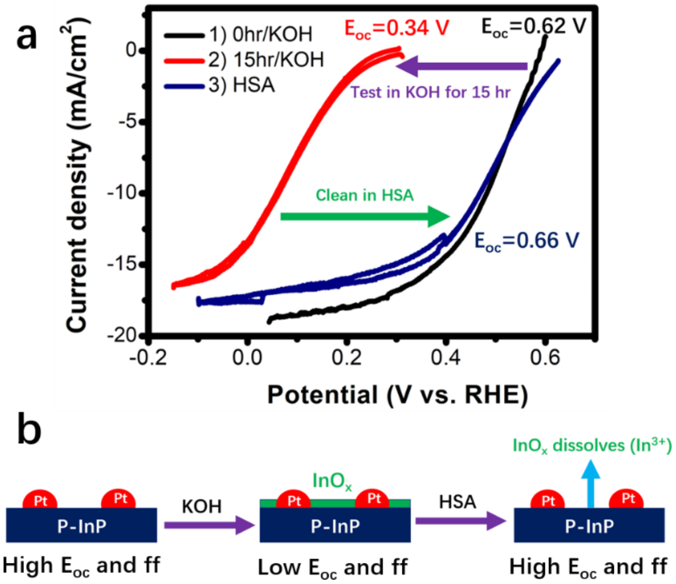

Figure 2.6 (a) Comparison of the *J-E* behavior of the illuminated p-InP/Pt electrode before (black) and after (red) testing at 0 V vs RHE for 15 h in 1.0 M KOH(aq) and then after (blue) exposure to 1.0 M H_2SO_4(aq). Scan rate: 50 mV s^{-1}. (b) Schematic illustration of the formation of InO_x on InP during the stability test in 1.0 M KOH(aq) and its subsequent dissolution in 1.0 M H_2SO_4(aq). E_{oc} and *ff* represent the open-circuit voltage and fill factor of the photoelectrode, respectively.

The XPS analyses of p-InP/Pt at pH 0 and pH 14 collectively indicate that under both conditions the presence of Pt inhibited the cathodic corrosion of p-InP to form metallic In^0. To further understand the kinetic effect of the Pt HER catalyst, the stability of n-InP and n-InP/Pt electrodes was evaluated in the dark at E = -0.1 V vs RHE in 1.0 M H_2SO_4(aq) or 1.0 M KOH(aq). The value of E = -0.1 V vs RHE matched the overpotential of a Pt catalyst when producing J ~ -10 mA cm^{-2} for the HER.[144] Use of n-InP electrodes, in which electrons are majority charge carriers, in the dark allows deconvolution of photovoltage effects that are inherent in illuminated p-InP electrodes. A dissolution rate of ~0.3 nm h^{-1} was observed for an etched n-InP electrode evaluated for 72 h in 1.0 M H_2SO_4(aq) (Figure S 2.22). After the CAs at *E* = -0.1 V vs RHE, three different etched n-InP electrodes, as well as an n-InP/Pt electrode, displayed stoichiometric InP surfaces (In/P=1.2) with no appreciable additional detectable species such as In^0 and PO_x (Figure S 2.23 and Figure S 2.26). In 1.0 M KOH(aq), dissolution of In ions was not observed for n-InP or n-InP/Pt electrodes (Figure S 2.22 and Figure S 2.25). Two n-InP samples tested for different durations of CA showed a slight enrichment (In/P=1.4) in In, in the form of $In(OH)_3$, at the electrode surface (Figure S 2.24). In contrast, in contact with KOH, the n-InP/Pt electrode displayed a stoichiometric InP surface (Figure S 2.26). In contrast to previous results in which n-InP electrodes were tested by CA at more much more negative *E* than those used herein, metallic In^0 was not detected for n-InP electrodes operated at *E* = -0.1 V vs RHE. These collective results indicate that the dissolution and surface conditions of illuminated p-InP/Pt electrodes resemble those of both n-InP and n-InP/Pt tested at *E* = -0.1 V vs RHE in the dark, at both pH 0 and pH 14.

2.4 Discussion

Pourbaix diagrams[125] that represent thermodynamic electrochemical equilibria in aqueous solutions are useful for analysis of the electrochemical corrosion of semiconductors. Although Pourbaix diagrams typically only consider ions and compounds formed between single elements and water, simultaneous consideration of the diagrams for each element in a compound provides insight into the reactions that can occur under various conditions of pH and *E*. Figure S 2.27 shows a combined In-P Pourbaix diagram obtained from the Materials Project. The formal oxidation states in InP are In^{+3} and P^{-3}. Moreover, the reaction of either element with water is irreversible, as In^{+3} and P^{-3} do not co-exist in any *E*-pH region. Table S 2.1 shows the half-reactions of In and P relevant to the decomposition of InP at pH 0 and pH 14. Table S 2.2 summarizes the experimental results obtained herein.

Cathodic corrosion of InP: At sufficiently negative *E*, electrochemical reduction of InP to metallic In^0 can occur, with the production of PH_3(g) at both pH = 0 and pH = 14 (Eq 3a-b):[136,137]

In acid: $$\mathrm{InP(s) + 3H^+(aq) + 3e^- \longrightarrow In(s) + PH_3}(g) \qquad (3a)$$

In base: $$\mathrm{InP(s) + 3e^- + 3H_2O(l) \longrightarrow In(s) + PH_3(g) + 3OH^-}(aq) \qquad (3b)$$

For Eq 3a, a calculation using the values of the formation energy reveals that $E(\mathrm{InP/In^0})$ is ~-0.31 V vs RHE, which is close to the standard redox potential of the $\mathrm{In^{3+}/In^0}$ couple (-0.34 V vs RHE at pH = 0). Eq 3a and 3b contain mutually the same number of protons/water and electrons, suggesting that as the pH is varied the $\mathrm{E(InP/In^0)}$ should stay fixed relative to the RHE potential. Therefore, at pH = 14, the $E(\mathrm{InP/In^0})$ is predicted to be slightly more negative than either $E(\mathrm{In_2O_3/In^0})$ = -0.19 V vs RHE or $E(\mathrm{In(OH)_3/In^0})$ = -0.172 V vs RHE. In this work, appreciable $\mathrm{In^0}$ plating on the n-InP surface in the dark was observed at $E \leq$ -0.6 V vs RHE for pH 0 and at $E \leq$ -0.4 V vs RHE for pH 14, respectively. These results are thus consistent with the calculated value of $E(\mathrm{InP/In^0})$.

Mott-Schottky analysis was performed at both pH 0 and pH 14 to estimate the band-edge positions of InP relative to RHE (Figure S 2.28a-d). For n-InP, the flat-band potentials (E_{fb}) were -0.34 V vs RHE in $\mathrm{H_2SO_4}$ and -0.27 V vs RHE in KOH, whereas for p-InP, E_{fb} was 0.91 V vs RHE in $\mathrm{H_2SO_4}$ and was 0.95 V vs RHE in KOH. E_{fb} of both n-InP and p-InP thus remained essentially constant relative to the RHE potential as the solution pH was varied from 0 to 14. Figure S 2.28e shows an analysis of interfacial energetics between the band-edge positions of InP, the value of $E(\mathrm{InP/In^0})$ and the RHE potential, and applies to both pH 0 and pH 14.[101,102]

The $\mathrm{In^0}$ stripping waves shifted substantially (>0.4 V) between dark n-InP electrodes and illuminated p-InP photoelectrodes. As shown in Scheme 2.1a, the positive shifts suggest a photovoltage effect produced by the p-InP photoelectrode, leading to a splitting between the potentials of the quasi-Fermi levels (E_{qf}) of minority carriers (electrons) and majority carriers (holes). Under negative bias, the surface potential (E_{surf}) is expected to be much more negative than the potential applied to the back contact of the electrode (E_{app}). Moreover, substantial $\mathrm{In^0}$ plating was observed at the surface of illuminated p-InP electrodes when $E \leq$ 0.2 V vs RHE for both pH = 0 and pH 14. Despite $E_{\mathrm{app}} > \mathrm{E(InP/In^0)}$, the occurrence of cathodic corrosion at the surface of the illuminated p-InP electrode suggests that the photogenerated electrons from the conduction band of p-InP are energetically able to promote the reduction of InP to $\mathrm{In^0}$ at the InP/electrolyte interface.

The cathodic photocorrosion of p-InP to In^0 comprises a primary failure mode for the p-InP photocathode. The deposition of In^0 on the p-InP surface led to a rapid decay in *J* at negative potentials characterized by cathodic current flow, as metallic In^0 is optically opaque with a high overpotential for the HER (Figure S 2.29). Under negative bias, the plated In^0 metal on the InP surface was partially soluble at pH = 0 but almost insoluble at pH = 14. The cathodic corrosion of InP to In^0 can occur due to the slow kinetics of HER at etched InP surfaces, resulting in a large overpotential (η) to effect $J > 10$ mA cm^{-2}. In the dark, an etched n-InP electrode produced $J = -1$ mA cm^{-2} at $E = -0.78$ V vs RHE in 1.0 M H_2SO_4(aq) and at $E = -0.66$ V vs RHE in 1.0 M KOH(aq), with both of these potentials much more negative than either $E(InP/In^0)$ or the RHE potential (Figure S 2.30). As a consequence, under negative bias sufficient to produce cathodic currents through the InP, photogenerated electrons of illuminated etched p-InP electrodes compete between effecting the HER and the reduction of InP.

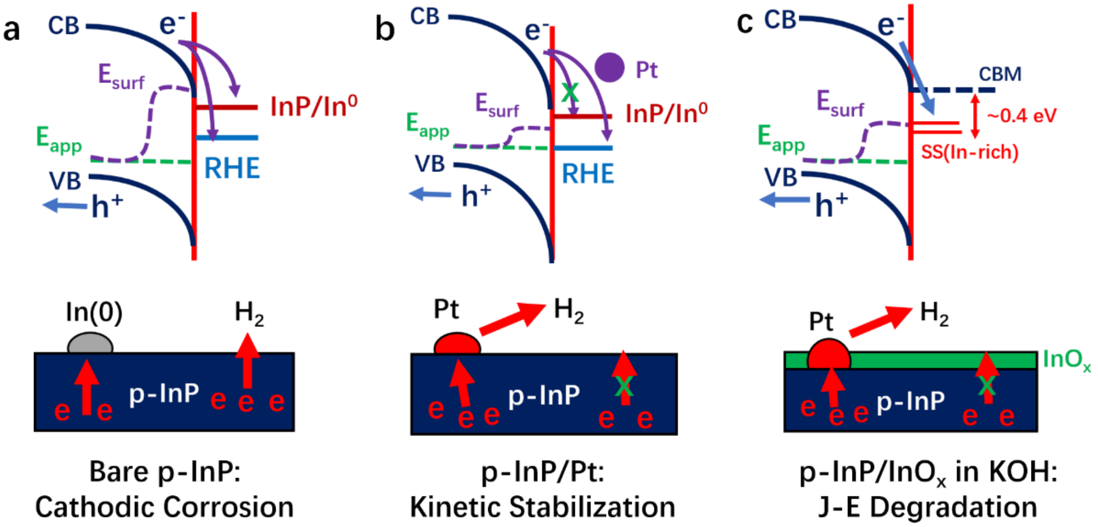

Bare p-InP: Cathodic Corrosion

p-InP/Pt: Kinetic Stabilization

p-InP/InO_x in KOH: J-E Degradation

Scheme 2.1 Comparison of the band energy diagram and the direction of photogenerated electron (e^-) flow for (a) an etched p-InP electrode, (b) a p-InP/Pt electrode and (c) a p-InP/InO_x/Pt electrode under illumination in contact with KOH. E_{app} and E_{surf} represent the applied potential at the back contact and the surface potential of photogenerated minority carriers (e^-), respectively. SS represents the surface states produced by an In-rich surface of p-InP, ~0.4 eV below the conduction-band minimum (CBM).[99] $E(InP/In^0)$ and RHE represent the thermodynamic equilibrium potentials for the cathodic corrosion of p-InP and for the HER, respectively, which are ~ -0.31 V vs RHE and 0 V vs RHE at both pH 0 and pH 14.

Kinetic stabilization of p-InP by Pt catalyst: Metallic In^0 was not detected by XPS on illuminated p-InP/Pt electrodes after extended periods of CA at 0 V vs RHE at either pH 0 or pH 14. These results suggest that the presence of Pt at p-InP surface inhibits cathodic corrosion. During the CA tests, a large portion of the p-InP surface was nevertheless still exposed to the acidic or alkaline electrolyte. Because $E(InP/In^0)$ was more negative than the RHE, the HER is thermodynamically favored compared with the cathodic corrosion of InP. Hence, the lack of metallic In^0 formation reveals a kinetic effect of the Pt HER catalyst, consistent with expectations for Pt substantially reducing the kinetic η of the HER at the electrode surface. Based on the HER activity of Pt, a small η of < 200 mV is required to produce J = -20 mA cm^{-2}.[144,145] Under light-limited current densities (J_{ph}) for p-InP, the E_{surf} of p-InP/Pt occurs in a potential region between the RHE potential and $E(InP/In^0)$, due to the facilitated surface kinetics (Scheme 2.1b). In this scenario, the photogenerated electrons from the p-InP can selectively perform the HER at these photocurrent densities without effecting the self-reduction of InP. Previous studies using the dual working electrode (DWE) technique support the expectation that the E_{surf} of the semiconductor photoelectrode is largely determined by the surface kinetics, and becomes fixed by J_{ph} even at increasingly negative E_{app} values.[75–77] These results thus reveal that the specific energy level of E_{surf} and the surface kinetics are important for defining the corrosion chemistry of p-InP photoelectrodes, in accord with expectations based on early theories of semiconductor stability.[71,146]

To verify such a hypothesis, we also carried out dual-working photoelectrochemistry experiments on p-InP and p-InP/Pt electrodes for the HER, which were shown in the appendix. The results confirmed that the E_{surf} saturated at <-0.2 V vs. RHE when J reached the values of J_{sc}, even when E_{app} approached -1 V vs. RHE. These results again suggested that the value of E_{surf} can be simply considered as a function of J at front surface together with catalytic kinetics, regardless of E_{app}.

The reaction pathways can be determined by referring to the around E = -0.1 V vs RHE in the In-P Pourbaix diagram at both pH 0 and pH 14:[147]

In acid: $\mathrm{InP(s) + 4H_2O(l) + 3H^+(aq) \longrightarrow In^{3+}(aq) + H_3PO_4(aq) + 4H_2(g)}$ (4a)

In base: $2\mathrm{InP(s)} + 6\mathrm{OH^-(aq)} + 5\mathrm{H_2O(l)} \longrightarrow \mathrm{In_2O_3(s)} + 2\mathrm{PO_4^{-3}(aq)} + 8\mathrm{H_2(g)}$ (4b)

At pH 14, only the insoluble In_2O_3 instead of the InO_2^- ion is considered here, due to the negligible observed dissolution of In ions. In both cases, the Fermi level (E_f) of electrons or the surface potentials ($E_{f,n}$) are not sufficient energetically to trigger the self-reduction of In^{3+} cations in InP. The main driving force of these corrosion reactions is assigned to the reduction of water or protons by the highly reducing P^{3-} anions of InP. The oxidation potentials of PH_3(g) to species in the P(III) oxidation state (H_3PO_3 at pH 0 and HPO_3^{2-} at pH 14) are ~ -0.28 V vs RHE and ~ -0.48 V vs RHE at pH 0 and pH 14, respectively (Table S 2.1). The more negative values of $E(P^{3+}/P^{3-})$ relative to the RHE potential corrobates the hypothesis that the P^{3-} anions in InP have sufficient reducing power to reduce water or protons to H_2.

XPS analyses and ICP-MS measurements both support the above corrosion pathways (Eq 4a-b). In acidic electrolyte, the illuminated p-InP/Pt electrode displayed a slow dissolution rate of ~0.15 nm h^{-1} for the first 50 h, which slowed down to ~0.03 nm h^{-1} after 150 h. The XPS data also show that during the CA at 0 V vs RHE, the p-InP/Pt surface remained nearly stoichiometric (In/P=1.2) in the first 25 h, corresponding to a stoichiometric dissolution of In and P into the electrolyte based on Eq 4a. Despite the predicted thermodynamic instability, the dissolution kinetics of illuminated p-InP/Pt electrodes is sufficiently slow to provide an operationally stable photocathode for >285 h. The decreased dissolution rate after long-term operation of the HER (>150 h) is attributable to passivation of the surface with a PO_x/P^0 layer, resulting in a P-rich surface of p-InP. Under alkaline conditions, the p-InP/Pt electrode evaluated by CA at 0 V vs RHE exhibited negligible dissolution over 72 h. However, the surface of p-InP was enriched with InO_x, indicating a surface conversion process (Eq 2b). The preserved InO_x layer at the p-InP surface after the 72-h CA at 0 V vs RHE also suggests a much lower solubility of InO_x in KOH than in H_2SO_4, leading to different surface conditions depending on the pH of electrolyte.

pH-dependent evolution of *J-E* behavior: The long-term evolution of the *J-E* behavior of illuminated p-InP/Pt electrodes also depends on the pH of the electrolyte. In acidic electrolytes, the *J-E* behavior remained nearly unchanged for as long as 285 h, despite the slightly lower E_{oc}. This behavior was accompanied by: (1) a nearly stoichiometric InP surface in the initial 25 h of CA, which then converted into a P-rich surface; and (2) a slow but continuous leaching of In^{3+} ions from electrode surface. In contrast, continuous leaching of In ions was not observed for the illuminated p-InP/Pt electrode in KOH. Instead, the surface passivation of p-InP with InO_x caused substantial degradation in the *J-E* behavior of a p-InP/Pt electrode. These results reveal the importance of surface stoichiometry (In/P atomic ratio) for determining the long-term evolution of the *J-E* behavior of p-InP/Pt photocathodes.

Based on the unified defect model by Spicer et al, a non-stoichiometric surface of InP with additional In or P atoms can lead to surface states (SS) within the band gap, altering the electrical behavior of the interface.[99,148,149] According to this model, an In-rich surface and a P-rich surface of InP create surface states located 0.4 eV and 0.1 eV below the conduction-band minimum (CBM), respectively. Thus, for p-InP, the impact of Fermi level pinning by surface states is expected to be more pronounced for an In-rich surface (Scheme 2.1c). In this study, the observed evolution in the *J-E* behavior of illuminated p-InP/Pt electrodes is consistent with this model. After long-term CAs, the In-rich surface of p-InP that formed in alkaline electrolytes caused a more substantial degradation of the *J-E* behavior than surfaces in acidic electrolytes which did not contain metallic In.

These results moreover suggest that the physical stability (dissolution) and electrochemical stability (decay in *J*) of a p-InP/Pt electrode need to be considered separately. At pH = 0, the p-InP/Pt photoelectrode is physically unstable with a slow rate of dissolution while providing stable PEC performance. At pH = 14, the p-InP/Pt photoelectrode remains physically robust without continuous dissolution but its PEC performance degrades over time.

As shown in the In-P Pourbaix diagram (Figure S 2.27), InP is not predicted to be a stable phase in any *E*-pH region, indicating its thermodynamic tendency to undergo surface corrosion via In-P dissociation in an aqueous environment. A comparison between the different changes in surface conditions of p-InP/Pt at pH = 0 and pH 14 suggests that the formation of InO_x at the surface of p-InP/Pt may be universal regardless of pH. However, the higher solubility of InO_x in acidic electrolytes caused the rapid and continuous dissolution upon formation of the oxide, whereas in alkaline electrolytes the insoluble InO_x layer led to surface passivation. The stable PEC performance of p-InP/Pt at pH 0 is thus ascribable to a “self-cleaning” behavior that maintains a nearly stoichiometric surface by slowly dissolving the InO_x layer and leaching out In^{3+} ions. This hypothesis is further supported by the immediate recovery of the *J-E* behavior of the KOH-degraded p-InP/Pt electrode after exposure to acidic electrolytes. Further strategies for the development of stable p-InP photocathodes in either acidic or alkaline electrolytes could consequently focus on minimization of continuous dissolution while preserving a stoichiometric surface to enable stable PEC performance.

Outlook: The present work has implications that can be generalized for understanding the stability and corrosion mechanism of semiconductor photoelectrodes. The photovoltage produced by the semiconductor may complicate a direct analysis of the thermodynamic potentials of corrosion reactions. Hence, this photovoltage effect needs to be deconvoluted from the surface thermodynamic potentials to understand the fundamentals of the corrosion chemistry at the front-surface of the photoelectrode. Due to varied overpotentials at a given *J*, the catalytic kinetics at electrode surface are crucial for defining the corrosion pathways at semiconductor/electrolyte interfaces, based on the Pourbaix diagram. For the HER, the presence of electrocatalysts such as Pt moves the surface potential closer to the RHE potential, which may result in a different corrosion chemistry than is present at an etched semiconductor surface. The onset potentials for the corrosion reactions should moreover be compared to the potentials for the fuel-forming reactions to identify a possible stability window that would take advantage of both thermodynamics and kinetics. For p-InP, cathodic corrosion can be systematically inhibited by accelerating the surface kinetics of the thermodynamically favored HER. Moreover, the *J-E* behavior of the semiconductor photoelectrode is sensitive to the changes in surface stoichiometry, and a non-stoichiometric surface can lead to operational instability. Thus, the physical stability and electrochemical stability of semiconductor photoelectrodes needs to considered separately. Overall, this work provides insights into rational understanding of the stability of semiconductor photoelectrodes and consequently is beneficial for designing further strategies towards the realization of stable solar fuel devices.

2.5 Conclusions

The stability of p-InP has been evaluated for use as a photocathode for the HER in both 1.0 M H_2SO_4 (aq) and 1.0 M KOH (aq), with or without an electrodeposited Pt catalyst. The corrosion mechanisms of etched p-InP and p-InP/Pt photoelectrodes were systematically established using XPS to monitor changes in the surface conditions after electrochemical tests, and the electrode dissolution over time was assessed using ICP-MS. In either H_2SO_4 or KOH, illuminated etched p-InP photoelectrodes underwent cathodic corrosion to form metallic In^0 at the electrode surface. In contrast, electrodeposited Pt at p-InP surfaces kinetically stabilizes illuminated p-InP electrode against self-reduction in both H_2SO_4 and KOH. When held at $E = 0$ V vs RHE in acidic electrolytes, the p-InP/Pt photoelectrode exhibited a stable J of ~ -18 mA cm^{-2} for >285 h. The long-term evolution of the J-E behavior of the p-InP/Pt photoelectrode was dependent on the pH of the electrolyte, and strongly correlated with surface changes as well as with dissolution of the p-InP electrode. In 1.0 M H_2SO_4(aq), the surface of p-InP/Pt electrode gradually turned P-rich with slow and continuous leaching of In ions, while the J-E behavior remained essentially unchanged. In 1.0 M KOH(aq), the p-InP/Pt electrode exhibited negligible dissolution while forming a passivating surface a InO_x layer that caused substantial degradation in J-E performance. This work reveals the importance of both catalytic kinetics and surface stoichiometry for defining the long-term stability of semiconductor photoelectrodes.

Acknowledgement

This material is based upon work performed by the Joint Center for Artificial Photosynthesis, a DOE Energy Innovation Hub, supported through the office of Science of the U.S. Department of Energy under Award Number DE-SC0004993. Research was in part carried out at the Molecular Materials Research Center (MMRC) of the Beckman Institute of the California Institute of Technology. W. Yu and C. G. Read acknowledge the Resnick Sustainability Institute (RSI) at Caltech for fellowship support. I. M. Hernandez acknowledges a National Science Foundation Graduate Research Fellowship (Grant No. DGE-1144469). Prof. Dr. Hans-Joachim Lewerenz, Dr. Ke Sun and Dr.

Chengxiang Xiang are gratefully acknowledged for inspiring discussions. Dr. Nathan Dalleska is thanked for assistance with ICP-MS analyses. Ryan Jones is acknowledged for assistance with the design of the compression cell. Sean Byrne and Heng Dong are acknowledged for assistance with experiments.

2.6 Experimental

2.6.1 Materials

All chemicals and materials were used as received, including sulfuric acid (H_2SO_4, Fisher Scientific, TraceMetal Grade, 93-98%), 1.0 M sulfuric acid solutions (H_2SO_4, VWR Chemicals), potassium hydroxide (KOH, Sigma-Aldrich, semiconductor grade, 99.99 % trace-metal basis), bromine (Br_2, reagent grade, Sigma-Aldrich), ammonia/methanol solution (4.0 M, Sigma-Aldrich), and methanol (CH_3OH, VWR Analytical, ACS, 99.8 %). Deionized water with a resistivity of 18.2 MΩ cm was obtained from a Barnstead Millipore system. Single-side polished, (100)-oriented, Sn-doped (N_d = 1-5×10^{17} cm^{-3}), n-type InP wafers and Zn-doped (N_d = 1-5×10^{17} cm^{-3}), p-type InP wafers were obtained from AXT Inc. Indium foil (0.25 mm thick, 99.99 %) was purchased from VWR International. Nafion (proton-exchange membrane) and Fumasep (anion-exchange membrane) were purchased from the Fuel Cell Store.

2.6.2 Purification of 1.0 M H_2SO_4(aq) and 1.0 M KOH(aq) by pre-electrolysis

Prior to use, the prepared 1.0 M H_2SO_4(aq) and 1.0 M KOH(aq) electrolytes were pre-electrolyzed in a two-compartment electrochemical cell, with the two compartments separated by either a Nafion (acid) or Fumasep (base) membrane. The pre-electrolysis was performed for > 24 h under either a constant > 3 V bias or under a constant current of 6 mA, using two separate carbon cloth or carbon rod electrodes. In some pre-electrolysis experiments, a Ni foil electrode was also used as the anode for pre-electrolysis of 1.0 M KOH(aq). Only the pre-electrolyzed electrolyte in the cathode compartment was used in subsequent electrochemical measurements. After the electrolysis, H_2O_2 was not detectable in the catholyte, as determined by spectrophotometric analysis using titanium oxalate.[150]

2.6.3 Back contacts to InP electrodes

Ohmic back contacts to n-type InP were obtained by sputtering 20 nm of Ni onto the back (unpolished) side of the n-InP wafer and then annealing the sample under forming gas at 400 °C for 10 min. Sputter deposition of Ni was performed in an AJA Orion sputtering system. Ohmic back contacts to p-type InP were obtained by sputtering 10 nm of Zn and then 90 nm of Au onto the back side of the wafer and then annealing the sample under forming gas at 400 °C for 10 min.[134]

2.6.4 Epoxy-encapsulated electrodes

For electrochemical measurements made outside the glovebox, the back contact to the InP sample was attached to a coiled, tin-plated Cu wire (McMaster-Carr) using high-purity Ag paint (SPI supplies). The Cu wire was then threaded through a piece of glass tubing (Corning Incorporated, Pyrex tubing, 7740 glass). The sample was encapsulated in, and sealed to, the glass tube using Hysol 9460F epoxy, which was allowed to dry overnight under ambient conditions. The exposed areas of each electrode were imaged using a high-resolution optical scanner (Epson Perfection V370 with a resolution of 1200 psi) and the geometric areas of the electrodes (typically 0.03-0.10 cm^2) were analyzed using ImageJ software.

2.6.5 InP etching

Prior to electrochemical measurements, n-InP and p-InP electrodes were etched in 0.04% (by volume) Br_2/CH_3OH for 30 s, then in 4.0 M NH_3/CH_3OH for 30 s, and then rinsed in pure CH_3OH for 10 s.[59] The etching and rinsing cycle was then repeated two more times. The electrodes were blown dry for >10 s under a stream of flowing N_2(g). Etching was performed outside the glove box.

2.6.6 Electrochemical measurements in an O_2-free environment

Electrochemical measurements on samples that were analyzed by XPS were performed in a nitrogen-filled glovebox (VAC, OMNI-LAB) using electrolytes that had been degassed in a Schlenk line (Figure S 2.2a). The concentration of O_2 in the glove box was < 1.0 ppm as monitored by an O_2-sensitive electrode (Fuel Cell Sensor, AMI Acetic, Type T2).

To facilitate XPS analysis of the samples, electrochemical measurements were performed using a custom compression cell fabricated from PEEK (Figure S 2.1).[151] The cell had two compartments separated by an ion-exchange membrane (Nafion for measurements in H_2SO_4, and Fumasep for measurements in KOH). Electrochemical measurements were performed using a SP-200 potentiostat (BioLogic Science Instruments) and a three-electrode set-up with either a Pt foil (for H_2SO_4) or a Ni foil (for KOH) as the counter electrode, and either a leakless miniature AgCl/Ag electrode (eDAQ, ET072-1) or a hydrogen electrode HydroFlex (Gaskatel) as the reference electrode. Electrochemical data were acquired without compensation for the series resistance of the solution. During electrochemical experiments, H_2(g) was fed into the glovebox, passed through a gas bubbler, and fed into the catholyte to constantly purge the solution (Figure S 2.2b). Separate outlets were provided for H_2 from the cathode chamber and for O_2 from the anode chamber. Prior to each experiment, the electrochemical cell was assembled immediately after InP etching, and the assembled cell was then promptly transferred into the glovebox.

Electrochemical data were acquired on an SP-200 potentiostat (BioLogic Science Instruments) without compensation for the series resistance of the solution. To periodically measure the *J*-*E* behavior of illuminated p-InP/Pt electrodes, chronoamperometry (CA) was first interrupted by a short period (15 s) of open circuit to measure E_{oc}. In each cycle, cyclic voltammetry (CV) was started from $E_{start} = E_{oc}$-30 mV to < 0 V vs RHE and then ended at $E_{end} = E_{oc}$-80 mV, to minimize passing anodic current through the electrodes. Three CVs were measured during each cycle.

A miniature fiber-optic adjustable-arm light equipped with a 150 W halogen bulb was used as the illumination source. Illumination was introduced from the source into the glove box via the fiber optic. The illumination intensity at the location of the sample in the cell was calibrated to 1 Sun (100 mW cm^{-2}) using a Si photodiode (FDS100, Thorlabs). The volume of electrolyte in the cathode chamber was 3-4 mL. For each ICP-MS analysis, 0.2 mL of electrolyte was removed from the cell at different time intervals and 0.2 mL of fresh electrolyte was added into the cell. After each experiment was completed, the cell was disassembled inside the glove box, and the electrode sample was thoroughly cleaned with deionized water, dried under stream of flowing N_2(g), and stored inside the glove box until the surface was analyzed by XPS.

2.6.7 Electrodeposition of Pt particles

A solution of 5 mM K_4PtCl_6 and 0.5 M KCl was used to electrodeposit Pt particles onto InP samples. A constant current density of -0.2 mA cm^{-2} was applied using a two-electrode configuration until 20 mC cm^{-2} had passed. Before each deposition, bubbles accumulating in the electrode area were carefully removed to ensure the uniformity of electrodeposition. The deposition was performed under ~1 Sun illumination for p-InP and in the dark for n-InP. Either a Pt wire or a carbon rod was used as the counter electrode for the deposition. The cell was then thoroughly cleaned with deionized water at least 3 times before the 1.0 M H_2SO_4 or 1.0 M KOH electrolyte used for electrochemical experiments was added to the cell. For the stability test of p-InP/Pt in 1.0 M KOH(aq), the Pt deposition and the subsequent hydrogen-evolution reaction (HER) process were performed in two separate cells to minimize cross-contamination.

2.6.8 Electrochemistry outside glovebox

A series of chronoamperometry (CA) and cyclic voltammetry (CV) experiments for n-InP (dark) and p-InP (light) were performed in a two-compartment cell outside the glove box under a continuous H_2 purge (Figure S 2.2). These experiments did not involve XPS analyses after electrochemical operation. The CA experiments were performed by potentiostatically holding freshly etched InP electrodes at specified potentials for 30 min. At least three voltammetric cycles were then scanned in the positive direction from the original polarization potential to potentials sufficient to oxidize any deposited In metal.

Electrochemical measurements were performed using a custom two-compartment electrochemical cell with a Nafion (1.0 M H_2SO_4) or Fumasep (1.0 M KOH) membrane separating the two compartments. The electrochemical cell was cleaned with aqua regia before use. The volume of the electrolyte used in the cathode compartment was 20 or 25 mL. A mercury/mercurous sulfate ($Hg/HgSO_4$ in saturated K_2SO_4(aq), CH Instruments, CH151) reference electrode was used for measurements in 1.0 M H_2SO_4(aq). A mercury/mercury oxide (Hg/HgO in 1.0 M KOH (aq), CH Instruments, CH152) reference electrode was used for measurements in 1.0 M KOH (aq). A carbon rod placed within a fritted glass tube (gas dispersion tube Pro-D, Aceglass, Inc.) was used as the counter electrode. Both the $Hg/HgSO_4$ and the Hg/HgO reference electrodes were calibrated versus a reversible hydrogen electrode (RHE). The Hg/HgO electrode potential was 0.910 V versus RHE in 1.0 M KOH (aq). The $Hg/HgSO_4$ electrode potential was 0.683 V versus RHE in 1.0 M H_2SO_4 (aq).

Electrochemical data were acquired on an MPG-2 multichannel potentiostat (BioLogic Science Instruments) without compensation for the series resistance of the solution. During measurements, the electrolyte was continually bubbled with 1 atm of H_2(g) and vigorously agitated with a magnetic stir bar driven by a model-train motor (Pittman) with a Railpower 1370 speed controller (Model Rectifier Corporation) or a magnetic stirrer (IKA Topolino). 50 W ENH-type (Philips MR16) W-halogen lamps with dichroic rear reflectors and custom housings and transformers (Staco Energy Products Co.) were used for photoelectrochemical measurements. The illumination intensity at the position of the working electrode in the electrochemical cell was determined by placing a calibrated Si photodiode (FDS100-Cal, Thor Labs) into the cell at the same position occupied by the photoelectrode. To illuminate the bottom-facing photoelectrodes, a broadband reflection mirror (Newport dielectric mirror) was used to direct the uniform light beam in the vertical direction.

2.6.9 Mott-Schottky Analyses

Impedance measurements of freshly etched n-InP and p-InP electrodes, in contact with 1.0 M H_2SO_4(aq) or 1.0 M KOH(aq) under H_2(g) bubbling, were collected in the dark over a frequency range of 20 Hz to 20 kHz with a sinusoidal wave amplitude of 25 mV. The measurements were performed outside the glove box. The impedance measurements were fit with a circuit consisting of a resistor in series with an additional component consisting of a resistor and a capacitor in parallel.[51,152] The potential dependence of the differential capacitance was analyzed using the Mott-Schottky relationship:

$$C_d{}^{-2} = \frac{2}{qA^2\varepsilon_0\varepsilon_r N_d}(V_{app} + V_{bi} - \frac{k_B T}{q})$$

where C_d is the differential capacitance, q is the unsigned charge of an electron, A is the electrode area, ε_0 is the vacuum permittivity, ε_r is the relative permittivity of the semiconductor, N_d is the dopant concentration of the semiconductor, E_{app} is the applied electrode potential, V_{bi} is the built-in voltage in the semiconductor, and T is the temperature of the electrode while the impedance data were collected. A relative permittivity of $\varepsilon_r = 8.8$ was used to analyze data for InP electrodes.

2.7 Analytical Methods

2.7.1 Inductively coupled plasma mass spectrometry (ICP-MS)

Inductively coupled plasma mass spectrometry (ICP-MS) data were collected using an Agilent 8800 Triple Quadrupole ICP-MS system. Calibration solutions were prepared by diluting the multi-element standard solutions for ICP with water having a resistivity of 18.2 MΩ cm. All electrolyte samples were acidified to pH ≤2 before the ICP-MS measurements. The total amounts of In dissolved from the electrodes were calculated and normalized to the geometric electrode area to yield the equivalent depth of material removed from the InP electrode. The error bars of each data point represent the standard deviations of five consecutive measurements using the instrument. Due to the high detection limit of phosphorus (P) by ICP-MS, only the concentrations of In ions were used to calculate the corrosion thickness of InP. The conversion equation relating the In concentration (ug/L) as measured by ICP-MS to the dissolution thickness of InP (nm) is shown below:

$$InP\ Thickness\ (nm) = \frac{x\ \mu g}{1\ L}(In\ concentration) * \frac{3.2\ mL}{0.2\ mL}(dilution\ factor) *$$

$$4\ mL(total\ volumer\ of\ catholyte) * \frac{1\ L}{1000\ mL} * \frac{1*10^{-6}\ g}{1\ \mu g} * \frac{1\ mol}{114.8\ g}(In\ molar\ mass) *$$

$$\frac{(114.8+31)\ g}{1\ mol}\ (InP\ molar\ mass) * \frac{1\ cm^3}{4.81\ g}\ (InP\ density) * \frac{1}{0.2\ cm^2}\ (electrode\ area) * \frac{1*10^7\ nm}{1\ cm}$$

The dilution factor, the total volume of catholyte and the electrode area shown above are typical values which are specific to each experiment.

2.7.2 X-ray photoelectron spectroscopy

X-ray photoelectron spectroscopy (XPS) was performed using a Kratos Axis Ultra system with a base pressure of $< 1\times10^{-9}$ Torr equipped with a monochromatic Al Kα X-ray source with a photon energy of 1486.6 eV. Photoelectrons were collected at 0° from the surface normal with a retarding pass energy of 160 eV for survey XPS scans (step sizes of 1.0 eV and 10 eV) and for high-resolution core-level scans (step size 0.025 eV).

Prior to XPS measurements, samples were mounted on a sample holder and loaded in a transfer box inside the glove box under nitrogen. The transfer box was attached to the load lock of the Kratos

Axis Ultra system with the transfer box gate valve (VAT) still closed (Figure S 2.2c). The load lock was first pumped down and purged again with N_2. After pumping down the load lock again to 1×10^{-2} Torr, the gate valve to the transfer box was opened and the turbo molecular pump was switched on. After achieving a pressure of $<1 \times 10^{-6}$ Torr, the sample was transferred to the sample-transfer chamber (base pressure $<1\times10^{-9}$ Torr) before further transfer to the analysis chamber.

All XPS peak fitting was performed using CasaXPS software version 2.3.18. All binding energies are referenced to the adventitious carbon peak at 284.8 eV. Before fitting the data, a Shirley background was calculated and subtracted from the original spectra. The major peak of the In^{3+} cations of InP in the In 3d spectra was fit using an asymmetric Lorentzian function LF(1,1,15,80). All other peaks were fit using the 70% Gaussian/30% Lorentzian Voigt-function. The surface In/P atomic ratios were calculated using the relative sensitive factors (RSF) in the database of the Kratos instrument and the peak areas (In=7.265, P=0.486). In addition, the criteria of XPS peak assignments to various In-containing species including InP, InO_x, $In(OH)_3$, and $InPO_x$ is shown in Table S 2.3.[101,138,140,143,153–161] We also collected XPS data of various control samples (InP with native oxide, ITO and In foils) on the same instrument to further support the XPS peak assignment, which are shown in Figure S 2.31-2.33.

2.7.3 Microscopy

Scanning-electron microscopy (SEM) images were obtained using a calibrated Nova NanoSEM 450 (FEI) with an accelerating voltage of 5 kV.

Transmission-electron microscopy (TEM) cross-sections of the samples were prepared using a focused Ga ion beam (FIB), on a FEI Nova-600 Nanolab FIB/FESEM or a FEI Helios NanoLab G4 Dual Beam. Pt and C protection layers were applied prior to exposure to the FIB. TEM images of the prepared lamella samples were obtained using a Tecnai Polara (F30) TEM at an accelerating voltage of 300 kV, or a FEI Osiris at an accelerating voltage of 200 kV equipped with a Gatan 2K TEM camera and Bruker EDS.

Atomic-force microscopy (AFM) images were obtained on a Bruker Dimension Icon using Bruker ScanAsyst-Air probes (silicon tip, silicon nitride cantilever, spring constant: 0.4 N m^{-1}, frequency: 50-90 kHz), operating in the ScanAsyst mode. Images were analyzed using the Nanoscope Analysis software (version 1.9).

2.8 Supplementary figures and tables

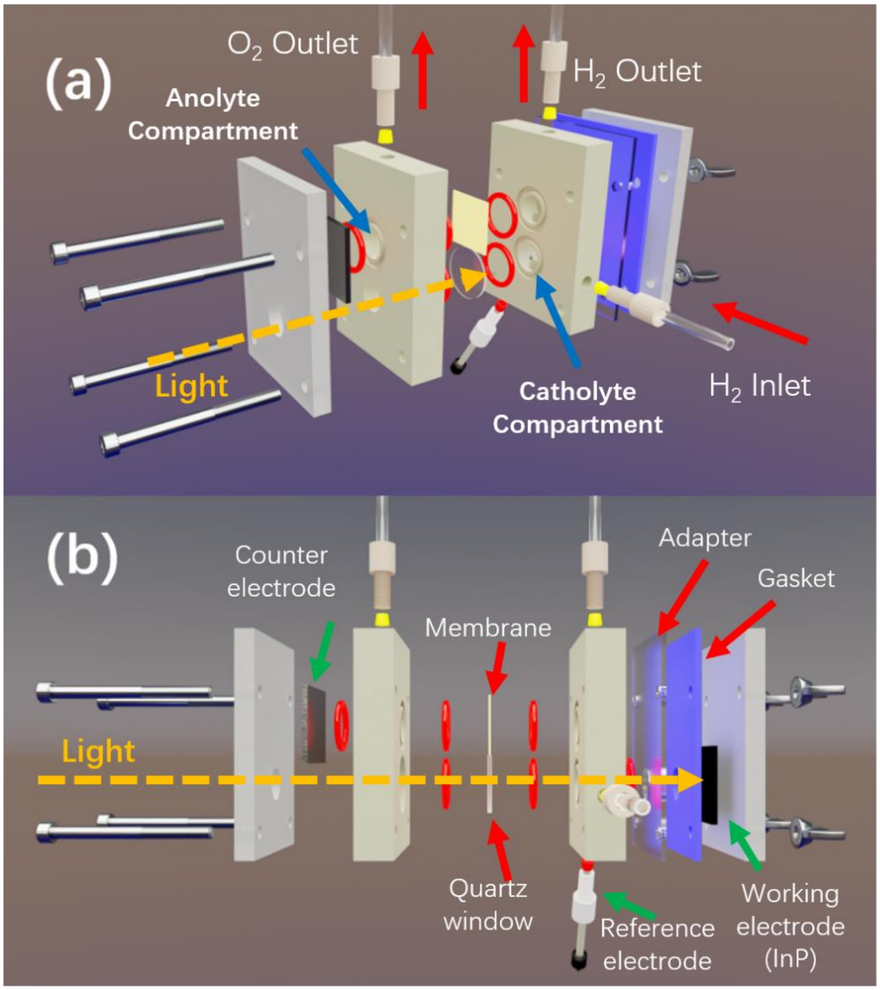

Figure S 2.1 (a,b) Two views of the design of the photoelectrochemical compression cell used for electrochemical measurements in an O_2-free environment. The current collector (Al foil) at the back of both working and counter electrode are omitted for simplicity. Before each experiment, electrolyte was added through the ports of H_2 and O_2 outlets before the respective tubes were connected. During each experiment, the electrolyte in the catholyte compartment was sampled (0.2 mL) through the H_2-outlet port after disconnecting the tube, while the working electrode was still under potential control.

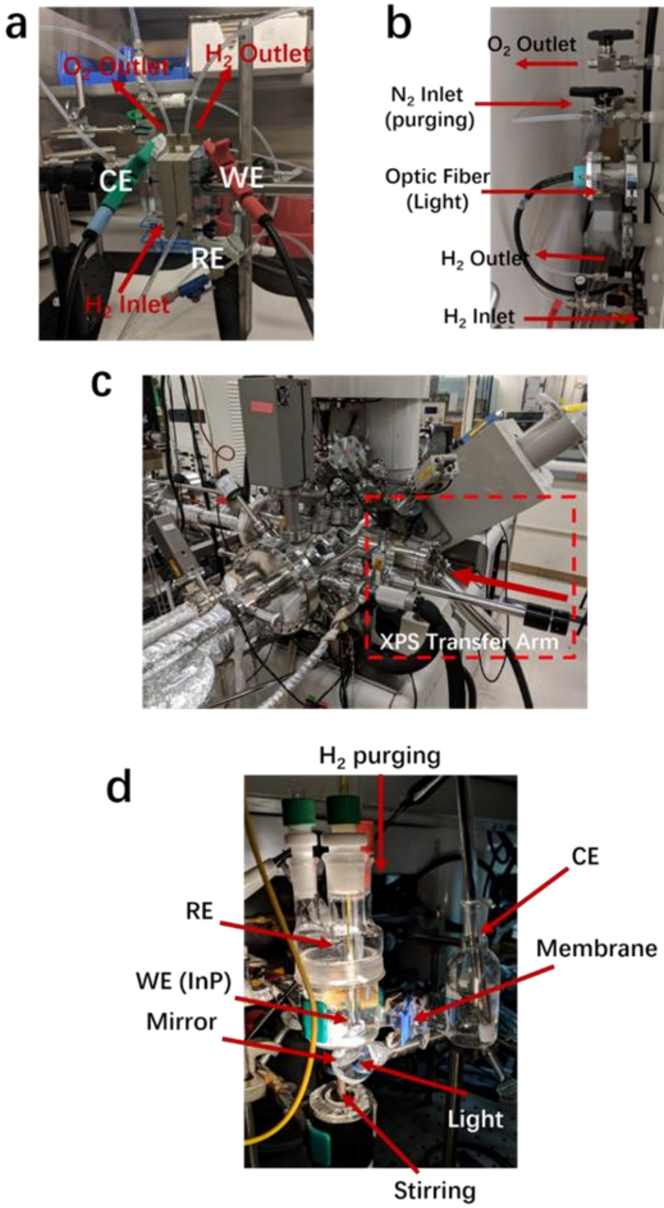

Figure S 2.2 Experimental setup. (a) The custom cell illustrated in Figure S 2.1 being tested inside a N_2-filled glovebox. (b) Modifications to the glove box to allow experiments to be performed with H_2 purging, light illumination and post-test N_2 purging. (c) The air-free transfer arm attached to the XPS instrument. After the EC cell was disassembled, the sample was rinsed with deionized water, purged with N_2, and loaded onto the transfer arm inside the glove box. The transfer arm was transferred from the glove box to the XPS. (d) A two-compartment cell used for testing outside the glove box while purging with H_2.

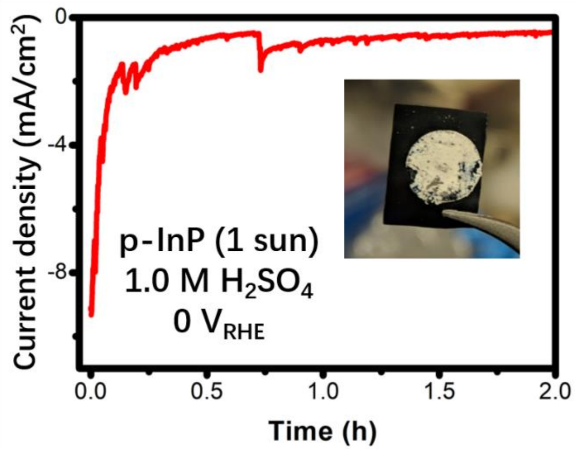

Figure S 2.3 (a) Chronoamperometry (CA) for 2 h at 0 V vs RHE in 1.0 M H_2SO_4(aq) of an illuminated etched p-InP electrode. The inset shows the p-InP electrode after the CA; the whitish area was inside the O-ring and exposed to the electrolyte.

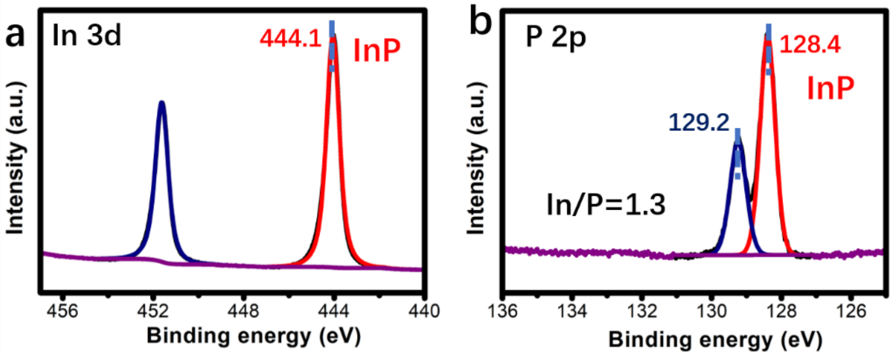

Figure S 2.4 XPS data of (a) In 3d and (b) P 2p regions of a p-InP sample without exposure to electrolyte.

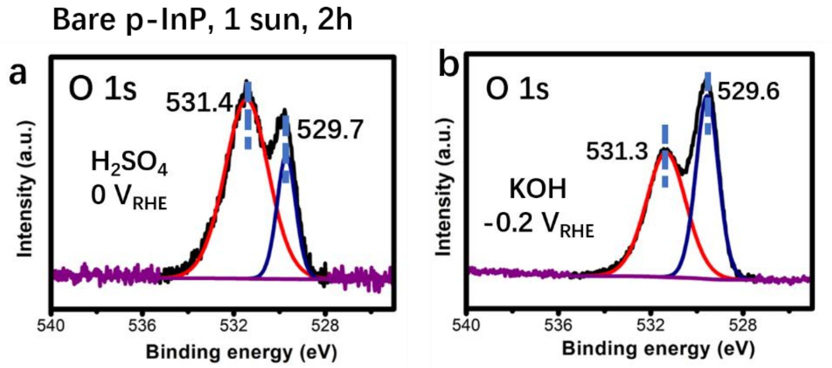

Figure S 2.5 Comparison of XPS data for the O 1s region of an illuminated etched p-InP electrode (1 sun) tested (a) for 2 h at 0 V vs RHE in 1.0 M H_2SO_4(aq) and (b) for 2 h at -0.2 V vs RHE in 1.0 M KOH(aq).

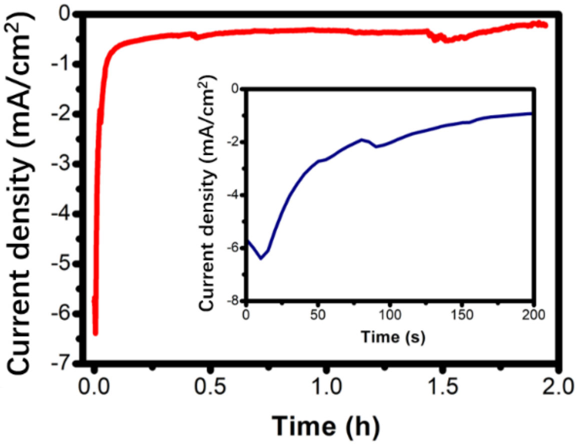

Figure S 2.6 (a) Chronoamperometry (CA) of an illuminated etched p-InP electrode for 2 h at -0.2 V vs RHE in 1.0 M KOH(aq). The inset shows the data for the first 200 s.

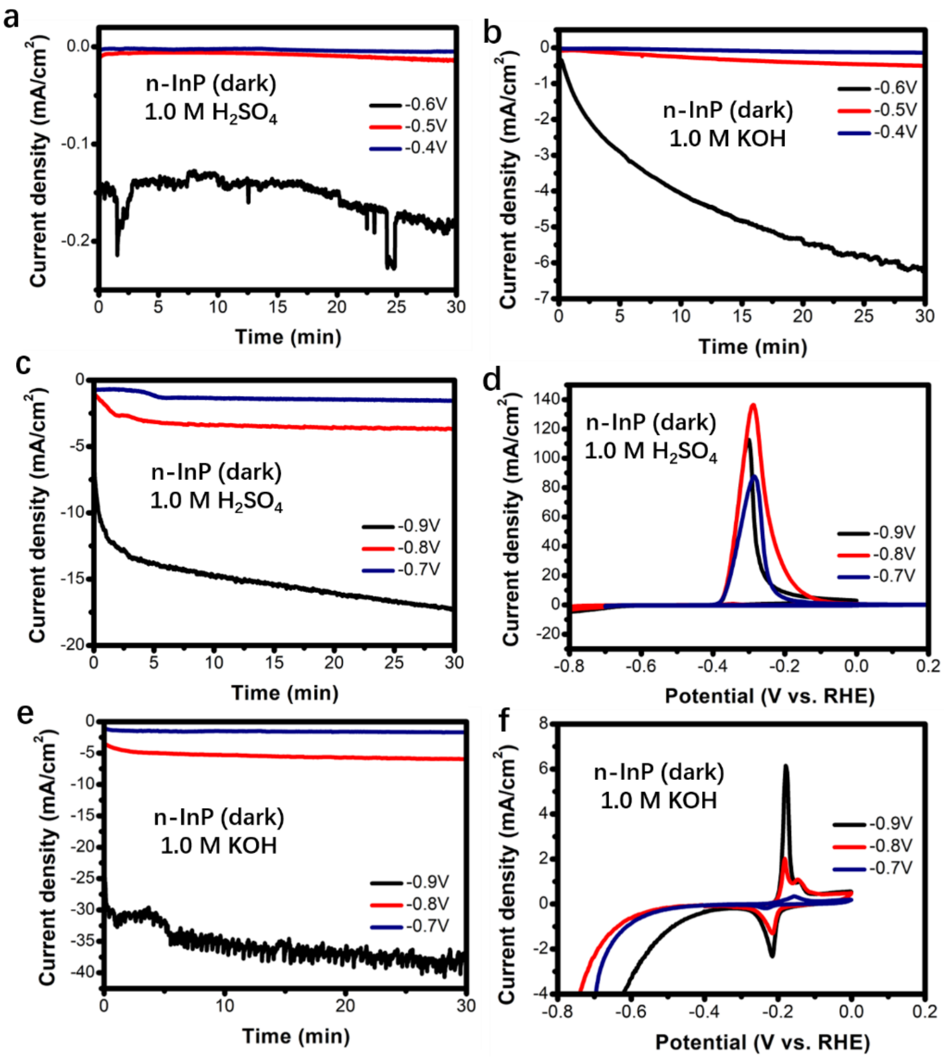

Figure S 2.7 (a-c,e) Chronoamperometry of n-InP electrodes held at various potentials, *E* (from -0.4 to -0.9 V vs RHE) in the dark, while in contact with (a,c) 1.0 M H_2SO_4(aq) and (b,e) 1.0 M KOH(aq). (d,f) Comparison of CVs performed after the CAs shown in (c,e), scanning in aa positive direction from the initially applied *E* (scan rate: 20 mV s^{-1}).

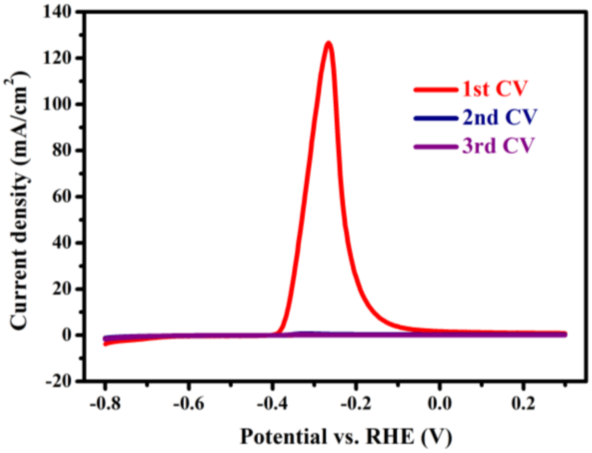

Figure S 2.8 Three consecutive CVs collected for an n-InP electrode after the electrode was held for 30 min at -0.8 V vs RHE in 1.0 M H_2SO_4(aq) in the dark. Scan rate: 20 mV s^{-1}.

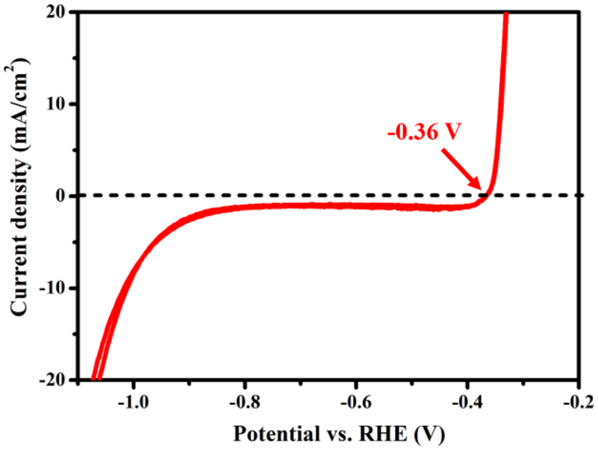

Figure S 2.9 CV of an In metal foil electrode in 1.0 M H_2SO_4(aq). The onset potential for anodic current was -0.36 V vs RHE. Scan rate: 20 mV s^{-1}.

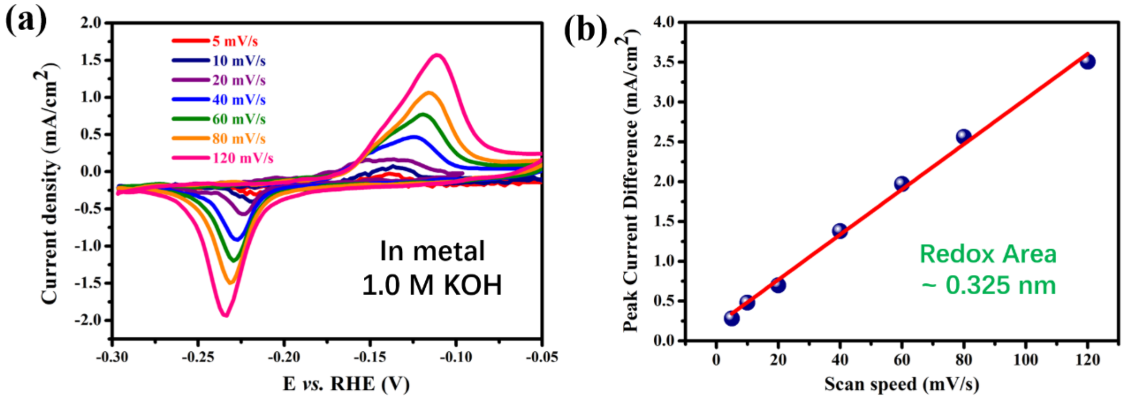

Figure S 2.10 (a) Scan-rate dependence of CVs of an In metal foil electrode in contact with 1.0 M KOH(aq). (b) Dependence of the differences between the anodic and cathodic peaks in *J* as a function of scan rate. The thickness of the redox-active layer on the electrode was calculated as 0.33 nm.

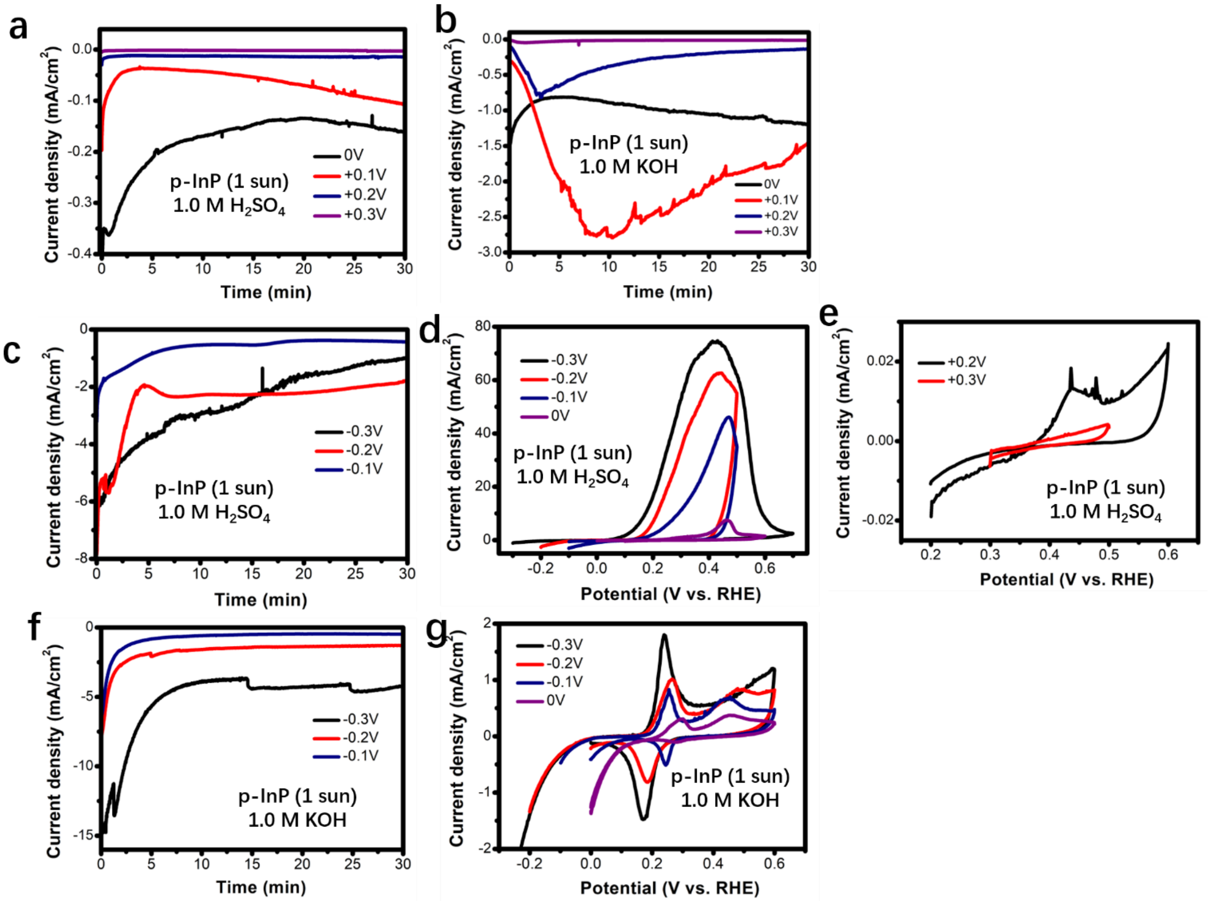

Figure S 2.11 (a-b) Chronoamperometry of illuminated p-InP electrodes held for 30 min at 0-+0.3 V vs. RHE in (a) 1.0 M H_2SO_4(aq) and (b) 1.0 M KOH(aq). (c,f) Chronoamperometry of illuminated p-InP electrodes held for 30 min at -0.3-0 V vs RHE in (c) 1.0 M H_2SO_4(aq) and (f) 1.0 M KOH(aq). (d,e,g) CVs performed after the experiment shown in (c,f), scanning in a positive direction from the initially applied potential using a scan rate of 20 mV s^{-1}. The illumination intensity was 100 mW cm^{-2} (1 sun).

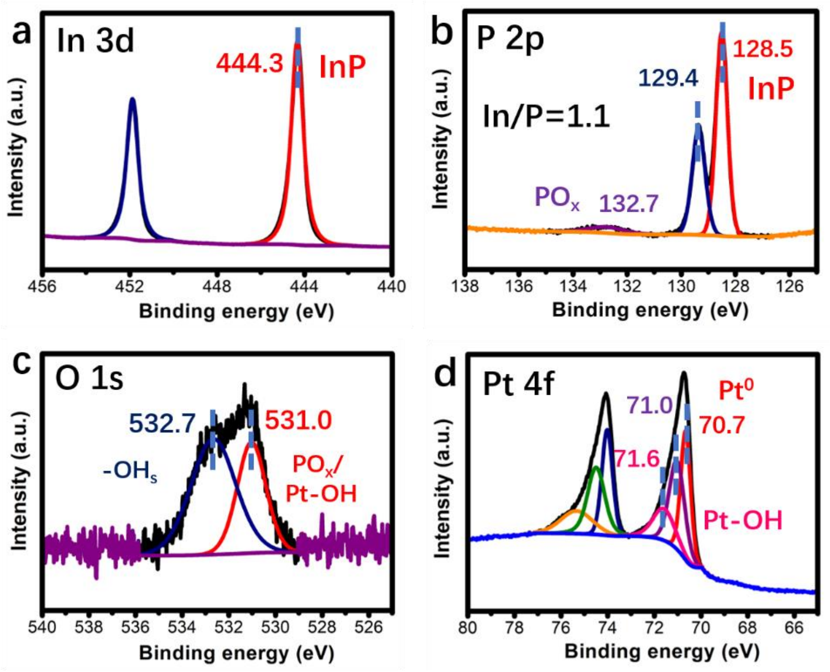

Figure S 2.12 XPS data of (a) In 3d, (b) P 2p, (c) O 1s and (d) Pt 4f regions for an as-prepared p-InP/Pt electrode before CA.

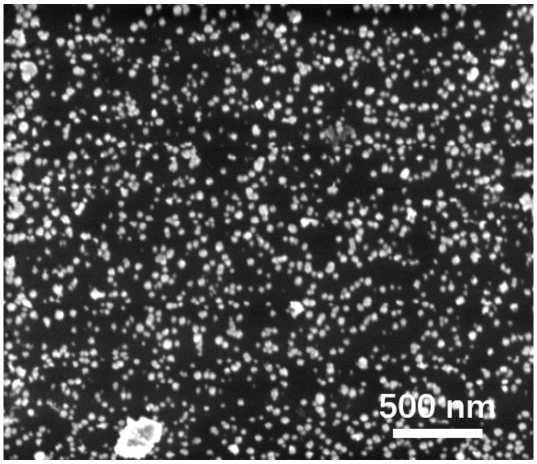

Figure S 2.13 SEM image of the surface morphology of an as-prepared p-InP/Pt electrode

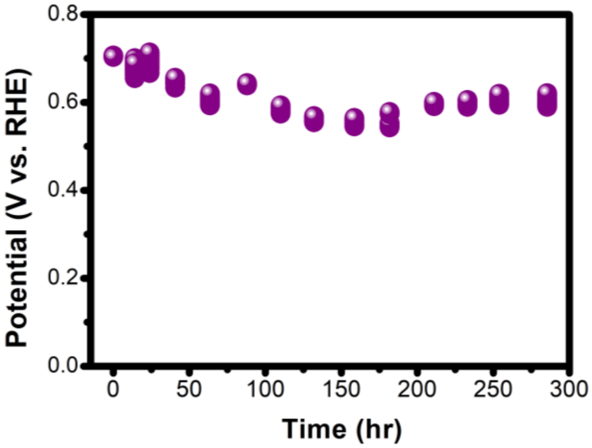

Figure S 2.14 E_{oc} versus time periodically measured for a p-InP/Pt electrode tested for 285 h at 0 V vs RHE in 1.0 M H_2SO_4(aq) under 1-sun illumination.

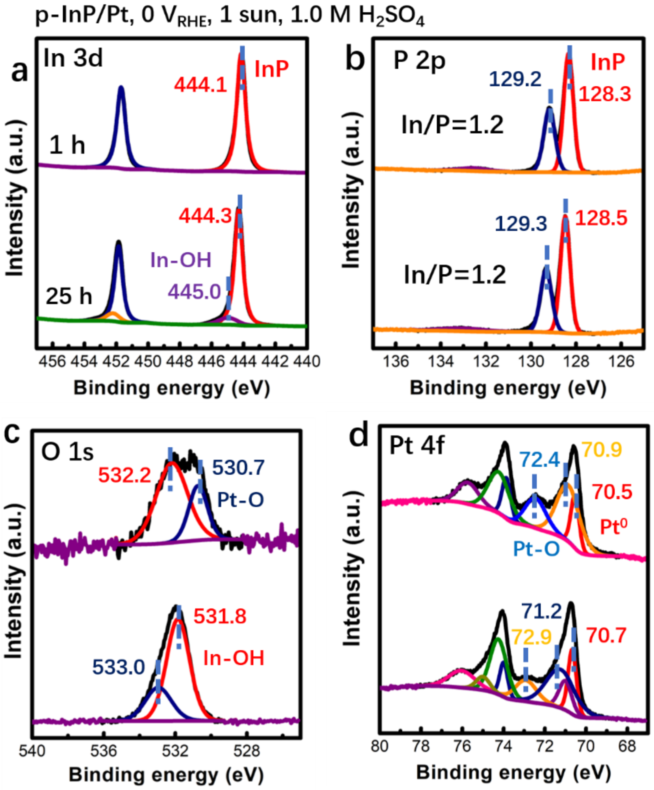

Figure S 2.15 XPS data of (a) In 3d, (b) P 2p, (c) O 1s and (d) Pt 4f regions for illuminated p-InP/Pt electrodes (1 sun) at 0 V vs RHE for 1 h and 25 h, respectively, in 1.0 M H_2SO_4(aq).

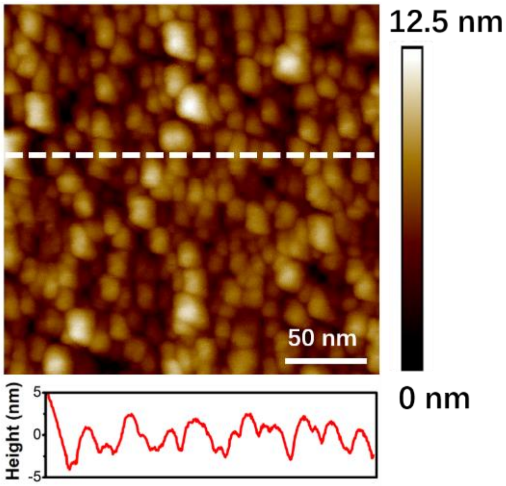

Figure S 2.16 AFM image of the flat region of an illuminated p-InP/Pt electrode (1 sun) held for 72 h at 0 V vs RHE in 1.0 M KOH(aq).

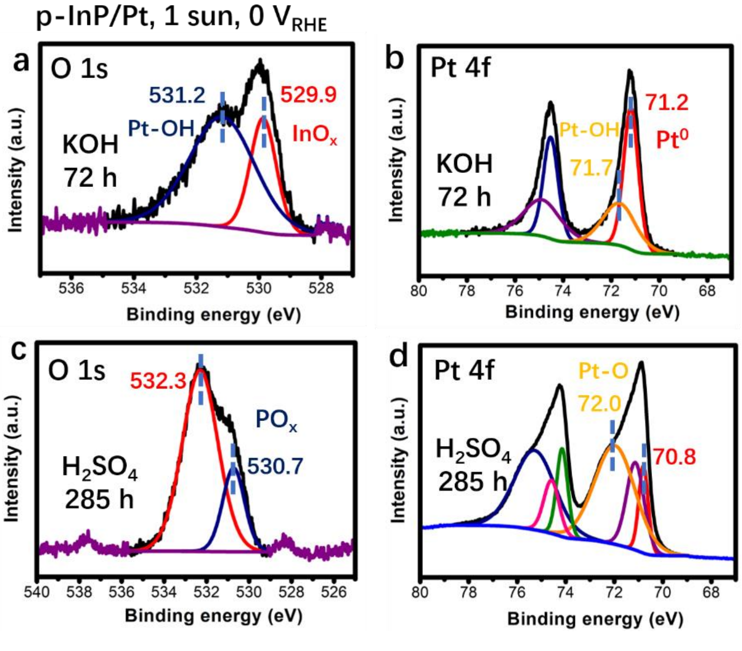

Figure S 2.17 Comparison of the XPS data of (a,c) O 1s and (b,d) Pt 4f regions for illuminated p-InP/Pt electrodes (1 sun) tested for 72 h at 0 V vs RHE (a-b) in 1.0 M KOH(aq) and (c-d) for 285 h in 1.0 M H_2SO_4(aq).

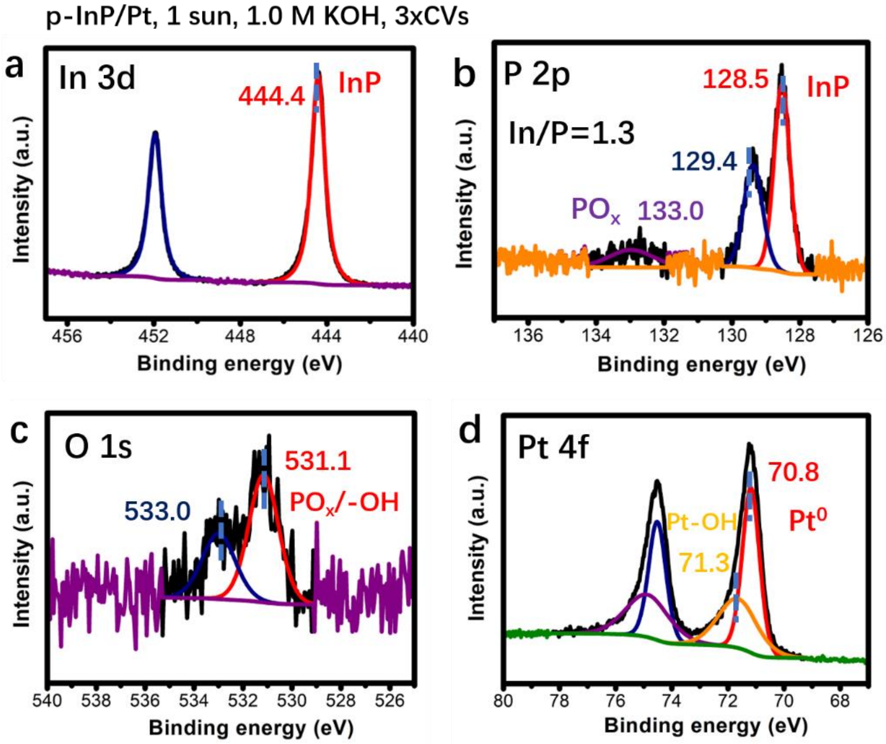

Figure S 2.18 XPS data of (a) In 3d, (b) P 2p, (c) O 1s and (d) Pt 4f regions of a p-InP/Pt electrode after undergoing 3 cycles of CVs in 1.0 M KOH(aq) under 1-sun illumination. The scan direction was from -25 mV vs. E_{oc} to -0.1 V vs RHE and the scan rate was 50 mV s^{-1}.

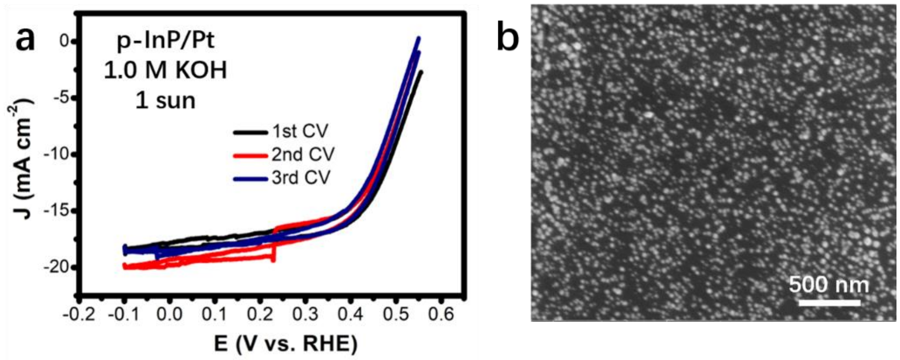

Figure S 2.19 (a) Comparison of three consecutive CV scans of an illuminated p-InP/Pt electrode (same as Figure S 2.18). The scan direction was from -25 mV vs. E_{oc} to -0.1 V vs RHE and the scan rate was 50 mV s^{-1}. (b) SEM image of the p-InP/Pt electrode after undergoing 3 CVs in (a).

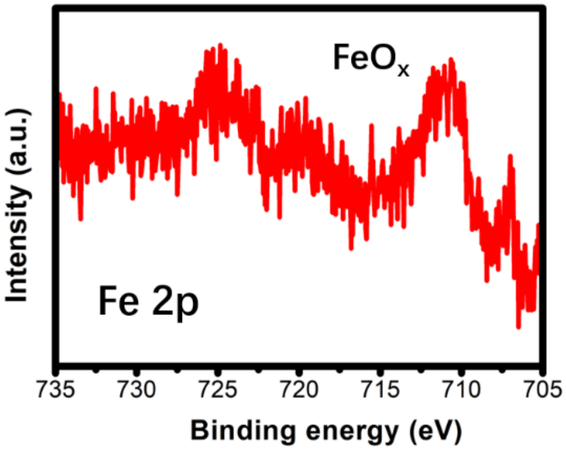

Figure S 2.20 XPS data of the Fe 2p region of a p-InP/Pt electrode after the CA test in Figure 4, showing the presence of trace FeO$_x$ (BE~711 eV).

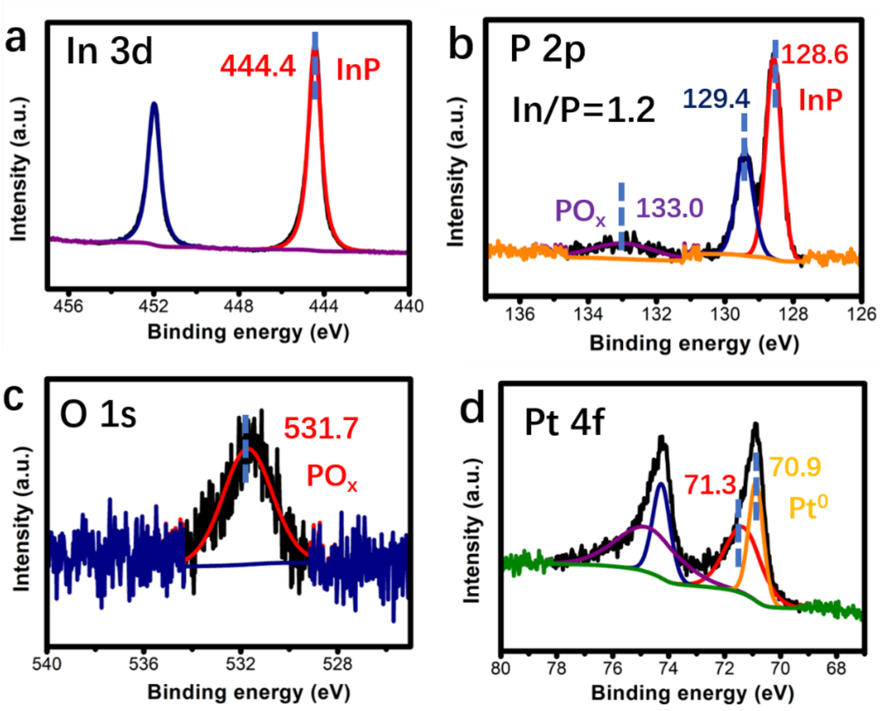

Figure S 2.21 XP spectra of the (a) In 3d, (b) P 2p, (c) O 1s and (d) Pt 4f spectral regions of the p-InP/Pt electrode after the series of electrochemical experiments shown in Figure 2.6.

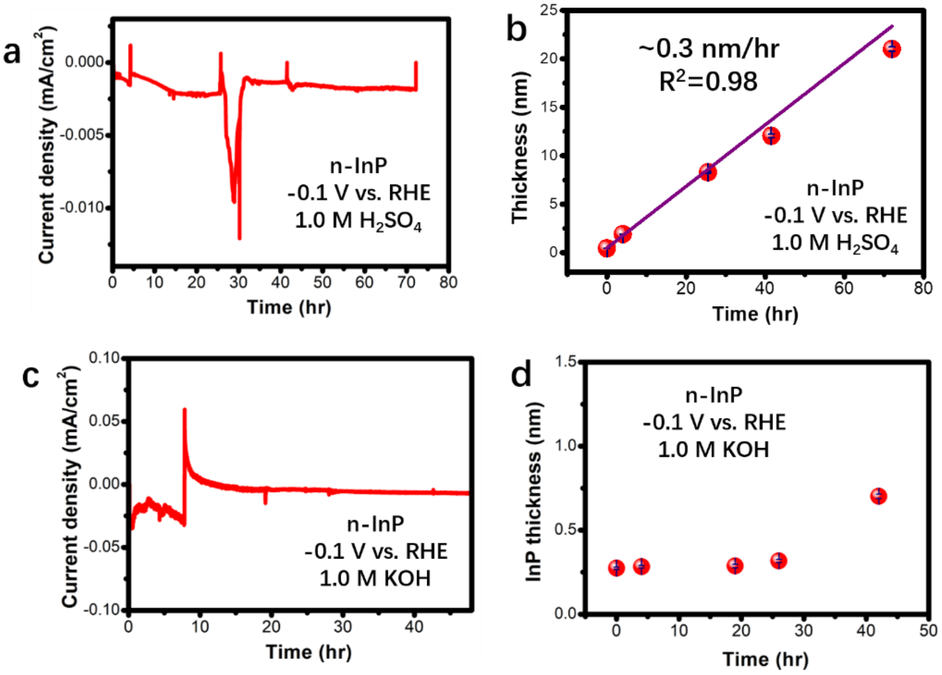

Figure S 2.22 (a,c) Chronoamperometry of n-InP electrodes held at -0.1 V vs RHE in the dark in (a) 1.0 M H_2SO_4(aq) and (c) 1.0 M KOH(aq) and (b,d) the electrode dissolution thickness measured throughout the CA in (a,c).

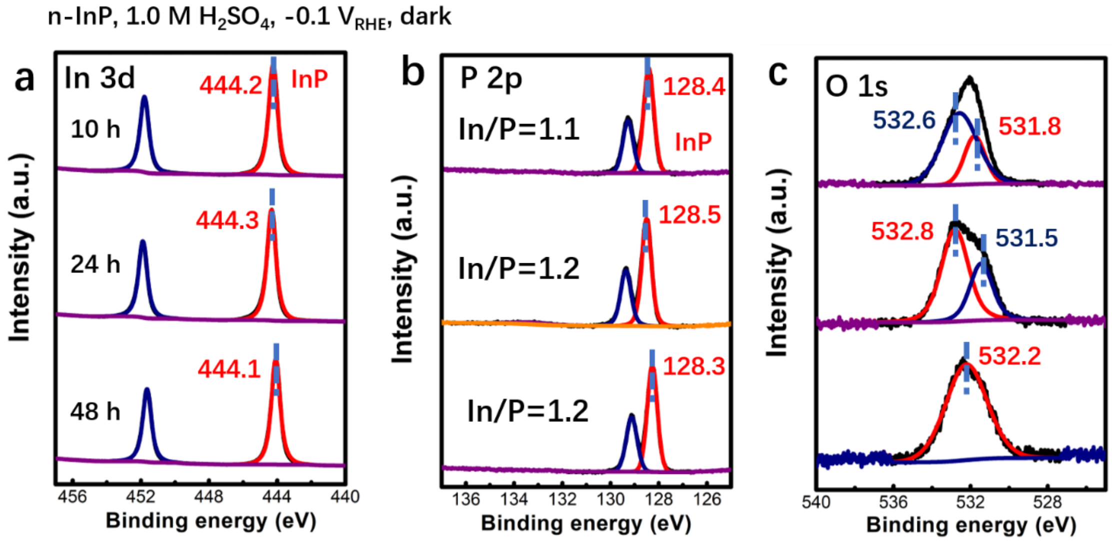

Figure S 2.23 XPS data of the (a) In 3d, (b) P 2p and (c) O 1s regions of three different n-InP electrodes held at -0.1 V vs RHE in 1.0 M H_2SO_4(aq) for 10 h, 24 h and 48 h, respectively.

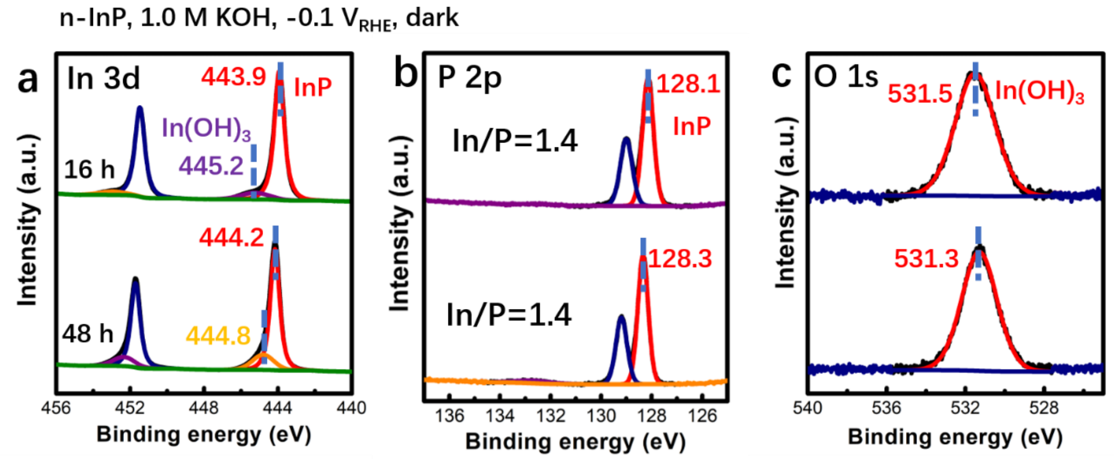

Figure S 2.24 XPS data of the (a) In 3d, (b) P 2p and (c) O 1s regions of two different n-InP electrodes held at -0.1 V vs RHE in 1.0 M KOH(aq) for 10 h, 24 h and 48 h, respectively. The small peaks seen at high BE (444.8/445.2 eV) of the In 3d XPS are ascribable to the surface $In(OH)_3$ species.

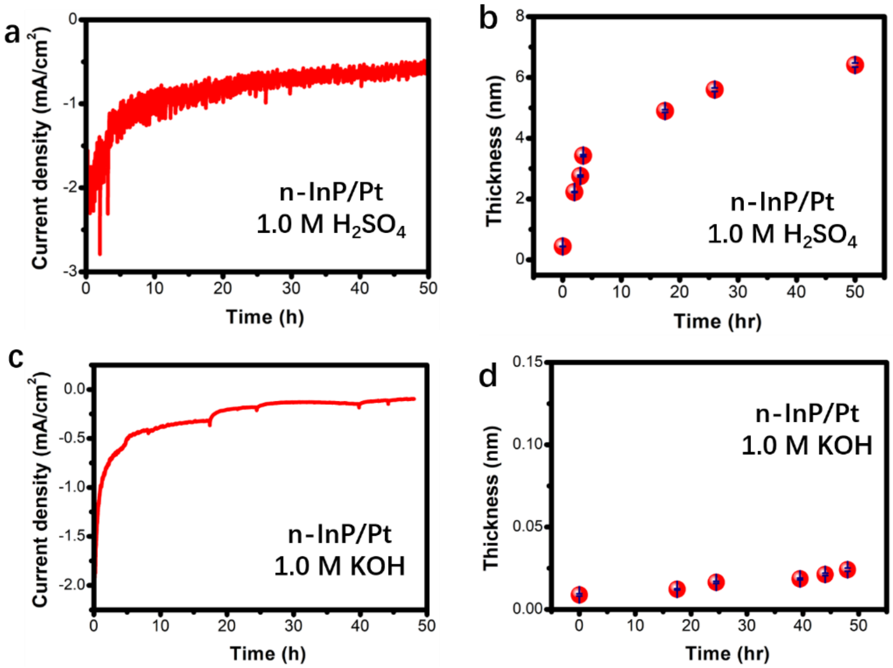

Figure S 2.25 (a,c) Chronoamperometry of n-InP/Pt electrodes held at -0.1 V vs RHE in the dark in (a) 1.0 M H_2SO_4(aq) and (c) 1.0 M KOH(aq) and (b,d) the electrode dissolution thickness measured throughout the CA in (a,c).

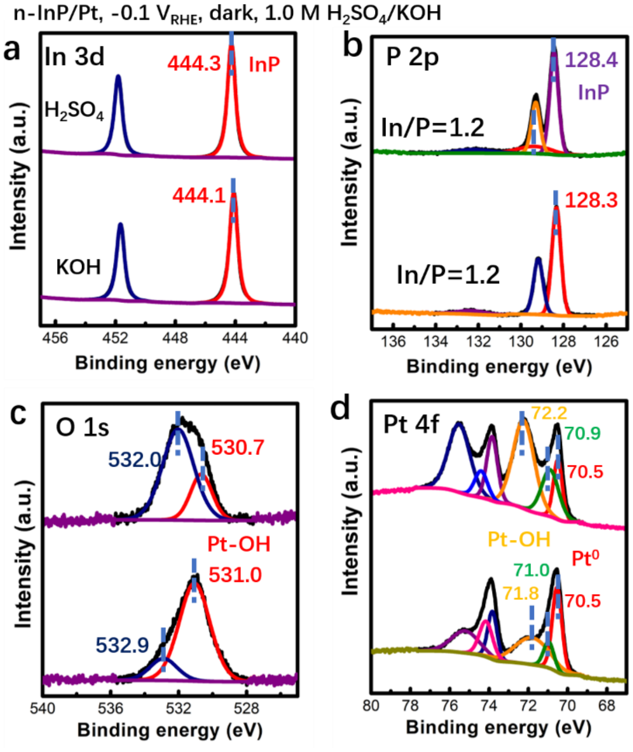

Figure S 2.26 XPS data of the (a) In 3d, (b) P 2p, (c) O 1s and (d) Pt 4f region of n-InP/Pt electrodes held at -0.1 V vs RHE in 1.0 M H_2SO_4(aq) and 1.0 M KOH(aq) in Figure S 2.25.

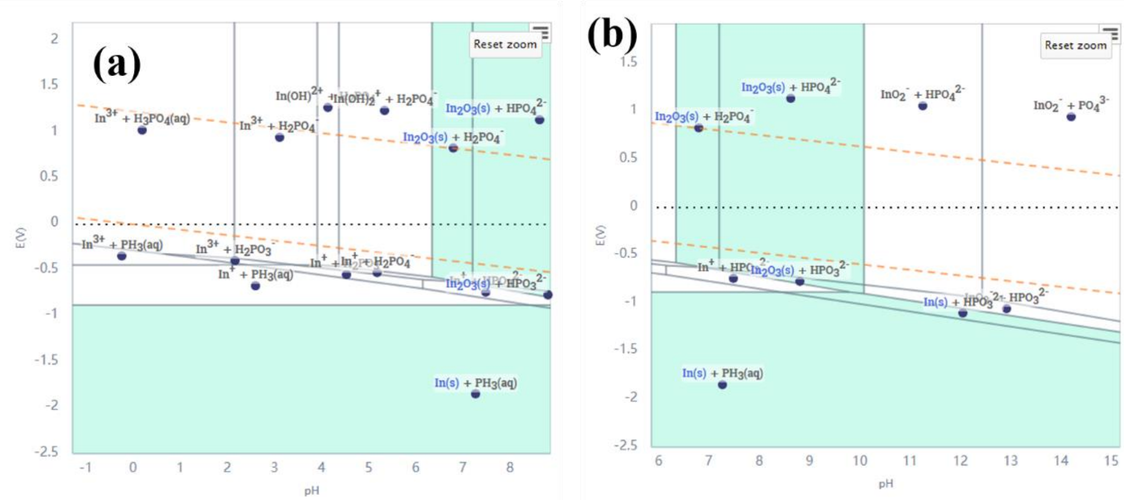

Figure S 2.27 Calculated Pourbaix diagrams for the In-P (In/P=1) system at low concentration of $1x10^{-8}$ mol kg^{-1} in (a) acidic and (b) alkaline electrolyte, produced by the Materials Project.[126]

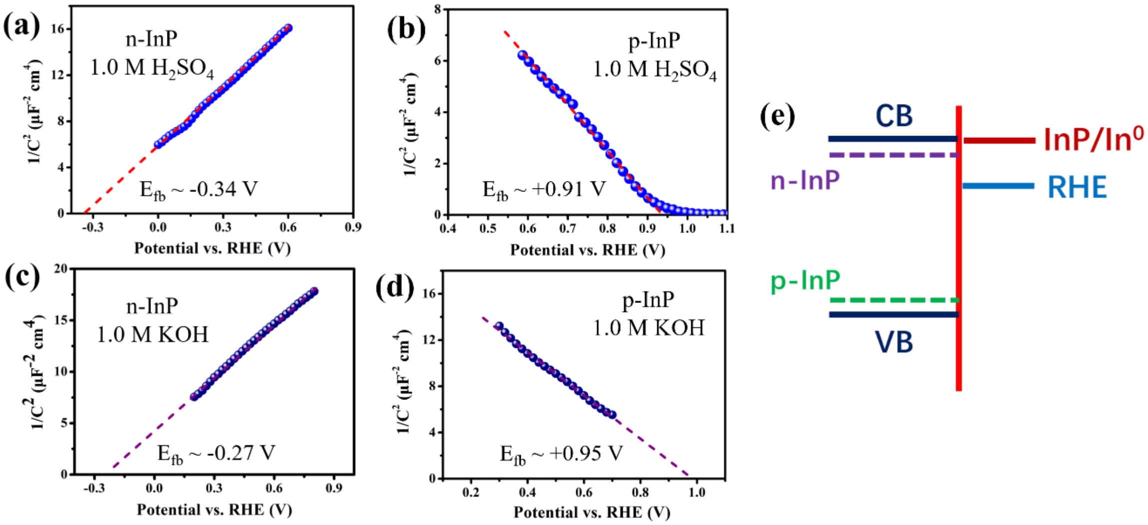

Figure S 2.28 (a-d) Mott-Schottky analyses for (a,c) n-InP and (b,d) p-InP electrodes measured in the dark while in contact with (a,b) 1.0 M H_2SO_4(aq) and (c,d) 1.0 M KOH(aq). (e) Analysis of the interfacial energetics comparing the band edges of InP with the potentials of *E*(InP/In^0) and RHE.

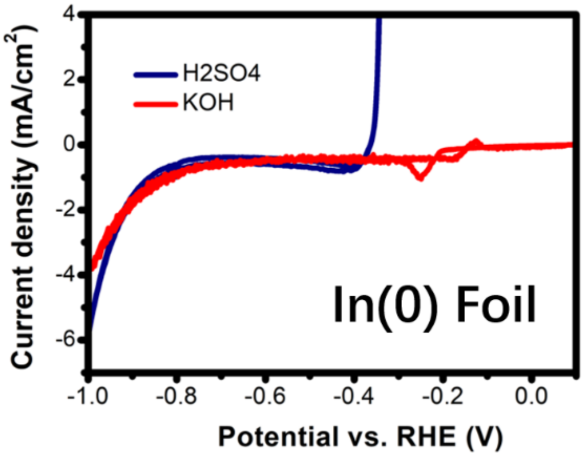

Figure S 2.29 Comparison of CV of an In metal electrode in contact with 1.0 M H_2SO_4(aq) and 1.0 M KOH(aq), demonstrating slow HER kinetics at both pH = 0 and 14. Scan rate: 20 mV s^{-1}.

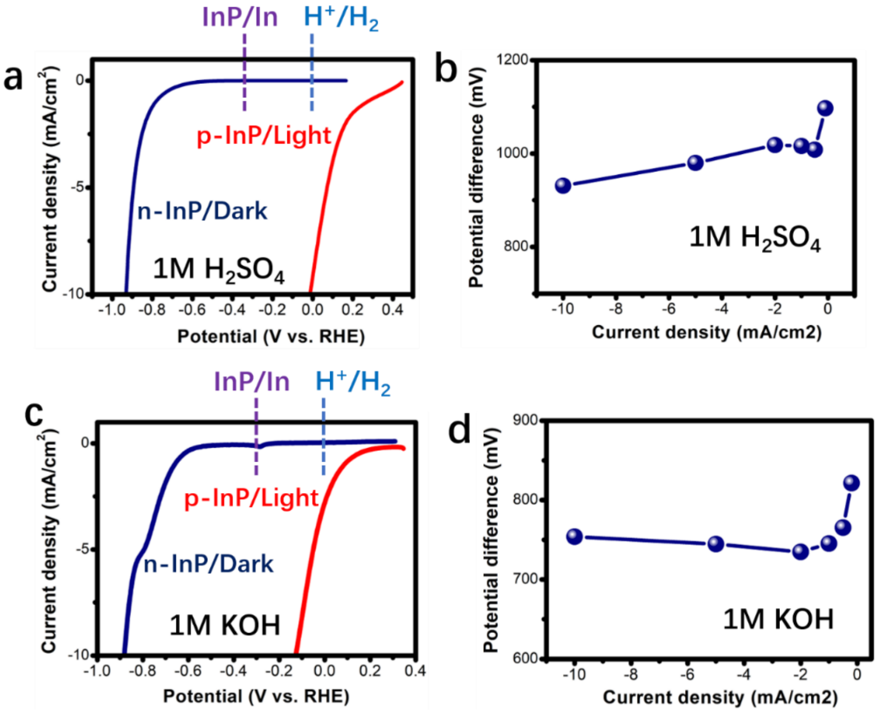

Figure S 2.30 (a,c) Comparison of linear sweeps of n-InP electrodes in the dark to sweeps of illuminated p-InP electrodes (1 sun) in contact with (a) 1.0 M H_2SO_4(aq) and (c) 1.0 M KOH(aq). The scan direction was from positive to more negative potentials (scan rate: 50 mV s^{-1}). (b,d) Potential differences between the n-InP dark electrodes and p-InP photoelectrodes at mutually the same current densities in (b) 1.0 M H_2SO_4(aq) and (d) 1.0 M KOH(aq). For etched p-InP under 1-sun illumination, the potential required to produce -1 mA cm^{-2} of current density was +0.23 V vs RHE and +0.085 V vs RHE in 1.0 M H_2SO_4(aq) and 1.0 M KOH(aq), respectively. Comparison of linear sweeps of n-InP dark electrodes and illuminated p-InP electrodes revealed positive shifts in potential from n-InP (dark) to p-InP (light) of >900 mV in 1.0 M H_2SO_4(aq) and of >750 mV in 1.0 M KOH(aq).

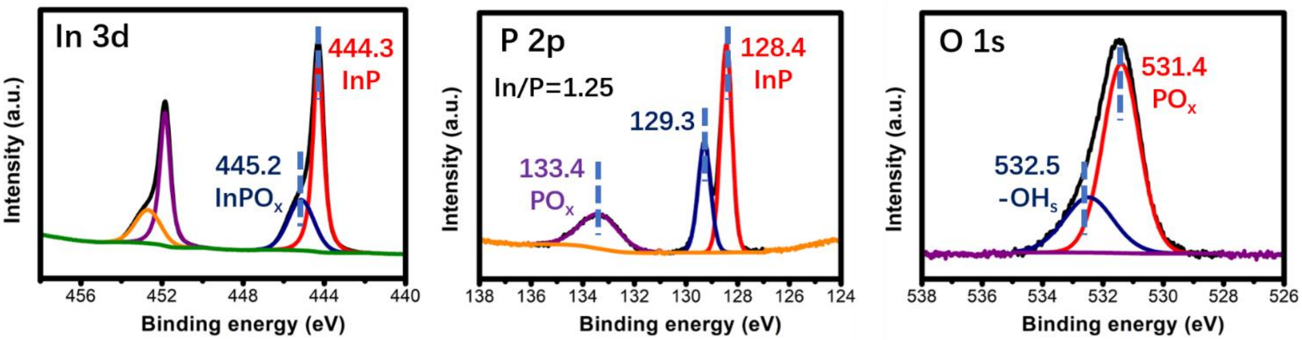

Figure S 2.31 XPS data of p-InP with native oxide (InPO$_x$). Besides the peaks of InP, the distinct peak at high BE=445.2 eV in the In 3d region corresponds to native oxide (InPO$_x$). The peaks at BE=133.4 eV in the P 2p region, and 531.4 eV in the O 1s region are attributed to surface phosphate (PO$_x$).

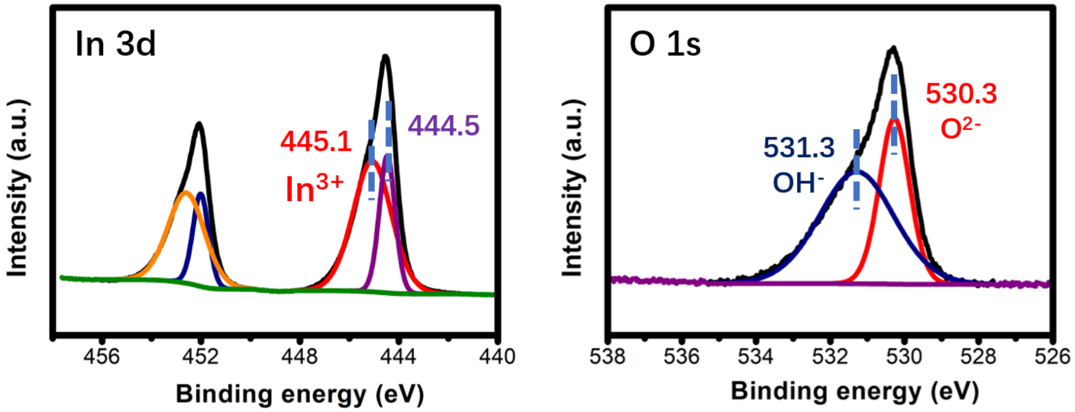

Figure S 2.32 XPS data of cleaned indium tin oxide (ITO). Before XPS analysis, the ITO sample was cleaned by sonication in acetone, methanol and water (in order) for 5 min. The peaks at BE=444.5 eV and 445.1 in the In 3d region are assigned to InO$_x$. The peaks at BE=530.3 eV and 531.3 eV in the O 1s region are attributed to oxide (O^{2-}) and surface hydroxyl (OH$^-$), respectively.

(a) As-received In metal foil

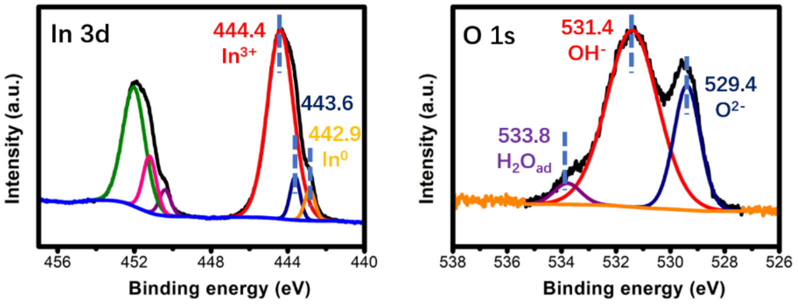

(b) In metal foil etched in 1M H_2SO_4 for 8 min

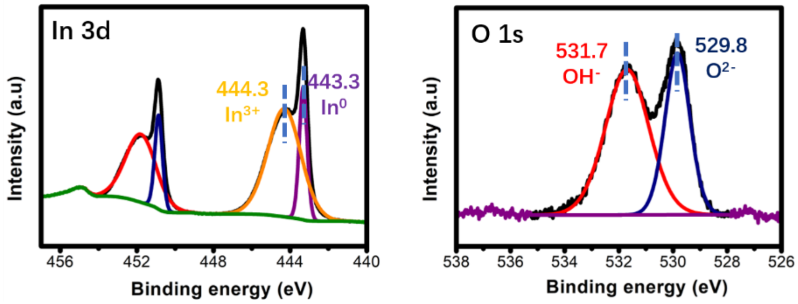

(c) Etched In metal foil in (b) after immersion in 1M KOH for 21 h

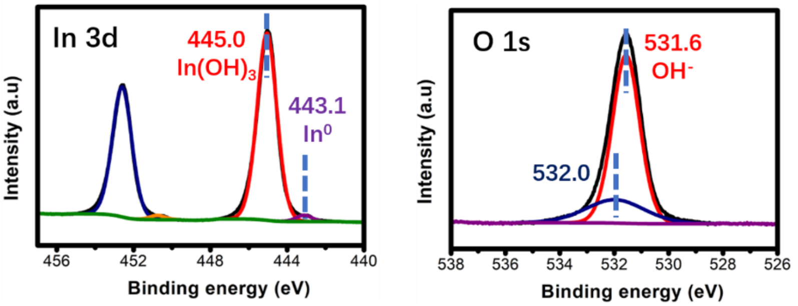

Figure S 2.33 Comparison of XPS data for (a) as-received In metal foil, (b) In metal foil etched in 1.0 M H_2SO_4(aq) for 8 min and (c) etched In metal foil in (b) immersed in 1.0 M KOH(aq) for 21 h. In (a), the peaks at low BE=442.9 eV and 443.6 eV in the In 3d region are assigned to metallic In^0; the large peak at BE=444.4 eV is assigned to native oxide; the peaks at BE=529.4, 531.4 and 533.8 eV in the O 1s region are assigned to surface oxide (O^{2-}), hydroxyl (OH^-) and adsorbed water (H_2O_{ad}), respectively. In (b), the peak of metallic In^0 at BE=443.3 eV became much larger compared with the other peak at BE=444.3 eV assigned to surface oxide/hydroxide, indicating removal of native oxide by acid etching; the peaks at BE=529.8 and 531.7 eV in the O 1s region are assigned to surface oxide (O^{2-}) and hydroxyl (OH^-), respectively. In (c), the large peak at BE=445.0 eV in the In 3d region and the peak at BE=531.6 eV are attributed to $In(OH)_x$, suggesting the conversion of metallic In^0 into $In(OH)_x$ by prolonger immersion in 1.0 M KOH(aq).

Table S 2.1 Standard Electrode Potentials in Aqueous Electrolytes at 25 °C for InP in V vs. RHE.[125]

Equilibria in 1.0 M H_2SO_4 (aq):	*E^0 (V vs. RHE)*	*Eqn. No.*
$In^{+3} + 3e^- \rightleftarrows In$	-0.342	(1)
$H_3PO_3 + 6\,H^+ + 6e^- \rightleftarrows PH_3 + 3H_2O$	-0.282	(2)
$H_3PO_4 + 2H^+ + 2e^- \rightleftarrows H_3PO_3 + H_2O$	-0.276	(3)
$2H^+ + 2e^- \rightleftarrows H_2$	0.000	(4)
Equilibria in 1.0 M KOH (aq):		
$HPO_3^{-2} + 5H_2O + 6e^- \rightleftarrows PH_3 + 8OH^-$	-0.480	(5)
$PO_4^{-3} + 2H_2O + 2e^- \rightleftarrows HPO_3^{-2} + 3OH^-$	-0.291	(6)
$In_2O_3 + 3H_2O + 6e^- \rightleftarrows 2In + 6OH^-$	-0.190	(7)
$In(OH)_3 + 3e^- \rightleftarrows In + 3OH^-$	-0.172	(8)
$2H_2O + 2e^- \rightleftarrows H_2 + 2OH^-$	0.000	(9)

Table S 2.2 Summary of experimental results of InP stability tests under varied conditions.

Sample	Electrolyte	E (V $_{\text{vs RHE}}$)	light/ dark	Duration (h)	In/P ratio	In $3d_{5/2}$	P 2p	O 1s	Pt $4f_{7/2}$	PO_x at.%[a]
n-InP	N/A	N/A	N/A	0	1.2	444.1, 444.7	128.3, 129.1, 132.6	529.5, 531.1, 532.6		8
p-InP	N/A	N/A	N/A	0	1.3	444.1	128.4, 129.2			
n-InP	HSA	-0.1	dark	48	1.2	444.1	128.3, 129.1	532.2		0
n-InP	HSA	-0.1	dark	24	1.2	444.3	128.5, 129.4, 133.3	532.8, 531.5		3
n-InP	HSA	-0.1	dark	10	1.1	444.2	128.4, 129.3	531.8, 532.6		0
p-InP	HSA	0	light	2	3.2	443.3, 444.1, 444.3	128.3, 129.2, 132.9	529.7, 531.4		8
n-InP	KOH	-0.1	dark	48	1.4	444.2, 444.8	128.3, 129.2, 132.7	531.3		4
n-InP	KOH	-0.1	dark	16	1.4	443.9, 445.2	128.1, 129	531.5		0

p-InP	KOH	-0.2	light	2	8.1	443.3, 443.9, 444.5	128.1, 128.9	529.6, 531.3		0
p-InP/Pt	N/A	N/A	N/A	as-prepared	1.1	444.3	128.5, 129.4, 132.7	531, 532.7	70.7, 71, 71.6	5
n-InP/Pt	HSA	-0.1	dark	50	1.2	444.3	128.4, 129.3, 132.2	530.7, 532.	70.5, 70.9, 72.2	5
p-InP/Pt	HSA	0	light	1	1.2	444.1	128.3, 129.2, 132.5	532.2, 530.7	70.5, 70.9, 72.4	5
p-InP/Pt	HSA	0	light	25	1.2	444.3, 445	128.5, 129.3, 133	531.8, 533.0	70.7, 71, 71.2, 72.9	5
p-InP/Pt	HSA	0	light	285	0.67	444.4	128.6, 129.5, 130.0, 132.6	532.3, 530.7	70.8, 71.1, 72.0	33
n-InP/Pt	KOH	-0.1	dark	48	1.2	444.1	128.3, 129.2, 132.3	531, 532.9	70.5, 71, 71.8	6
p-InP/Pt	KOH	0	light	72	3.1	444.2, 444.8	128.5, 129.4, 132.5	531.7, 529.9	71.2, 71.7	18

p-InP/Pt	KOH	N/A	light	3CVs	1.3	444.4	128.5, 129.4, 133	533, 531.1	70.8, 71.3	13
p-InP/Pt	KOH	0	light	15hr, then HSA	1.2	444.4	128.6, 129.4, 133	531.7	70.9, 71.3	16

[a]at.% represents the percentage of P as PO_x relative to detected P atoms.

Table S 2.3 Criteria of XPS peak assignments for different In-containing species.[101,138,140,143,153–161]

Species	**In $3d_{5/2}$/eV**	**O 1s/eV**	**In/P ratio**
InP	444.2±0.2	N/A	1.2
$In(OH)_3$	444.9±0.2	531±0.5	>1.2
$InPO_x$	444.9±0.2	531±0.5	~1.2
InO_x	444.9±0.2	530±0.5	>1.2

Chapter 3

3 STABILITY OF GAAS FOR PHOTOELECTROCHEMICAL H_2 EVOLUTION IN ACIDIC AND ALKALINE AQUEOUS ELECTROLYTES

3.1 Abstract

The long-term stability of p-GaAs photocathodes performing the hydrogen-evolution reaction (HER) has been investigated, in contact with either 1.0 M H_2SO_4(aq) or 1.0 M KOH(aq). Stability for the HER was evaluated using p-GaAs electrodes that were either etched or coated with active catalysts (Pt and CoP). Changes in surface characteristics of GaAs after exposure to electrochemical conditions were monitored by X-ray photoelectron spectroscopy (XPS), whereas electrode dissolution processes were assessed by inductively coupled plasma mass spectrometry (ICP-MS). Consistent with the thermodynamic predictions, illuminated etched p-GaAs electrodes exhibited minimal dissolution while preserving nearly stoichiometric surface after operation of the HER at both pH 0 and pH 14. Either electrodeposition or sputtering of Pt catalyst on p-GaAs surface, promoted the formation of excessive As^0 via an interfacial galvanic reaction under conditions of the HER. The resulting non-stoichiometric and As^0-rich surface of p-GaAs/Pt electrodes, caused a loss in photoactivity as well as substantial cathodic dark current. In contrast, p-GaAs electrodes coated with thin-film CoP catalysts displayed no increase in surficial As^0 after operation of the HER in acidic electrolytes. This work reveals that the non-stoichiometric surface of p-GaAs with excessive As^0 causes shunting of photocathodes, whereas a proper integration between semiconductor and catalyst is important to avoid unfavorable interfacial reaction.

3.2 Introduction

Photoelectrochemical (PEC) water splitting devices, using light-absorbing semiconductors and fuel-forming catalysts, offer one step solar-to-hydrogen conversion.[10,162,163] However, strongly acidic or alkaline electrolytes are required to prevent the formation of pH gradient within the device that reduce energy-conversion efficiency.[124] For long-term operation, this requirement presents substantial challenges to the material stability of semiconductors, catalysts, and membranes used in the device.

Extensive research efforts have been devoted to improving the stability of PEC devices. Strategies such as applying protective and/or catalytic coatings to semiconductors have shown promise.[53,164,165] In a few cases, photoelectrode lifetimes of a few hundred hours have been achieved;[49–51] still an increase from 100 to 1000 h in stability is required to extend device lifetime to ≥10 years. More importantly, a fundamental understanding of the corrosion mechanism of semiconductors under operating conditions will benefit further rational strategies of stabilizing photoelectrodes for long term. For solar water-splitting devices, over-potentials (η) of ≥100 mV and ≥350 mV are required to drive the hydrogen and oxygen evolution half-reactions (HER/OER), respectively, at current densities (J) of 10 mA cm^{-2}.[166] Hence, the stability and corrosion pathways of semiconductors should be primarily evaluated for photocathode and photoanode at thermodynamic potentials (E) ≤-0.1 V and ≥1.58 V vs. the reversible hydrogen electrode (RHE), respectively.[71] Moreover, combing experimental investigations of semiconductor stability with the Pourbaix diagram is beneficial for revealing both the thermodynamics and kinetics of corrosion chemistry.

A tandem solar water-splitting device uses a combination of a large and a small band-gap semiconductors.[44] Gallium arsenide (GaAs) is a promising light-absorber for solar-fuel devices due to its small band gap of 1.42 eV. However, n-type GaAs (n-GaAs) photoanode rapidly corrodes under potentials of the OER, limiting its stability in aqueous electrolytes.[46,61] Such corrosion of GaAs is promoted by the migration of photogenerated holes (h^+) to the GaAs/H_2O interface, resulting in the oxidation of As^{3-} anions as well as the irreversible dissolution of GaAs. Over the past decades, the electrochemical characteristics of this anodic corrosion process together with the associated surface transformation, have been extensively studied in both strong acidic and alkaline electrolytes.[60,167–172] Under certain conditions, n-GaAs photoanodes self-passivate by forming As^0 and AsO_x as well as non-stoichiometric surfaces. Oxidants such as Fe^{3+} and Br_2 accelerate the kinetics of anodic etching (**Eq 1**) of GaAs via a galvanic pathway, enabling the development of electrochemical nanoimprint lithography to fabricate anisotropic nanostructures of GaAs.[172–175]

$$GaAs(s) + 10OH^-(aq) \rightarrow GaO_3^{3-}(aq) + AsO_2^-(aq) + 6e^- + 5H_2O(l) \text{ (in alkaline electrolyte)} \quad (1)$$

Other redox couples such as Se_2^{2-}/Se^{2-} inhibit the anodic corrosion of GaAs by kinetic competition.[176,177] To physically mitigate the anodic corrosion of GaAs, surface passivation layers including amorphous TiO_2 (a-TiO_2) or single-layer graphene are necessary for sustaining operation of GaAs photoanodes over long periods.[46,178]

However, the long-term stability of p-type GaAs (p-GaAs) photocathodes performing the HER in either acidic or alkaline aqueous electrolytes is not well established. A systematic understanding of the corrosion mechanism of p-GaAs photocathodes during the HER calls for further experimental studies. Early works by Bard et al revealed the Fermi level pinning for p-GaAs electrodes in contact with various redox couples, limiting its PEC performance.[179] Recently, Deutsch et al demonstrated the remarkable stability (96 h) of unmodified GaAs photocathodes performing the HER with minimal surface etching in 3.0 M H_2SO_4(aq).[180] This report is in contrast to the general perception that III-V semiconductors would rapidly corrode in strong acidic and alkaline aqueous electrolytes.[41,61,122] Notably, etched p-GaAs photocathodes display both low open-circuit potential (E_{oc}) and PEC performance.[180] Overcoming the high η of the HER at GaAs surface require active HER catalysts such as Pt or CoP.[145] By accelerating surface kinetics, the HER catalysts may also influence the corrosion pathway of p-GaAs photocathodes by modifying surface potential.[71] Therefore, a comparative study of corrosion chemistry between p-GaAs electrodes with and without HER catalysts is necessary.

Herein, we present a systematic study of the stability of p-GaAs photocathodes for the HER in either 1.0 M H_2SO_4(aq) or 1.0 M KOH(aq), with or without HER catalysts (Pt or CoP). Our experimental approach consists of: (1) long-term chronoamperometry (CA) experiments of GaAs electrodes in an oxygen-free environment, (2) measurement of the concentrations of dissolved Ga and As ions in the electrolyte by ICP-MS during CA, and (3) characterization of GaAs surface by X-ray photoelectron spectroscopy (XPS). Before XPS measurements we use an air-free sample transport to prevent possible oxidation by ambient air, which is beneficial for probing the pristine surface of GaAs samples after testing. Experimental results of n-GaAs electrodes tested at -0.1 V vs. RHE in the dark were compared with those of illuminated p-GaAs electrodes evaluated under cathodic bias. Changes in the surface characteristics of p-GaAs electrodes after electrochemical measurements were correlated with the evolution of the current density-potential (*J-E)* behavior. This work provides fundamental insights into both the physical and electrochemical stability of p-GaAs photocathodes for the HER, as well as the interfacial interactions between GaAs and various HER catalysts.

3.3 Results

3.3.1 Stability of GaAs electrodes at open-circuit potential (E_{oc}) in the dark

The dissolution rates of n- and p-GaAs(100) electrodes at open-circuit potential (E_{oc}) in the dark in 1.0 M H_2SO_4(aq) and 1.0 M KOH(aq) were measured in a N_2-filled glove box (Figure S 3.2). The E_{oc} values of all GaAs electrodes stabilized in the range of +0.1 to +0.5 V vs. RHE for >20 hours after initial drift. In acidic electrolytes, some initial dissolution of Ga and As ions was observed varying between different samples (Figure S 3.3), which the calculation of long-term dissolution rates should account for. For all GaAs electrodes, the concentrations of dissolved Ga and As ions in the electrolytes linearly increased with time. Ignoring initial dissolution, the measured corrosion rates were similar for Ga and As ions, suggesting stoichiometric dissolution of GaAs at E_{oc} in the dark. The corrosion rates of n- and p-GaAs in 1.0 M H_2SO_4(aq), were ~0.7 and 0.2 nm h^{-1}, respectively, whereas in 1.0 M KOH(aq) the rates were ~6 and 7 nm h^{-1}, respectively.

3.3.2 Stability of n-GaAs electrodes at -0.1 V vs. RHE in the dark

During CA at E=-0.1 V vs. RHE in the dark, the |*J*| of n-GaAs(100) electrodes remained low in both 1.0 M H_2SO_4(aq) and 1.0 M KOH(aq). In 1.0 M H_2SO_4(aq), |*J*| initially decreased and remained ~0.014 mA cm^{-2} in the first 10 h (Figure 3.1a). Afterwards, small abrupt increases in |*J*| were observed once every few hours with |*J*| gradually increasing to 0.026 mA cm^{-2} after 30 h. The calculated corrosion thickness of n-GaAs, based on the amount of dissolved Ga ions, rose from ~0.86 to 1.25 nm after 35 h. However, the As concentration in the electrolyte did not increase over time (Figure 3.1b). Approximately 3 times more Ga than As was detected in the acidic electrolyte after CA. In 1.0 M KOH(aq), |*J*| was initially ~0.005 mA cm^{-2}, dropped to <0.003 mA cm^{-2} and remained stable for the next 30 h (Figure 3.1a). The dissolved Ga and As ions slightly increased during the first 10 h but remained constant afterwards, accounting for <1 nm in GaAs thickness (Figure 3.1c).

XPS data of the Ga $2p_{3/2}$ region exhibited a single peak at binding energy (BE) of 1116.9 ± 0.1 eV for all n-GaAs samples before and after CA, attributable to the Ga^{3+} cations of GaAs (Figure 3.1d). The As 3d XP spectrum of the n-GaAs sample before CA was fit with two doublets; the larger Ga $3d_{5/2}$ peak at BE=40.8 eV was assigned to the As^{3-} anions of GaAs, whereas the minor peak at BE=41.3 eV was assigned to surficial As^0.[181–183] Before CA, the As^0/As ratio was 0.22. After the CA in H_2SO_4 and KOH, this ratio increased to 0.41 and decreased to 0.11, respectively. Scanning electron microscopy (SEM) images of n-GaAs samples revealed negligible changes in surface morphology after the CA in either H_2SO_4 or KOH (Figure S 3.4). Atomic-force microscopy (AFM) images of the n-GaAs electrodes showed the surface roughness remained ~0.4 nm in flat regions after both CA tests (Figure S 3.5).

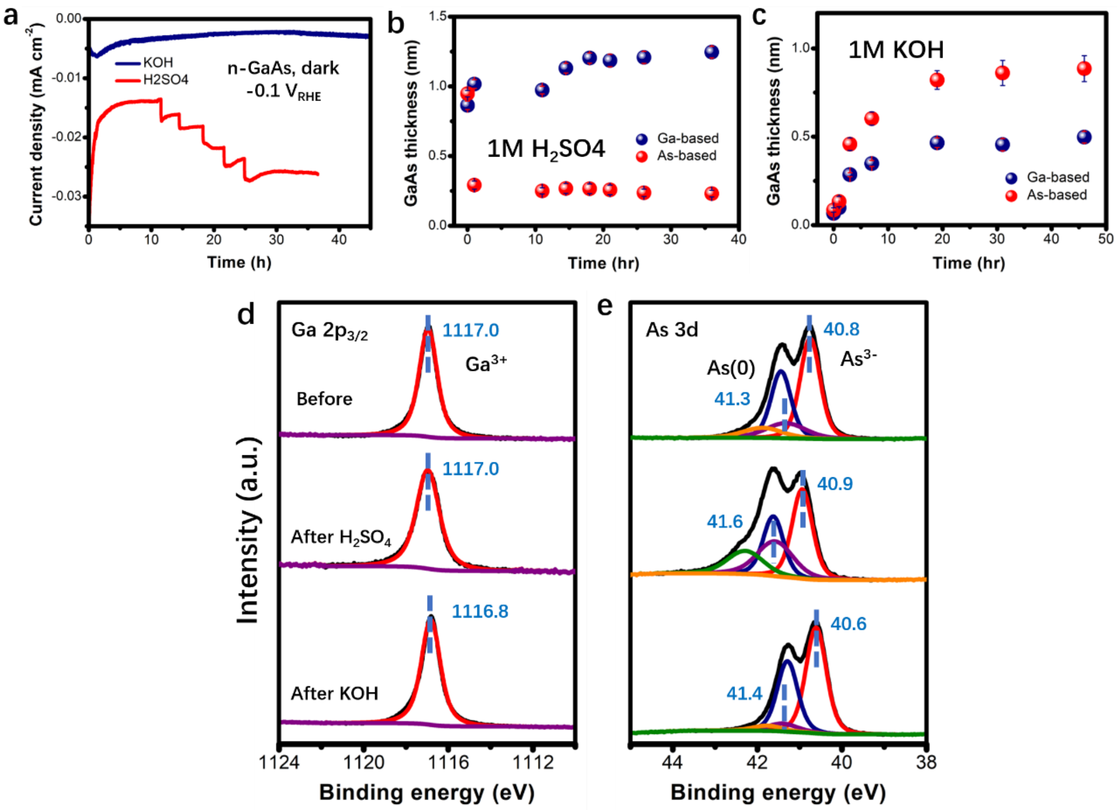

Figure 3.1 Results of n-GaAs electrodes tested at -0.1 V vs. RHE in the dark. (a) CA of n-GaAs electrodes at -0.1 V vs. RHE in the dark in 1.0 M H_2SO_4(aq) and 1.0 M KOH(aq). (b-c) Corrosion thickness (nm) of n-GaAs versus time for the electrodes tested in (b) 1.0 M H_2SO_4(aq) and (c) 1.0 M KOH(aq), determined by the concentrations of dissolved Ga and As ions in the electrolyte by ICP-MS. (d-e) Comparison of XP spectra in the (d) Ga $2p_{3/2}$ and (e) As 3d regions for the n-GaAs electrodes before and after CA in (a).

3.3.3 Stability of etched p-GaAs electrodes under cathodic biases with 1-sun illumination

The stability of etched p-GaAs(100) electrodes were first evaluated at -0.2 and -0.6 V vs. RHE in 1.0 M H_2SO_4(aq) under 1-sun illumination (Figure 3.2a&d). The variation in J during CA is due to the formation and release of H_2 bubbles.[184,185] During CA at -0.2 V vs. RHE, $|J|$ decreased from ~11 to 3 mA cm^{-2} in the first 2 h and remained stable afterwards (Figure 3.2a). The decrease in $|J|$ was consistent with an initial cathodic shift in the J-E behavior of the illuminated p-GaAs electrode (Figure 3.2b). After 20 h, the E at -10 mA cm^{-2} (E_{10}) shifted from -0.14 V to -0.26 V vs. RHE. The measured *J-E* behavior of etched p-GaAs photoelectrodes were comparable to other recent reports.[180,186–189] At -0.6 V vs. RHE, the maximum |*J*| of a p-GaAs photoelectrode remained stable at ~20 mA cm^{-2} (Figure 3.2d). A similar cathodic shift in the *J-E* behavior was observed with E_{10} shifting from -0.17 V to -0.41 V vs. RHE after 65 h (Figure 3.2e).

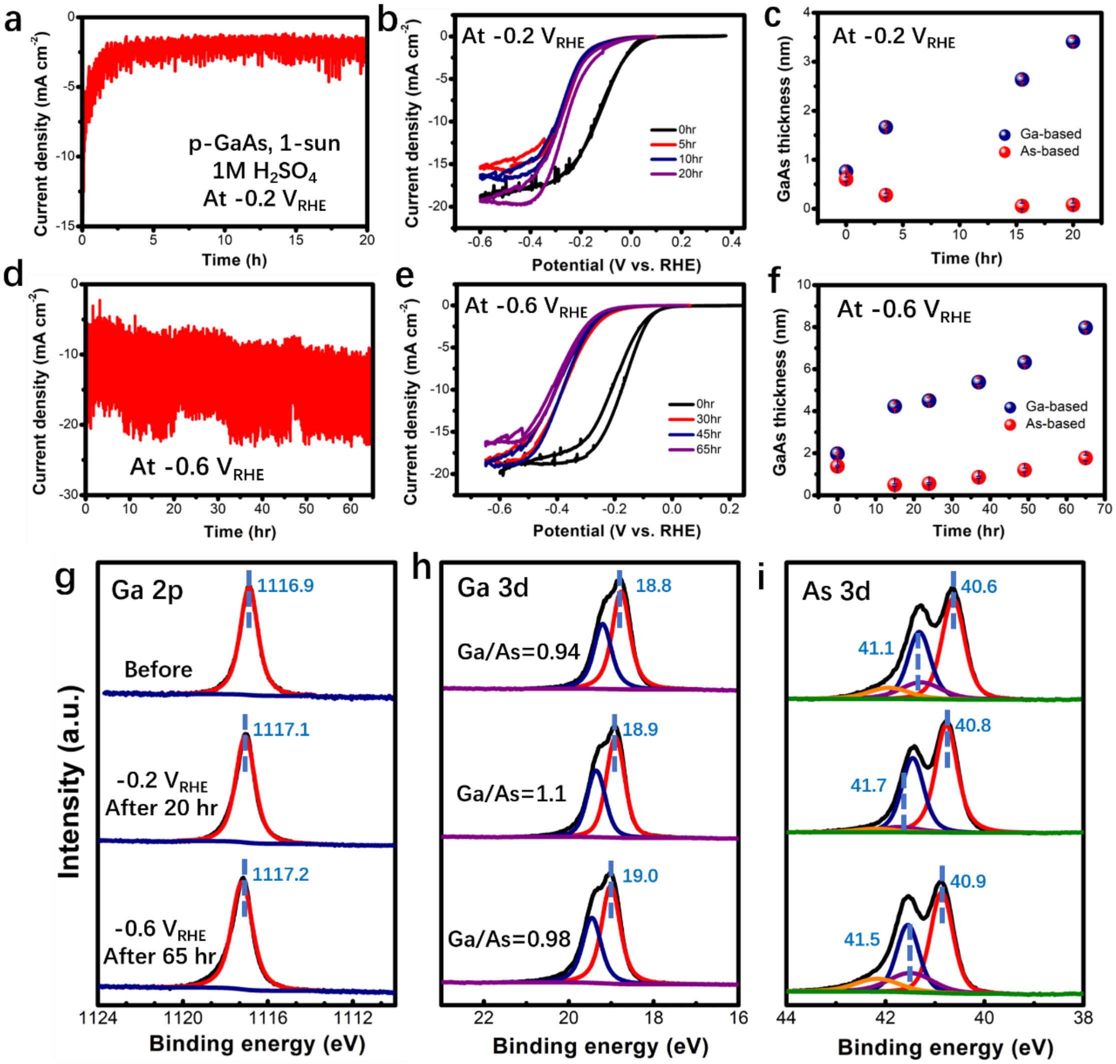

Figure 3.2 Results of etched p-GaAs photoelectrodes tested in acidic electrolytes. (a,d) CA of p-GaAs electrodes at (a) -0.2 V and (d) -0.6 V vs. RHE in 1.0 M H_2SO_4(aq) under 1-sun illumination. (b,e) Comparison of the *J-E* behavior of illuminated p-GaAs electrodes periodically measured over time during CA at (b) -0.2 V vs. RHE for 20 h and (e) -0.6 V vs. RHE for 65 h. Scan rates: 50 mV s^{-1}. (c,f) Corrosion thickness (nm) of p-GaAs versus time for the p-GaAs electrodes during CA in (a,d) determined by the concentrations of dissolved Ga and As ions in the electrolytes. (g-i)

Comparison of XP spectra in the (g) Ga $2p_{3/2}$, (h) Ga 3d and (i) As 3d regions for p-GaAs electrodes before and after CA in (a,d).

In H_2SO_4, the concentrations of Ga ions in the electrolytes increased linearly with time, giving corrosion rates of 0.12 and 0.09 nm h^{-1} for the p-GaAs electrodes tested at -0.2 V and -0.6 V vs. RHE, respectively (Figure 3.2c&f). However, the As concentrations remained low and did not increase with time. XPS data showed negligible changes of the p-GaAs surface after both CA tests (Figure 3.2g-i). The As^0/As ratio was 0.15 for an etched p-GaAs sample before CA, which slightly changed to <0.1 and ~0.2 after the CA at -0.2 V and -0.6 V vs. RHE, respectively. For both samples, the Ga/As ratios of ~1 indicated that the surface of p-GaAs electrodes retained nearly stoichiometric after operation of the HER. Furthermore, the SEM and AFM images showed the surface of both p-GaAs electrodes remained generally flat after CA (Figure S 3.6).

During CA at -0.6 V vs. RHE in 1.0 M KOH(aq), an etched p-GaAs electrode exhibited a stable $|J|$ of ~20 mA cm^{-2} for 46 h under 1-sun illumination (Figure 3.3a). Within the first 5 h of CA, the p-GaAs electrode exhibited negligible J in the dark, which however increased to ~7.4 mA cm^{-2} after 20 h. The increased $|J|$ in the dark paralleled changes in the J-E behavior of the illuminated p-GaAs electrode over time (Figure 3.3b). After 46 h of CA, a comparison of the J-E curves in the dark and under illumination showed that the electrode photoactivity was preserved despite the substantial dark J (Figure S 3.7). ICP-MS analysis of the sampled electrolytes revealed a dissolution of ~1 nm GaAs during the initial 10 h of CA, whereas no further dissolution was observed (Figure 3.3c).

Under illumination, a second p-GaAs electrode exhibited a gradually decreasing $|J|$ during the 4-h CA at E=-0.6 V vs. RHE in KOH (Figure S 3.8). The J was restored to its original value after a short pause (15 s) at E_{oc}, followed by three CV cycles (Figure S 3.8a). The J-E behavior under illumination remained nearly constant over 4 h, but the dark J considerably increased after 4 h (Figure S 3.8b-c).

SEM images of both p-GaAs samples tested in KOH showed their surfaces remained flat, whereas AFM images revealed distinct nano-sized particles (Figure S 3.9). XPS analyses (Figure 3.3e-f) showed similar surface conditions for both samples after CA, without forming new species.

The Ga/As ratios of the p-GaAs electrodes slightly increased to ~1.4 and 1.1 after the 4-h and 46-h CA, respectively.

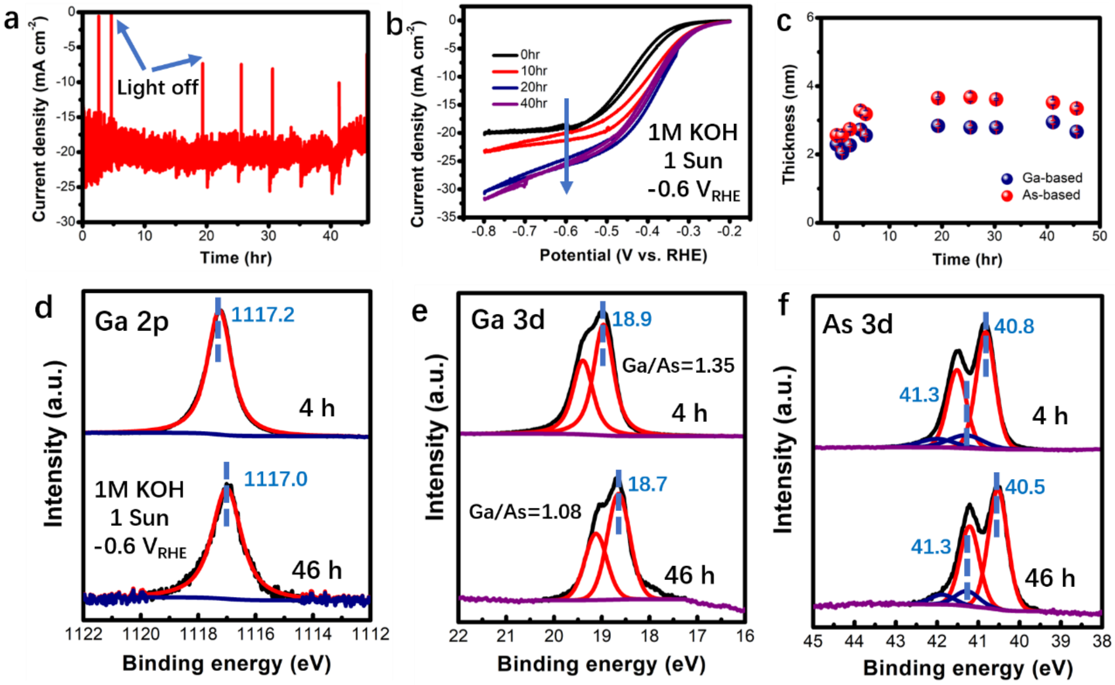

Figure 3.3 Results of etched p-GaAs photoelectrodes tested in alkaline electrolytes. (a) CA of a p-GaAs electrode at -0.6 V vs. RHE in 1.0 M KOH(aq) under 1-sun illumination; the inset arrows represent the times when light was turned off. (b) J-E behavior of an etched p-GaAs electrode under 1-sun illumination during CA in (a). (c) Corrosion thickness (nm) of a p-GaAs electrode versus time during CA in (a) determined by the concentrations of dissolved Ga and As ions in the electrolyte. (d-f) Comparison of XP spectra in the (d) Ga $2p_{3/2}$, (e) Ga 3d, (f) As 3d regions for two different p-GaAs electrodes tested at -0.6 V vs. RHE for 4 h and 46 h.

3.3.4 Preparation and characterization of p-GaAs/Pt_{ed} electrodes.

Pt was electrodeposited on the surface of p-GaAs under illumination, giving p-GaAs/Pt_{ed}(x) electrodes with an estimated thicknesses of x=0.5 nm and 5 nm of Pt, respectively. SEM and AFM images in Figure S 3.10 revealed that both as-prepared p-GaAs/Pt_{ed}(0.5) and p-GaAs/Pt_{ed}(5) samples displayed nano-particulate morphology with increased surface roughness (R_q). For an as-prepared p-GaAs/Pt_{ed}(0.5) electrode, the Ga 3d XPS data showed the Ga^{3+} cations of GaAs at BE=18.9 eV as well as GaO_x at BE=20.7 eV (Figure S 3.11). The XP spectrum of the As 3d region revealed the As^{3-}

anions of GaAs at BE=40.8 eV, As^0 at BE=41.3 and AsO_x at BE=44.0 eV (Figure S 3.11). The oxides of As and Ga likely formed during the Pt electrodeposition. Moreover, the as-prepared p-GaAs/Pt_{ed}(0.5) exhibited a nearly stoichiometric surface (Ga/As=1.1) with a As^0/As ratio of 0.36 (Figure S 3.11).

3.3.5 Stability of p-GaAs/Pt_{ed}(0.5) electrodes at -0.2 V vs. RHE under 1-sun illumination

The stability of a p-GaAs/Pt_{ed}(0.5) electrode was evaluated at E=-0.2 V vs. RHE in 1.0 M H_2SO_4(aq) (Figure 3.4). The first three J-E cycles under illumination showed a light-limited J (J_{ph}) of ~-16 mA cm^{-2}. Within the first 30 min of CA, $|J|$ quickly increased from 10 to 40 mA cm^{-2}, and then gradually decreased to ~10 mA cm^{-2} after 4 h (Figure S 3.12). After CA, the J-E behavior of the illuminated p-GaAs/Pt_{ed}(0.5) electrode exhibited losses of both photoactivity and J_{ph}, resembling the J-E behavior of a Pt electrode (Figure 3.4a). SEM imaging revealed a smooth surface morphology with only few particles after the CA (Figure 3.4c).

XPS analyses of the p-GaAs/Pt_{ed}(0.5) electrode after CA revealed substantial enrichment of As^0 at surface, with weak Ga $2p_{3/2}$ and 3d signals (Figure 3.4d&f). The As 3d XPS data showed three doublets at BE=41.3, 41.8, and 42.7 eV, attributable to the As^{3-} anions of GaAs, As^0 and AsO_x, respectively (Figure 3.4e). A doublet at BE=19.0 eV assigned to Ga^{3+} was identified in the Ga 3d XPS spectrum, whereas the new doublet peak at BE=17.0 eV is likely due to the In impurities (Figure 3.4f). During the 4-h CA, the amounts of dissolved Ga and As ions in the electrolyte increased with rates of ~0.9 and ~0.2 nm h^{-1}, respectively (Figure S 3.14).

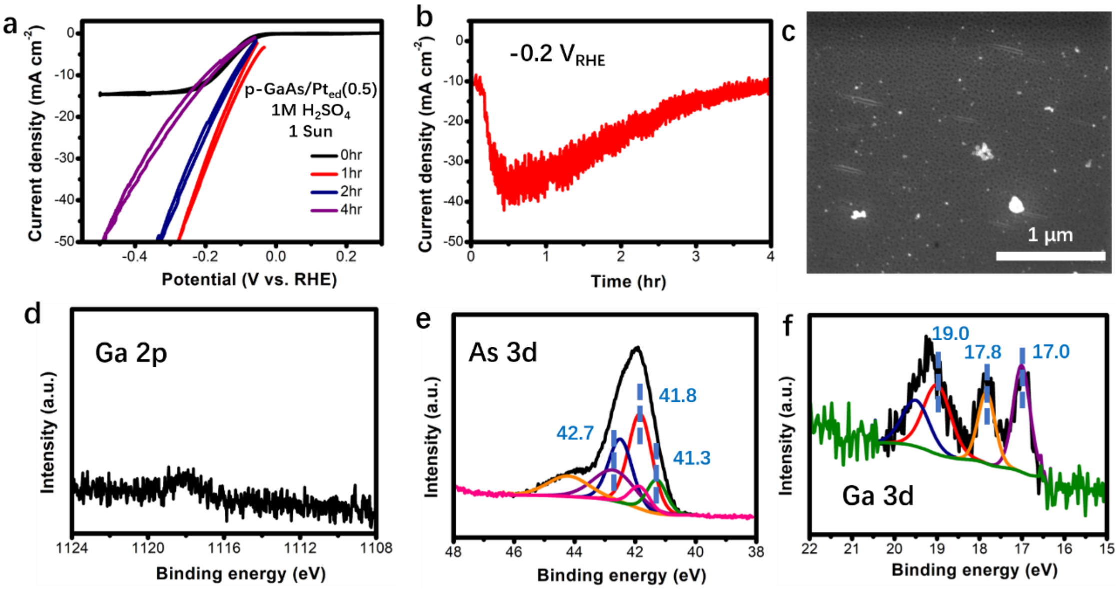

Figure 3.4 Results of a p-GaAs/Pt_{ed}(0.5) electrode tested in acidic electrolyte. (a) Changes in the *J-E* behavior over time and (b) CA of a p-GaAs/Pt_{ed}(0.5) electrode at -0.2 V vs. RHE in 1.0 M H_2SO_4(aq) under 1-sun illumination. (c) SEM image of the p-GaAs/Pt_{ed}(0.5) electrode after CA. (d-f) XPS data in the (d) Ga $2p_{3/2}$, (e) As 3d, (f) Ga 3d regions for the illuminated p-GaAs/Pt_{ed}(0.5) electrode after CA in (b).

Figure 3.5a presents a cross-sectional transmission electron microscopy (TEM) image of the p-GaAs/Pt_{ed}(0.5) electrode after the 4-h CA in H_2SO_4. An amorphous region with a thickness of ~4 nm conformally covered the crystalline GaAs substrate, corresponding to the surface transformation in the XPS data. The EDS line scan and mapping consistently revealed four different layers at the surface region of p-GaAs: GaAs/$Ga_{1-x}As$/GaO_x/As:Pt (Figure 3.5b-c). Moving from bulk GaAs towards surface, the Ga concentration gradually fell and the As concentration rose giving an As-rich layer ($Ga_{1-x}As$). Then the As concentration fell to almost zero giving a GaO_x layer with a Ga/O ratio of ~1.2 close to the Ga_2O_3 phase. The outer most layer (As:Pt) represented a mixture of As and Pt (As/Pt ~3.1), as consistent with the XPS data.

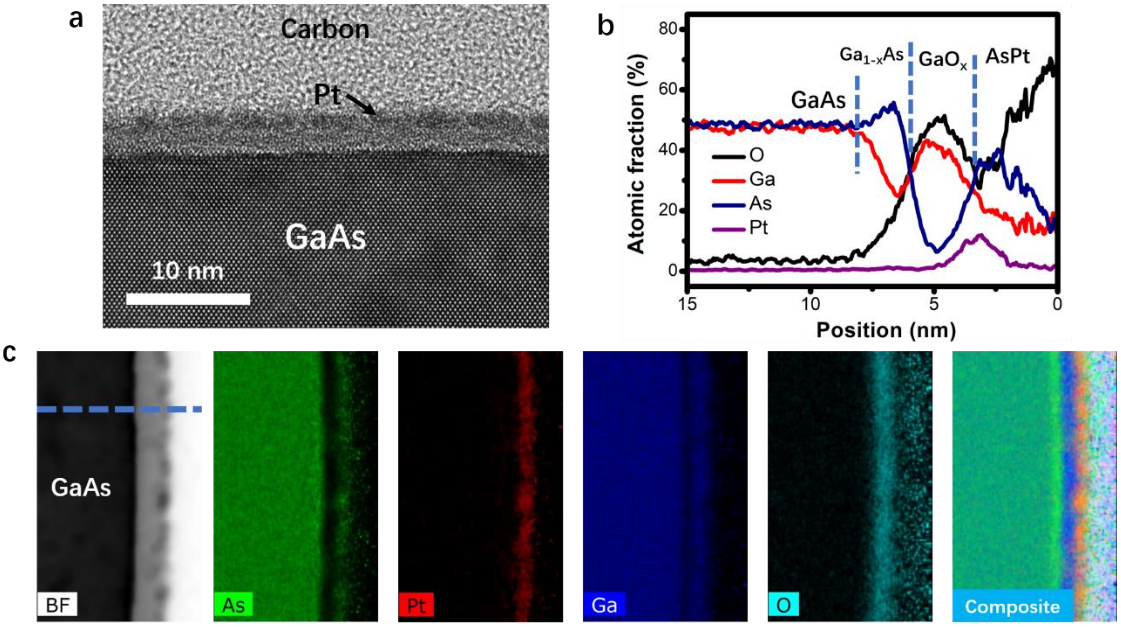

Figure 3.5 (a) cross-sectional TEM image, (b) EDS line scan and (c) EDS mapping across the surface of the p-GaAs/Pted(0.5) electrode after the 4-h CA in 1.0 M H2SO4(aq).

In 1.0 M KOH(aq), the *J*-*E* behavior of a p-GaAs/Pt_{ed}(0.5) electrode was the same under illumination and in the dark with no J_{ph}, indicating a loss of photoactivity (Figure 3.6a). In comparison, an etched p-GaAs electrode in the dark exhibited negligible *J* within the same *E* range in 1.0 M KOH(aq) (Figure S 3.8c). During CA at -0.2 V vs. RHE, an illuminated p-GaAs/Pt_{ed}(0.5) electrode had a *J* of -0.42±0.06 mA cm^{-2} over 4 h (Figure 3.6b). The *J*-*E* behavior of the electrode remained constant during CA (Figure 3.6c). Slightly more As than Ga ions was detected in the electrolyte with a dissolution rate of ~0.3 nm h^{-1} (Figure 3.6d). After CA, XPS data of the Ga $2p_{3/2}$ and 3d regions showed additional peaks at higher BE than those assigned to the Ga^{3+} cations of GaAs, attributable to GaO_x (Figure 3.6e-f). The XP spectrum in the As 3d region showed a substantial amount of As^0 (As^0/As=0.44) with observable AsO_x (Figure 3.6g). The AFM image of p-GaAs/Pt_{ed}(0.5) electrode after CA showed distinct particles sparsely distributed over surface (Figure 3.6h).

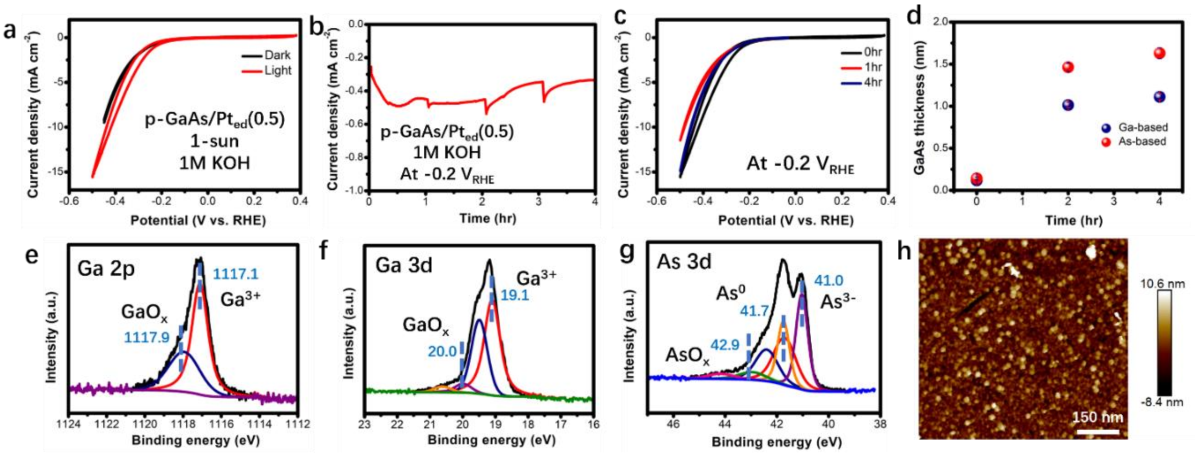

Figure 3.6 Results of a p-GaAs/Pt$_{ed}$(0.5) electrode tested in alkaline electrolyte. (a) Comparison of the J-E behavior for a p-GaAs/Pt$_{ed}$(0.5) electrode in 1.0 M KOH(aq) under 1-sun illumination and in the dark. (b) CA of a p-GaAs/Pt$_{ed}$(0.5) electrode at -0.2 V vs. RHE in 1.0 M KOH(aq) under 1-sun illumination, and (c) comparison of the J-E behavior measured periodically during CA in (b). (d) Corrosion thickness (nm) of a p-GaAs/Pt$_{ed}$(0.5) electrode versus time during CA in (b) determined by the concentrations of dissolved Ga and As ions in the electrolyte. (e-h) XPS data of the (e) Ga 2p$_{3/2}$, (f) Ga 3d and (g) As 3d regions and (h) AFM image (R_q=2.6 nm) for the p-GaAs/Pt$_{ed}$(0.5) electrode after CA in (b).

3.3.6 Stability of p-GaAs/Pt$_{ed}$(5) electrodes at -0.2 V vs. RHE with 1-sun illumination.

With higher Pt loading, a p-GaAs/Pt$_{ed}$(5) electrode was tested at E=-0.2 V vs. RHE in 1.0 M H_2SO_4(aq) under 1-sun illumination (Figure 3.7). Prior to CA, the first three *J-E* cycles of an illuminated p-GaAs/Pt$_{ed}$(5) electrode showed rapid changes at $E \leq$-0.2 V vs. RHE (Figure 3.7a). While the first *J-E* cycle showed a J_{ph} of ~-18 mA cm^{-2}, the third *J-E* cycle appeared similar to those of the above p-GaAs/Pt$_{ed}$(0.5) electrode after the CA in H_2SO_4. The anodic waves at E >0 V vs. RHE were attributed to the oxidation of H_2 by Pt (Figure 3.7a). Initially the electrode had a E_{oc} of +0.46 V vs. RHE that decreased to ~0 V vs. RHE shortly after the CA. After the loss of E_{oc}, the *J-E* behavior of the electrode became the same in the dark and under illumination.

During CA, the periodically measured *J-E* behavior of the p-GaAs/Pt$_{ed}$(5) electrode remained similar to its third *J-E* cycle measured before CA (Figure 3.7c). ICP-MS analysis revealed a higher amount (>2 nm) of Ga than As, whereas the As dissolution remained negligible (Figure 3.7d). After the 50-h CA, XPS data showed no peaks in the Ga 3d or 2p regions (Figure 3.7e-f), while a single doublet at BE=42.1 eV represented As^0 in the As 3d region (Figure 3.7g). After CA, the electrode surface appeared flat in the SEM image (Figure 3.7h), whereas the AFM image revealed a nano-particulate morphology (Figure S 3.15). A second p-GaAs/Pt_{ed}(5) electrode reproduced similar electrochemical behavior and surface characteristics after 48 h of CA in 1.0 M H_2SO_4(aq) (Figure S 3.16).

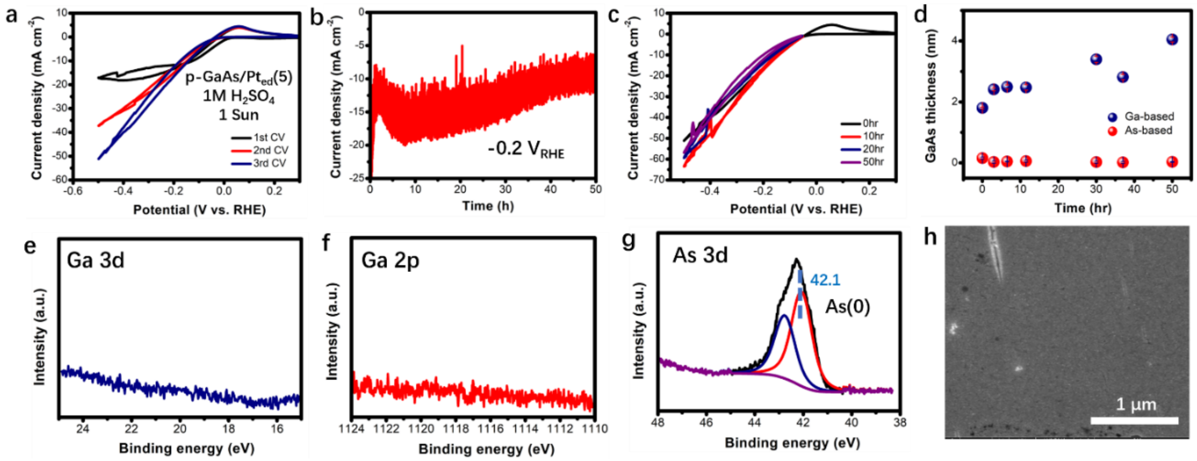

Figure 3.7 Results of a p-GaAs/Pt_{ed}(5) electrode tested in acidic electrolyte. (a) The first three J-E cycles of a p-GaAs/Pt_{ed}(5) electrode under 1-sun illumination in 1.0 M H_2SO_4(aq) (scan rate: 50 mV s^{-1}). (b) CA of a p-GaAs/Pt_{ed}(5) electrode held at -0.2 V vs. RHE in 1.0 M H_2SO_4(aq) under 1-sun illumination and (c) Comparison of its J-E behavior under 1-sun illumination measured periodically during CA in (b) (scan rate: 50 mV s^{-1}). (d) Corrosion thickness (nm) of a p-GaAs/Pt_{ed}(5) electrode versus time during CA in (b) determined by the concentrations of dissolved Ga and As ions in the electrolyte. (e-h) XP spectra in the (e) Ga 3d, (f) Ga $2p_{3/2}$ and (g) As 3d regions and (h) SEM image collected at the p-GaAs/Pt_{ed}(5) electrode surface after CA in (b).

In 1.0 M KOH(aq), the initial *J-E* cycles of an illuminated p-GaAs/Pt_{ed}(5) electrode displayed a similar shunting type behavior to the above p-GaAs/Pt_{ed}(0.5) electrode (Figure 3.8a). During CA at -0.2 V vs. RHE under illumination, the p-GaAs/Pt_{ed}(5) electrode had a *J* of -0.8±0.1 mA cm^{-2} (Figure 3.8b), whereas the *J-E* behavior remained unchanged over 24 h (Figure 3.8c). ICP-MS analysis showed no continuous dissolution of Ga and As ions in the electrolyte, besides an initial dissolution of ~1 nm (Figure 3.8d). After CA, XPS data revealed an increased amount of As^0 (As^0/As~0.7) as well as newly formed GaO_x (Figure 3.8e-g). The peak at BE=531.5 eV in the O 1s

XP spectrum corresponded to the surficial GaO_x (Figure S 3.17).[190,191] AFM image showed a densely packed nano-particulate morphology for the p-GaAs/Pt_{ed}(5) electrode after CA (Figure 3.8h).

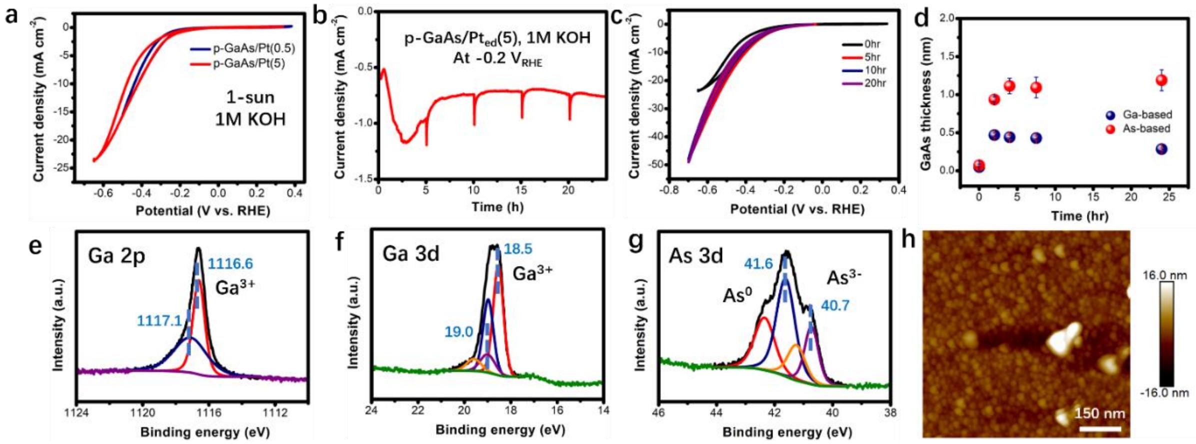

Figure 3.8 Results of a p-GaAs/Pt_{ed}(5) electrode tested in alkaline electrolyte. (a) Comparison of the J-E behavior before CA for a p-GaAs/Pt_{ed}(0.5) and a p-GaAs/Pt_{ed}(5) electrode in 1.0 M KOH(aq) under 1-sun illumination. (b) CA of a p-GaAs/Pt_{ed}(5) electrode at -0.2 V vs. RHE in 1.0 M KOH(aq) under 1-sun illumination and (c) comparison of CVs periodically measured during CA in (b). (d) Corrosion thickness (nm) of a p-GaAs/Pt_{ed}(5) electrode versus time during CA in (b) determined by the concentrations of dissolved Ga and As ions in the electrolyte. (e-h) XP spectra of the (e) Ga $2p_{3/2}$, (f) Ga 3d and (g) As 3d regions and (h) AFM image (R_q=2.9 nm) for the p-GaAs/Pt_{ed}(5) electrode after CA in (b).

3.3.7 Stability of p-GaAs/Pt_{sp}(5) at -0.2 V vs. RHE under 1-sun illumination.

P-GaAs electrodes with 5 nm of sputtered Pt, p-GaAs/Pt_{sp}(5), were tested at E=-0.2 V vs. RHE in 1.0 M H_2SO_4(aq) and 1.0 M KOH(aq) under 1-sun illumination. In both electrolytes, the *J-E* behavior of p-GaAs/Pt_{sp}(5) electrodes showed similar *J-E* behavior in the dark and under illumination, indicating losses of photoactivity (Figure S 3.18). During CA at -0.2 V vs. RHE, within the first 5 hours the |J| of p-GaAs/Pt_{sp}(5) electrodes dropped to <0.1 mA cm^{-2} in both electrolytes (Figure 3.9a&c). The J-E behavior of p-GaAs/Pt_{sp}(5) electrodes displayed more pronounced changes during the CA in H_2SO_4 (Figure 3.9b), whereas the J-E behavior remained constant throughout the CA in KOH (Figure 3.9d).

XPS data of an as-prepared p-GaAs/Pt$_{sp}$(5) sample exhibited two As 3d doublets at BE=40.6 eV (GaAs) and BE=41.4 eV (As^0), with a Ga/As ratio of 1.24 and a As^0/As ratio of 0.6. After CA, surface enrichment of As with mostly As^0 was observed for both electrodes tested in acidic (Ga/As=0.11) and alkaline (Ga/As =0.38) electrolytes (Figure 3.9e-f). Notably, a substantial amount of AsO$_x$ (BE=43.8 eV) appeared for the p-GaAs/Pt$_{sp}$(5) electrode after the CA in KOH. Dissolution of GaAs plateaued at ~10 nm after 10 h for both samples (Figure S 3.19). SEM images of the p-GaAs/Pt$_{sp}$(5) electrodes revealed minimal changes in surface morphology after the CA in acid, but revealed dissolution pits after the CA in KOH (Figure S 3.20).

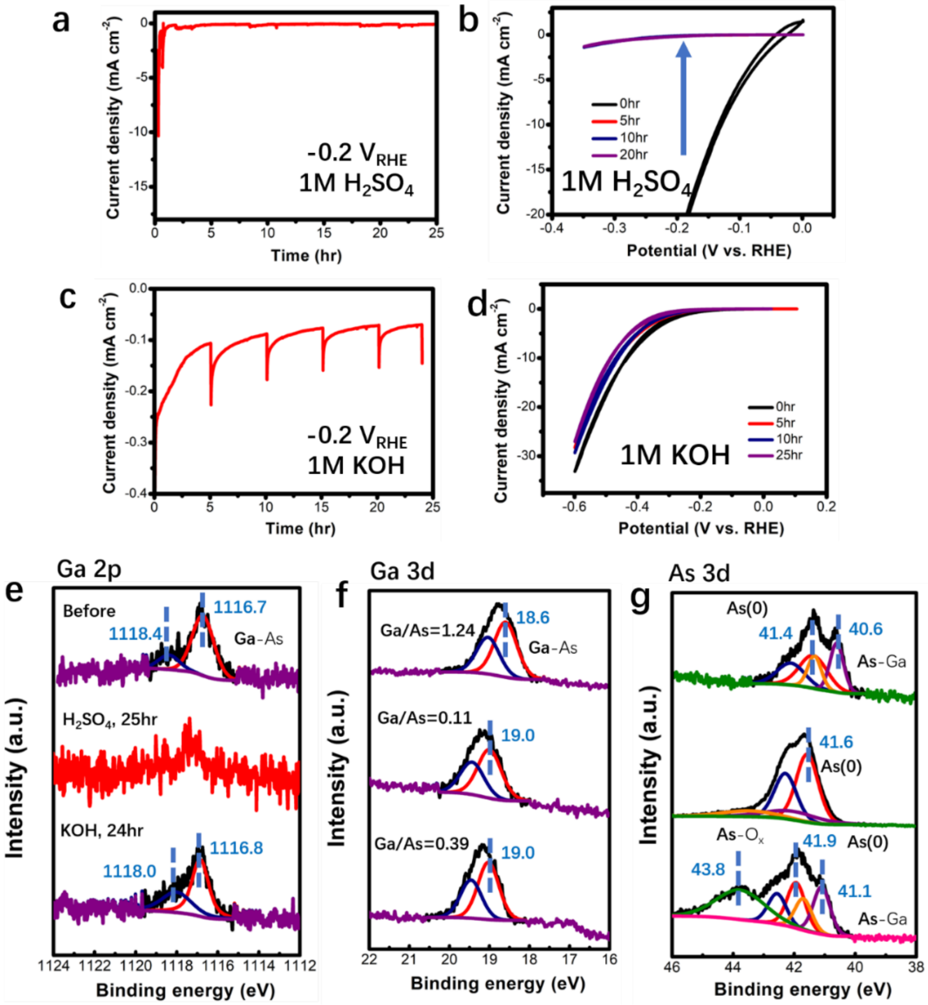

Figure 3.9 Results of p-GaAs/Pt_{sp}(5) electrodes tested in acidic and alkaline electrolytes. (a,c) CA of p-GaAs/Pt_{sp}(5) electrodes at -0.2 V vs. RHE in (a) 1.0 M H_2SO_4(aq) and (c) 1.0 M KOH(aq) under 1-sun illumination. (b,d) Comparison of the J-E behavior over time of illuminated p-GaAs/Pt_{sp}(5) electrodes during CA in (a,c). (e-f) XP spectra in the (g) Ga $2p_{3/2}$, (h) Ga 3d and (i) As 3d regions for p-GaAs/Pt_{sp}(5) electrodes before and after CA in (a,c).

3.3.8 Preparation and characterization of p-GaAs/CoP electrodes.

To compare with Pt, CoP was photo-electrodeposited onto the surface of p-GaAs following a published procedure.[145] Three different p-GaAs/CoP(x) electrodes were prepared where x represents the charge density passed during deposition (50/200/400 mC cm^{-2}). The CA of CoP deposition for the three electrodes was shown in Figure S 3.21a. As the loading of CoP increased from 50 to 400 mC cm^{-2}, the dark cathodic *J* of p-GaAs/CoP electrodes substantially increased at *E* <-0.1 V vs. RHE, when tested in 1.0 M H_2SO_4(aq) (Figure S 3.21b). SEM imaging of an as-prepared p-GaAs/CoP(200) electrode showed a thin-film morphology with cracks (Figure S 3.22). The CoP thin-film was composed of individual islands, whereas each island was an aggregate of small nanoparticles (Figure S 3.22).

For an as-prepared p-GaAs/CoP(200) electrode, XPS data in the Ga $2p_{3/2}$ and 3d regions showed peaks only ascribable to the Ga^{3+} cations of GaAs at BE=1116.9 and 18.7 eV, respectively (Figure S 3.25). The As 3d region exhibited peaks for the As^{3-} anions of GaAs and As^0 at BE=40.5 and 41.0 eV, respectively. The Ga/As ratio was 0.7, whereas the As^0/As was 0.2. The low signal-to-noise ratios in the Ga and As XP spectra were due to the thick coating of CoP. In the Co 2p region, the peaks at BE=777.8 and 780.4 eV were assigned metallic Co^0 and CoO_x, respectively.[145] The P 2p region showed peaks at BE=129.1 and 129.9 eV attributable to CoP, and peaks at BE=131.5 and 133.0 eV assigned to a Co orthophosphate compound.

3.3.9 Stability of p-GaAs/CoP electrode at -0.2 V vs. RHE under 1-sun illumination in acid.

A comparison of the *J-E* behavior of three p-GaAs/CoP electrodes revealed decreased photocurrent as well as increasing dark *J*, with increased loading of CoP (Figure 3.10a-c). During CA at -0.2 V vs. RHE, all three p-GaAs/CoP(x) electrodes exhibited stable *J* under 1-sun illumination (Figure 3.10d-f), whereas their *J-E* behavior remained nearly unchanged during CA (Figure 3.10g-i). After CA, the p-GaAs/CoP(400) electrode displayed a similar morphology to the as-prepared p-GaAs/CoP(200) electrode, whereas the surface of both p-GaAs/CoP(50) and p-GaAs/CoP(200) electrodes showed sparsely distributed particles (Figure S 3.23-24).

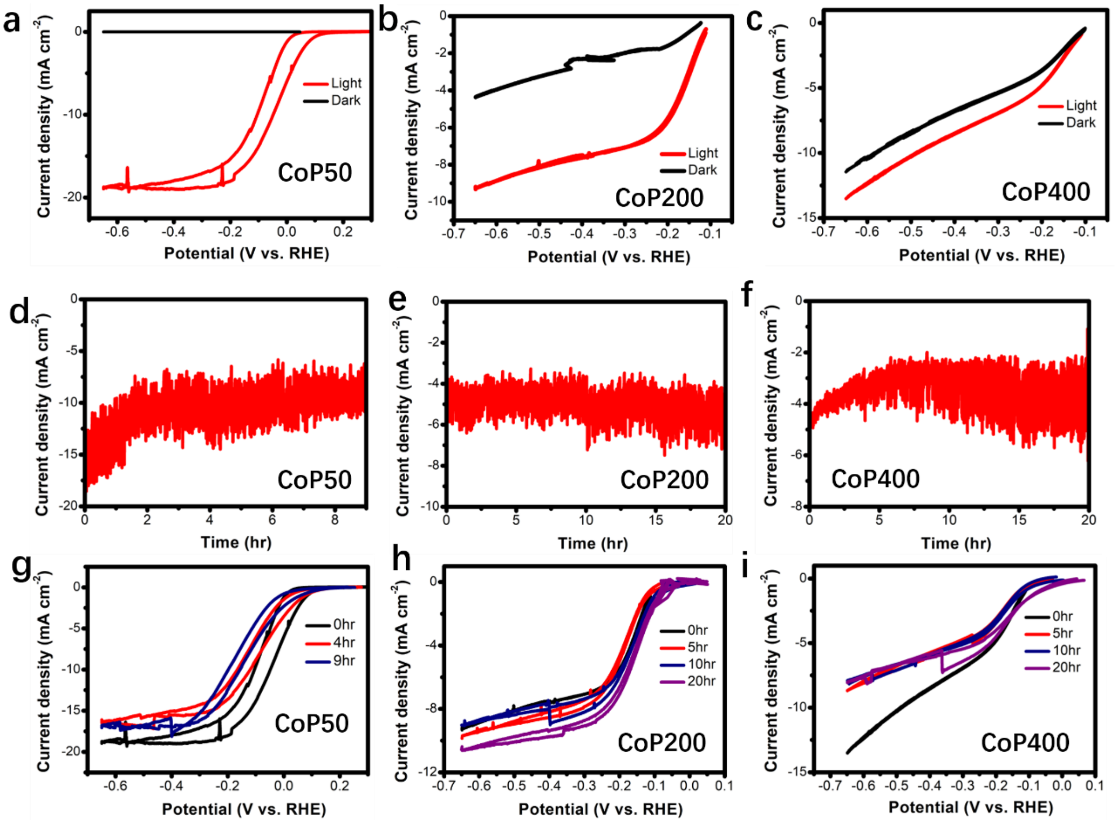

Figure 3.10 Results of p-GaAs/CoP electrodes tested in acidic electrolytes. (a-c) Comparison of the J-E behavior of (a) a p-GaAs/CoP(50), (b) a p-GaAs/CoP(200) and (c) a p-GaAs/CoP(400) electrode, measured in the dark and under 1-sun illumination in 1.0 M H_2SO_4(aq) (d-f) CA of (a) a p-GaAs/CoP(50), (b) a p-GaAs/CoP(200) and (c) a p-GaAs/CoP(400) electrode at -0.2 V vs. RHE under 1-sun illumination in 1.0 M H_2SO_4(aq). (g-i) Comparison of the J-E behavior periodically measured during the CA of (a) p-GaAs/CoP(50), (b) p-GaAs/CoP(200) and (c) p-GaAs/CoP(400) electrodes.

XPS analyses of the three p-GaAs/CoP electrodes after CA were shown in Figure 3.11. For the p-GaAs/CoP(200) electrode, the increased signal-to-noise ratios in the Ga and As XP spectra after

CA indicates partial dissolution of CoP deposit during the HER in acidic electrolyte, corroborated by a decreased Co/As atomic ratio from 39.7 to 0.6.[192] The Co^0 peak at BE=777.8 eV disappeared in the Co 2p XP spectrum, whereas a new peak emerged at BE=778.8 eV ascribable to CoP.[145] In the P 2p XP spectrum, the PO_x peak at BE=133.0 eV became more pronounced after CA, relative to the CoP peaks at BE=129.1 and 129.9 eV. Besides, GaO_x appeared at BE=1118.5 eV in the Ga $2p_{3/2}$ region (Figure S 3.25).

XP spectra of the p-GaAs/CoP(50) and p-GaAs/CoP(400) electrodes after CA were similar to those of the p-GaAs/CoP(200) electrode. In contrast to all p-GaAs/Pt electrodes, the As 3d XP spectra showed no increase in surficial As^0 for all three p-GaAs/CoP(x) electrodes. Both the p-GaAs/CoP(50) (Ga/As=1.03) and p-GaAs/CoP(200) (Ga/As=0.89) electrodes displayed nearly stochiometric GaAs surface. The deposited CoP with PO_x (BE>132 eV) remained at the surface of all three electrodes after operation of the HER. For the p-GaAs/CoP(400) electrode after CA, the Ga and As XPS data showed much weaker signals due to the CoP coating, with substantial AsO_x (BE=43.3 eV) in the As 3d region.

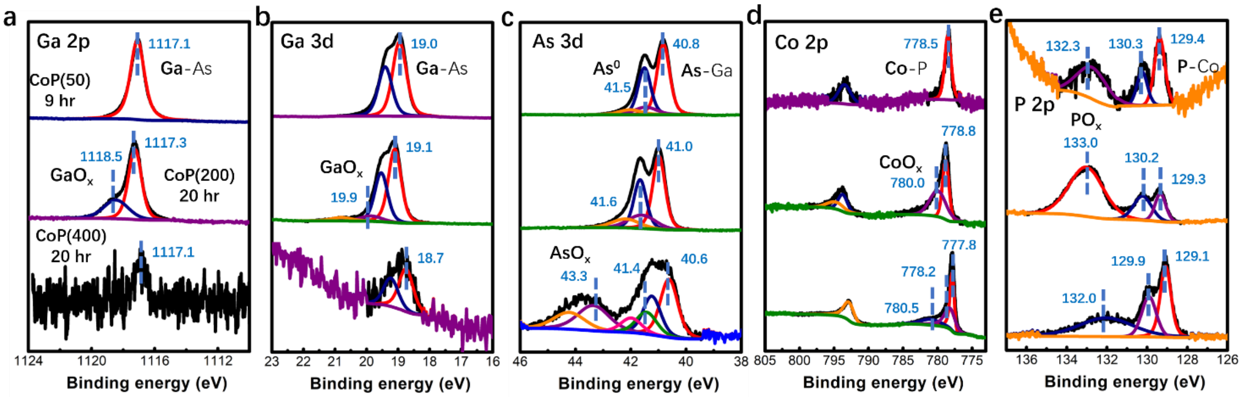

Figure 3.11 Comparison of XP spectra in the (a) Ga $2p_{3/2}$, (b) Ga 3d, (c) As 3d, (d) Co 2p, and (e) P 2p regions for three different p-GaAs/CoP electrodes after CA at -0.2 V vs. RHE in 1.0 M H_2SO_4(aq) under 1-sun illumination: p-GaAs/CoP(50) after 9 h (upper panels), p-GaAs/CoP(200) after 20 h (middle panels), and p-GaAs/CoP(400) after 20 h (bottom panels).

3.4 Discussions

GaAs dissolution under E_{oc} and negative E: Thermodynamic Pourbaix diagram is useful for determining corrosion pathways of GaAs at a given pH and E.[127] Herein, we focus on the stability of GaAs under conditions of the HER (E<0 V vs. RHE) at both pH=0 and pH=14. A calculated Pourbaix diagram of GaAs by the Materials Project predicts a stable GaAs phase at negative E<-0.4 V vs. RHE across the whole pH (Figure S 3.1), indicating cathodic protection. However, a positive E≥-0.1 V vs. RHE favors the oxidation of GaAs to soluble As(III) and Ga(III) ions (Eq 2a-b), whereas a E between -0.4 and -0.1 V vs. RHE results in elemental As^0 and Ga(III) ions (Eq 3a-b).

pH=0, E >-0.1 V_{RHE}: $2GaAs(s) + 4H_2O(l) + 6H^+(aq) \rightarrow 2Ga^{3+}(aq) + 2HAsO_2(aq) + 6H_2(g)$ (2a)

pH=14, E >-0.2 V_{RHE}: $GaAs(s) + 4OH^-(aq) + 2H_2O(l) \rightarrow GaO_3^{3-}(aq) + H_2AsO_3^-(aq) + 3H_2(g)$ (2b)

pH=0, -0.5<E<-0.1 V_{RHE}: $2GaAs(s) + 6H^+(aq) \rightarrow 2Ga^{3+}(aq) + 2As^0(s) + 3H_2(g)$ (3a)

pH=14, -0.4<E<-0.2 V_{RHE}: $2GaAs(s) + 6OH^-(aq) \rightarrow 2GaO_3^{3-}(aq) + 2As^0(s) + 3H_2(g)$ (3b)

Experiments of etched n- and p-GaAs electrodes at E_{oc} in the dark showed positive values of E_{oc} (+0.1 to +0.5 V vs. RHE), as well as continuous and stoichiometric dissolution at rates of <1 and ~6 nm h^{-1} in acidic and alkaline electrolytes, respectively. Based on the measured E_{oc} values, the corrosion reactions of GaAs should follow Eq 2a-b, where the oxidation of GaAs by water or protons forms soluble Ga and As ions at both pH=0 and pH=14.

Compared with the conditions of E_{oc}, the CA experiments of n-GaAs electrodes at E=-0.1 V vs. RHE in the dark showed negligible dissolution in both acidic and alkaline electrolytes. The Pourbaix diagram in Figure S 3.1 predicts that the formation of As^0 is likely at E=-0.1 V vs. RHE for both pH=0 and pH=14 following Eq 3a-b. However, only a small increase of As^0 was found at the surface of the n-GaAs electrode tested in 1.0 M H_2SO_4(aq). These results suggest that applying a cathodic bias of -0.1 V vs. RHE to n-GaAs electrodes mitigates its continuous dissolution at E_{oc} in the dark, whereas the kinetics of As^0 formation is slow for etched n-GaAs electrodes.

Further, holding illuminated etched p-GaAs electrodes at cathodic biases (-0.2 or -0.6 V vs. RHE) again resulted in little continuous corrosion of GaAs. Importantly, the p-GaAs electrodes maintained photoactivity after operation of the HER, with minimal surface changes and no excessive As^0 formation (Scheme 3.1a). Considering the slow kinetics of the HER at the surface of etched GaAs, these results indicate that the surface potential of p-GaAs photoelectrodes during the HER is more negative than the E region favoring As^0 formation, thereby enabling cathodic protection of GaAs. For etched p-GaAs photoelectrodes tested in acidic electrolytes, slow rates of dissolution (~0.1 nm h^{-1}) were observed only for Ga ions. Previous spectroscopic studies revealed that the HER at the etched GaAs surface occurs via As-H interaction.[193,194] Thus, the absence of As ion in the electrolyte is attributed to the $AsH_3(g)$ formation under negative E (Eq 4), which is carried away by the concurrent H_2 bubbles from electrode surface.[195]

$$\text{pH=0: } \mathrm{GaAs}(s) + 3\mathrm{H}^{+}(aq) \rightarrow \mathrm{AsH}_3 \ + \mathrm{Ga}^{3+}(aq) \ (4)$$

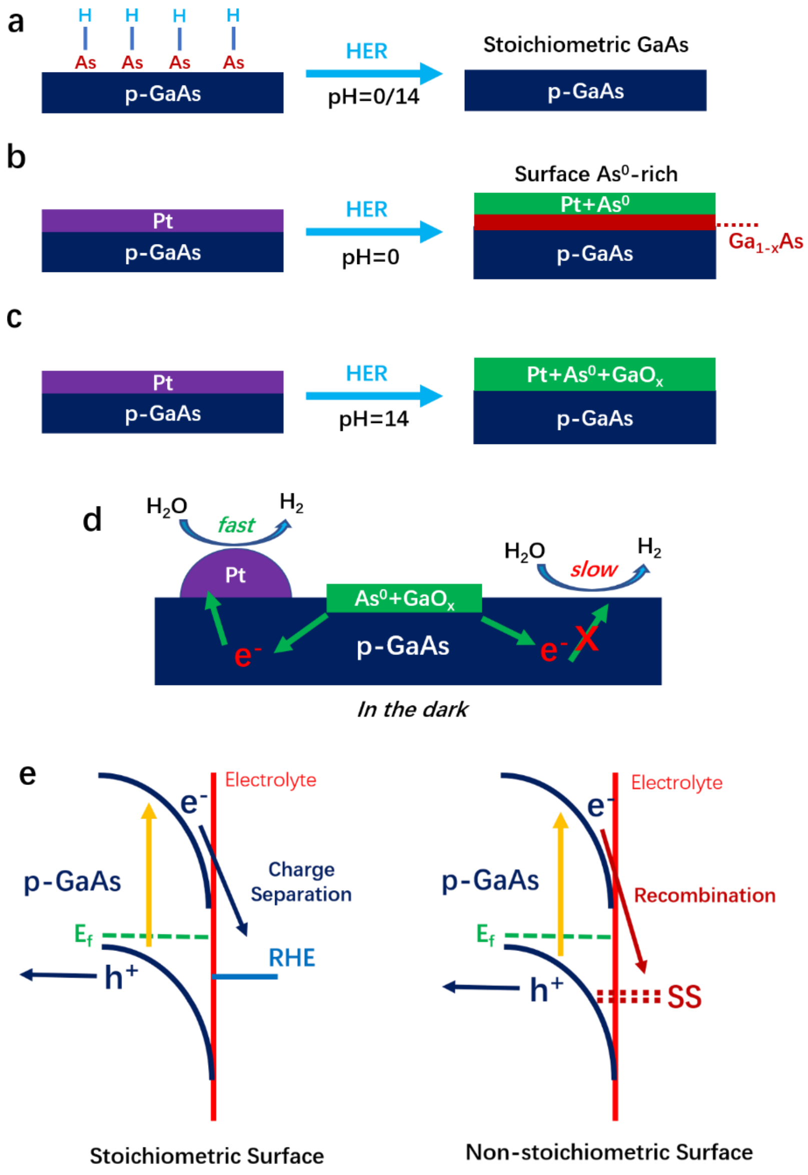

Scheme 3.1 (a-c) Schematic illustration of the changes of surface conditions for (a) etched p-GaAs and (b-c) p-GaAs/Pt electrodes before and after operation of the HER under illumination at pH=0 and pH=14. (d) Galvanic corrosion of GaAs forming surficial As^0 and GaO_x species assisted by Pt catalyst. (e) Comparison of band energy diagram of illuminated p-GaAs electrodes with a stoichiometric or a non-stoichiometric surface under cathodic bias; a stoichiometric GaAs surface promotes effective charge separation, whereas charge recombination occurs for a non-stoichiometric GaAs surface due to surface states (SS).

Pt-induced As^0 formation causes a loss in the p-GaAs photoactivity: As shown by the XPS data, electrodeposition of Pt at p-GaAs surface leads to the formation of excessive As^0 under conditions of the HER at both pH=0 and pH=14. Experiments of p-GaAs/Pt_{ed}(0.5) and p-GaAs/Pt_{ed}(5) electrodes yielded similar results of both electrochemical measurements and surface characteristics after the CA in H_2SO_4 and KOH. Mostly As^0 was observed for p-GaAs/Pt_{ed} electrodes after CA at pH=0 (Scheme 3.1b), whereas both GaO_x and As^0 formed at the surface of p-GaAs/Pt_{ed} electrodes after CA at pH=14 (Scheme 3.1c). Hence, the Ga(III) species in Eq 3d manifested as insoluble oxides (GaO_x) instead of the GaO_3^{3-} ions at pH=14. The absence of GaO_x at pH=0 is attributed to its higher solubility, resulting in a higher amount of Ga than As ions in the electrolytes detected by ICP-MS. Sputtering of Pt onto the surface of etched p-GaAs directly induced the formation of excessive As^0 even before any electrochemical measurement, again causing electrode shunting. After CA, the surfaces of p-GaAs/Pt_{sp} electrodes became more As^0-rich with decreased Ga/As ratios at both pH=0 and pH=14. For all p-GaAs/Pt electrodes, the formation of excess surficial As^0 closely correlated with: (1) losses of photoactivity, (2) emergence of dark cathodic *J* of HER, and (3) a shunting behavior in both acidic and alkaline electrolytes. In comparison, etched p-GaAs electrodes initially displayed negligible *J* in the dark in the same E range, as well as a well-defined J_{ph} of ~-20 mA cm^{-2} under illumination.

Based on the unified defect model proposed by Spicer et al,[99] the electronic properties of GaAs are sensitive to changes in surface stoichiometry. Excessive As or Ga atoms at GaAs surface produce mid-gap surface states (SS), located at 0.5 eV and 0.75 eV above the valence band maximum (VBM), respectively.[148] The above findings are consistent with this model, as the J-E behavior of p-GaAs electrode is highly dependent on the surface changes under conditions of the HER. Previous studies estimate the conduction band edge of GaAs above the potential of RHE by 0.8 to 1.0 eV, whereas their relative positions stay fixed as pH is varied.[196–199] Therefore, the low PEC performance of p-GaAs photocathodes may be partially explained by the low barrier height between the Fermi level (E_f) of p-GaAs and the RHE potential in electrolytes. As shown in Scheme 3.1e, etched p-GaAs electrodes preserve nearly stoichiometric surface as well as photoactivity, leading to effective separation of photogenerated electrons under cathodic bias.[200,201] For p-GaAs/Pt electrodes, the formation of either surficial As^0 (shown by XPS) or an As-rich interlayer (shown by TEM) during the HER, result in surface states at a non-stoichiometric GaAs surface. The mid-gap surface states create a recombination pathway for photogenerated electrons, thereby leading to a loss in photoactivity (Scheme 3.1f). Moreover, such surface states also promote a shunting pathway for passing dark J under cathodic bias, due to their similar energy levels as the RHE potential. Additionally, the increased J measured in the dark for etched p-GaAs photocathodes after operation of the HER for >4 h in KOH, is also likely attributed to the slight Ga-enrichment at surface.

Collectively, these results suggest that Pt catalyst facilitates the oxidation of GaAs to As^0 via Eq. 3a-b by forming an interfacial galvanic pathway (Scheme 3.1d).[173] Also, the fast kinetics of the HER by Pt lowers the surface potential of p-GaAs into the E region favoring the formation of As^0. In contrast, the slow HER kinetics at an etched GaAs surface inhibits such corrosion pathway, as supported by the results of n-GaAs dark electrodes at E=-0.1 V vs. RHE. Consequently, both thermodynamic and kinetic factors are necessary to promote the As^0 formation. Despite the surface transformations, sustained dissolution of GaAs over time remained slow for both etched p-GaAs electrodes and those coated with Pt catalysts under cathodic biases in acidic and alkaline electrolytes. As a result, p-GaAs (photo)-cathodes remained physically robust when performing the HER at negative E at pH=0 and pH=14. These results are in contrast to the rapid anodic corrosion of GaAs or the continuous dissolution of GaAs at E_{oc} in the dark.[60] Furthermore, although analogous to the metal-assisted chemical etching (MacEtch), the corrosion of GaAs to As^0 catalyzed by Pt is self-limiting without continuous dissolution while requiring no other oxidant than H_2O or H^+.[202–204]

Comparison of CoP and Pt catalysts: Excess As^0 was not observed for p-GaAs/CoP electrodes after operation of the HER in acidic electrolytes. This behavior indicates that the p-GaAs/CoP/H_2O tri-phase interface does not result in the same galvanic corrosion pathway as occurs for p-GaAs/Pt/H_2O tri-phase interfaces. Despite the slightly lower HER activity of CoP than Pt, the overpotentials at J = -10 mA cm^{-2} of both catalysts should be within or close to the E range that favors formation of As^0.[145] Compared to metallic Pt, the lack of As^0 formation for CoP is consistent with the low conductivity of CoP and/or a different coverage configuration on GaAs (thin-film vs. nano-particulate), resulting in a lack of ability to form local redox centers that are in good electrical communication with the substrate. Use of the earth-abundant CoP catalyst instead of the noble-metal Pt catalyst on p-GaAs also provides a constructive example situation in which an unfavorable surface conversion of GaAs can be mitigated by tailoring the morphology and composition of the HER catalyst. However, the increases in dark *J* of p-GaAs/CoP electrodes as the CoP loading is increased indicates an unfavorable band alignment at the interface, which will require further interface engineering techniques to optimize both the stability and high performance of such systems as photocathodes for solar fuels production.

3.5 Conclusions

The long-term stability of p-GaAs photocathodes for the HER has been evaluated in contact with acidic and alkaline electrolytes, with or without active catalysts (Pt or CoP). Illuminated etched p-GaAs electrodes preserved nearly stoichiometric surfaces as well as photoactivity, after operation of the HER at both pH=0 and pH=14. However, either electrodeposited or sputtered Pt catalyst at p-GaAs surface led to the formation of excessive As^0 via an interfacial galvanic reaction. P-GaAs/Pt electrodes with excessive surficial As^0 displayed a shunting type behavior as well as a loss of photoactivity, resulting from mid-gap surface states by an As-rich surface. In contrast, the p-GaAs electrodes coated with a thin-film of CoP catalyst did not produce excess As^0 after performing the HER in acidic electrolytes. Under cathodic bias, illuminated p-GaAs electrodes exhibited negligible dissolution over long term at pH=0 and pH=14, while the J-E behavior of p-GaAs is influenced by the changes of surface stoichiometry. This work reveals the importance of surface characteristics for determining the photo-electrochemical behavior of p-GaAs electrodes, and emphasizes a proper semiconductor-catalyst integration to mitigate unfavorable interfacial reactions.

Acknowledgement

This material is based upon work performed by the Joint Center for Artificial Photosynthesis, a DOE Energy Innovation Hub, supported through the office of Science of the U.S. Department of Energy under Award Number DE-SC0004993. Research was in part carried out at the Molecular Materials

Research Center (MMRC) of the Beckman Institute of the California Institute of Technology. Phil Jahelka and Dr. Chengxiang Xiang are gratefully acknowledged for fruitful discussions. Dr. Nathan Dalleska is thanked for assistance with ICP-MS analysis. Pakpoom Buabthong is thanked for assistance with XPS analysis.

3.6 Experimental

3.6.1 Materials

1.0 M sulfuric acid solution (H_2SO_4, VWR Chemicals), 1.0 M potassium hydroxide aqueous solution (KOH, TitriPUR volumetric solution and Supelco), bromine (Br_2, reagent grade, Sigma-Aldrich), and methanol (CH_3OH, VWR Analytical, ACS, 99.8 %). Deionized water (18.2 MΩ cm) was obtained from a Barnstead Millipore system. Single-side polished, (100)-oriented, Si-doped (N_d=1-5×10^{17} cm^{-3}) n-type GaAs wafers and Zn-doped (N_d=1-5×10^{17} cm^{-3}) p-type GaAs wafers were obtained from AXT Inc. Nafion (proton-exchange membrane) and Fumasep (anion-exchange membrane) were purchased from the Fuel Cell Store.

3.6.2 Purification of electrolytes by pre-electrolysis

Prior to use in CA experiments, 1.0 M H_2SO_4(aq) and 1.0 M KOH(aq) were pre-electrolyzed in a two-compartment electrochemical cell (Pyrex), with the compartments separated by either a Nafion (acid) or Fumasep (base) membrane. Carbon rod electrodes were used as the cathode and anode. Pre-electrolysis was carried out under a constant bias of >3 V or a constant current of 6 mA for >24 h. Only the catholyte was collected for further electrochemical measurements. No H_2O_2 was found in the catholyte after the electrolysis, as determined by the spectro-photometrical analysis using titanium oxalate.[150]

3.6.3 Back contacts to GaAs electrodes

For n-GaAs, 100 nm of metallic In was evaporated onto the back side of the wafer. Then the sample was annealed under forming gas at 400 °C for 10 min. For p-GaAs, 50 nm of metallic Ni was sputtered onto the back side of the wafer at room temperature. Sputter deposition was performed in an AJA Orion sputtering system.

3.6.4 GaAs etching

Prior to electrochemical measurements, both n-type or p-type GaAs electrodes were etched in 0.04 % Br_2/CH_3OH for 30 s, then in 1.0 M KOH(aq) for 15 s.[46] Samples were then rinsed with methanol and blown dry under a nitrogen gun for > 10 s.

3.6.5 (Photo)-electrochemical measurements

Electrochemical measurements, including chronoamperometry (CA) and cyclic voltammograms (CV), were performed in a nitrogen-filled glovebox (VAC, OMNI-LAB) with a O_2 concentration of <0.3 ppm. All electrolytes were degassed using a Schlenk line to remove the dissolved oxygen prior to transfer into the glovebox.

To facilitate XPS analysis, electrochemical measurements were performed using a custom-made compression cell fabricated from PEEK. The cell had two compartments separated by an ion-exchange membrane (Nafion for H_2SO_4, Fumasep for KOH). All electrochemical data were acquired on a SP-200 potentiostat (BioLogic Science Instruments), without compensation for solution resistance. Electrochemical measurements were performed in a three-electrode set-up, with Pt or Ni foil as the counter electrode (CE), a hydrogen electrode HydroFlex (Gaskatel) as the reference electrode (RE), and GaAs as the working electrode (WE). H_2 gas was fed into the glovebox, passed through an aqueous gas bubbler, and used to continuously purge the catholyte during electrochemical experiments. The $H_2(g)$ from the cathode chamber and $O_2(g)$ from the anode chamber were separately vented to outside the glove box.

Prior to each experiment, the compression cell was assembled immediately after etching of GaAs samples and transferred into the glovebox. The long-term stability of GaAs were evaluated by CA in the dark or under illumination. The J-E behaviors of p-GaAs electrodes were periodically measured by CV during CA. Typically, the CV cycles were measured after a pause of 15 s at open-circuit potential (E_{oc}), starting from $E=E_{oc}-0.035V$ to more negative potentials to avoid passing anodic current through the WE. A scan rate of 50 mV s^{-1} was used for all CVs. After each experiment, the cell was disassembled inside the glovebox and the electrode sample was thoroughly rinsed with deionized water, blown dried with nitrogen, and stored inside the glovebox until further XPS analysis.

A miniature fiber-optic adjustable-arm light equipped with a 150 W halogen bulb was used as the illumination source and was introduced from outside the glovebox via a fiber optic. The illumination intensity at the sample position within the electrochemical cell was calibrated to 1 sun (100 mW cm^{-2}) using a Si photodiode (FDS100, Thorlabs). The total volume of electrolyte in the cathode chamber was 4 mL. For the ICP-MS analysis, 0.2 mL of electrolyte was withdrawn from the catholyte at intervals with the WE still under potential control, and replaced with 0.2 mL of fresh electrolyte to keep the total volume of electrolyte constant.

3.6.6 Electrodeposition of Pt catalyst and CoP catalyst

For electrodeposition of Pt catalyst onto p-GaAs samples, a solution of 5 mM K_4PtCl_6 and 0.5 M KCl was used and a current density of -0.2 mA cm^{-2} was applied under illumination in a two-electrode configuration until a fixed charge density of -2 or -20 mC cm^{-2} had passed. A carbon rod was used as the counter electrode.

Electrodeposition of CoP catalyst onto p-GaAs samples was performed based on a published procedure.[145] A “leakless” miniature AgCl/Ag electrode and a carbon rod were used as the reference and counter electrodes, respectively. The electrodeposition was performed at a constant potential of -1.2 V vs. AgCl/Ag under illumination until a fixed charge density of -50, -200, or -400 mC cm^{-2} had passed.

After each deposition, the cell was thoroughly cleaned with deionized water at least 3 times before further stability tests by CA in acidic and alkaline electrolytes.

3.6.7 Sputter deposition of Pt onto p-GaAs

Sputter deposition was performed in an AJA Orion sputtering system with a typical base pressure of 5×10^{-8} Torr. Before deposition of Pt, p-GaAs samples were freshly etched and dried using $N_2(g)$, and promptly transferred to the sputtering chamber. The deposition of Pt was performed at room temperature under an Ar flow of 20 sccm to maintain a working pressure of 5 mTorr.

3.7 Analytical Methods

3.7.1 Inductively coupled plasma mass spectrometry (ICP-MS) of catholytes

Inductively coupled plasma mass spectrometry (ICP-MS) data were collected using an Agilent 8800 Triple Quadrupole ICP-MS system. Calibration solutions were prepared by diluting the multi-element standard solutions for ICP with 18.2 MΩ cm resistivity water. The total amounts of dissolved Ga or As ions from the electrodes were calculated and normalized to the geometric electrode area to obtain the equivalent depth of material removed from the crystalline electrode. To account for different acidic and basic solution matrixes, standards were prepared and diluted using the same solution matrix as the analytes.

3.7.2 X-ray photoelectron spectroscopy with air-free transfer

X-ray photoelectron spectroscopy (XPS) was performed using a Kratos Axis Ultra system with a base pressure of < 1×10^{-9} Torr equipped with a monochromatic Al Kα X-ray source with a photon energy of 1486.6 eV. Photoelectrons were collected at 0° from the surface normal with a retarding pass energy of 160 eV for survey XPS scans (step size of 1.0 eV) and for high-resolution core-level scans (step size 0.025 eV).

Prior to XPS measurements, samples were mounted on a Kratos sample holder in the glove box under N_2, inserted into a transfer suitcase sealed by a gate valve. The transfer suitcase was attached to the load lock of the Kratos Axis Ultra system. The load lock was pumped down to 1×10^{-6} Torr and then purged with N_2 to 1 atm. After pumping the load lock to ~100 Torr, the gate valve to the transfer suitcase was opened and the turbo molecular pump was switched on. After achieving a pressure of < $1 \text{ x } 10^{-6}$ Torr, the sample was transferred into the sample transfer chamber. After closing the gate valve to transfer suitcase, the sample was pumped down to $<1\times10^{-8}$ Torr before being transferred to the analysis chamber.

3.7.3 Fitting of XPS spectra

All XPS peak fitting was performed using CasaXPS software version 2.3.18. All binding energies are referenced to the adventitious carbon peak at 284.8 eV. Before fitting the data, a Shirley background was calculated and subtracted from the original spectra. The As 3d and the Ga 3d spectra were fitted to a series of 70% Gaussian/30% Lorentzian Voigt-function doublets for the $3d^{5/2}$ and $3d^{3/2}$ spin−orbit components of each peak. The peaks that comprised each doublet were constrained to have an area ratio of 3:2 and the same full width at half maximum (FWHM). The single peak of GaAs in the Ga 2p spectra was fit using the asymmetric Lorentzian function. All other peaks were fit using the 70% Gaussian/30% Lorentzian Voigt-function. The surface atomic ratios were calculated using the relative sensitive factors (RSF) in the database of the Kratos instrument and the peak areas. The Ga/As atomic ratios were calculated based on the Ga 3d and As 3d spectra.

3.7.4 Scanning-electron microscopy (SEM)

Scanning-electron microscopy (SEM) images were obtained using a Nova NanoSEM 450 (FEI) with an accelerating voltage of 5 kV, with a working distance of 5 mm and an in-lens secondary electron detector.

3.7.5 Transmission-electron microscopy (TEM)

Transmission-electron microscopy (TEM) cross-sections of the samples were prepared using a focused Ga ion beam (FIB), on a FEI Helios NanoLab G4 Dual Beam. A carbon protection layer was applied prior to exposure to the FIB. TEM images of the prepared lamella samples were obtained using a FEI Osiris at an accelerating voltage of 200 kV equipped with a Gatan 2K TEM camera and Bruker EDS.

3.7.6 Atomic-force Microscopy (AFM)

Atomic-force microscopy (AFM) images were obtained on a Bruker Dimension Icon using Bruker ScanAsyst-Air probes (silicon tip, silicon nitride cantilever, spring constant: 0.4 N m^{-1}, frequency: 50-90 kHz), operating in the ScanAsyst mode. Images were analyzed using the Nanoscope Analysis software (version 1.9).

3.8 Supplementary figures

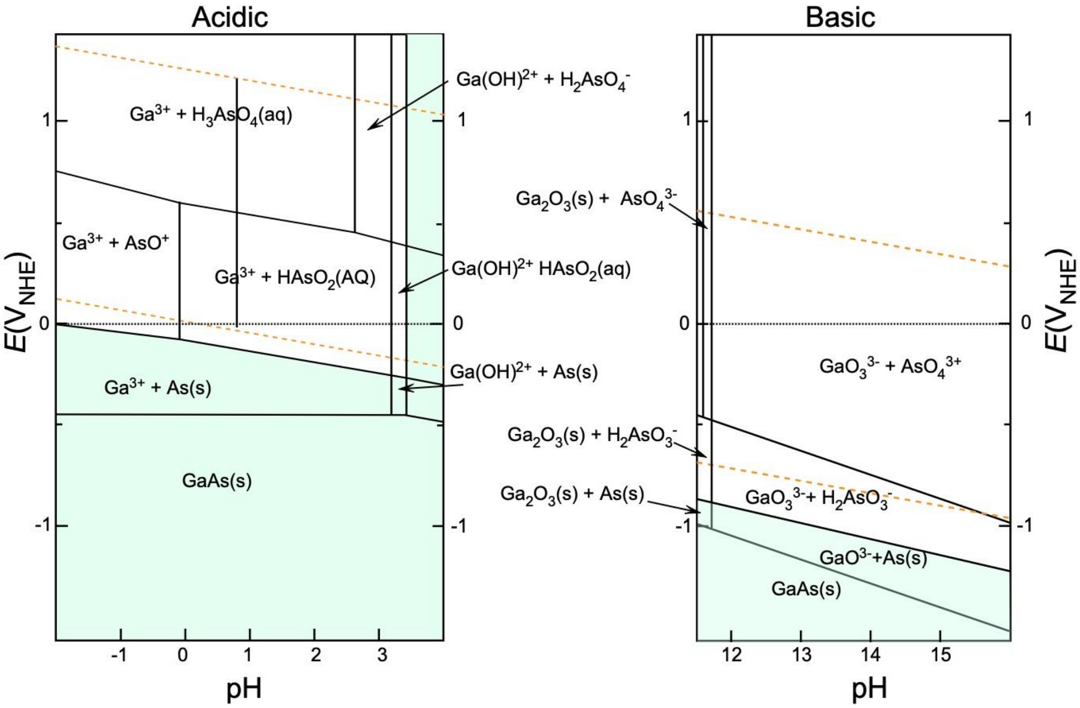

Figure S 3.1 Calculated Pourbaix diagram of GaAs (Ga/As=1) in the low (left) and high (right) pH range, as obtained from the Materials Project.[127] The concentrations of Ga and As ions are assumed as 1x10^{-8} mol/kg.

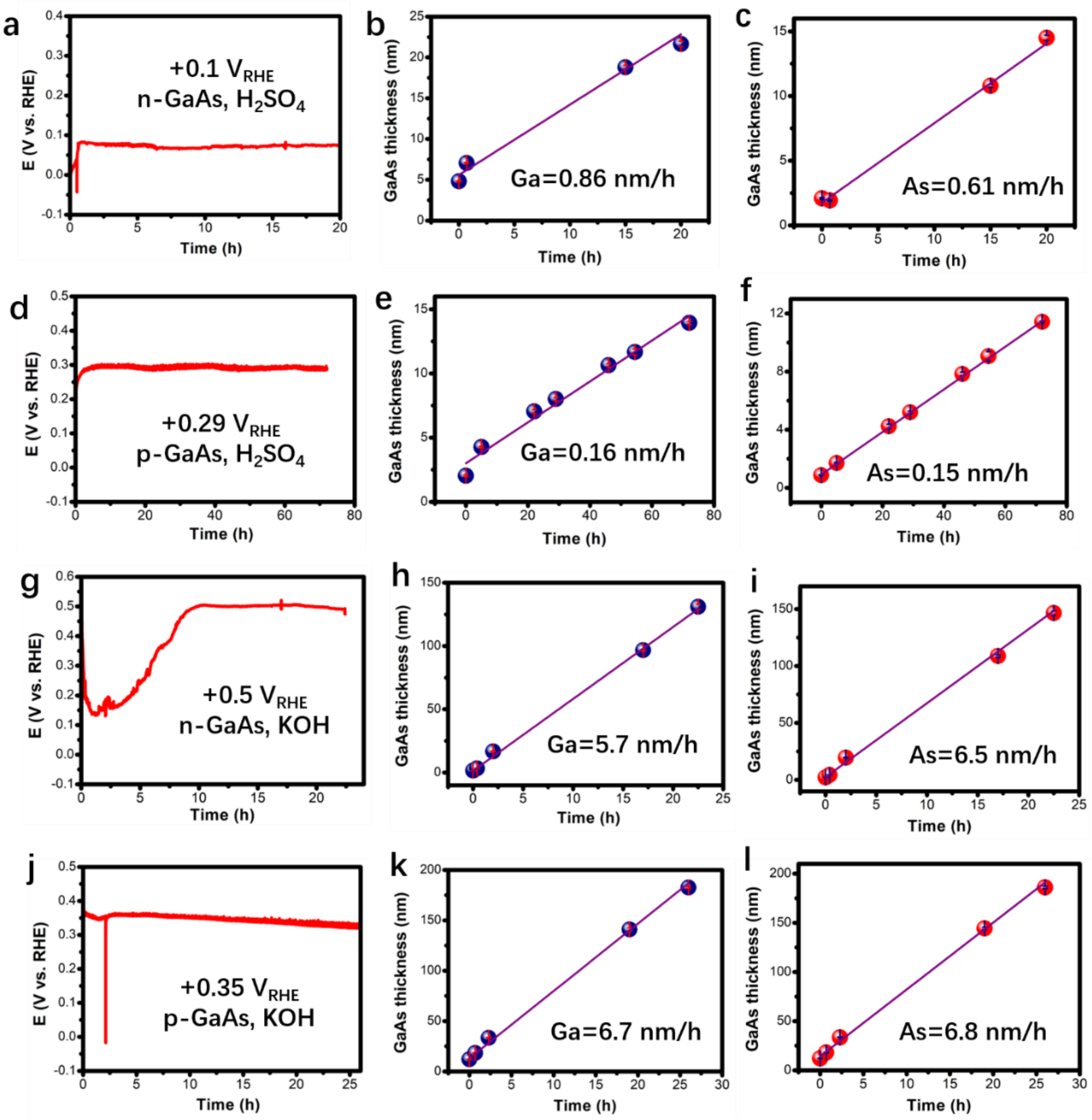

Figure S 3.2 Corrosion rates of GaAs at open-circuit potential (E_{oc}) in the dark. Comparison of (a,d,g,j) the measured E_{oc} values versus time in the dark, and the corrosion thickness of GaAs based on the concentrations of (b,e,h,k) Ga ions and (c,f,I,l) As ions, for (a-c) n-GaAs and (d-f) p-GaAs in 1.0 M H_2SO_4(aq) and (g-i) n-GaAs and (j-l) p-GaAs in 1.0 M KOH(aq).

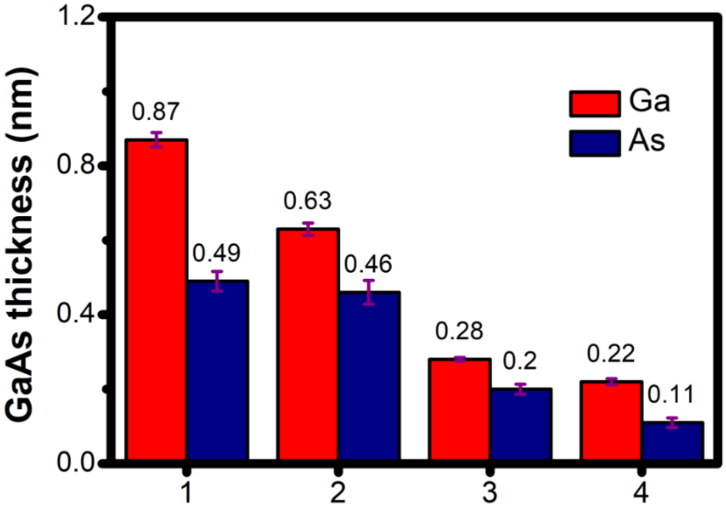

Figure S 3.3 Comparison of initial GaAs dissolution for four different n-GaAs samples (No.1-4) when exposed to 1.0 M H_2SO_4(aq).

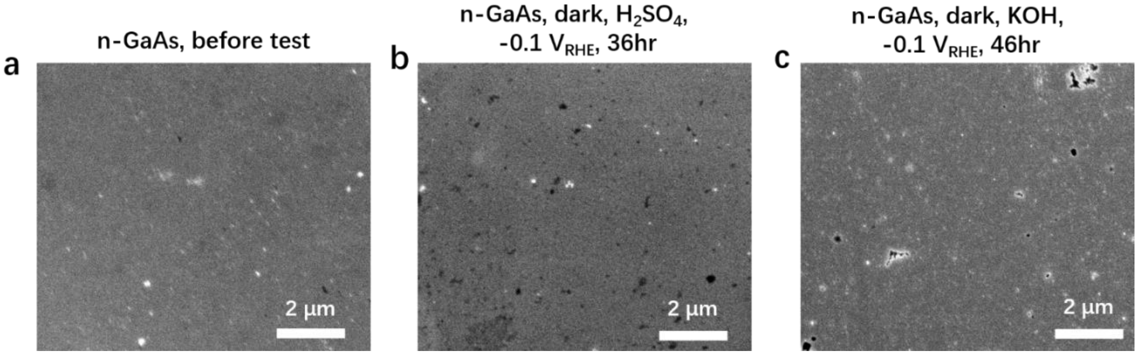

Figure S 3.4 Comparison of SEM images of n-GaAs electrodes (a) before and, (b) after the CA at -0.1 V vs. RHE (V_{RHE}) in 1.0 M H_2SO_4(aq) in the dark for 36 h and (c) after the CA at -0.1 V vs. RHE in 1.0 M KOH(aq) in the dark for 46 h.

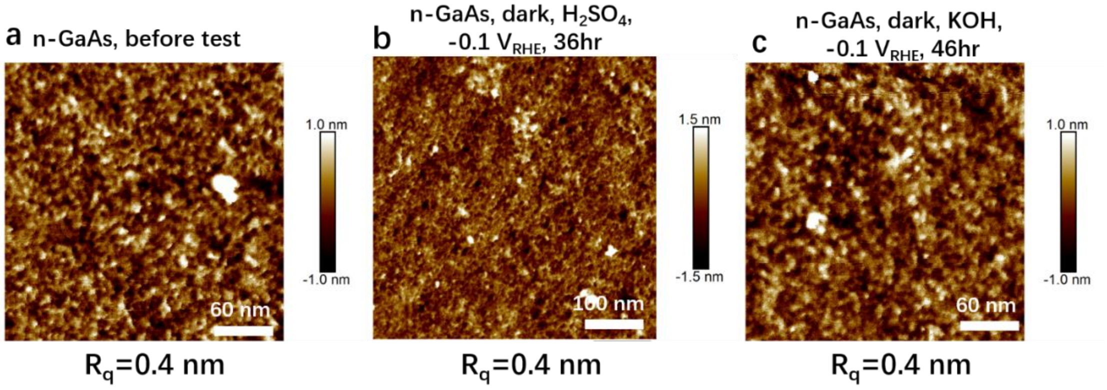

Figure S 3.5 Comparison of AFM images of n-GaAs electrodes (a) before and (b) after CA at -0.1 V vs. RHE in 1.0 M H_2SO_4(aq) in the dark for 36 h and (c) after CA at -0.1 V vs. RHE in 1.0 M KOH(aq) in the dark for 46 h. R_q is the surface roughness.

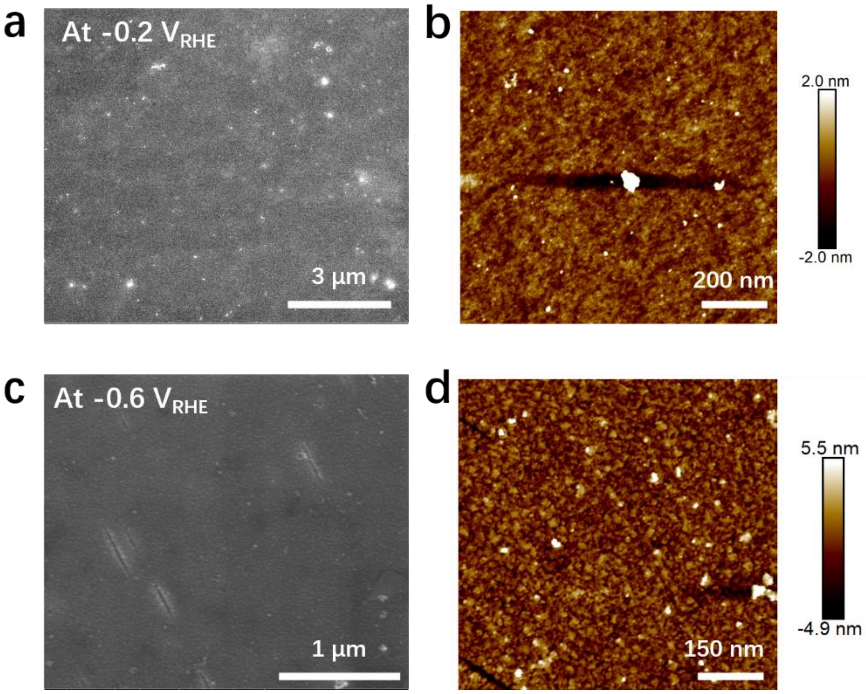

Figure S 3.6 Comparison of (a,c) SEM and (b,d) AFM images of the bare p-GaAs electrodes after CA at (a-b) -0.2 V vs. RHE for 20 h and (c-d) -0.6 V vs. RHE for 65 h, in 1.0 M H_2SO_4(aq) under 1-sun illumination. The surface roughness (R_q) in (b) and (d) were 0.73 and 1.3 nm, respectively.

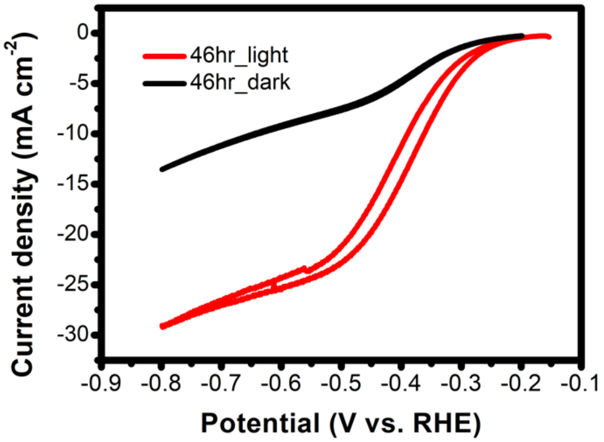

Figure S 3.7 Comparison of the J-E behaviors of a bare p-GaAs electrode in the dark (black) and under 1-sun illumination (red) after the 46-h CA at E=-0.6 V vs. RHE in 1.0 M KOH (aq), showing substantial J in the dark.

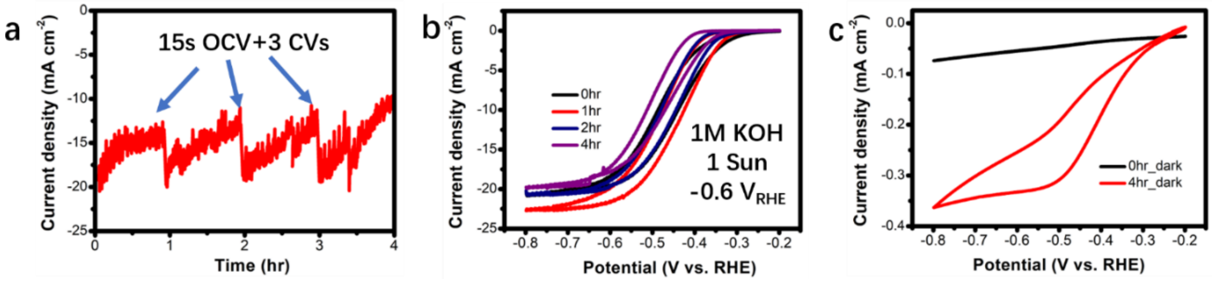

Figure S 3.8 (a) CA of a bare p-GaAs electrode at -0.6 V vs. RHE for 4 h under 1-sun illumination in 1.0 M KOH(aq); the arrows indicate hourly interruptions for collection of CV data (15 s at E_{oc} followed by three cycles of CV at 50 mV s^{-1}), (b) Comparison of the J-E behaviors of p-GaAs electrode under illumination during the CA in (a), (c) J-E behaviors for p-GaAs electrode measured in the dark in 1.0 M KOH(aq) before and after the CA in (a).

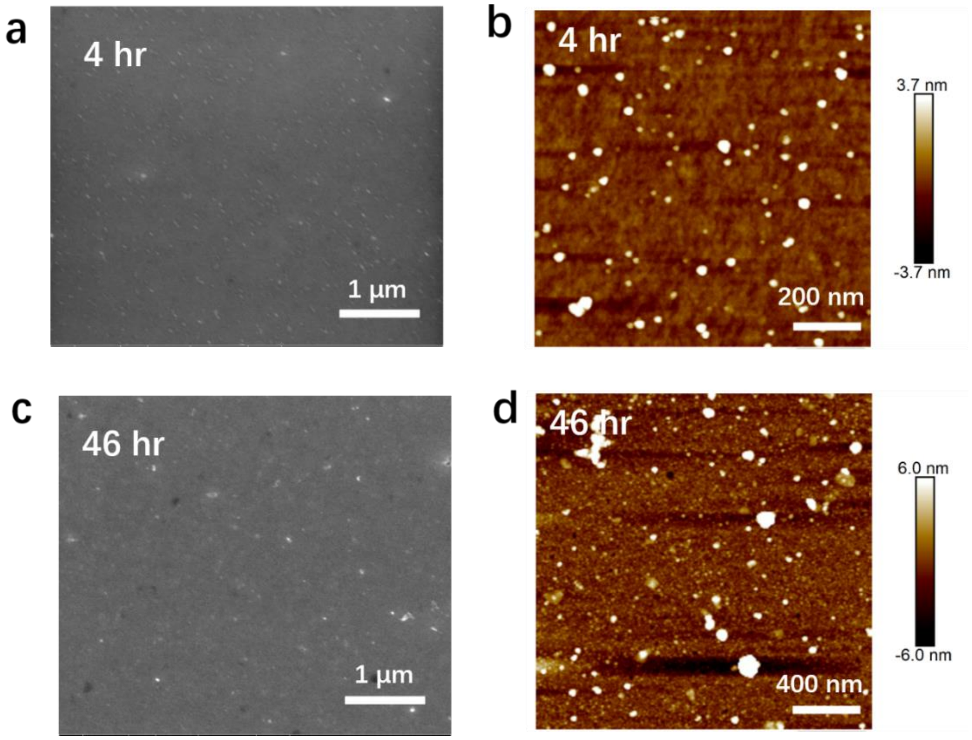

Figure S 3.9 (a-b) SEM images and (c-d) AFM images of bare p-GaAs photoelectrodes after the CA tests at -0.6 V vs. RHE in 1.0 M KOH(aq) under 1-sun illumination for (a,c) 4 h and (b,d) 46 h.

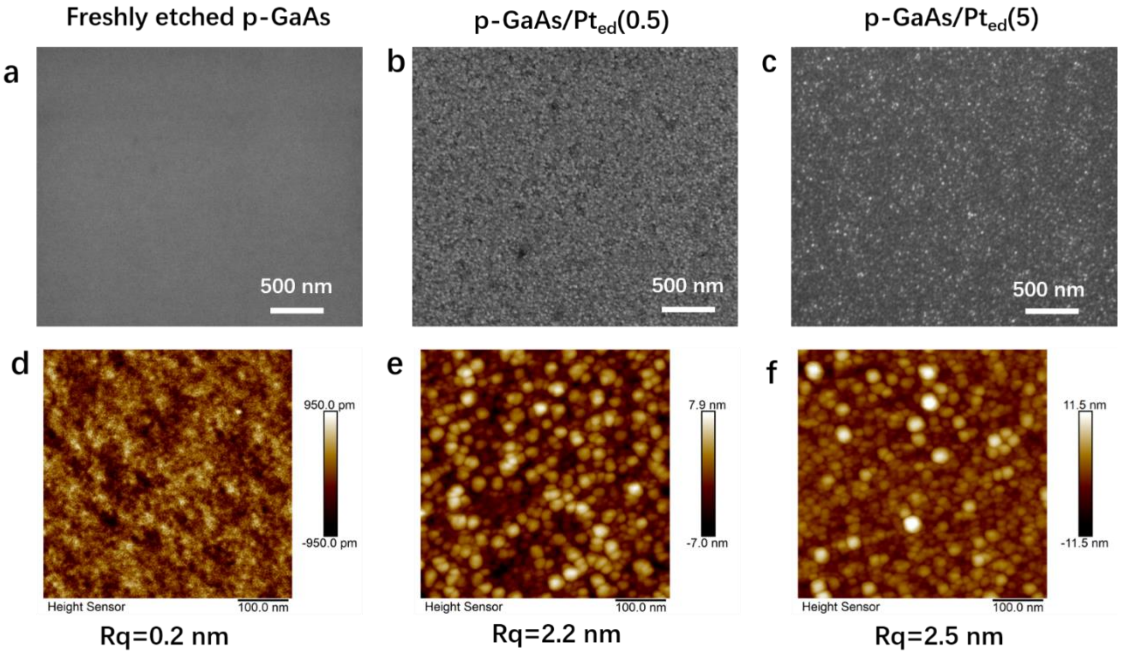

Figure S 3.10 Comparison of (a-c) SEM and (d-f) AFM images taken for (a,d) a freshly etched p-GaAs, (b,e) an as-prepared p-GaAs/Pt$_{ed}$(0.5) sample and (c,f) an as-prepared p-GaAs/Pt$_{ed}$(5) sample. R_q is the surface roughness.

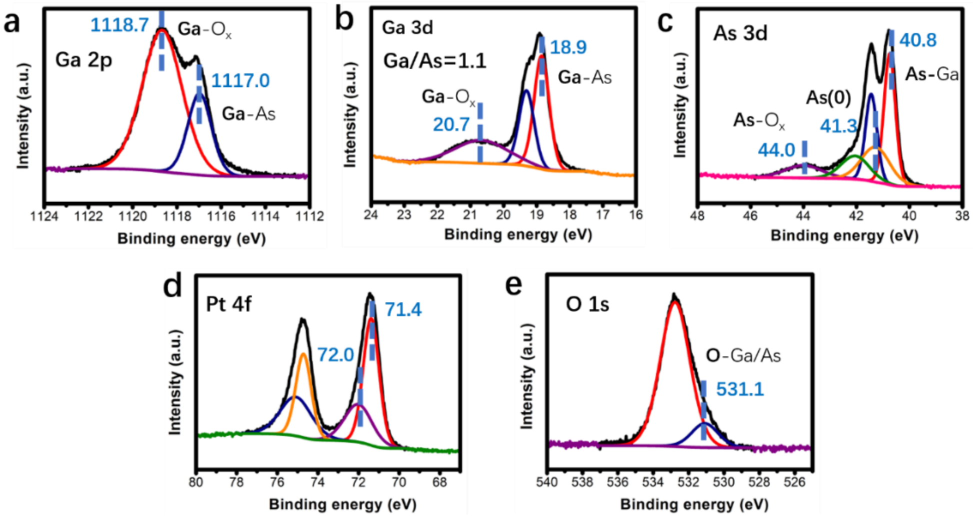

Figure S 3.11 XP spectra in the (a) Ga 2p, (b) As 3d, (c) Ga 3d, (d) Pt 4f and (e) O 1s regions for an as-prepared p-GaAs/Pt$_{ed}$(0.5) electrode.

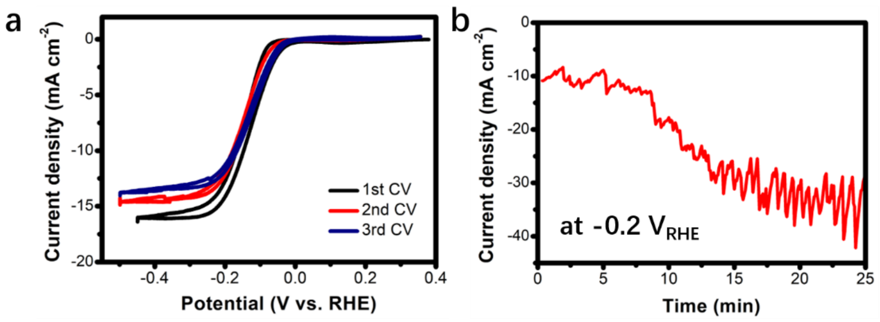

Figure S 3.12 (a) Comparison of the first three CVs of p-GaAs/Pt$_{ed}$(0.5) electrode in 1.0 M H_2SO_4(aq) under 1-sun illumination before the CA test. (b) CA of p-GaAs/Pt$_{ed}$(0.5) electrode in the first 25 min of CA at -0.2 V vs. RHE.

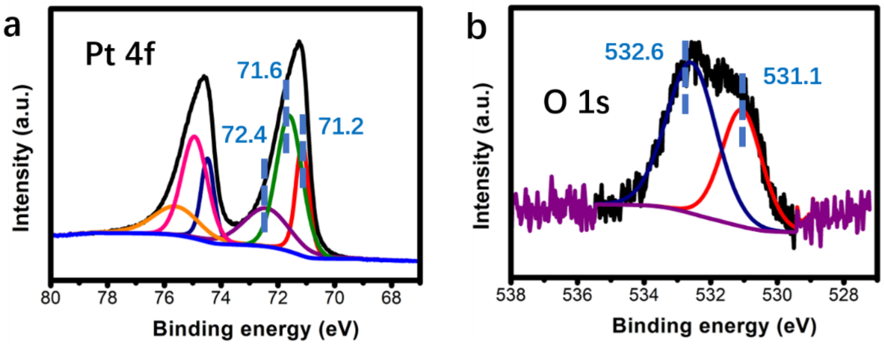

Figure S 3.13 XP spectra in the (a) Pt 4f and (b) O 1s regions for a p-GaAs/Pt$_{ed}$(0.5) electrode after CA at -0.2 V vs. RHE for 4 h in 1.0 M H_2SO_4(aq) under 1-sun illumination.

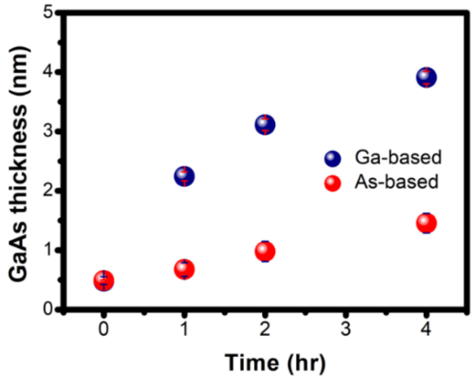

Figure S 3.14 Corrosion thickness of GaAs vs. time for a p-GaAs/Pt$_{ed}$(0.5) electrode held at -0.2 V vs. RHE in 1.0 M H_2SO_4(aq) under illumination.

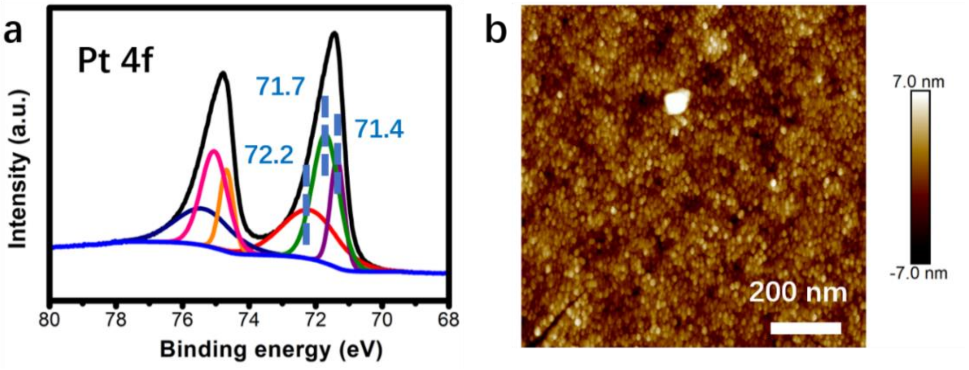

Figure S 3.15 (a) XP spectrum in the Pt 4f region and (b) AFM image for a p-GaAs/Pt$_{ed}$(5) electrode after the CA at -0.2 V vs. RHE in 1.0 M H_2SO_4(aq) (R_q~1.7 nm).

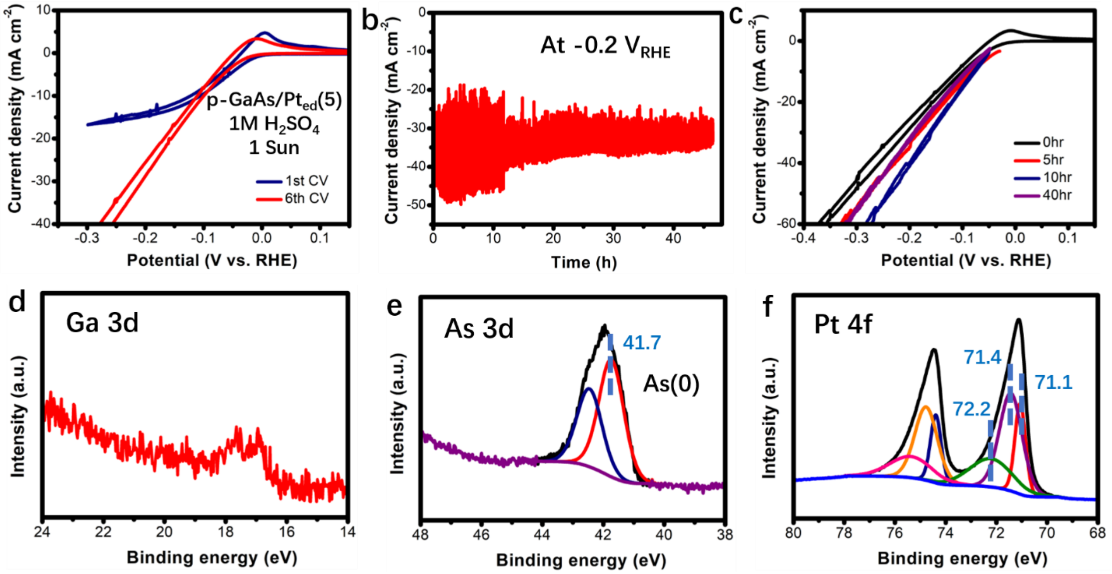

Figure S 3.16 (a) comparison of the 1st and the 6th J-E cycle of a p-GaAs/Pt$_{ed}$(5) electrode exhibiting a loss in J_{ph}; (b) CA of the p-GaAs/Pt$_{ed}$(5) electrode at -0.2 V vs. RHE under 1-sun illumination; (c-d) comparison of the J-E behaviors collected periodically during CA in (b). (d-f) XP spectra in the (d) Ga 3d, (e) As 3d and (f) Pt 4f regions for the p-GaAs/Pt$_{ed}$(5) electrode after CA in (b).

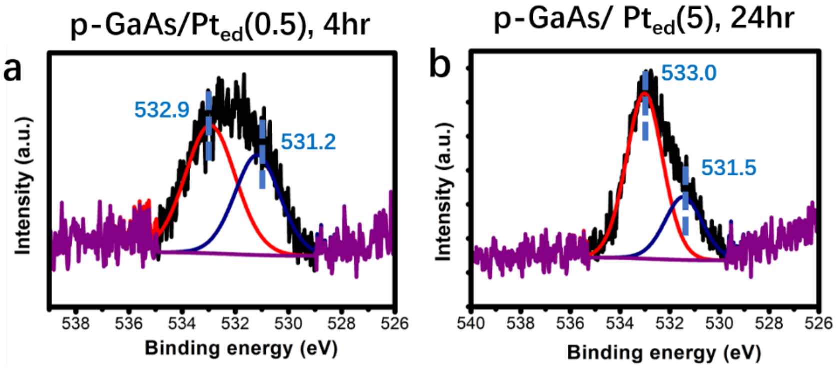

Figure S 3.17 Comparison of XP spectra in the O 1s region for (a) a p-GaAs/Pt$_{ed}$(0.5) electrode after a 4-h CA and (b) p-GaAs/Pt$_{ed}$(5) electrode after a 24-h CA, at -0.2 V vs. RHE in 1.0 M KOH(aq) under 1-sun illumination.

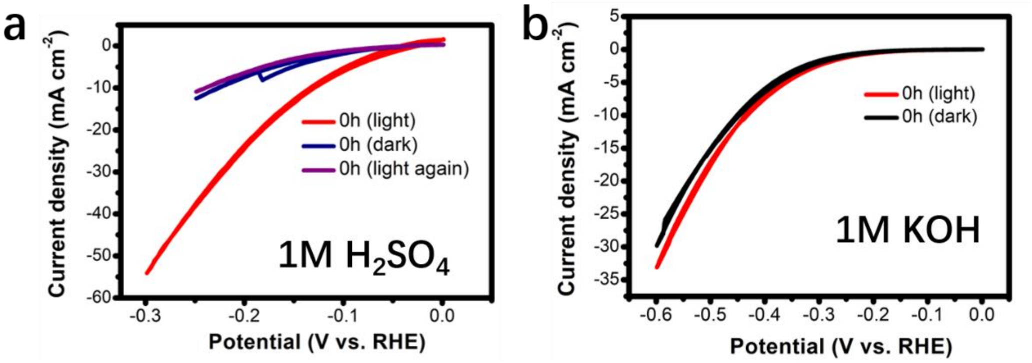

Figure S 3.18 Comparison of the J-E behaviors in (a) 1.0 M H_2SO_4 and (b) in 1.0 M KOH for p-GaAs/Pt$_{sp}$(5) electrodes prior to CA, under 1-sun illumination and in the dark. For (a), CVs were performed first under illumination (red), then the dark (blue), and again under illumination (purple).

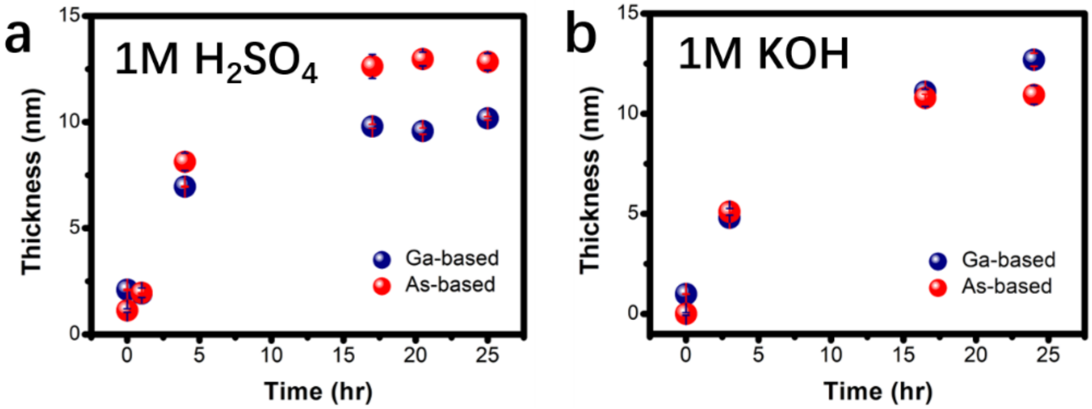

Figure S 3.19 Corrosion thickness of GaAs vs. time for p-GaAs/Pt$_{sp}$(5) electrodes tested at -0.2 V vs. RHE under 1-sun illumination in (a) 1.0 M H_2SO_4(aq) and (b) 1.0 M KOH(aq).

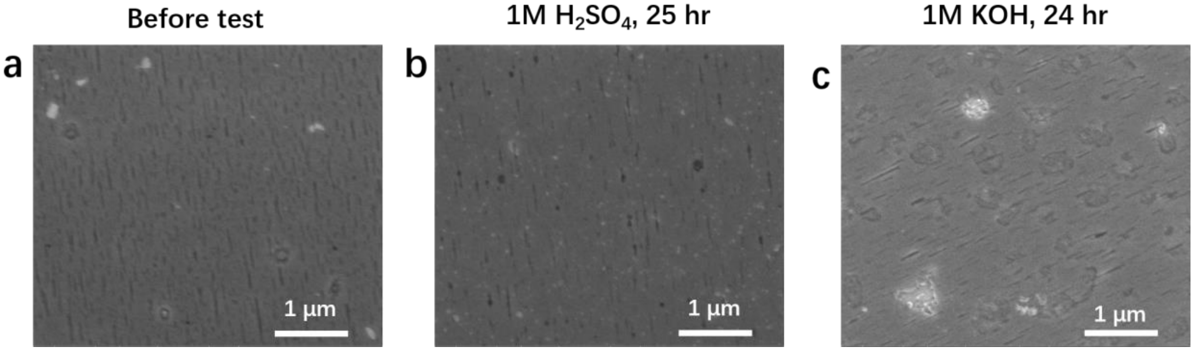

Figure S 3.20 Comparison of SEM images of (a) an as-prepared p-GaAs/Pt$_{sp}$(5) sample, (b) after CA at -0.2 V vs. RHE for 25 h in 1.0 M H_2SO_4(aq) under 1-sun illumination and (c) after CA at -0.2 V vs. RHE for 24 h in 1.0 M KOH(aq) under 1-sun illumination.

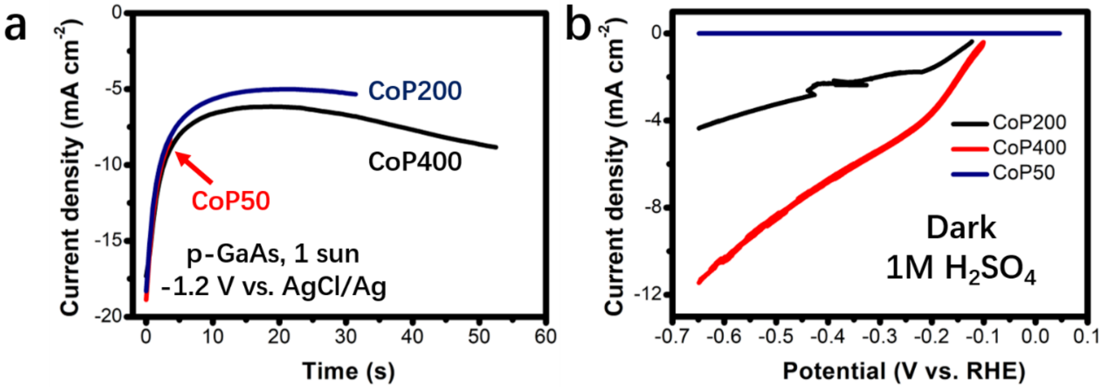

Figure S 3.21 (a) CA of the CoP electrodeposition on p-GaAs electrode under 1-sun illumination. (b) Comparison of the J-E behaviors in the dark of as-prepared p-GaAs/CoP(x) electrodes in 1.0 M H_2SO_4(aq).

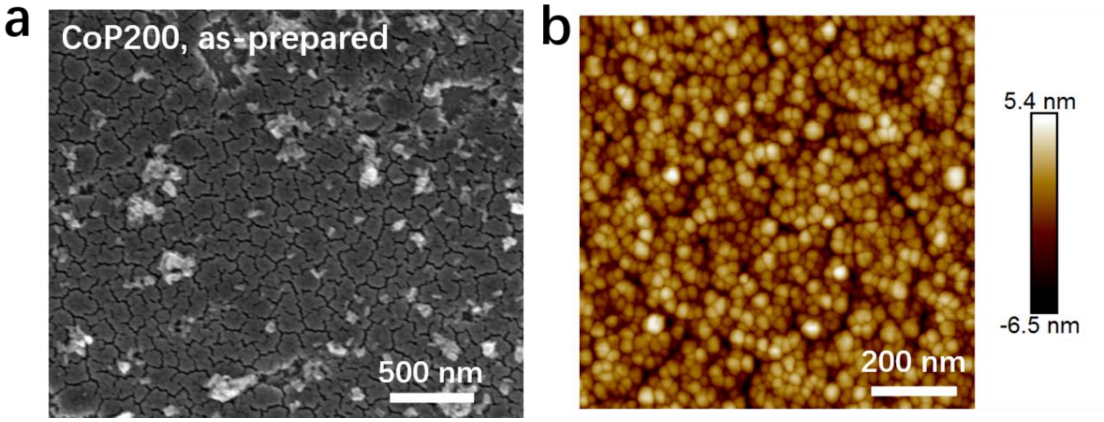

Figure S 3.22 (a) SEM and (b) AFM images of an as-prepared p-GaAs/CoP(200) electrode.

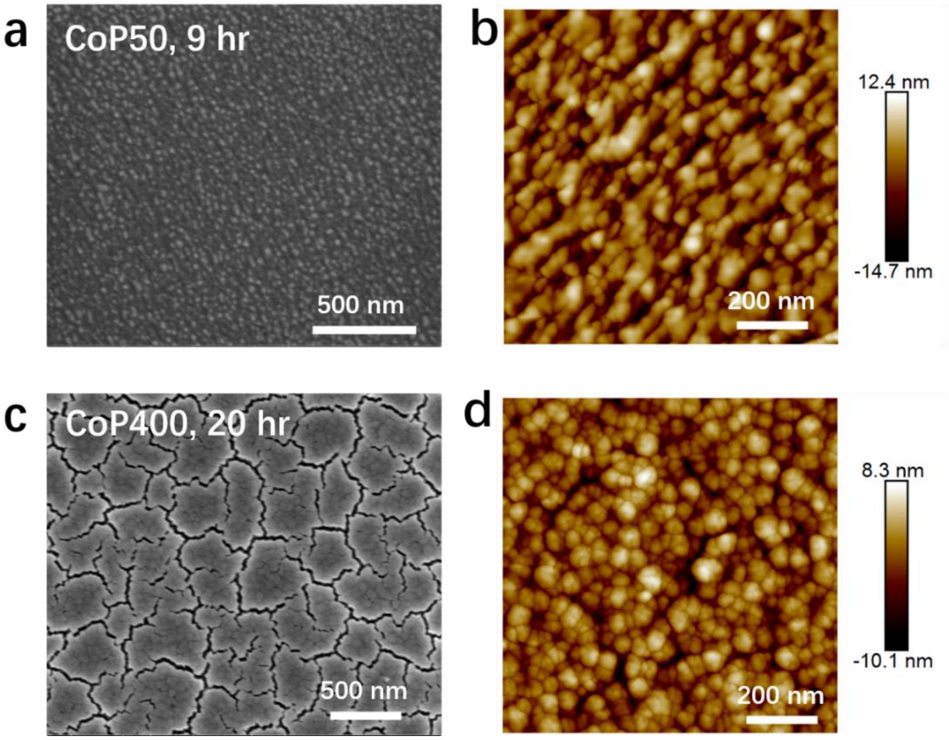

Figure S 3.23 (a,c) SEM and (b,d) AFM images of (a-b) a p-GaAs/CoP(50) electrode after a 9-h CA at -0.2 V vs. RHE and (c-d) a p-GaAs/CoP(400) electrode after a 20-h CA at -0.2 V vs. RHE in 1.0 M H_2SO_4(aq) under 1-sun illumination.

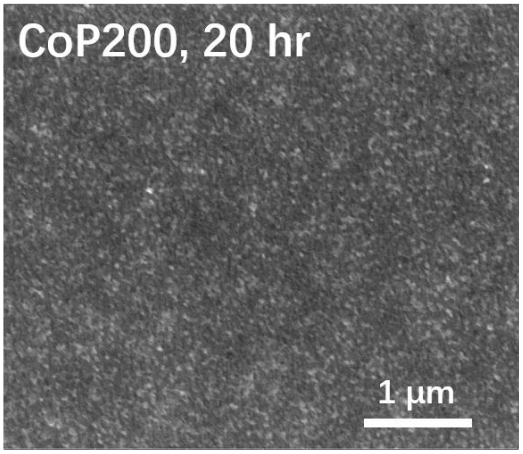

Figure S 3.24 SEM image of (a-b) a p-GaAs/CoP(200) electrode after a 20-h CA at -0.2 V vs. RHE in 1.0 M H_2SO_4(aq) under 1-sun illumination.

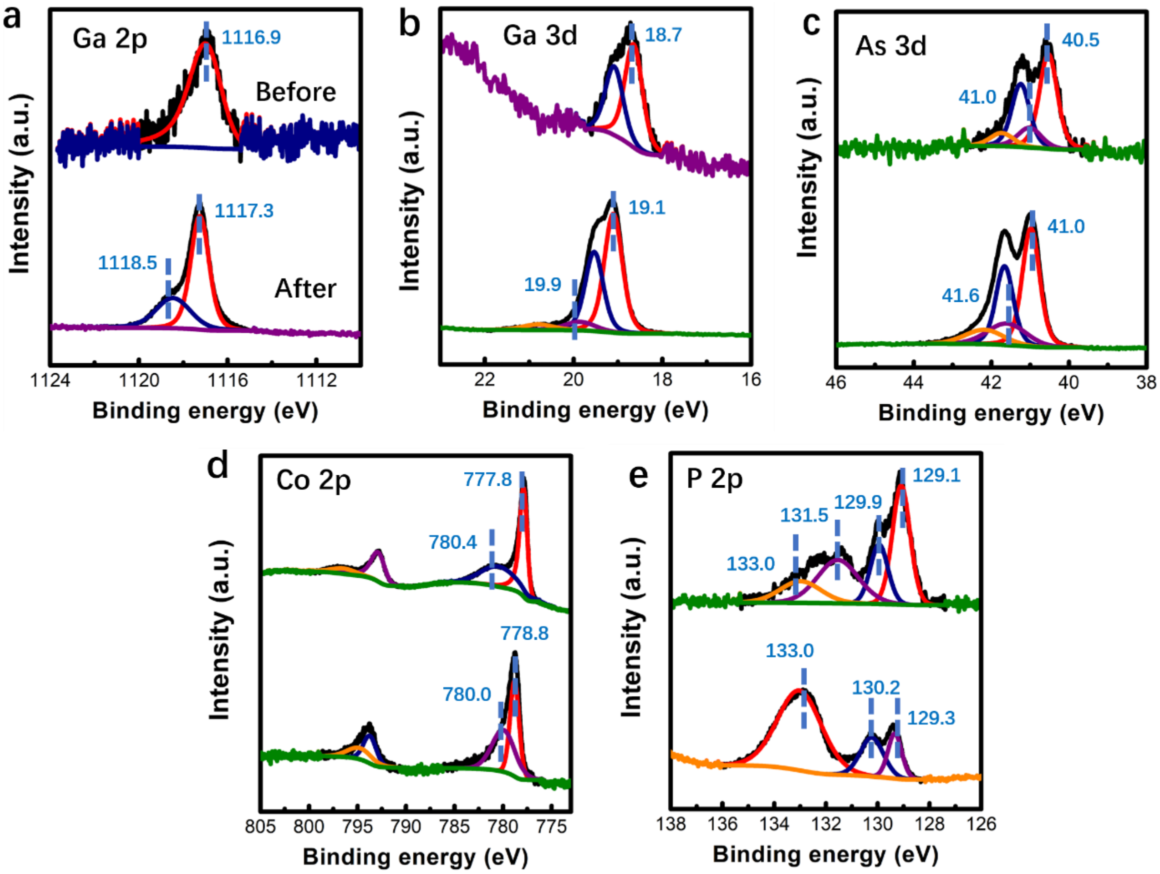

Figure S 3.25 Comparison of XP spectra in the (a) Ga 2p, (b) Ga 3d, (c) As 3d, (d) Co 2p, and (e) P 2p regions for a p-GaAs/CoP(200) electrode before and after the 20-h CA at -0.2 V vs. RHE in 1.0 M H_2SO_4(aq) under 1-sun illumination.

Chapter 4

4 UNDERSTANDING THE STABILITY OF P-INGAP$_2$ PHOTOCATHODES FOR SOLAR-DRIVEN H$_2$ EVOLUTION

4.1 Abstract

The long-term stability of p-InGaP$_2$ photocathodes, with a band gap of ~1.8 eV, for the solar-driven hydrogen-evolution reaction (HER) has been systematically investigated in both acidic and alkaline aqueous electrolytes. Both p-InGaP$_2$ electrodes that were either etched or coated with electrodeposited Pt were studied. Etched p-InGaP$_2$ electrodes corroded cathodically under illumination forming metallic In^0. In contrast, electrodeposition of Pt catalyst stabilized p-InGaP$_2$ electrodes against such cathodic decomposition, by facilitating the HER kinetics. At 0 V vs. the reversible hydrogen electrode (RHE), the p-InGaP$_2$/Pt electrodes exhibited long-term stable current densities (J) of up to ~-9 mA cm^{-2} for >139 h under simulated 1-sun illumination at both pH=0 and pH=14. During the stability tests, the current density-potential (J-E) behaviors of the p-InGaP$_2$/Pt photoelectrodes degraded owing to the pH-dependent evolution of surface conditions. This work provides a rational understanding of the stability and corrosion mechanism of p-InGaP$_2$ photocathodes, a crucial top light-absorber for achieving tandem solar-fuel generators.

4.2 Introduction

Photoelectrochemical (PEC) hydrogen evolution from water by semiconductor photoelectrodes offers a promising route to achieve solar-to-H_2 conversion in one step.[1,163] To support sustained operation at such a high current density (J) of >10 mA cm^{-2}, either strong acidic or alkaline electrolytes is necessary to avoid pH gradient between cathode and anode.[123,205] This requirement of electrolytes casts considerable challenges over the material stability of all device components, including semiconductors, catalysts, and ion-conducting membranes.[206]

Tandem solar fuel generators, combining a large and small band-gap semiconducting light absorbers, can simultaneously realize high photovoltage and high photocurrent to efficiently drive unassisted water photolysis.[12,44,162] For example, a combination of two semiconductors with band gaps of 1.8 eV and 1.1 eV can potentially attain an energy conversion efficiency of >10 %. Silicon (Si), with a small band gap of 1.12 eV, has been extensively studied for solar-driven water-splitting reaction. Previous works have established the remarkable stability (> 100 h) of Si for not only the hydrogen-evolution reaction (HER) in acidic electrolyte, but also the oxygen-evolution reaction (OER) with various protective layers. In this regard, another semiconductor with a large band gap (1.8 eV) is urgently needed to pair up with Si for realizing an integrated tandem solar water-splitting device.

Alloying III-V elements is a technologically viable approach to fine tune the band gap of the resulting semiconducting materials. For instance, tertiary compounds of InGaP, GaAsP and AlGaAs can all achieve the desired band gap of 1.8 eV.[130,207] However, many III-V semiconductors, such as InP and GaAs, suffer from anodic photocorrosion under oxidation potentials sufficient to drive the OER.[59–61] In comparison, much less is known regarding the cathodic stability of most III-V semiconductors, especially under the HER conditions at pH 0 and pH 14. Our previous investigation has revealed that a As^0-enrichment at p-GaAs surface under the HER conditions, deleteriously led to a complete loss of electrode photoactivity via creating unfavorable surface states. Moreover, incorporation of Al into the III-V semiconductors may cause additional concerns in material durability in both strong acidic and alkaline electrolytes, due to the high solubility of Al species over wide potential (E) and pH ranges.[125] All these considerations render the InGaP combination the primary target of investigation for constructing a robust HER photocathode, which can be combined a protected Si photoanode for achieving a tandem solar-fuel device.

$InGaP_2$ with a band gap of 1.8 eV is an ideal top light absorber used in many tandem photovoltaic (PV) devices with high efficiencies.[54,61,130,208,209] However, p-type $InGaP_2$ photocathodes exhibited unstable performances for the HER, either as a single photoelectrode or within a tandem cell.[36–39,41] In recent years, much promising progress has been achieved to enhance the electrode durability of p-$InGaP_2$ by various strategies, including leveraging protective layers, earth-abundant and molecular catalysts, and surface passivation.[40,58,67–70,122,210,211] Nevertheless, the underlying corrosion pathways of $InGaP_2$ under the HER conditions have remained ambiguous for both acidic and alkaline electrolytes. Further progress on enhancing the electrode durability, calls for a rational and quantitative understanding towards the surface corrosion chemistry of p-$InGaP_2$ photocathodes. In a previous study of InP photocathodes, we identified the importance of catalytic kinetics at electrode surface for inhibiting the cathodic corrosion of In^{3+} cations into metallic In^0. Besides, we found that the current density-potential (J-E) behaviors of p-InP/Pt photoelectrodes evolved with the changes in the electrode surface characteristics. Moving from p-InP to p-$InGaP_2$ mostly moves the position of the condition band after incorporation of new Ga^{3+} cations, resulting in a enlarged band gap. Consequently, the Fermi level (E_f) of a p-$InGaP_2$ should stay relatively fixed to the potentials of both the reversible hydrogen electrode (RHE) and the reduction of In^{3+} cations. Therefore, our prior findings on p-InP motivated us to apply a similar approach to establish the corrosion mechanism for p-$InGaP_2$ photoelectrode, which has remained a long-standing knowledge gap in this field.

Herein, we systematically examined the stability of p-$InGaP_2$ photocathodes under conditions of the HER in both 1.0 H_2SO_4(aq) and 1.0 M KOH(aq), with and without Pt catalyst. We applied X-ray photoelectron spectroscopy (XPS) together with an air-free transfer protocol, to carefully examine the changes in electrode surface conditions after electrochemical tests. Moreover, we used inductively coupled plasma mass spectrometry (ICP-MS) to monitor the ion leaching over time from the surface of p-$InGaP_2$ electrodes. Combining the results of these analytical techniques with electrochemical measurements, offers comprehensive pictures of both physical stability and electrochemical stability of p-$InGaP_2$ for the HER. This work offers a rational understanding of the electrode stability of p-$InGaP_2$ photocathodes for the HER, benefiting further stabilization strategies.

4.3 Results

4.3.1 Stability of etched p-$InGaP_2$ photoelectrodes for the HER.

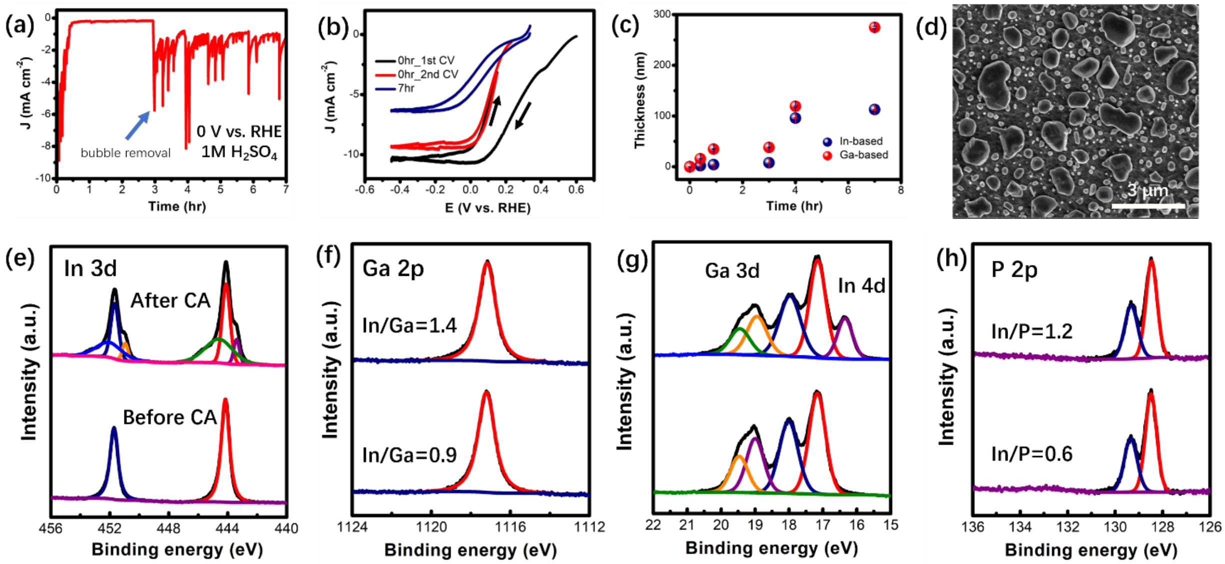

Figure 4.1 (a) Chronoamperometry (CA) of an etched p-$InGaP_2$ photoelectrode at 0 V vs. RHE in 1.0 M H_2SO_4(aq) under 1-sun illumination. (b) Comparison of the J-E behavior of an etched p-$InGaP_2$ photoelectrode measured before and after the CA in (a). (c) Corrosion thickness of p-$InGaP_2$ over time during the CA in (a) based on the concentrations of In and Ga ions in the electrolyte. (d) SEM image of the p-$InGaP_2$ electrode after the CA in (a). (e-h) Comparison of the XP spectra of the (e) In 3d, (f) Ga 2p, (g) Ga 3d/In 4d and (h) P 2p regions for the p-$InGaP_2$ photoelectrode before and after the CA in (a).

An etched p-$InGaP_2$ electrode was first tested by chronoamperometry (CA) at 0 V vs. RHE in 1.0 M H_2SO_4(aq) under 1-sun illumination (Figure 4.1). The 7-h CA showed variation in current density (J), due to the formation and release of H_2 bubbles from electrode surface (Figure 4.1a).[184] The |J| was initially 7.8 mA cm^{-2} and quickly decayed to <1 mA cm^{-2} after 20 min. An abrupt increase in |J| was observed from ~0.2 mA cm^{-2} to 5.8 mA cm^{-2} after 3 h, indicating release of a H_2 bubble. Prior to CA, the illuminated p-$InGaP_2$ electrode exhibited an open-circuit potential (E_{oc}) of +0.64 V vs.

RHE and a light-limited |J| (|J_{ph}|) of -10.7 mA cm^{-2} (Figure 4.1b). A comparison of the initial two J-E cycles of the p-$InGaP_2$ electrode revealed a shift in the onset E (E_{on}) at J=-0.5 mA cm^{-2} from +0.56 V (1st cycle) to +0.24 V vs. RHE (2nd cycle) (Figure 4.1b). After CA, the J-E behavior of the p-$InGaP_2$ electrode shifted cathodically and exhibited a lower |J_{ph}| of -6.4 mA cm^{-2}.

During CA at 0 V vs. RHE, ICP-MS analysis revealed that the dissolution of Ga ions in the electrolyte increased linearly with time at a rate of ~37 nm h^{-1}. In contrast, the dissolution of In ions remained low (< 10 nm) within the first 3 h (Figure 4.1c), while a dramatic increase (88 nm) from 3 h to 4 h corresponded to the concurrent increase of |J| during the CA. After 7 h of CA, much more Ga ions than In ions dissolved into the electrolyte, accounting for 162 nm of $InGaP_2$. SEM image revealed that after CA large compact micro-particles formed at electrode surface (Figure 4.1d). Post-test XPS analysis of the In 3d region showed two distinct peaks at binding energy (BE) of 443.4 eV for metallic In^0 and 444.6 eV for surface oxide (InO_x), in addition to the peak at BE=444.1 eV for the In^{3+} cations of p-$InGaP_2$ (Figure 4.1e). XPS spectra of the Ga and P regions only showed the same peaks assigned to the Ga^{3+} cations and P^{3-} anions of p-$InGaP_2$, both before and after CA (**Figure** 1f-h). Notably, a new peak appeared at BE=16.4 eV in the XPS of the In 4d region (Figure 4.1g), assigned to metallic In^0. After CA, the In/Ga atomic ratio increased from 0.9 to 1.4, whereas the In/P ratio also increased from 0.6 to 1.2.

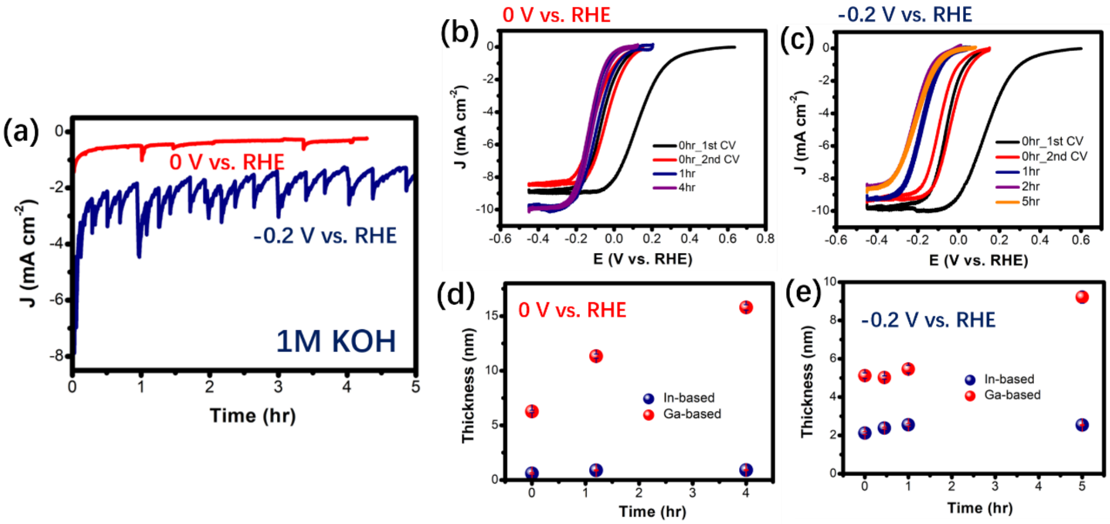

Figure 4.2 (a) CA of etched p-$InGaP_2$ electrodes at 0 V and -0.2 V vs. RHE in 1.0 M KOH(aq) under 1-sun illumination. (b-c) Comparison of the J-E behavior of etched p-$InGaP_2$ electrodes during the CA at (b) 0 V and (c) -0.2 V vs. RHE. (d-e) Corrosion thickness of p-$InGaP_2$ over time during the CA in (a) based on the concentrations of In and Ga ions in the electrolyte for the p-$InGaP_2$ electrodes tested at (d) 0 V and (e) -0.2 V vs. RHE.

Etched p-$InGaP_2$ electrodes were tested at 0 V and -0.2 V vs. RHE in 1.0 M KOH(aq) under 1-sun illumination for 4 h and 5 h, respectively (Figure 4.2). Figure 4.2a showed that the |J| decreased from -1.4 mA cm^{-2} to -0.2 mA cm^{-2} after 4 h of CA at 0 V vs. RHE, while the |J| decreased from -7.8 mA cm^{-2} to -1.9 mA cm^{-2} after 5 h of CA at -0.2 V vs. RHE. Prior to CA, comparisons of the initial two J-E cycles for both electrodes, showed similar cathodic shifts in E_{on} from ~+0.37 V (1st cycle) to ~+0.1 V vs. RHE (2nd cycle) (Figure 4.2b-c). The $|J_{ph}|$ of p-$InGaP_2$ electrodes remained ~10 mA cm^{-2} after 4 h of CA at 0 V vs. RHE, but decreased to -8.6 mA cm^{-2} after 5 h of CA at -0.2 V vs. RHE (Figure 4.2c). ICP-MS analyses revealed the dissolution of more Ga ions than In ions in the electrolytes for both electrodes after CA, whereas the dissolution of In ions remained negligible (Figure 4.2d-e). The higher concentrations of Ga ions than In ions amounted to 15 nm and 6.7 nm of $InGaP_2$ after the CA at 0 V and -0.2 V vs. RHE, respectively.

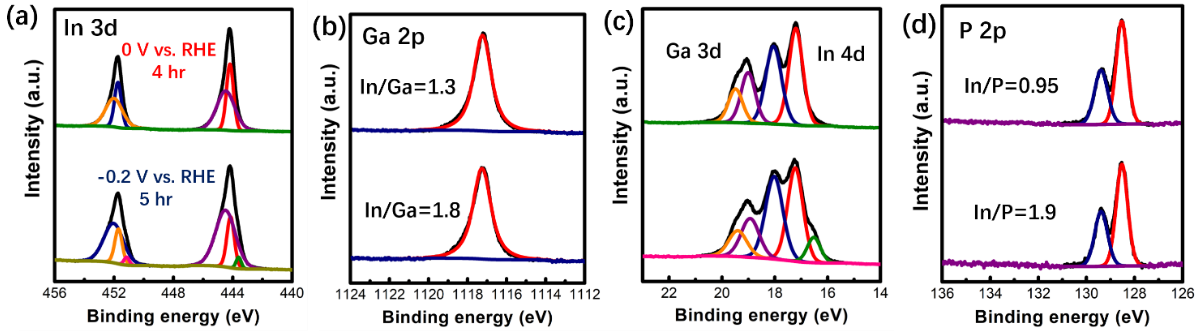

Figure 4.3 Comparison of XP spectra of the (a) In 3d, (b) Ga 2p, (c) Ga 3d/In 4d and (d) P 2p regions for the etched p-$InGaP_2$ electrodes after the CA at 0 V vs. RHE for 4 h and -0.2 V vs. RHE for 5 h, in 1.0 M KOH(aq) under 1-sun illumination.

The XP spectra of both illuminated p-$InGaP_2$ electrodes tested in 1.0 M KOH(aq) are compared in Figure 4.3. Compared with the surface of etched p-$InGaP_2$ before CA (Figure 4.1e-h), the XP spectra of the In 3d region showed peaks at BE=444.5 eV attributable to InO_x for both electrodes (Figure 4.3a). A small peak at BE=443.6 eV, assigned to metallic In^0, was only observed for the p-$InGaP_2$ electrode tested -0.2 V vs. RHE. For both samples, the XP spectra of both Ga and P regions only displayed peaks ascribable to the Ga^{3+} cations and P^{3-} anions of $InGaP_2$ (Figure 4.3b-d). Again, a new peak emerged at BE=16.5 eV in the In 4d region for the electrode tested at -0.2 V vs. RHE, corresponding to metallic In^0 (Figure 4.3c). Importantly, the increased In/Ga and In/P ratios suggested surface enrichment of In over Ga and P for both electrodes.

SEM images showed that the etched p-$InGaP_2$ electrodes remained flat after the CA at 0 V vs. RHE, but formed small nanoparticles after the CA at -0.2 V vs. RHE (Figure S 4.1a-b). AFM images revealed that both electrodes exhibited densely packed nano-particulate morphology, whereas the particle size was slightly larger for the electrode tested at -0.2 V vs. RHE (Figure S 4.1c-d). In contrast, both p-$InGaP_2$ samples before and after etching, did not exhibit such features (Figure S 4.2). This suggests the surficial nanoparticles formed after the CA tests in KOH, corresponding to the formation of InO_x and In^0 shown by the XPS data.

4.3.2 Stability of p-InGaP$_2$ photoelectrodes with electrodeposited Pt (p-InGaP$_2$/Pt) for the HER.

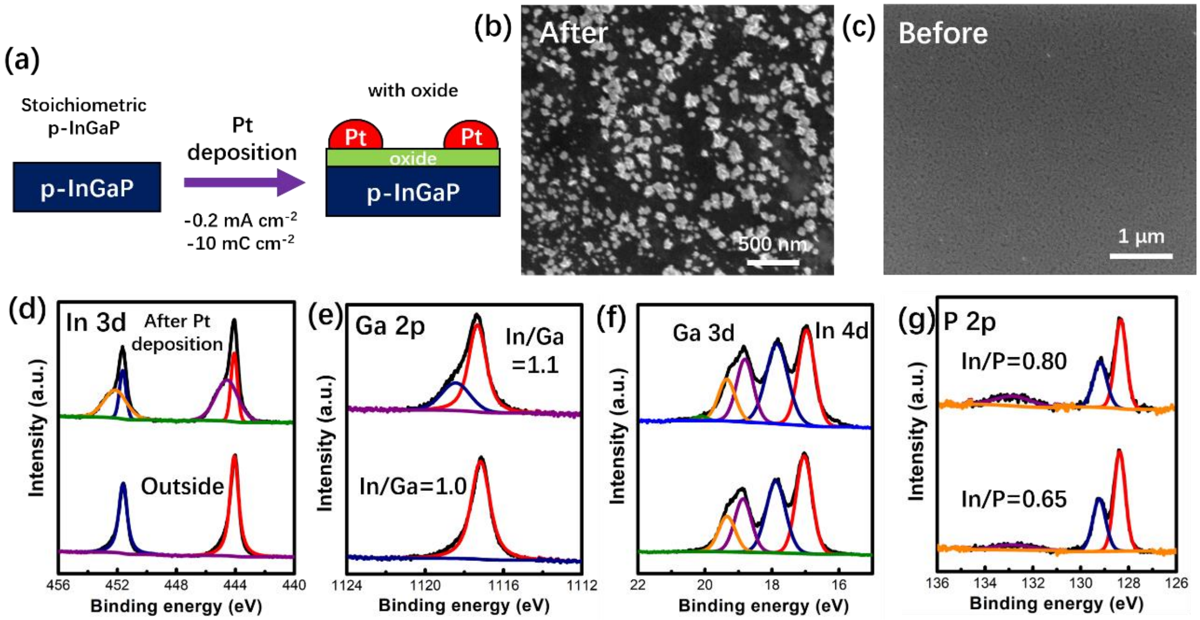

Figure 4.4 (a) schematic illustration of the electrodeposition of Pt at the surface of a p-InGaP$_2$ electrode under illumination. (b-c) SEM images of p-InGaP$_2$ electrodes (b) after and (c) before Pt deposition. (d-g) Comparison of XP spectra of the (d) In 3d, (e) Ga 2p, (f) Ga 3d/In 4d, and (g) P 2p regions collected at sample area within and outside the electrodeposition region (o-ring) of a p-InGaP$_2$/Pt electrode.

To evaluate the effect of the HER kinetics over the stability of p-InGaP$_2$ electrodes, Pt was electrodeposited at the surface of p-InGaP$_2$ electrodes at J=-0.2 mA cm^{-2} under 1-sun illumination (Figure 4.4a), until a total charge density of -10 mC cm^{-2} had passed (t=50 s). SEM images showed that the electrodeposited Pt displayed as discrete nanoparticles with irregular shapes, sparsely distributed over the surface of p-InGaP$_2$ (Figure 4.4b). Before deposition, the p-InGaP$_2$ surface appeared flat and clean (Figure 4.4c).

XPS data showed that after Pt deposition, new peaks emerged at BE=444.6 eV in the In 3d region and at BE=1118.4 eV in the Ga 2p region, ascribable to InO$_x$ and GaO$_x$, respectively (Figure 4.4d-e). Consistently, the XP spectrum of Ga 3d region exhibited a small peak at BE=20.1 eV for GaO$_x$ (Figure 4.4f). The higher peak intensity of GaO$_x$ in XP spectrum of the Ga 2p region than the

Ga 3d region, is due to the higher surface sensitivity for the Ga 2p region resulting from a much lower kinetic energy (KE) of photoelectrons. XP spectrum of the P 2p region (Figure 4.4g) exhibited a small and broad peak at BE=132.8 eV assigned to surface phosphate (PO_x). Compared with the sample region with no Pt deposition, the In/Ga ratio of the p-$InGaP_2$/Pt electrode remained 1.1, whereas the In/P ratio slightly increased to 0.8 from 0.65. Altogether these results indicated a thin oxide layer of $InGaPO_x$ was present at the electrode surface after Pt deposition.

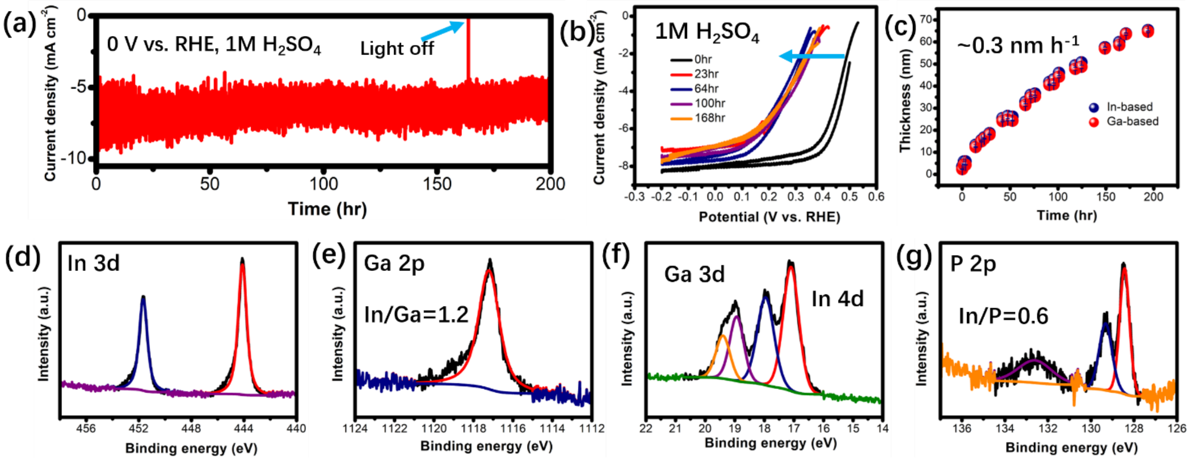

Figure 4.5 (a) CA of a p-$InGaP_2$/Pt electrode at 0 V vs. RHE in 1.0 M H_2SO_4(aq) under 1-sun illumination. The inset arrow represents the time when light was turned off. (b) Comparison of the J-E behavior of the p-$InGaP_2$/Pt electrode during the CA in (a). (c) Corrosion thickness of the p-$InGaP_2$/Pt electrode over time during the CA in (a) based on the concentrations of In and Ga ions in the electrolyte. (d-g) XP spectra of the (e) In 3d, (f) Ga 2p, (g) Ga 3d/In 4d, and (h) P 2p regions for the p-$InGaP_2$/Pt photoelectrode after the CA in (a).

During CA at 0 V vs. RHE, a p-$InGaP_2$/Pt electrode exhibited a stable maximum |J| of 8-9 mA cm^{-2} for >200 h in 1.0 M H_2SO_4(aq) under 1-sun illumination (Figure 4.5a). At 164 h, J turned negligible as light was turned off, confirming the observed |J| was attributed to photocurrent. The J-E behavior of the p-$InGaP_2$/Pt electrode, periodically measured during the CA, exhibited a cathodic shift after 23 h and remained unchanged afterwards (Figure 4.5b). The E_{on} at J=-1 mA cm^{-2} shifted from +0.51 V before CA to +0.38 V vs. RHE after 23 h of CA. ICP-MS analysis revealed stoichiometric dissolution of In and Ga ions at a rate of ~0.3 nm h^{-1} from the electrode into the electrolyte (Figure 4.5c). SEM image revealed that the surface of p-$InGaP_2$ substantially roughened after the CA whereas Pt particles were identified (Figure S 4.3).

Post-test XPS data of the p-$InGaP_2$/Pt electrode (Figure 4.5d-g) mainly showed the In^{3+} and Ga^{3+} cations and the P^{3-} anions of $InGaP_2$, together with surface phosphate (PO_x) at BE=132.6 eV. Notably no metallic In^0 was observed in the In 3d XPS region. Compared with the as-prepared p-$InGaP_2$/Pt electrode (Figure 4.4d-g), the pre-existing oxide ($InGaPO_x$) dissolved after >200 h of CA in acidic electrolyte, whereas the In/Ga and In/P ratios remained nearly unchanged.

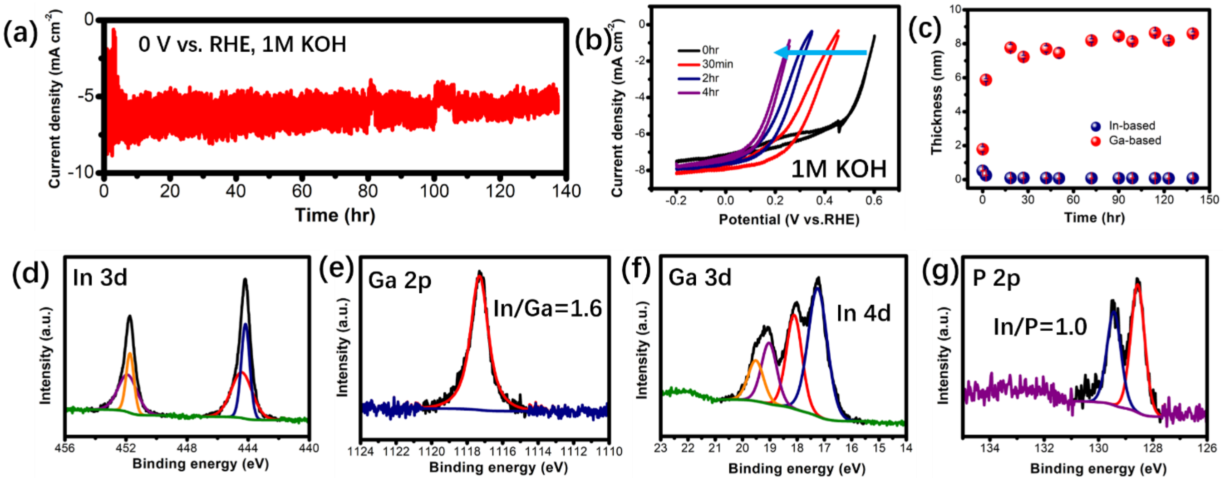

Figure 4.6 (a) CA of a p-$InGaP_2$/Pt electrode at 0 V vs. RHE in 1.0 M KOH(aq) under 1-sun illumination. (b) Comparison of the J-E behavior of the p-$InGaP_2$/Pt photoelectrode during the first 4 h of CA in (a). (c) Corrosion thickness of the p-$InGaP_2$/Pt electrode over time during the CA in (a) based on the concentrations of In and Ga ions in the electrolyte. (d-g) XP spectra of the (e) In 3d, (f) Ga 2p, (g) Ga 3d/In 4d, and (h) P 2p regions for the p-$InGaP_2$/Pt photoelectrode after the CA in (a).

During CA at 0 V vs. RHE, a different p-$InGaP_2$/Pt electrode exhibited a stable maximum |J| of >7 mA cm^{-2} for 139 h in 1.0 M KOH(aq) under 1-sun illumination (Figure 4.6a). However, the periodically measured J-E behavior of the p-$InGaP_2$/Pt electrode displayed substantial cathodic shifts during the first 4 h of CA (Figure 4.6b). The E_{on} at J=-1 mA cm^{-2} shifted from ~+0.6 V before CA to +0.26 V vs. RHE after 4 h of CA. After 4 h, the J-E behavior of the p-$InGaP_2$/Pt electrode remained nearly unchanged throughout the CA (Figure S 4.4). SEM imaging showed that the surface morphology of the p-$InGaP_2$/Pt electrode remained similar after the CA in KOH Figure S 4.5).

ICP-MS analysis showed that the dissolution of Ga ions plateaued at ~8 nm after 18 h, while the dissolution of In ions remained negligible (<0.1 nm) throughout the entire CA (Figure 4.6c). This result suggested a selective and self-limited leaching of Ga ions from the surface of p-$InGaP_2$/Pt electrode. Post-test XPS data of the In 3d region revealed InO_x at BE=444.4 eV, besides the peak at BE=444.2 eV assigned to the In^{3+} cations of $InGaP_2$ (Figure 4.6d). XP spectra of the Ga and P regions only showed peaks attributable to the Ga^{3+} cations and P^{3-} anions of p-$InGaP_2$. Again, no metallic In^0 or surface phosphate (PO_x) was found. Compared with the as-prepared p-$InGaP_2$/Pt electrode, both In/Ga and In/P ratios increased to 1.6 and 1.0, respectively. These results collectively indicated an enrichment of InO_x at the surface of the p-$InGaP_2$/Pt electrode resulting from a selective leaching of Ga ions.

To demonstrate the reproducibility of the above results for p-$InGaP_2$/Pt electrodes, we repeated the stability tests using different p-$InGaP_2$ electrodes for > 2 days in 1.0 M H_2SO_4(aq) and 1.0 M KOH(aq), respectively. Similar results were obtained in both electrochemical measurements and surface conditions, as summarized in Figure S 4.6-7.

4.4 Discussion

The present study identifies two important factors of determining the stability of p-$InGaP_2$ photocathodes for the HER: (1) catalytic kinetics of the HER for inhibiting cathodic corrosion of In^{3+} cations, and (2) the pH effect over the long-term evolution of the J-E behaviors.

Firstly, etched p-$InGaP_2$ electrodes formed metallic In^0 under illumination after a few hours of CA at 0 V vs. RHE at pH=0 and at -0.2 V vs. RHE at pH=14, suggesting cathodic corrosion following Eqs.1-2:[102]

pH=0: $InGaP_2(s) + 6H^+(aq) + 3e^- = In^0(s) + Ga^{3+}(aq) + 2PH_3(g)$ (**Eq.1**)

pH=14: $InGaP_2(s) + 3H_2O(l) + 3e^- = In^0(s) + GaO_3^{3-}(aq) + 2PH_3(g)$ (**Eq.2**)

The standard potentials of $In^{3+/0}$ and $Ga^{3+/0}$ redox couples are -0.34 V and -0.53 V versus the normal hydrogen electrode (NHE), respectively.[125,212] Thermodynamically, In^{3+} cations are more susceptible to cathodic corrosion than Ga^{3+} cations.[180] The Pourbiax diagram of P predicts that at pH=0, the formation of PH_3(g) is preferred at E<-0.34 V vs. RHE.[125,137] The leaching of Ga(III) ions from the electrodes was supported by the higher amounts of Ga ions than In ions detected in the electrolytes by ICP-MS. Consequently, the cathodic corrosion of p-$InGaP_2$ caused substantial electrode dissolution as well as decreases in $|J_{ph}|$ due to the opacity of metallic In^0, comprising the primary failure mode.

These observations concurred with the results from our prior investigations on both p-InP and p-GaAs photocathodes. Etched p-InP photoelectrodes displayed similar behaviors of cathodic corrosion forming metallic In^0 at both pH 0 and pH 14. In contrast, etched p-GaAs photoelectrodes retained its stoichiometric surface after prolonged operation of the HER, proving the stability of Ga^{3+} cations against self-reduction under negative E. As a result, the cathodic stability of p-$InGaP_2$ should depend more on the reduction of In^{3+} cations than Ga^{3+} cations.

Notably, Eq.1 and Eq.2 show different pH-dependence due to their different numbers of electrons and protons or water. At T=298 K, Eq.1 predicts a pH dependence of -118 mV/dec, whereas Eq.2 predicts a pH dependence of -59 mV/dec. As the potential of RHE shifts with pH value by -59 mV/decade, Eq.1 suggests a larger difference between the RHE potential and the standard potential of $In^{3+/0}$ redox couple for p-$InGaP_2$, when the pH increases from 0 to 7. Such different pH dependence may offer an additional potential difference of up to 0.41 V, making the reduction of In^{3+} cations of $InGaP_2$ thermodynamically more difficult at a higher pH.

In 1.0 M KOH(aq), the formation of InO_x instead of metallic In^0, at the surface of the etched p-$InGaP_2$ electrode after 4 h of CA at 0 V vs. RHE suggested the following reaction (Eq.3):

pH=14: $2InGaP_2(s) + 7H_2O(l) + 18OH^-(aq) = In_2O_3(s) + 2GaO_3^{3-}(aq) + 4PO_4^{3-}(aq) + 16H_2(g)$ (**Eq.3**)

The absence of metallic In^0 corresponded to the lower J (>-1 mA^{-2}) during the CA at 0 V vs. RHE in 1.0 M KOH(aq). Hence, the reduction of In^{3+} cations to In^0 is likely more facile at pH=0 than pH=14, as it requires a less negative applied potential (E_{app}) of illuminated p-$InGaP_2$ electrodes.

Besides, the In^0 formation by cathodic corrosion caused more dramatic changes in surface morphology as well as a faster leaching rate of Ga ions in acidic electrolytes than in alkaline electrolytes. The In^0 metal partially dissolved into the electrolyte from the surface of p-$InGaP_2$ at pH=0 while remaining nearly insoluble at pH=14. Notably, the E_{app} of etched p-$InGaP_2$ electrodes (0 V or -0.2 V vs. RHE) at which metallic In^0 formed was more positive than the thermodynamic potential of the $In^{3+/0}$ redox couple (-0.34 V vs. RHE). As illustrated in Scheme 4.1a, these results suggest a photovoltage effect produced by the etched p-$InGaP_2$ electrodes. The splitting of quasi Fermi-level by photogenerated electrons results in a more negative surface potential (E_{surf}) than the applied potential at back contact (E_{app}). Although the HER is thermodynamically preferred than the cathodic corrosion of In^{3+} cations, the occurrence of In^0 plating at the $InGaP_2$ surface indicated the position of E_{surf} is more negative than the potentials of both reactions, resulting in a competition for photogenerated electrons.

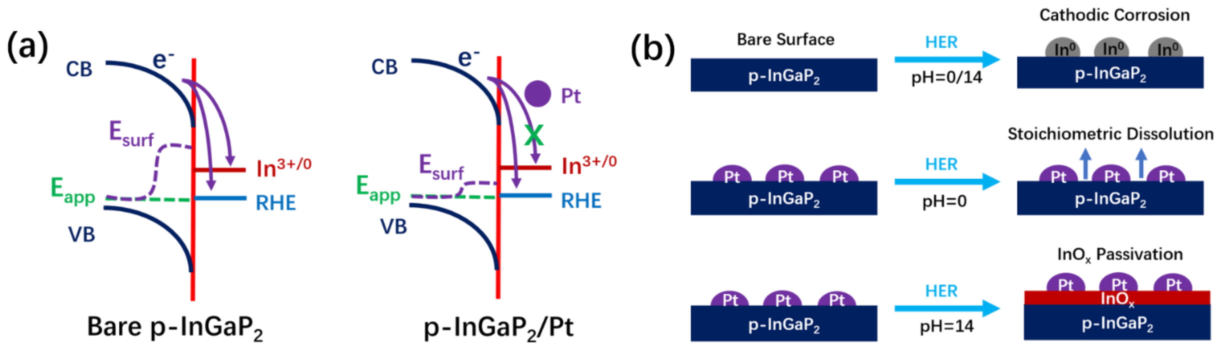

Scheme 4.1 (a) Comparison of band energy diagram and interfacial energetics of etched p-$InGaP_2$ electrodes and p-$InGaP_2$/Pt electrodes under illumination and cathodic bias; Pt catalyst inhibits the cathodic corrosion of p-$InGaP_2$ by accelerating the catalytic kinetics of the HER and lowering the surface potential (E_{surf}). (b) Comparison of the long-term evolution in electrode surface conditions for etched p-$InGaP_2$ electrodes and p-$InGaP_2$/Pt electrodes at pH=0 and pH=14.

In contrast, no metallic In^0 formed at the surface of the p-$InGaP_2$/Pt electrodes during the CA at 0 V vs. RHE in either acidic or alkaline electrolytes, suggesting the absence of cathodic corrosion. Instead, long-term stable J (>139 h) was observed for the illuminated p-$InGaP_2$/Pt electrodes in both electrolytes. Such striking contrast in stability between the etched p-$InGaP_2$ electrodes and the p-$InGaP_2$/Pt electrodes, reveals that the effect of catalytic kinetics of the HER for defining the corrosion chemistry of p-$InGaP_2$.[71,146] As illustrated in Scheme 4.1a, electrodeposition of Pt at the surface of p-$InGaP_2$ electrodes dramatically accelerates the HER kinetics while reducing the over-potential (η) to <200 mV for a J ~10 mA cm^{-2}.[144,166,213] As a result, such low η fixes the position of E_{surf} under J_{ph} within a stability window between the RHE potential and the $In^{3+/0}$ redox potential. Hence, photogenerated electrons from the p-$InGaP_2$ electrodes will favor the HER over the cathodic corrosion that is thermodynamically more demanding. Without Pt, the slow kinetics of the HER at the surface of etched p-$InGaP_2$ electrodes leads to a more negative E_{surf} than the $In^{3+/0}$ redox potential, thus promoting cathodic corrosion. Furthermore, this explanation is supported by the previous studies using dual-working electrode (DWE) photoelectrochemistry showing the electrochemical potentials at the front surface of semiconductor photoelectrodes is controlled by the catalytic kinetics, regardless of applied potentials.[75–77] Altogether these results emphasize that the thermodynamic environment (E_{surf}) at the front surface of p-$InGaP_2$ electrode is crucial for determining the corrosion chemistry. Under a solar-flux relevant J of -10 mA cm^{-2}, HER catalysts such as Pt can largely reduce the kinetic η at the surface of p-$InGaP_2$ surface, thus mitigating the cathodic corrosion of forming In^0. Such kinetic control over the stability of p-$InGaP_2$ also suggests that the failure mode of cathodic corrosion of p-$InGaP_2$ can be initiated upon delamination or gradual dissolution of HER catalysts.

Despite the electrodeposited Pt, the surface of p-$InGaP_2$ was still partially in contact with the electrolytes during CA. The facilitated kinetics by Pt catalysts results in different corrosion pathways for the p-$InGaP_2$/Pt electrodes compared with the etched p-$InGaP_2$ electrodes. At pH=0, the p-$InGaP_2$/Pt photoelectrode displayed a slow and stoichiometric dissolution of both In and Ga ions (~0.3 nm h^{-1}) despite its stable J for >200 h, suggesting the following corrosion pathway (Eq.4):

pH 0: $InGaP_2(s) + 6H^+(aq) + 8H_2O(l) = In^{3+}(s) + Ga^{3+}(aq) + 2H_3PO_4(g) + 8H_2(g)$ (**Eq.4**)

The 194-h CA yielded a total dissolution of ~65 nm of p-$InGaP_2$, thus leaving a much roughened but stoichiometric $InGaP_2$ surface with preserved Pt catalyst. The Pt catalyst may have dynamically re-deposited on the surface of p-$InGaP_2$ under cathodic bias, during its continuous dissolution. At pH=14, the surface of p-$InGaP_2$/Pt self-passivated with a layer of InO_x after a few hours of CA via a selective and self-limited leaching of Ga ions (~ 8 nm), as consistent with the reaction in **Eq.3**. The main driving forces of both reactions in Eq.3 and Eq.4 are attributed to the high reducing power of the P^{3-} anions of $InGaP_2$.

Furthermore, the long-term evolution of the J-E behavior of p-$InGaP_2$/Pt photoelectrodes depended on the pH of electrolytes as well as the resulting surface conditions. Scheme 4.1b summarizes the long-term evolution in the electrode surface conditions for both etched p-$InGaP_2$ and p-$InGaP_2$/Pt electrodes at pH=0 and pH=14. At pH=0, the degraded J-E behavior of the p-$InGaP_2$/Pt electrode after 23 h likely correlated with its continuous dissolution. At pH=14, the degradation of the J-E behavior with lowered E_{oc} of the p-$InGaP_2$/Pt electrode, corresponded to the surface passivation of InO_x as well as the resulting In-rich surface. Therefore, the solubility of InO_x is the primary cause for the different surface conditions of p-$InGaP_2$ in acidic and alkaline electrolytes. The lower solubility of InO_x in KOH led to the surface passivation as well as the self-limited dissolution of p-$InGaP_2$, unlike the slow but continuous corrosion (~0.3 nm h^{-1}) in H_2SO_4. Furthermore, impressive records in stability of >139 h were achieved for p-$InGaP_2$/Pt photoelectrodes at both pH 0 and pH 14, when tested at 0 V vs. RHE. However, such long-term stable J was accompanied by surface changes, electrode dissolution and the degradation in the J-E behavior, all of which were pH-dependent. Consequently, the physical stability of p-$InGaP_2$ electrodes needs to be considered separately from its electrochemical stability.

The above results of the p-$InGaP_2$/Pt electrodes were in agreement with those from our previous investigations of the p-InP/Pt electrodes. Initially, both p-InP/Pt and p-$InGaP_2$/Pt photocathodes offered similar photovoltages of ~0.6 V, despite their different band gaps. The similar photovoltages are assigned to the similar barrier heights at the semiconductor/liquid junction, formed between their similar positions of valence band edge and the RHE. The presence of Pt catalyst similarly inhibited the cathodic reduction of In^{3+} cations and thus kinetically stabilized both p-InP and p-$InGaP_2$ photocathodes. Similar trends in electrode dissolution were also observed. During the HER operation, p-InP/Pt and p-$InGaP_2$/Pt both showed similar slow dissolution rates at pH 0. At pH 14, both electrodes displayed negligible dissolution as well as similar behaviors of surface passivation by an InO_x layer. In addition, such surface passivation in alkaline electrolyte caused similar degradation in the J-E behaviors for both cases, with lowered E_{oc} to ~+0.3 V vs. RHE. A notable difference by the p-$InGaP_2$/Pt electrode is the absence of any surface P-enrichment with a P^0/PO_x layer, whereas a slight degradation in the J-E behavior was observed upon continuous dissolution.

Previous works on the unified defect model proposed by Spicer et al, have established that the electrical properties of III-V semiconductors are highly sensitive to surface stoichiometry.[99,148] For InP with a smaller band gap of 1.34 eV, an In-rich surface leads to surface states (SS) below the conduction band maximum (CBM) by ~0.4 eV. Considering the similar positions of valence band edges between p-InP and p-$InGaP_2$, the degraded J-E behavior of p-$InGaP_2$/Pt is again attributable to the Fermi-level pinning by the surface states produced by an InO_x-rich surface. In contrast, the J-E degradation of p-$InGaP_2$/Pt electrode in acidic electrolyte may be explained by a preferential leaching of either In or Ga ions, resulting in a temporarily non-stoichiometric surface upon dissolution.

The findings of the present works shed light on future opportunities of improving the stability of p-$InGaP_2$ electrodes: (1) developing strategies of surface protection and/or passivation to mitigate the continuous dissolution in acidic electrolyte and the formation of InO_x in alkaline electrolyte, (2) integrating p-$InGaP_2$ and active earth-abundant catalysts such as CoP with more durable interfaces to effect kinetic stabilization towards long-term stable operation of the HER.[85,206] For integrated tandem solar-fuel generators, the photovoltage by the top $InGaP_2$ light-absorber can be substantially improved to > 1 V by incorporation of an n^+-emitter layer to produce homojunctions.[70,210] Combining the $InGaP_2$ photocathode with protected Si photoanodes with a maximum photovoltage of 0.6 V is a promising route to achieve stable and unassisted solar water-splitting.[52,103,152] Our ongoing works have extended the stability investigations to such high-performing $InGaP_2$ photocathodes with higher device complexity, which can eventually benefit this development. Importantly, the present study points out a crucial advantage of employing $InGaP_2$ photocathodes in alkaline electrolyte for long-term HER than in acidic electrolyte, due to its negligible solubility. Creating a buried homojunction is also likely an effective strategy to overcome the performance degradation caused by the emergence of surficial InO_x layer.

Broadly, this work offers insights into rationally understanding the stability of semiconductor photoelectrodes for solar-fuel generation: (1) The stability of bare semiconductor electrodes and integrated semiconductor/catalyst electrodes needs to be studied independently due to their different catalytic kinetics. Comparing the onset potentials of corrosion reactions and fuel-forming reactions is beneficial for identifying opportunities of inhibiting unfavorable corrosion by kinetic control; (2) for compound semiconductors, the J-E behavior of photoelectrodes can be influenced by surface stoichiometry, especially during long-term operation in electrolytes.[98] Changes in the J-E behavior and electrode surface conditions should be closely correlated before and after electrochemical tests; (3) physical dissolution may not necessarily result a degradation in J during the CA of photoelectrodes. The physical stability and operational stability of semiconductor photoelectrodes need to be considered separately.

4.5 Conclusions

In summary, the stability of p-InGaP$_2$ photoelectrodes for the solar-driven HER has been evaluated in both acid and alkaline electrolytes, with and without Pt catalyst. At both pH=0 and pH=14, cathodic corrosion occurred at the surface of etched p-InGaP$_2$ photoelectrodes forming metallic In^0 under cathodic biases. However, electrodeposition of Pt catalyst at the surface of p-InGaP$_2$ mitigated such cathodic corrosion by kinetic competition, and enabled long-term stable operation of the HER in both acid and alkaline electrolytes. During stability tests, the p-InGaP$_2$/Pt photoelectrodes exhibited slow and stoichiometric dissolution in 1.0 M H_2SO_4(aq), while self-passivating with a layer InO$_x$ in 1.0 M KOH(aq). Importantly, the degradation of the J-E behavior of p-InGaP$_2$/Pt photoelectrodes were attributed to the mid-gap surface states produced by a non-stoichiometric surface, according to the unified defect model. This work reveals the importance of both catalytic kinetics and electrolytes for determining the physical and operational stability of p-InGaP$_2$ photocathodes, while offering further opportunities for realizing stable tandem solar-fuel devices based on III-V semiconductors.

Acknowledgement

This material is based upon work performed by the Joint Center for Artificial Photosynthesis, a DOE Energy Innovation Hub, supported through the office of Science of the US. Department of Energy under Award Number DE-SC0004993. Research was in part carried out at the Molecular Materials Research Center (MMRC) of the Beckman Institute of the California Institute of Technology. Dr. Nathan Dalleska is thanked for assistance with ICP-MS analysis.

4.6 Experimental

4.6.1 Materials

1.0 M sulfuric acid solution (H_2SO_4, VWR Chemicals), 1.0 M potassium hydroxide aqueous solution (KOH, TitriPUR volumetric solution), bromine (Br_2, reagent grade, Sigma-Aldrich), and methanol (CH_3OH, VWR Analytical, ACS, 99.8 %). Deionized water with a resistivity of 18.2 MΩ cm was obtained from a Barnstead Millipore system. Nafion (proton-exchange membrane) and Fumasep (anion-exchange membrane) were purchased from the Fuel Cell Store.

Zn-doped p-$InGaP_2$ epilayers with nominal thicknesses of 1 μm or 2 μm, and 1 x 10^{17} cm^{-3} dopant density were grown by metalorganic vapor phase epitaxy on p^+-GaAs(100) substrates, miscut 4° toward (111B). Electroplated gold was used to form an ohmic contact to the GaAs substrate.

4.6.2 Purification of electrolytes by pre-electrolysis

Prior to use, the electrolytes of 1.0 M H_2SO_4(aq) and 1.0 M KOH(aq) were pre-electrolyzed in a two-compartment electrochemical cell (Pyrex), with compartments separated by either a Nafion membrane (H_2SO_4) or Fumasep membrane (KOH). Carbon rod electrodes were used as cathode and anode. Pre-electrolysis was carried out under a constant bias of >3 V for >24 h. Only the electrolyte in the cathode compartment was used for further electrochemical measurements.

4.6.3 P-$InGaP_2$ etching

Prior to electrochemical measurements, all p-$InGaP_2$ electrodes were etched in 0.04 % Br_2/CH_3OH for 30 s, then in 4.0 M NH_3/CH_3OH solution for 30 s. This cycle was repeated twice, and the samples were rinsed with methanol and blown dry under a nitrogen gun for > 10 s.

4.6.4 (Photo)-electrochemical measurements

Electrochemical measurements, including chronoamperometry (CA) and cyclic voltammograms (CV), were performed in a nitrogen-filled glovebox (VAC, OMNI-LAB) with a O_2 concentration of <0.3 ppm. All electrolytes were degassed using a Schlenk line to remove the dissolved oxygen prior to transfer into the glovebox.

To facilitate XPS analysis of the samples, electrochemical measurements were performed using a custom-made compression cell fabricated from PEEK. The cell had two compartments separated by an ion-exchange membrane (Nafion for H_2SO_4, Fumasep for KOH). Electrochemical data were recorded on a SP-200 potentiostat (BioLogic Science Instruments) without compensation for solution resistance. Electrochemical measurements were carried out in a three-electrode set-up, with a Pt foil (H_2SO_4) or a Ni foil (KOH) as the counter electrode (CE), a hydrogen electrode HydroFlex (Gaskatel) as the reference electrode (RE), and p-$InGaP_2$ as the working electrode (WE). H_2 gas was fed into the glovebox, passed through an aqueous gas bubbler, and continuously purged the catholyte during electrochemical experiments. The H_2(g) from the cathode chamber and the O_2(g) from the anode chambers were vented to outside glovebox through separate outlets.

Prior to each experiment, the cell was assembled immediately after p-$InGaP_2$ etching, and transferred into the glovebox. The long-term stability tests were carried out by CA under illumination. The J-E behavior was periodically measured by CV during CA. After a pause of 15 s at open-circuit (E_{oc}), the CV was started from $E=E_{oc}-0.035$ V to more negative E to avoid passing anodic current through p-$InGaP_2$. A scan rate of 50 mV s^{-1} was used. After each experiment, the cell was disassembled inside the glovebox and the electrode sample was rinsed with deionized water, dried with nitrogen and stored inside the glovebox until XPS analysis.

A miniature fiber-optic adjustable-arm light equipped with a 150 W halogen bulb was used as the illumination source and was introduced from outside the glovebox into the glovebox via a fiber optic. The illumination intensity at the location of the sample within the electrochemical cell was calibrated to 1 sun (100 mW cm^{-2}) using a Si photodiode (FDS100, Thorlabs). The total volume of electrolyte in the cathode chamber was 5 mL. For the ICP-MS analysis, 0.2 mL of electrolyte was withdrawn from the catholyte at intervals while the WE was still under potential control, and 0.2 mL of fresh electrolyte was added to the catholyte to keep the total volume of electrolyte constant.

4.6.5 Electrodeposition of Pt catalyst.

For electrodeposition of Pt catalyst onto p-$InGaP_2$ samples, a solution of 5 mM K_4PtCl_6 and 0.5 M KCl was used. A constant J of -0.2 mA cm^{-2} was applied under 1-sun illumination under a two-electrode configuration until a charge density of -10 mC cm^{-2} had passed. An Aluminum foil was used as the CE. The Pt deposition was carried out in a different electrochemical cell from the one used for CA testing. Prior to electrodeposition, the bubbles around the o-ring area were carefully checked and removed to ensure the uniformity of the deposition.

4.7 Analytical Methods

4.7.1 Inductively coupled plasma mass spectrometry (ICP-MS) of catholytes

Inductively coupled plasma mass spectrometry (ICP-MS) data were collected using an Agilent 8800 Triple Quadrupole ICP-MS system. Calibration solutions were prepared by diluting the multi-element standard solutions for ICP with 18.2 MΩ cm resistivity water. The total amounts of dissolved In or Ga ions from the electrodes were calculated, and normalized to the geometric electrode area to obtain the equivalent depth of material ($InGaP_2$) removed from the crystalline electrode. To account for the effect of different solution matrixes, standard solutions were prepared and diluted using the same solution matrix of the analytes diluted from acidic and alkaline electrolytes.

4.7.2 X-ray photoelectron spectroscopy with air-free transfer

X-ray photoelectron spectroscopy (XPS) was performed using a Kratos Axis Ultra system with a base pressure of $< 1\times10^{-9}$ Torr equipped with a monochromatic Al Kα X-ray source with a photon energy of 1486.6 eV. Photoelectrons were collected at 0° from the surface normal with a retarding pass energy of 160 eV for survey XPS scans (step size of 1.0 eV) and for high-resolution core-level scans (step size 0.025 eV).

Prior to XPS measurements, in the glove box under N_2, samples were mounted on a Kratos sample holder into a transfer suitcase and sealed with a gate valve. The transfer suitcase was attached to the load lock of the Kratos Axis Ultra system. The load lock was pumped down to 1×10^{-6} Torr and then purged with N_2 to 1 atm. After pumping down the load lock again to ~100 Torr, the gate valve to the transfer box was opened and the turbo molecular pump was switched on. After achieving a pressure of $< 1 \text{ x } 10^{-6}$ Torr, the sample was transferred into the sample transfer chamber. After closing the gate valve to transfer suitcase, the sample was pumped down to <1×10^{-8} Torr before transferring to the analysis chamber.

4.7.3 Fitting of XPS spectra

All XPS peak fitting were performed using the Casa XPS software version 2.3.18. All binding energies are referenced to the adventitious carbon peak at 284.8 eV. Before fitting the data, a Shirley background was calculated and subtracted from the original spectra. The single peak of GaAs in the Ga 2p spectra was fit using the Asymmetric Lorentzian function. All other peaks were fit using the 70% Gaussian/30% Lorentzian Voigt-function. The surface atomic ratios were calculated using the relative sensitive factors (RSF) in the database of the Kratos instrument.

4.7.4 Scanning-electron microscopy (SEM)

Scanning-electron microscopy (SEM) images were obtained using a Nova NanoSEM 450 (FEI) with an accelerating voltage of 5 kV, with a working distance of 5 mm and an in-lens secondary electron detector.

4.7.5 Atomic-force Microscopy (AFM)

Atomic-force microscopy (AFM) images were obtained on a Bruker Dimension Icon using Bruker ScanAsyst-Air probes (silicon tip, silicon nitride cantilever, spring constant: 0.4 N m^{-1}, frequency: 50-90 kHz), operating in the ScanAsyst mode. Images were analyzed using the Nanoscope Analysis software (version 1.9).

4.8 Supplementary figures

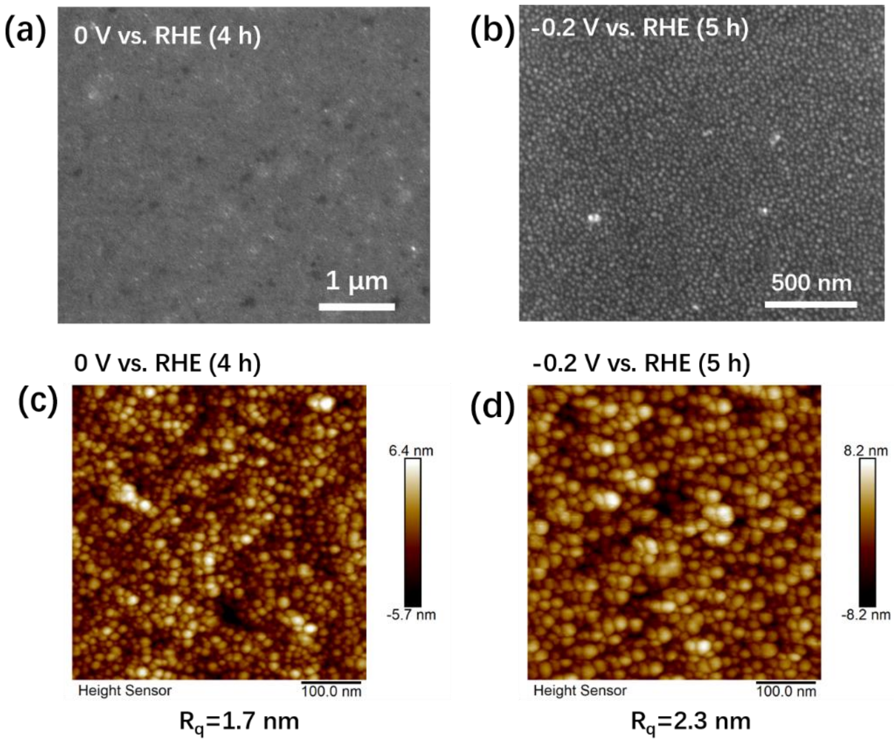

Figure S 4.1 Comparison of (a-b) SEM images and (c-d) AFM images of etched p-InGaP$_2$ electrodes tested at (a,c) 0 V vs. RHE for 4 h and (b,d) -0.2 V vs. RHE for 5 h, in 1.0 M KOH(aq) under 1-sun illumination. R$_q$ is surface roughness.

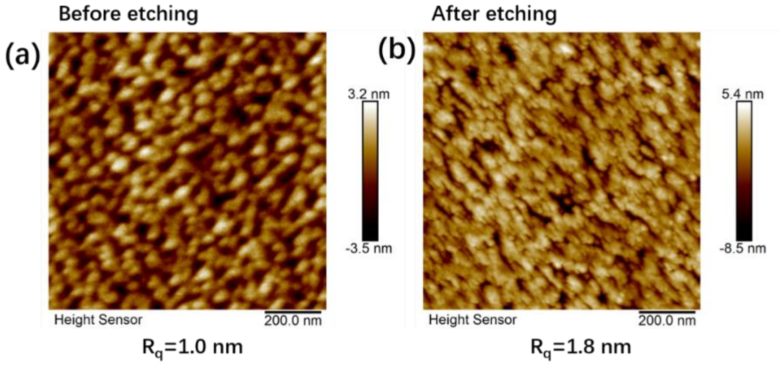

Figure S 4.2 Comparison of AFM images of p-InGaP samples (a) before and (b) after etching. R$_q$ is surface roughness.

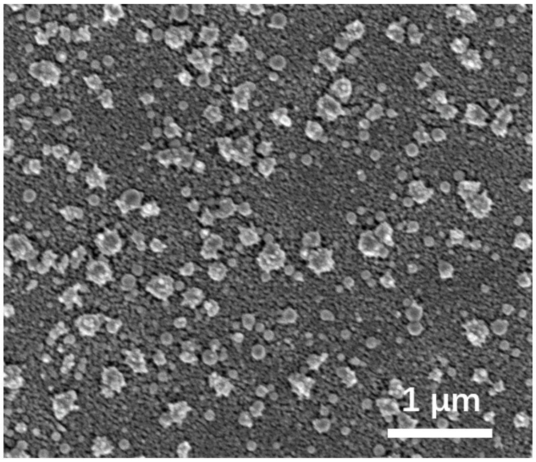

Figure S 4.3 SEM image of the p-InGaP$_2$/Pt electrode after 213 h of CA at 0 V vs. RHE in 1.0 M H_2SO_4(aq) under 1-sun illumination.

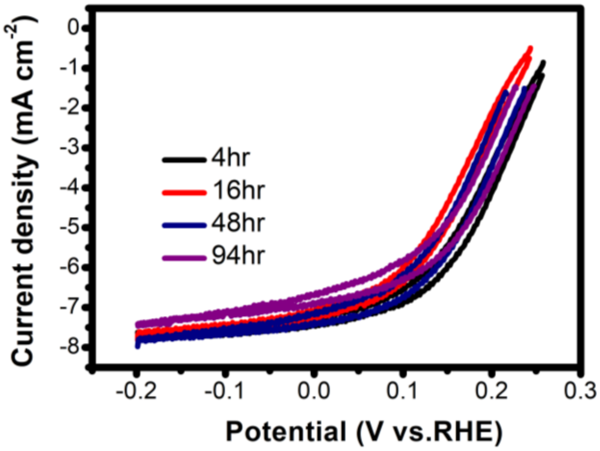

Figure S 4.4 Comparison of the J-E behavior of the p-InGaP$_2$/Pt electrode during CA at 0 V vs. RHE in 1.0 M KOH(aq) under 1-sun illumination.

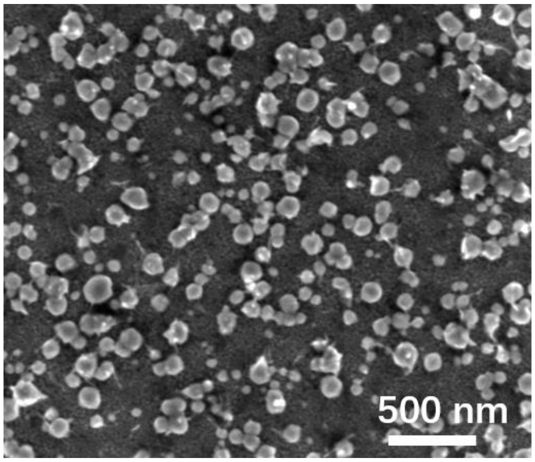

Figure S 4.5 SEM image of the p-InGaP_2/Pt electrode after 139 h of CA at 0 V vs. RHE in 1.0 M KOH(aq) under 1-sun illumination.

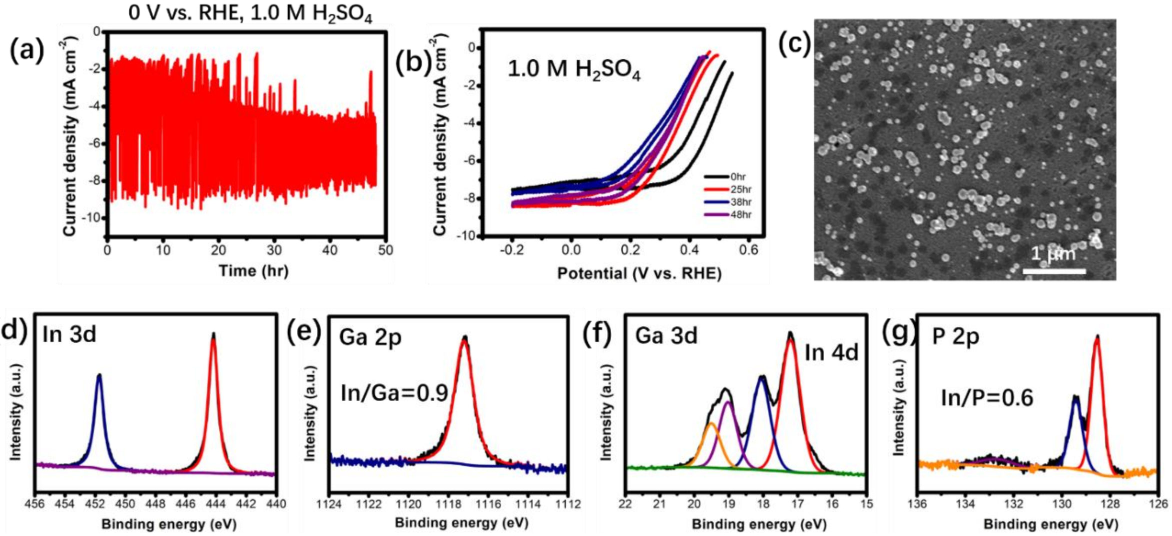

Figure S 4.6 Repeated stability test of a p-InGaP_2/Pt electrode in acidic electrolyte. (a) CA of the p-InGaP_2/Pt electrode at 0 V vs. RHE in 1.0 M H_2SO_4(aq) under 1-sun illumination. (b) Comparison of the J-E behavior of p-InGaP_2/Pt photoelectrode during the CA in (a). (c) SEM image of the p-InGaP_2/Pt electrode after CA in (a). (d-g) XP spectra of the (e) In 3d, (f) Ga 2p, (g) Ga 3d/In 4d and (h) P 2p regions for the p-InGaP_2/Pt photoelectrode after the CA in (a).

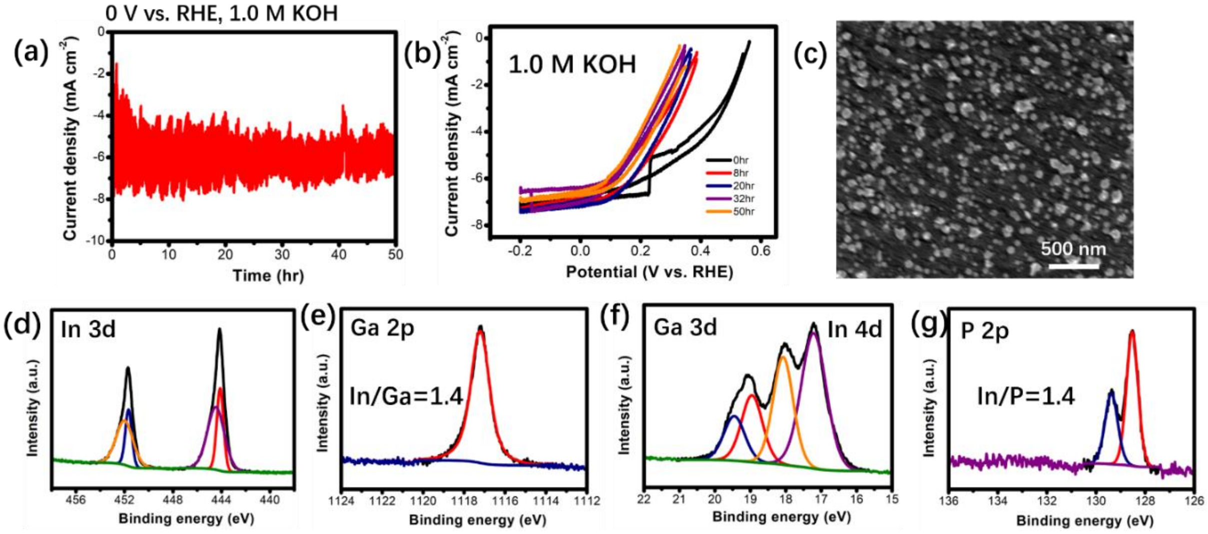

Figure S 4.7 Repeated stability test of a p-InGaP$_2$/Pt electrode in alkaline electrolyte. (a) CA of the p-InGaP$_2$/Pt electrode at 0 V vs. RHE in 1.0 M KOH(aq) under 1-sun illumination. (b) Comparison of the J-E behavior of p-InGaP$_2$/Pt photoelectrode during the CA in (a). (c) SEM image of the p-InGaP$_2$/Pt electrode after CA in (a). (d-g) XP spectra of the (e) In 3d, (f) Ga 2p, (g) Ga 3d/In 4d and (h) P 2p regions for the p-InGaP$_2$/Pt photoelectrode after the CA in (a). The XPS data collectively showed the formation of InO$_x$ and surface enrichment of In over Ga and P atoms.

Chapter 5

5 FAILURE MODES OF PLATINIZED HOMOJUNCTION PN+-INGAP$_2$ PHOTOCATHODE FOR SOLAR-DRIVEN H$_2$ EVOLUTION FROM AQUEOUS ACIDIC AND ALKALINE ELECTROLYTES

5.1 Abstract

The long-term stability of homojunction pn$^+$-InGaP$_2$ photocathodes with electrodeposited Pt catalyst (pn$^+$-InGaP$_2$/Pt) for the hydrogen-evolution reaction (HER) has been systematically evaluated in both acidic and alkaline electrolytes. The stability of pn$^+$-InGaP$_2$ light-absorbers grown on two different GaAs substrates were both studied and compared. To reveal the underlying failure mechanism, we focused on correlating electrode dissolution with the changes in the current density-potential (J-E) behavior over time, during potentiostatic measurements. Initially, as-prepared pn$^+$-InGaP$_2$/Pt photocathodes yielded superior photoelectrochemical performance with a photovoltage (E_{oc}) of > 900 mV and a light-limited current density (J_{sc}) of > 12 mA cm^{-2} under simulated 1-sun illumination. However, in 1.0 M H_2SO_4(aq), continuous dissolution of InGaP$_2$ layer led to a gradual thinning of the emitter layer resulting in a loss in E_{oc} down to ~ 0.5 V after 50 hours. In 1.0 M KOH(aq), a similar degradation in the J-E performance of pn$^+$-InGaP$_2$/Pt was observed with negligible dissolution of InGaP$_2$, which was mainly attributed to surface structural changes in electrolyte. Importantly, we revealed that the underlying GaAs substrate underwent substantial corrosion when the electrode was held at a positive potential of >+0.45 V vs. RHE in both acidic and alkaline solutions, causing severe damage to the structural integrity. Such GaAs corrosion caused delamination and cracking of the top InGaP$_2$ layer that remained electrochemically stable for the HER, further leading to operational instability of the device. This work shows the importance of enhancing structural integrity for the whole photoelectrode towards enabling stable solar fuel generation.

5.2 Introduction

Hydrogen (H_2) is a clean chemical fuel with high energy density that is crucial for constructing a global energy system with zero carbon emission.[2] Large-scale production of H_2 using renewable energy sources such as solar and wind has great potentials of addressing their intermittent issues as well as achieving on-demand delivery of energy.[8,11] Photoelectrochemical water-splitting using semiconductor photoelectrodes is a promising approach to directly convert solar energy into H_2 fuel in one step.[1,163]

The state-of-art electrocatalysts for the hydrogen-evolution reaction (HER) and oxygen-evolution reaction (OER) requires a total voltage of ~1.7 V to drive full water-splitting, at a current density (J) of 10 mA cm^{-2} that is operationally relevant to solar conditions.[45] An tandem solar-fuel device comprised of two semiconductors with a small and large band gaps can potentially offer spontaneous water-splitting at high energy conversion efficiency (η), by simultaneously producing high photovoltage and high photocurrent.[10,162] For such a high efficient solar water-splitting cell, strongly acidic or alkaline electrolytes are required to avoid the formation of pH gradient between cathode and anode under long-term operation.[10]

A previous analysis revealed that a combination of two semiconductors with band gaps of 1.1 eV and 1.8 eV can potentially realize a solar-to-hydrogen efficiency (η_{STH}) of > 25 %.[44] Silicon (Si) with a small band gap of 1.12 eV, is useful as a bottom light-absorber that can stably operate either as a photocathode in acidic solution or a protected photoanode.[46,74,84,103] Therefore, another large band-gap semiconductor is needed to pair up with Si for such a tandem solar-fuel device. In the family of III-V semiconductors, $InGaP_2$ with an optimal band gap of 1.8 eV is a promising candidate to be used as the top light absorber. For example, in 1998, Turner and coworkers demonstrated a solar water-splitting cell composed of a small band-gap GaAs and a large band-gap $InGaP_2$, achieving an energy conversion efficiency of > 9 % operating in 3 M H_2SO_4(aq).[36]

The stability of semiconductors in aqueous acidic or alkaline electrolytes is crucial for long-term operation of solar-fuel devices. Deciphering the underlying corrosion chemistry that gives rise to electrode instability is crucial for designing further rational strategies of stabilizing photoelectrodes. Typically, III-V semiconductors such as GaAs and InP corrode under anodic conditions required for the OER, whereas oxidation of their anions is both favored thermodynamically and kinetically.[59,60] However, the stability of these III-V semiconductors for use as HER photocathodes has remained elusive for long.

Previously, we revealed that both p-InP and p-InGaP$_2$ photoelectrodes corroded cathodically forming metallic In^0, which can be mitigated by using Pt catalyst to accelerate catalytic kinetics of the HER. Our results are consistent with other reports where the addition of active HER catalysts enhanced the operational stability of these electrodes in acidic electrolytes.[58,65,69,136,211] Moreover, both semiconductors exhibit pH-dependent dissolution and surface changes during long-term operation of the HER. However, many studies of solar-driven water splitting used multi-layered photovoltaic cells based on a stacked combination of different semiconductors. Moreover, the photovoltage generation typically relied on homojunction with emitter layers instead of direct semiconductor/liquid junctions which we investigated in previous studies. Therefore, investigating how the corrosion of the emitter layer impacts the photoelectrochemical performance of the whole photoelectrode can identify the limiting factors in the device stability for long-term operation. Furthermore, much less attention has been paid to the how the changes in the structural integrity of devices with complex multi-layered architectures under corrosion electrolytes influences the device stability. Quantifying the corrosion products in electrolytes as a function of operation time, together with surface characterization after long-term tests, can resolve the origin of device instability at different operation stages.

Herein, we investigated the stability of a homojunction pn$^+$-InGaP$_2$ photocathodes grown on degenerately doped p$^+$-GaAs substrates with two different crystal orientations. Starting from our previous findings, we first controllably electrodeposited Pt on the surface of pn$^+$-InGaP$_2$ electrodes to mitigate cathodic corrosion at both pH=0 and pH=14. Then we focused on evaluating how the changes in the J-E behavior of pn$^+$-InGaP$_2$/Pt photocathodes over time, correlated with both electrode dissolution and surface changes that were examined by the ICP-MS and XPS, respectively. Potentiostatic long-term experiments were performed at two different potentials to study its influence over the corrosion of underlying GaAs substrates. Through systematic experiments and characterizations, we revealed three different failure modes of pn$^+$-InGaP$_2$/Pt photocathodes performing long-term HER, which has important implications for further improving the stability of solar-fuel devices based on III-V semiconductors.

5.3 Results

5.3.1 Stability of pn$^+$-InGaP$_2$/Pt photocathodes for the HER in 1.0 M H_2SO_4(aq)

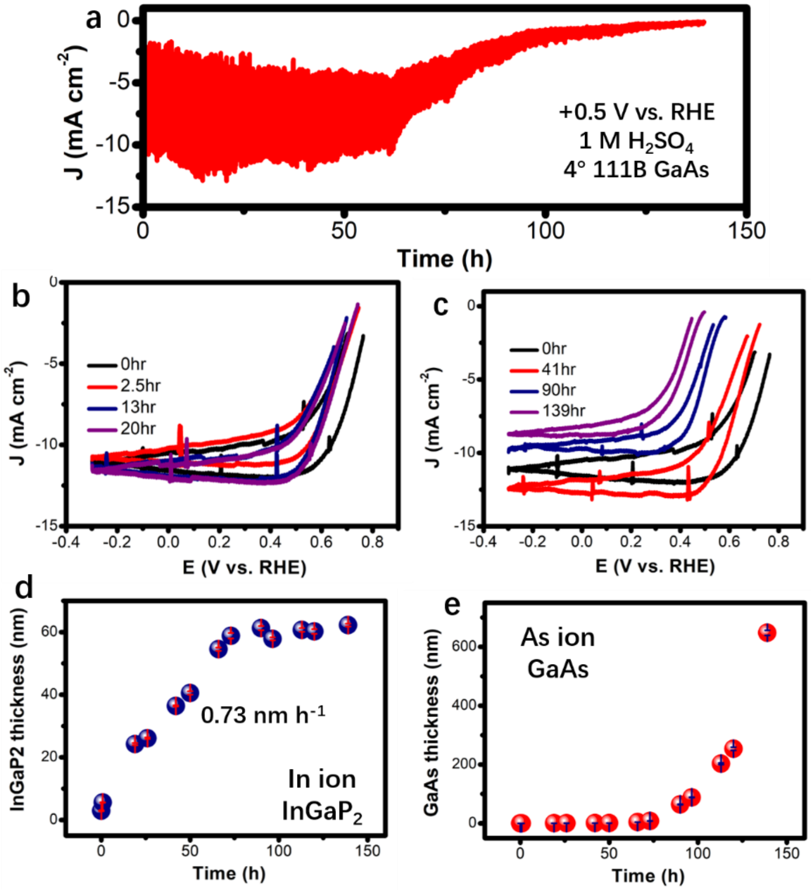

Figure 5.1 (a) Chronoamperometry (CA) of a pn$^+$-InGaP$_2$/Pt photocathode in 1.0 M H_2SO_4(aq) held at +0.5 V vs. RHE under 1-sun illumination; the pn$^+$-InGaP$_2$ epilayer was grown on a p$^+$-GaAs (111B) substrate by a 4° miscut. (b-c) Comparison of the J-E behavior of the pn$^+$-InGaP$_2$/Pt photocathode during the CA in (a) during (b) the first 20 h and (c) the whole 139 h. (d-e) Corrosion thicknesses of (d) InGaP$_2$ and (c) GaAs as a function of time, based on the concentrations of In and As ions dissolved in electrolyte measured by ICP-MS.

Prior to long-term stability tests, Pt catalyst was first electrodeposited onto the surface of pn$^+$-InGaP$_2$ electrodes to facilitate the HER kinetics, under galvanostatic conditions of J=-0.2 mA cm^{-2} until Q=-10 mC cm^{-2}. The pn$^+$-InGaP$_2$ epilayer consists of a p-type InGaP$_2$ (2 μm) base light absorber, together with a n$^+$-type InGaP$_2$ emitter layer (25 nm) to obtain a higher photovoltage (V_{oc}). The stability of pn$^+$-InGaP$_2$ epilayers grown on two different p$^+$-GaAs wafer substrates were evaluated and compared, namely a (111B) substrate by a 4° miscut and a (110) substrate by a 2° miscut. An intermediate AlInGaP$_2$ was grown between the InGaP$_2$ epi-layers and GaAs substrates for all samples.

Figure 5.1 presents the results of a pn$^+$-InGaP$_2$/Pt photocathode (GaAs 111B) tested at +0.5 V vs. RHE in 1.0 M H_2SO_4(aq) under 1-sun illumination. Initially, an as-prepared pn$^+$-InGaP$_2$/Pt photocathode displayed a E_{oc}~0.80 V vs. RHE and a light-limited current density (J_{sc}) of ~-12 mA cm^{-2}. At +0.5 V vs. RHE, the pn$^+$-InGaP$_2$/Pt electrode exhibited a stable J over the first 60 h with a maximum value of ~ -13 mA cm^{-2}, which then gradually decreased to < 1 mA cm^{-2} after 100 h (Figure 5.1a). The change in J was consistent with the evolution of the J-E behavior of the photoelectrode over time (Figure 5.1b-1c). The pn$^+$-InGaP$_2$/Pt electrode showed a stable J-E behaviors during the first 20 h, with positive onset E (J=-1 mA cm^{-2}) >+0.75 V vs. RHE (Figure 5.1b). From 41 to 139 h of CA, the J-E behavior of the electrode shifted cathodically with its onset E and J_{sc} decreasing to <+0.5 V vs. RHE and < 9 mA cm^{-2}, respectively (Figure 5.1c). During the 139-h CA, ICP-MS analysis revealed that the concentrations of dissolved In ions in electrolyte increased linearly at a rate of 0.73 nm h^{-1} in the InGaP$_2$ thickness, which then plateaued after 70 h (Figure 5.1d). Starting from 70 h, substantial amount of As ions was found in electrolyte which amounted to ~650 nm of GaAs after 139 h, indicating corrosion of GaAs substrate (Figure 5.1e).

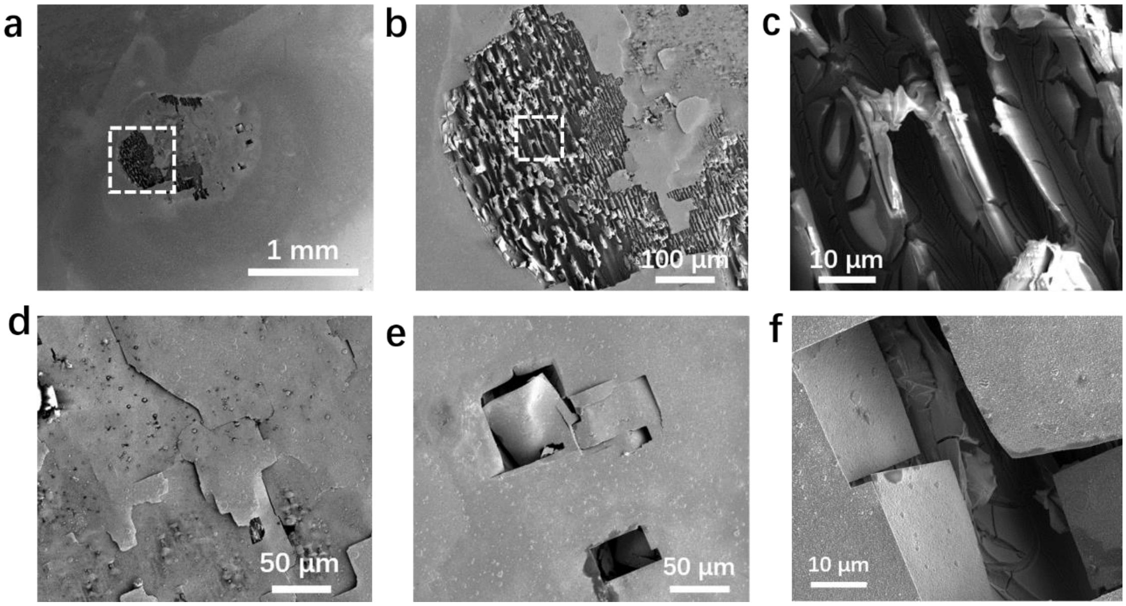

Figure 5.2 Surface morphology of the pn$^+$-InGaP$_2$/Pt photocathode after test in Figure 1a in 1.0 M H_2SO_4(aq). Figure 2b and 2c refers to the enlarged image of highlighted regions in 2a and 2b, respectively.

Figure 5.2 shows SEM images of the pn$^+$-InGaP$_2$/Pt electrode after the CA test in Figure 1a. Evident delamination of the top layers was observed over different regions across the surface of the pn$^+$-InGaP$_2$/Pt electrode. Figure 5.2a-c shows a region where a large area of the top InGaP$_2$ layer was removed, exposing the underlying GaAs substrate for corrosion in electrolyte. The corroded GaAs substrate manifested as line shapes with voids in between, suggesting removal of substantial materials. Another region showed apparent cracks of delaminated top layer that allowed penetration of electrolyte to reach the GaAs substrate (Figure 5.2d). Moreover, other regions displayed pieces of top layer with side length of ~50 μm that partially or completely collapsed due to crack formation (Figure 5.2e-f). Collectively these results revealed that cracking and delamination of the top InGaP$_2$ layer occurred during the 139-h CA in acidic electrolyte, leading to active corrosion of underlying GaAs observed by ICP-MS.

After the CA, the XPS data showed only features assigned to InGaP$_2$ in the spectra of the In, Ga and P regions (Figure S 5.1). However, the As 3d spectrum exhibited doublets assigned to both

As and AsO_x at binding energies (BE) of 41.4 and 42.5 eV, respectively, again confirming the exposure of underlying GaAs to corrosion.

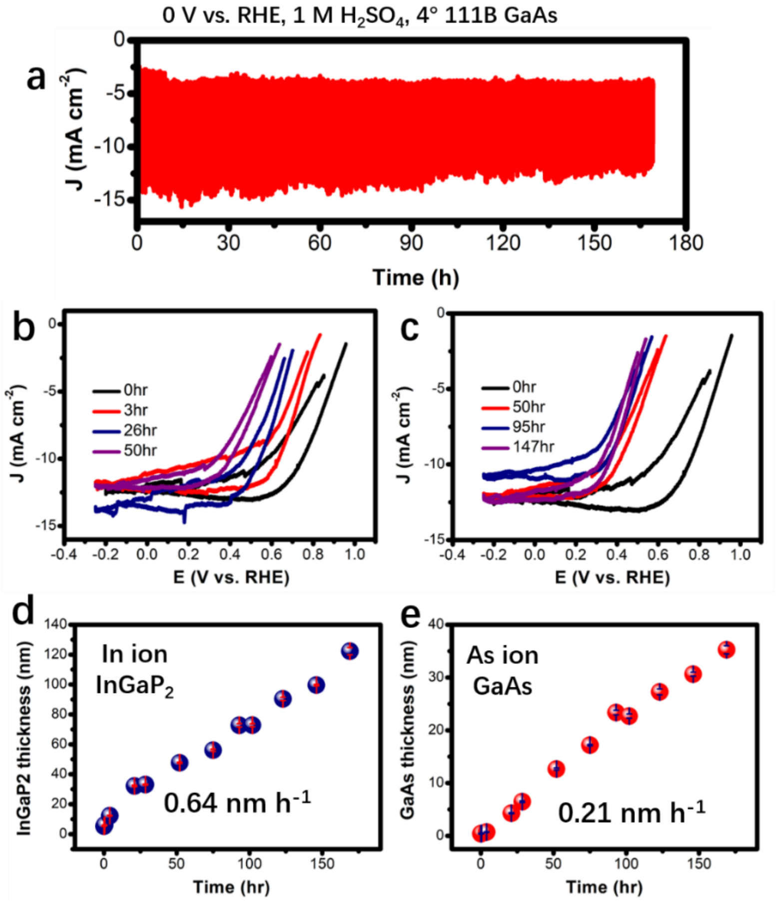

Figure 5.3 (a) CA of a pn^+-$InGaP_2$/Pt photocathode in 1.0 M H_2SO_4(aq) held at 0 V vs. RHE under 1-sun illumination; the pn^+-$InGaP_2$ epilayer was grown on a p^+-GaAs (111B) substrate by a 4° miscut. (b-c) Comparison of the J-E behavior of the pn^+-$InGaP_2$/Pt photocathode during the CA in (a) during (b) the first 50 h and (c) the whole 147 h. (d-e) Corrosion thicknesses of (d) $InGaP_2$ and (c) GaAs as a function of time, based on the concentrations of In and As ions dissolved in electrolyte measured by ICP-MS.

To evaluate the effect of applied back-contact potential towards electrode corrosion, the same pn^+-$InGaP_2$/Pt photocathode (GaAs 111B) was prepared and tested in 1.0 M H_2SO_4(aq) by CA at 0 V vs. RHE under 1-sun illumination (Figure 5.3). During the 147-h CA, the pn^+-$InGaP_2$/Pt photoelectrode maintained a stable J with a maximum value of ~-15 mA cm^{-2} during the whole period (Figure 5.3a). Initially, the pn$^+$-InGaP$_2$/Pt photocathode displayed a positive onset E of >+0.96 V vs. RHE at J=-1 mA cm^{-2} and a J$_{sc}$ of ~-13 mA cm^{-2}. A similar degradation in the J-E behavior was observed where the onset E gradually decreased to ~+0.6 V vs. RHE after 50 h and remained unchanged afterwards. Notably, no substantial decrease in J$_{sc}$ was observed in the J-E behavior after 147 h. During the CA, the pn$^+$-InGaP$_2$/Pt electrode exhibited a corrosion rate of 0.64 nm h^{-1} and 0.21 nm h^{-1} for InGaP$_2$ and GaAs, respectively. Compared with the above electrode tested at E=+0.5 V vs. RHE, this pn$^+$-InGaP$_2$/Pt electrode showed a similar dissolution rate of InGaP$_2$, and also a slightly higher E$_{oc}$ at start that decreased to a similar value (+0.5-0.6 V vs. RHE) after long periods. However, the accumulative amount of GaAs dissolved was largely reduced under a more negative E=0 V vs. RHE.

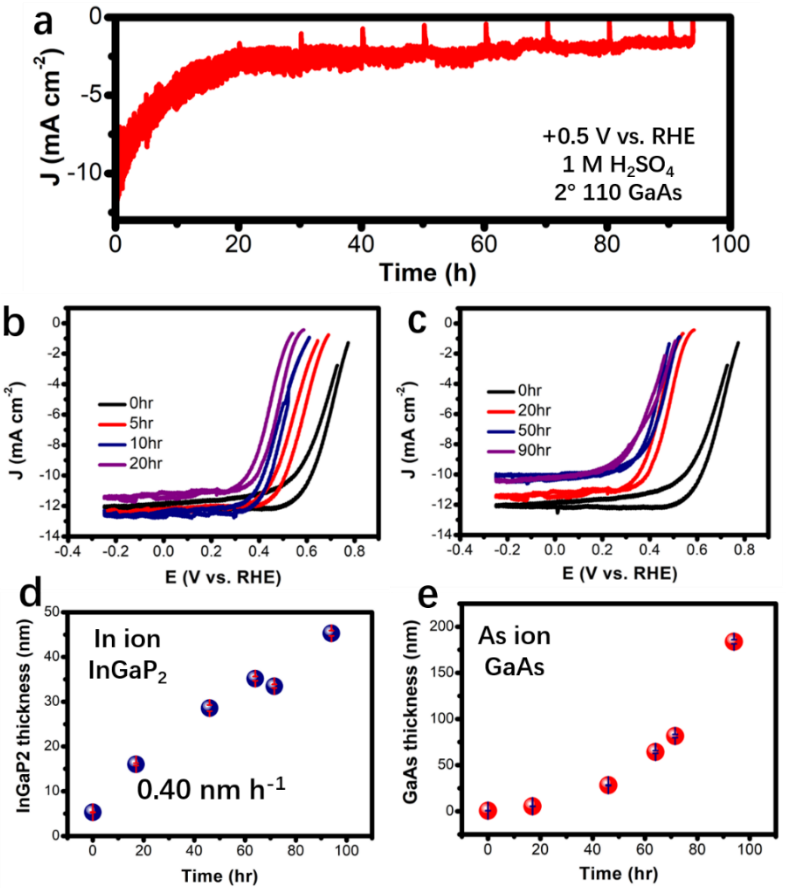

Figure 5.4 (a) CA of a pn$^+$-InGaP$_2$/Pt photocathode in 1.0 M H$_2$SO$_4$(aq) held at +0.5 V vs. RHE under 1-sun illumination; the pn$^+$-InGaP$_2$ epilayer was grown on a p$^+$-GaAs (110) substrate by a

2° miscut. (b-c) Comparison of the J-E behavior of the pn$^+$-InGaP$_2$/Pt photocathode during the CA in (a) during (b) the first 20 h and (c) the whole 90 h. (d-e) Corrosion thicknesses of (d) InGaP$_2$ and (c) GaAs as a function of time, based on the concentrations of In and As ions dissolved in electrolyte measured by ICP-MS.

To examine the impact of the crystal orientation of GaAs substrates, a pn$^+$-InGaP$_2$/Pt photocathode grown on a GaAs(110) wafer with a 2° miscut, was prepared and tested by CA at E=+0.5 and 0 V vs. RHE in 1.0 M H_2SO_4(aq) under 1-sun illumination. At E=+0.5 V vs. RHE, the J of the pn$^+$-InGaP$_2$/Pt photocathode decreased from ~12 mA cm^{-2} to < 2 mA cm^{-2} after 20 h (Figure 5.4a). Initially, the photoelectrode yielded a onset E of ~+0.8 V vs. RHE and a J_{sc} of ~ 12 mA cm^{-2}. In the first 20 h, the J-E behavior of the pn$^+$-InGaP$_2$/Pt electrode exhibited a cathodic shift, whereas the onset E gradually decreased to +0.6 V vs. RHE (Figure 5.4). From the 20 h to 90 h of the CA, a slight decrease in J_{sc} to ~10 mA cm^{-2} was observed while the onset E stayed nearly unchanged (Figure 5.4c). ICP-MS analysis of sampled electrolytes revealed a linear corrosion rate of 0.40 nm h^{-1} for the InGaP$_2$ layer (Figure 5.4d). Active dissolution of GaAs occurred after 40 h and amounted to ~200 nm after 90 h (Figure 5.4e).

In addition, we also tested the pn$^+$-InGaP$_2$/Pt (GaAs 110) electrode produced in a different batch in the same reactor, yielding similar results in both electrochemical tests and electrode dissolution under the same conditions (Figure S 5.2). The InGaP$_2$ exhibited a similar dissolution rate of 0.57 nm h^{-1}, whereas substantial corrosion of GaAs was again seen. After the test, SEM images of electrode surface showed stripe patterns with periods of ~1μm, together with micron-sized particles assigned to Pt catalyst (Figure S 5.3). AFM images revealed that the height of these stripe patterns reached 150 nm (Figure S 5.4). An examination of the surface morphology of an as-received pn$^+$-InGaP$_2$ (GaAs 110) sample showed that the formation of these stripe patterns correlated with the pre-existing surface bunching with a similar periodicity but a much smaller height (Figure S 5.5). This result suggested the dissolution of InGaP$_2$ and GaAs occurred along these surface features, which is different from the previous pn$^+$-InGaP$_2$/Pt (GaAs 111B) electrode. Post-CA XPS analysis showed only peaks assigned to InGaP$_2$ in the In, Ga and P regions, whereas the In/P and In/Ga atomic ratios remained similar to those before CA (Figure S 5.6-7). However, the As 3d spectrum displayed a doublet at binding energy (BE) of 41.4 eV attributable to As^0, implying both exposure and oxidation of the underlying GaAs substrate.

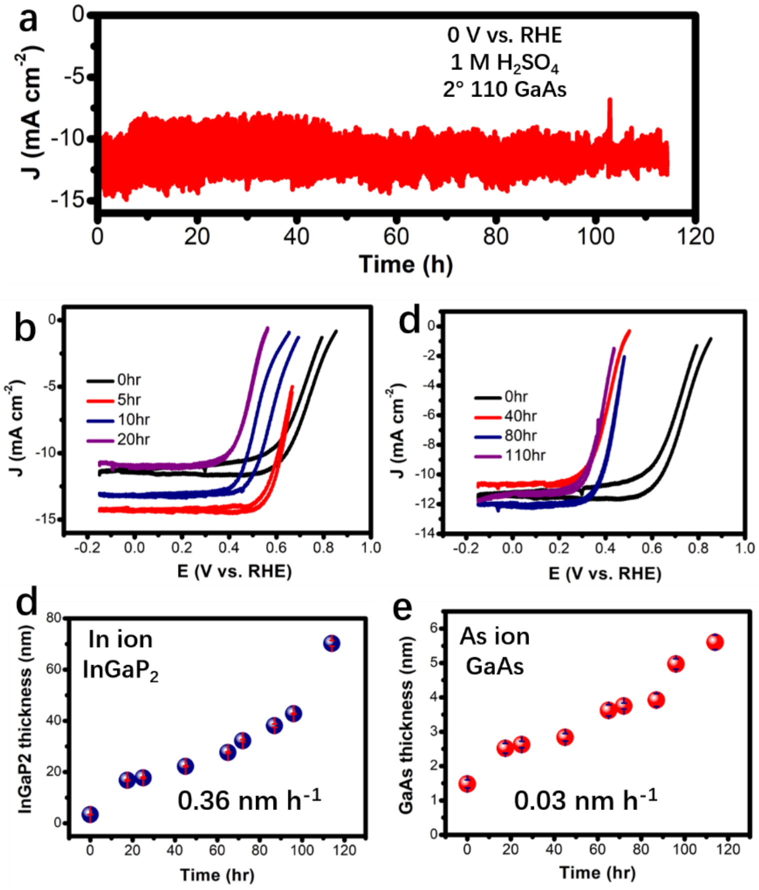

Figure 5.5 (a) CA of a pn^+-$InGaP_2$/Pt photocathode in 1.0 M H_2SO_4(aq) held at 0 V vs. RHE under 1-sun illumination; the pn^+-$InGaP_2$ epilayer was grown on a p^+-GaAs (110) substrate by a 2° miscut. (b-c) Comparison of the J-E behavior of the pn^+-$InGaP_2$/Pt photocathode during the CA in (a) during (b) the first 20 h and (c) the whole 110 h. (d-e) Corrosion thicknesses of (d) $InGaP_2$ and (c) GaAs as a function of time, based on the concentrations of In and As ions dissolved in electrolyte measured by ICP-MS.

At E=0 V vs. RHE, the same pn^+-$InGaP_2$/Pt photocathode (GaAs 110) gave a stable J with a maximum value of ~15 mA cm^{-2} over a period of 110 h (Figure 5.5a). Initially, the pn^+-$InGaP_2$/Pt electrode yielded an onset E of +0.85 V vs. RHE and a J_{sc} of ~ 12 mA cm^{-2}. A similar cathodic shift in the J-E behavior was seen over the initial 20 h, where as a slight increase in J_{sc} to ~ 15 mA cm^{-2}

occurred after 5 h (Figure 5.5b). From 40 to 110 h of CA, the J-E behavior stayed nearly the same with an onset E of ~+0.5 V vs. RHE (Figure 5.5c). During CA, the electrode displayed linear corrosion rates of 0.36 nm h^{-1} for $InGaP_2$, and 0.03 nm h^{-1} for GaAs (Figure 5.5d-e).

5.3.2 Stability of pn^+-$InGaP_2$/Pt photocathodes for the HER in 1.0 M KOH(aq)

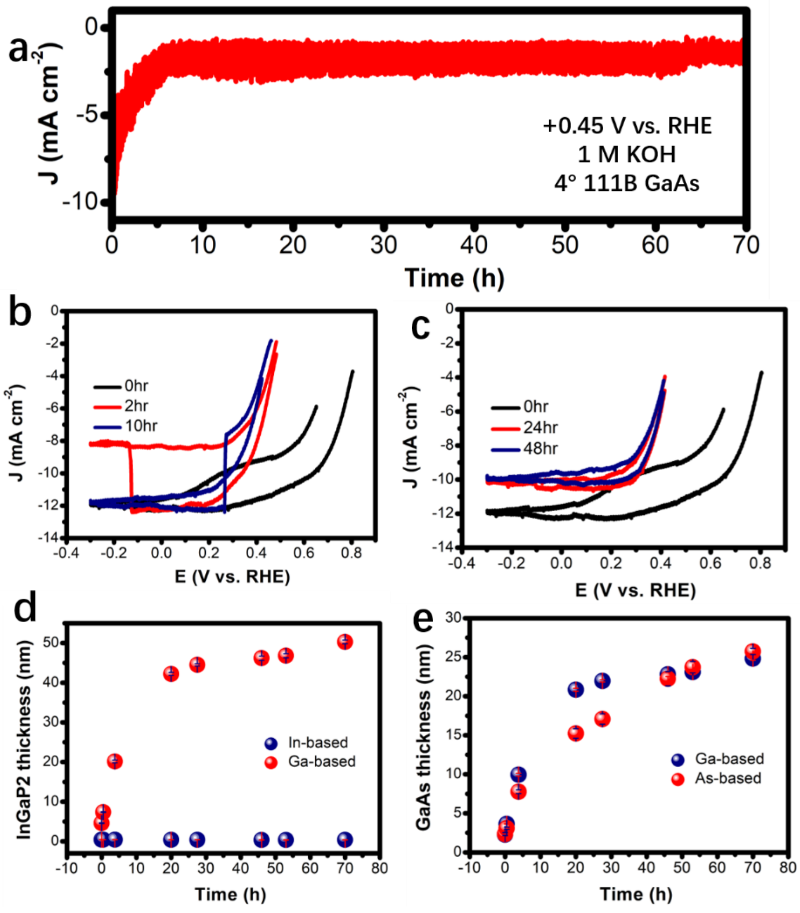

Figure 5.6 (a) CA of a pn^+-$InGaP_2$/Pt photocathode in 1.0 M KOH(aq) held at +0.45 V vs. RHE under 1-sun illumination; the pn^+-$InGaP_2$ epilayer was grown on a p^+-GaAs (111B) substrate by a 4° miscut. (b-c) Comparison of the J-E behavior of the pn^+-$InGaP_2$/Pt photocathode during the CA in (a) during (b) the first 10 h and (c) 48 h. (d-e) Corrosion thicknesses of (d) $InGaP_2$ and (c) GaAs as a function of time, based on the concentrations of dissolved ions in electrolyte measured by ICP-MS.

The stability of a pn$^+$-InGaP$_2$/Pt photocathode grown on a GaAs 111B substrate in 1.0 M KOH(aq) was first evaluated by CA at E=+0.45 V vs. RHE under 1-sun illumination. As seen in Figure 5.6a, the J of pn$^+$-InGaP$_2$/Pt electrode decreased from ~10 mA cm^{-2} to ~2 mA cm^{-2} in the first 10 h and then remained unchanged afterwards. Initially, the pn$^+$-InGaP$_2$/Pt photocathode offered a E$_{oc}$ of +0.88 V vs. RHE as well as a J$_{sc}$ of ~12 mA cm^{-2}, which was comparable to those in acidic electrolytes. After 2 h, the J-E behavior of the pn$^+$-InGaP$_2$/Pt electrode shifted cathodically with its onset E decreasing to ~+0.5 V vs. RHE that remained unchanged afterwards (Figure 5.6b). After 24 h, a slight decrease of J$_{sc}$ to ~ 10 mA cm^{-2} was observed (Figure 5.6c). ICP-MS analyses showed negligible dissolution of In ions during the entire CA, while the nearly stoichiometric dissolution of GaAs slowly amounted to ~25 nm after 70 h (Figure 5.6 e-f).

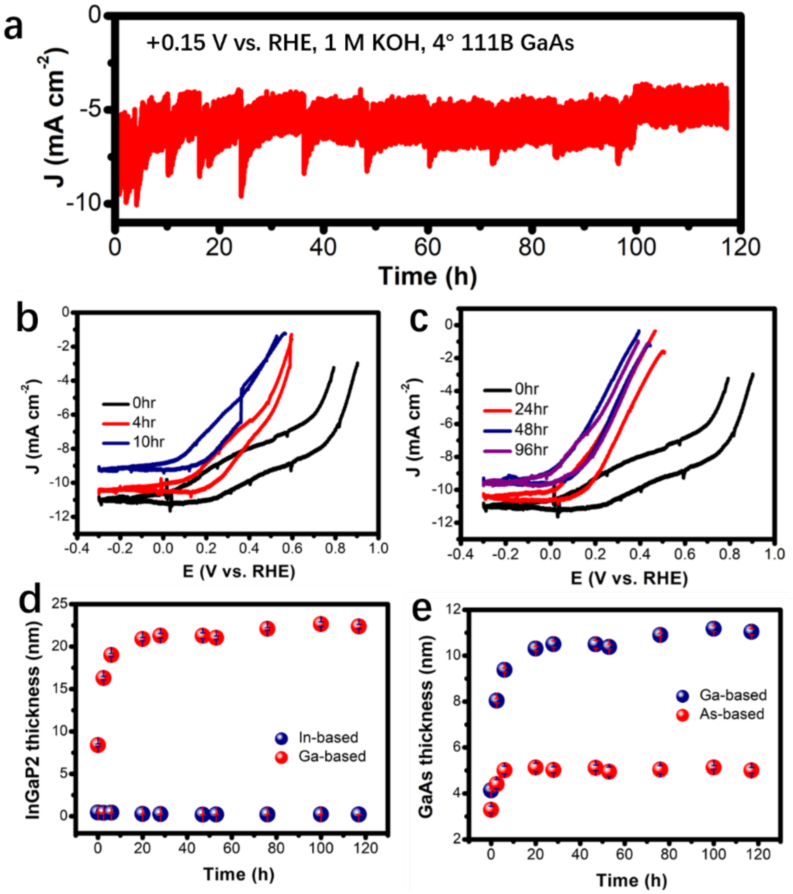

Figure 5.7 (a) CA of a pn$^+$-InGaP$_2$/Pt photocathode in 1.0 M KOH(aq) held at +0.15 V vs. RHE under 1-sun illumination; the pn$^+$-InGaP$_2$ epilayer was grown on a p$^+$-GaAs (111B) substrate by a

4° miscut. (b-c) Comparison of the J-E behavior of the pn$^+$-InGaP$_2$/Pt photocathode during the CA in (a) during (b) the first 10 h and (c) 96 h. (d-e) Corrosion thicknesses of (d) InGaP$_2$ and (c) GaAs as a function of time, based on the concentrations of dissolved ions in electrolyte measured by ICP-MS.

At E=+0.15 V vs. RHE, the same pn$^+$-InGaP$_2$/Pt photoelectrode (GaAs 111B) showed a slightly decreased J from ~10 mA cm^{-2} to ~8 mA cm^{-2} during the first 5 h, which then stayed nearly unchanged for the rest of 117 h (Figure 5.7a). Prior to CA, the pn$^+$-InGaP$_2$/Pt photoelectrode yielded a E_{oc} of ~0.94 V vs. RHE and a J_{sc} of ~11 mA cm^{-2}. Comparison of the measured J-E behavior as a function of time showed a rapid degradation in the first 10 h, with its E_{oc} decreasing to +0.6 V vs. RHE (Figure 5.7b). The J-E behavior remained nearly unchanged after 24 h, whereas only a slight decrease of J_{sc} to ~10 mA cm^{-2} were seen (Figure 5.7c). Again, ICP-MS analysis showed negligible dissolution of In ions, whereas a limited amount of As dissolution was observed accounting for only 5 nm of GaAs during the entire CA. However, additional Ga ions were found in electrolyte compared with In and As ions (Figure 5.7d-e). Compared with the above electrode tested at E=+0.45 V vs. RHE, this pn$^+$-InGaP$_2$/Pt photoelectrode showed similar changes in the J-E behavior over time during CA, while less dissolution of GaAs was observed at E=+0.15 V vs. RHE.

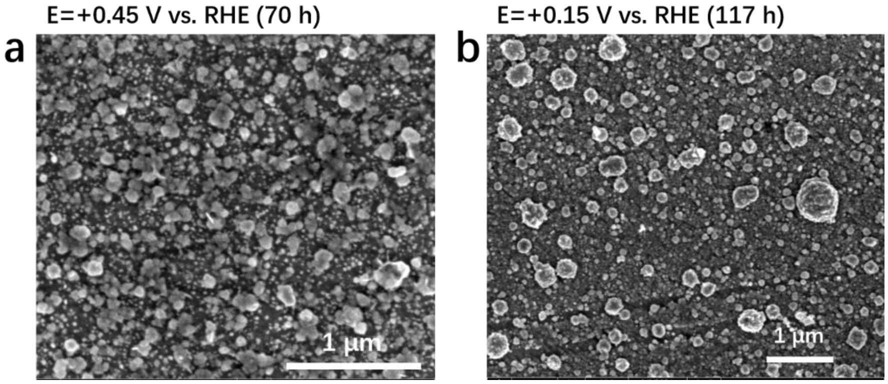

Figure 5.8 SEM images of the pn$^+$-InGaP$_2$/Pt photocathodes (GaAs 111B) tested in 1.0 M KOH(aq) under 1-sun illumination, (a) at E=+0.45 V vs. RHE for 70 h and (b) at E=+0.15 V vs. RHE for 117 h

After the CA in KOH, both pn$^+$-InGaP$_2$/Pt photoelectrodes (GaAs 111B) manifested roughened surface morphology with the formation of cracks and nanoparticles (Figure 5.8). For the electrode tested at E=+0.45 V vs. RHE, small nanoparticles densely packed over the surface. For the electrode tested at E=+0.15 V vs. RHE, large micro-sized particles could still be distinguished from the rest of surface which were assigned to Pt particles. Comparatively, the more pronounced changes in surface morphology at E=+0.45 V vs. RHE is likely correlated with a higher amount of GaAs dissolved into the electrolyte. XPS data showed that both pn$^+$-InGaP$_2$/Pt samples exhibited only peaks assigned to InGaP$_2$ after the CA, without forming any additional surficial species (Figure S 5.8-9). No substantial signals were detected in the As 3d spectra.

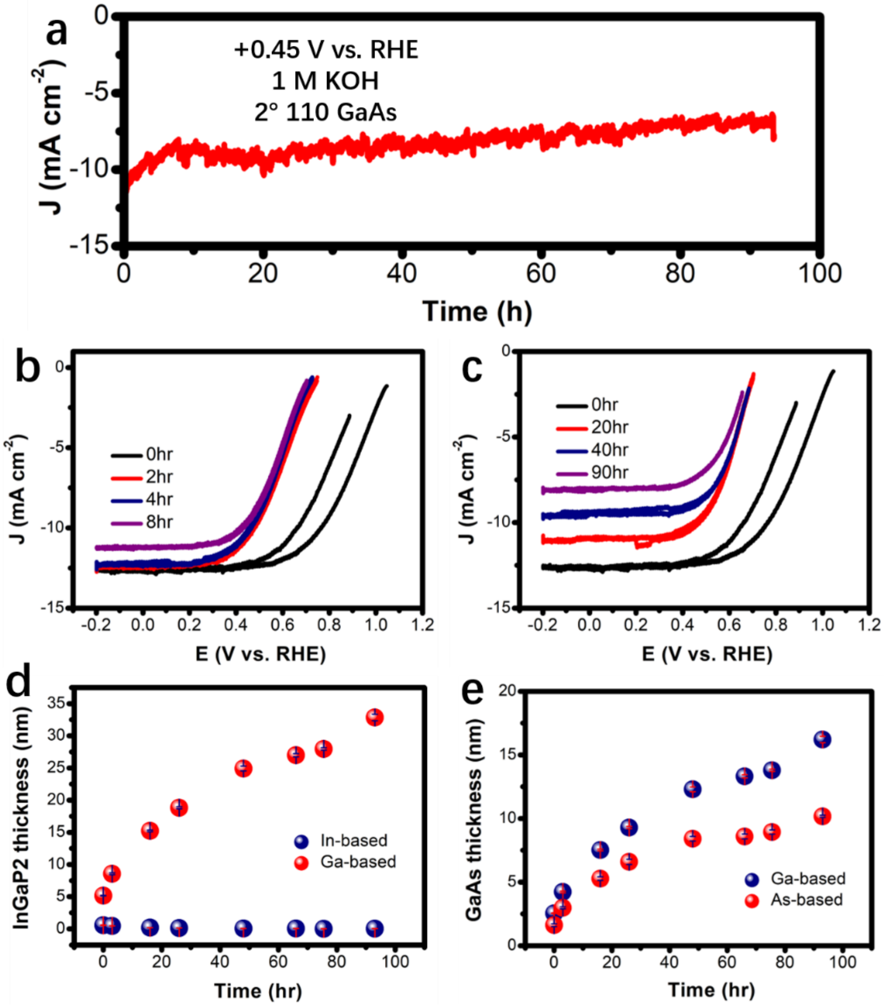

Figure 5.9 (a) CA of a pn$^+$-InGaP$_2$/Pt photocathode in 1.0 M KOH(aq) held at +0.45 V vs. RHE under 1-sun illumination; the pn$^+$-InGaP$_2$ epilayer was grown on a p$^+$-GaAs (110) substrate by a 2° miscut. (b-c) Comparison of the J-E behavior of the pn$^+$-InGaP$_2$/Pt photocathode during the CA in (a) during (b) the first 8 h and (c) 90 h. (d-e) Corrosion thicknesses of (d) InGaP$_2$ and (c) GaAs

as a function of time, based on the concentrations of dissolved ions in electrolyte measured by ICP-MS.

Similarly, the stability of a pn$^+$-InGaP$_2$/Pt photocathode grown on a GaAs(110) substrate in 1.0 M KOH(aq) was evaluated by CA at E=+0.45 V vs. RHE under 1-sun illumination (Figure 5.9). During CA, the J of the photoelectrode slightly decreased ~12 mA cm^{-2} to ~10 mA cm^{-2} during the first 2 h, and then gradually decreased to ~8 mA cm^{-2} during the rest 91 h. Initially, the pn$^+$-InGaP$_2$/Pt photocathode yielded a E_{oc} of +1.1 V vs. RHE and a J_{sc} of ~12.7 mA cm^{-2}. After 2 h, the J-E behavior of the electrode degraded with an onset E of +0.74 V vs. RHE that remained almost unchanged afterwards (Figure 5.9b). From 20 to 90 h, the J-E behavior of the pn$^+$-InGaP$_2$/Pt electrode exhibited a gradual decrease in J_{sc} from 11.3 mA cm^{-2} to 8 mA cm^{-2}, consistent with the decrease of J in CA (Figure 5.9c). ICP-MS analysis showed negligible dissolution of In ions, whereas ~10 nm GaAs dissolved into the electrolyte in 93 h. Additional Ga ions than As ions were also found. Moreover, the same test was repeated over a different sample under the same conditions, yielding less stable J-t profile but similar evolution of the J-E behavior over time (Figure S 5.10). XPS analyses over the sample surface showed the formation of InO_x and increased In/P and In/Ga atomic ratios, suggesting surface enrichment of In atoms (Figure S 5.11).

In addition, we tested another pn$^+$-InGaP$_2$/Pt (GaAs 110) sample which was produced in a different batch, which yielded a similar J-t profile together with degraded J-E behavior over time (Figure S 5.12). At E=+0.45 V vs. RHE, GaAs corrosion was again detected by ICP-MS, which plateaued at ~ 20 nm after 20 h but again increased after 50 h. SEM images showed crack formation as well as substantially roughened surface after CA (Figure S 5.13), whereas XPS analyses again revealed the formation of surficial InO_x layer (Figure S 5.14).

5.4 Discussion

5.4.1 Dissolution of pn$^+$-InGaP$_2$/Pt photoelectrodes during the HER.

Based on our previous findings, we have identified the corrosion pathways for platinized p-InGaP$_2$ photocathodes under the HER conditions (E_{surf}~-0.1 V vs. RHE):

pH 0: $InGaP_2(s) + 6H^+(aq) + 8H_2O(l) = In^{3+}(s) + Ga^{3+}(aq) + 2H_3PO_4(g) + 8H_2(g)$

pH=14: $2InGaP_2(s) + 7H_2O(l) + 18OH^-(aq) = In_2O_3(s) + 2GaO_3^{3-}(aq) + 4PO_4^{3-}(aq) + 16H_2(g)$

In the present works, the results of all pn$^+$-InGaP$_2$/Pt photoelectrodes were consistent with these two pathways in both acidic and alkaline aqueous electrolytes. Based on the XPS analyses, we found no In^0 formation confirming the kinetic stabilization of cathodic corrosion by Pt catalyst.

In 1.0 M H_2SO_4(aq), all pn$^+$-InGaP$_2$/Pt photocathodes exhibited a linear dissolution rate for InGaP$_2$ ranging from 0.4-0.7 nm h^{-1}, regardless of applied E and crystal orientation of GaAs substrates. Based on the limited thickness of emitter layer (25 nm), the InGaP$_2$ corrosion did not depend on the doping type. This measured dissolution rates were similar to those of p-InGaP$_2$/Pt electrodes (0.3 nm h^{-1}). The continuous dissolution of InGaP$_2$ may also give rise to variation in the initially measured J-E behavior of pn+-InGaP$_2$/Pt photoelectrodes prior to CA testing, depending on how much InGaP$_2$ was removed upon contact with electrolyte.

In alkaline electrolytes, no dissolution of In ions was found under all conditions, implying that the pn$^+$-InGaP$_2$ layer did not undergo continuous dissolution as in acidic solution. However, surface passivation by InO$_x$ was only found for the InGaP$_2$ layer grown on GaAs (110) substrates.

One significant consequence of the InGaP$_2$ dissolution is the thinning of n$^+$-InGaP$_2$ emitter layer, causing gradual decreases of E_{oc} from > +0.9 V vs. RHE down to +0.5-0.6 V vs. RHE. Based on the thickness of n$^+$-emitter layer (25 nm) used in this study, the total time required for a complete removal of the emitter layer is estimated as ~50 h, assuming an averaged dissolution rate of 0.5 nm h^{-1}. Our observed evolution in the J-E behavior of pn$^+$-InGaP$_2$/Pt photoelectrodes as a function of time were consistent with this claim. Similar trends in the changes of the J-E behaviors over time were also observed at varied applied E and different substrate orientations. These results collectively showed that the physical instability of pn$^+$-InGaP$_2$/Pt electrodes during the HER conditions in acidic solution limited the stability of its J-E behavior over long term.

Besides the InGaP$_2$ dissolution, we also observed substantial As dissolution into electrolytes indicating corrosion of GaAs substrates. At pH 0, a much higher amount of GaAs dissolution was seen at E=+0.5 V vs. RHE compared with that under E=0 V vs. RHE, for electrodes grown on both

GaAs (111B) and (110) substrates. The GaAs dissolution suggested the presence of structural defects within the upper epi-layers that enabled penetration of electrolyte to reach the underlying GaAs. As the anodic corrosion of p^+-GaAs is potential-dependent, holding the back-contact potential for the electrode at a more negative E can cathodically protect the GaAs from such anodic corrosion.[60] However, even at E=0 V vs. RHE at pH=0, we still observed slow and continuous dissolution (0.03-0.2 nm h^{-1}) of GaAs over long terms, showing the GaAs dissolution was not completely mitigated for both GaAs substrates. Besides, at E=+0.5 V vs. RHE, the dissolution of GaAs did not increase linearly with time. Instead, the dissolution of GaAs was slow at the beginning and then increased dramatically after 50 h. These results suggested that the structural defects that allowed the GaAs/electrolyte contact were gradually developing during the CA, partially owing to the gradual dissolution of $InGaP_2$. Consequently, the removal of a substantial amount of GaAs from underneath damaged the structural integrity of the multi-layered GaAs/$InGaP_2$ stack, leading to severe delaminating and cracking of the light-absorbing upper layer.

In alkaline electrolyte, similar GaAs dissolution was also observed for the same pn^+-$InGaP_2$/Pt electrodes at E=+0.45 V vs. RHE. These results again verified direct contact between GaAs and electrolyte. However, the accumulative amount of GaAs that dissolved within similar time periods was much smaller compared with those in acidic solution. The slower GaAs corrosion was likely attributed to the insolubility of the upper $InGaP_2$ layer in KOH which reduced the GaAs/electrolyte contact. Moreover, the samples grown on two different substrates exhibited similar corrosion rates of GaAs, suggesting the structural defects in the upper epi-layers were universally present and the GaAs corrosion did not display strong dependence on crystal orientation. In comparison, at E=+0.15 V VS. RHE, the pn^+-$InGaP_2$/Pt (GaAs 111B) electrode exhibited a much smaller and limited amount of GaAs corroded, again showing that the GaAs substrate was cathodically protected at more negative E.

5.4.2 Physical stability vs. electrochemical stability: importance of structural integrity

When held at a positive E close to the maximum power point of the initial J-E behavior (+0.45 V vs. RHE in KOH and +0.5 V vs. RHE in H_2SO_4), the pn$^+$-InGaP$_2$/Pt photoelectrodes started from a high J of > 10 mA cm^{-2}, decreased to a much lower values during the first 10-20 h and stabilized afterwards in both acidic and alkaline electrolytes. When held at a more negative E (+0.15 V vs. RHE in KOH and 0 V vs. RHE in H_2SO_4), the pn$^+$-InGaP$_2$/Pt photoelectrodes displayed a much more stable J-t profiles while operating at much higher J closer to J_{sc}. As the anodic corrosion of GaAs is electrochemical, occurrence of GaAs corrosion can also offset the photocurrent from the InGaP$_2$ layer, thus resulting in a reduction of the apparent cathodic J.

At both pH 0 and pH 14, the evolution in the J-t profiles of pn$^+$-InGaP$_2$/Pt photoelectrodes was consistent with the changes in their J-E behaviors as a function of time. At more positive E, the continuously decreased J during CA is mainly due to the cathodic shift of the J-E behaviors as well as the gradually lowered E_{oc} over time. As a result, the measured J-t profiles were sensitive to how much the J-E behaviors shifted positively. Notably, despite the shifts, both fill factor and general shape in the measured J-E behaviors remained similar throughout the CA at pH=0, manifesting preserved interfacial properties of charge separation and catalytic kinetics.

Therefore, all pn$^+$-InGaP$_2$/Pt photoelectrodes exhibited unstable J-E behaviors during the CA, although a stable J-t behaviors might be obtainable by applying a more negative E. Combined with previous discussion, the changes in the J-E behavior were closely correlated with (1) continuous dissolution of InGaP$_2$ in acidic solution, (2) delamination and cracking of upper epi-layer via corrosion of underlying GaAs, and (3) surface structural changes of InGaP$_2$ layer in alkaline electrolyte. Notably, we found the dissolution of InGaP$_2$ did not depend on the applied E, while the GaAs corrosion was mitigated at more negative E. These results showed that the dissolution of InGaP$_2$ layer was driven by its thermodynamic instability under the HER conditions (E_{surf}~-0.1 V vs. RHE), similar to our previous observation for p-InGaP$_2$/Pt electrodes. Therefore, despite a stable J-t profile obtained by at more negative E, the pn$^+$-InGaP$_2$/Pt photoelectrode was still physically dissolving in acidic solution or exhibited structural instability in alkaline solution. In this regard, the physical stability and electrochemical stability of pn^+-$InGaP_2$/Pt photoelectrode are mutually dependent but need to be evaluated separately.

Furthermore, we identified that the corrosion of underlying GaAs substrates can damage the structural integrity of the whole photoelectrode comprised of multiple layers of different III-V semiconductors. We observed such corrosion of GaAs in acidic media caused undercutting of the upper light-absorbing layer of $InGaP_2$, which could in turn impact the resulting J-E behaviors. This observation indicated that the instability of photoelectrode's performance was partially attributed to structural instability by the substrate, instead of direct corrosion from the light-absorbing layer. This finding emphasized that more attention should be paid to enhancing the structural integrity, and minimizing the structural defects as well as the substrate/electrolyte. However, in our previous works on p-$InGaP_2$, we found no leaching of As ions into either acidic or alkaline electrolyte when the electrodes were held at E=0 V vs. RHE. However, we still observed slow corrosion of GaAs (0.03-0.2 nm h^{-1}) from pn^+-$InGaP_2$/Pt electrodes under the same E in acidic electrolytes. We speculate that such difference in GaAs corrosion arise from fabrication of $InGaP_2$ epi-layers in different reactors, resulting in different compactness and pre-defined structures inherent in the deposited materials.

5.4.3 Failure modes of pn^+-$InGaP_2$/Pt photoelectrodes

Overall, the present works revealed three important failure modes of pn^+-$InGaP_2$/Pt photoelectrodes under the HER conditions, which caused both physical and electrochemical instability during prolonged operation (Scheme 5.1).

Firstly, the slow but continuous dissolution of $InGaP_2$ in acidic electrolyte caused gradual thinning of the n+-doped emitter layer, resulting in the lowered E_{oc} over time. Such slow etching of n^+-$InGaP_2$ layer turned the buried junction of the pn^+-$InGaP_2$ with a E_{oc}>+0.8 V vs. RHE into a p-$InGaP_2$/electrolyte junction with a E_{oc}~+0.5 V vs. RHE. Based on an etching rate of 0.5 nm h^{-1} and a total thickness of 25 nm for the n^+-$InGaP_2$ layer, the time required for such a transition is estimated as 50 h which is also consistent with experimental observations. This failure mode occurred in a similar manner for $InGaP_2$ grown on both GaAs (111B) and (110) substrates.

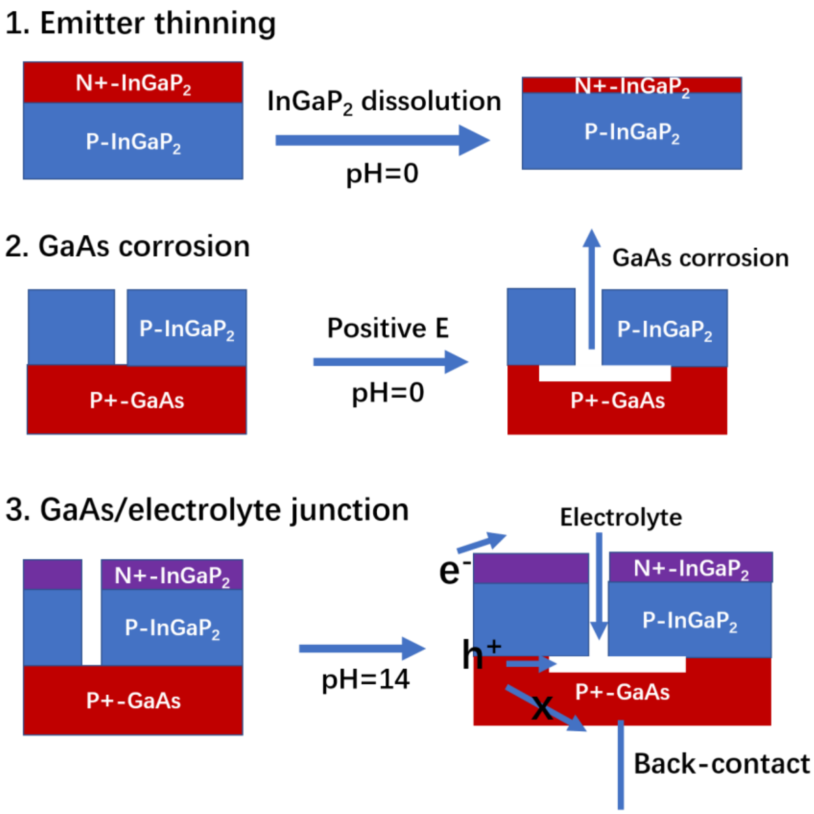

Scheme 5.1 Three different failure modes of pn$^+$-InGaP$_2$/p$^+$-GaAs photocathodes (with Pt catalyst) in both acidic and alkaline electrolytes: (1) slow and continuous dissolution of InGaP$_2$ at pH 0 causes gradual thinning of the n$^+$-InGaP$_2$ layer (25 nm), resulting in decreased E_{oc} over time; (2) active corrosion and dissolution of the GaAs substrate when the whole electrode is held at positive E; (3) formation of GaAs/electrolyte junction due to the inherent defects in the upper epilayers, pins the resulting E_{oc} of the whole photoelectrode by limiting the collection of majority carriers at back-contact.

Secondly, the structural defects present in the upper epi-layers allowed penetration of electrolytes to drive the corrosion of the underlying GaAs substrates, especially at positive E close to the maximum power point of the photoelectrodes. In acidic electrolyte, such corrosion of underlying GaAs was found to be developing with time, resulting in removal of substantial amounts of GaAs (hundreds of nm) after long periods. Importantly, the dissolution of GaAs damaged the structural integrity of the whole photoelectrode, leading to delamination, cracking and collapse of the upper layers. It is likely these structural damages to InGaP$_2$ light-absorber will eventually account for a decrease in J_{sc}. Similar failure mechanism of solar water-splitting cell based on multi-layered III-V semiconductors was also recently reported by Chorkendorff and coworkers.[214]

Lastly, substantial degradation in the J-E behavior of the pn$^+$-InGaP$_2$/Pt photoelectrode was also observed in 1.0 KOH(aq), despite much less dissolution of GaAs compared with the conditions of pH 0. Different from acidic solution, the InGaP$_2$ light-absorber remained nearly insoluble in basic media for long periods. Degradation in both J-t and J-E behaviors was consistently observed for the InGaP$_2$ layers grown on two different GaAs substrates. InO$_x$ formation was only seen for the InGaP$_2$ based on the GaAs (110) substrate, which cannot explain the performance degradation for the InGaP$_2$ on the GaAs (111B) substrate. A common observation for all tested samples is the apparent surface roughening and cracking of the top InGaP$_2$ layer after prolonged testing, corresponding to the slight dissolution of GaAs substrate via the inherent defects within the upper epilayers. Collectively, these results shed light on a new mechanism of performance degradation by forming the GaAs/electrolyte junction. Previous works identified that the E_{oc} of the p$^+$-GaAs/KOH junction in the dark was ~+0.5 V vs. RHE.[60] Thus, at E > +0.5 V vs. RHE, the anodic J of the GaAs/electrolyte junction will offset the cathodic J of the pn$^+$-InGaP$_2$, thus pinning the average E_{oc} of the whole electrode. In other words, the direct GaAs/electrolyte contact causes an inefficient collection of majority carriers at the electrode back-contact, especially at positive E > +0.5 V vs. RHE. As a result, the measured J-E behavior of the electrode is substantially compromised despite the limited amount of GaAs dissolution observed. Notably, this additional failure mode by the epilayer photoelectrode is also distinct from those of single-crystal photoelectrodes where the transport of majority carriers from the depletion region into the back-contact is fully isolated from the electrolyte.

Altogether these results revealed the significance of substrate (GaAs) stability towards both physical and electrochemical stability of the whole photoelectrode, which were not emphasized in previous works. We demonstrated the importance of systematically correlating the electrode dissolution with the changes in the J-E behavior, to reveal factors underlying the failure of photoelectrodes. Factors beyond the dissolution of light-absorbing materials, such as surface cracking under electrolyte environment also contributed to the degradation in the PEC performance. Further efforts should be paid to carefully improving the fabrication process during deposition of multi-layered device based on III-V semiconductors, with the goal of decreasing the inherent defects and enhancing the structural integrity. Stabilization and passivation strategies should be targeted at mitigating the continuous dissolution of $InGaP_2$ in acidic electrolyte while minimizing its structural changes in alkaline electrolyte.

5.5 Conclusion

We have identified three important failure modes of pn^+-$InGaP_2$/Pt photocathodes for long-term HER from acidic and alkaline aqueous electrolytes. In acidic solution, a slow and continuous dissolution of $InGaP_2$ caused a gradual etching of n^+-doped layer, which further led to a decrease in E_{oc} over time. When held at positive potentials, the underlying GaAs substrates underwent anodic corrosion resulting in cracking and delamination of the upper epi-layer, thus damaging structural integrity of the whole electrode. Occurrence of such GaAs corrosion also indicated the presence of structural defects inherent in the upper epi-layers during material fabrication. In alkaline electrolyte, although the $InGaP_2$ layer remained nearly physically insoluble, substantial degradation in the J-E performance was still consistently observed owing to the formation of GaAs/electrolyte junction. We emphasized that further efforts needs to be paid to reducing the structural defects and enhancing the structural integrity for solar fuel devices based on multi-layered semiconductors.

5.6 Supplementary figures

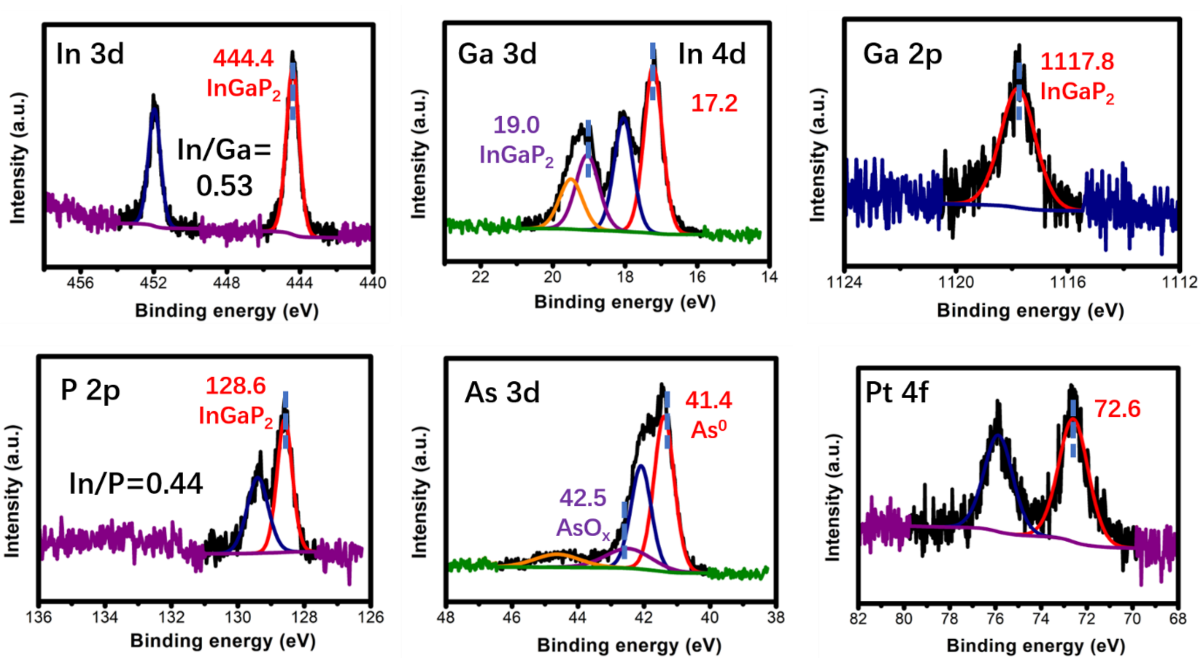

Figure S 5.1 XPS surface analyses of the pn$^+$-InGaP$_2$/Pt photocathode (GaAs 111B) after the CA in Figure 1 in 1.0 M H_2SO_4(aq) for 139 h. The results showed the formation of surficial As^0 due to exposure of GaAs to electrolyte.

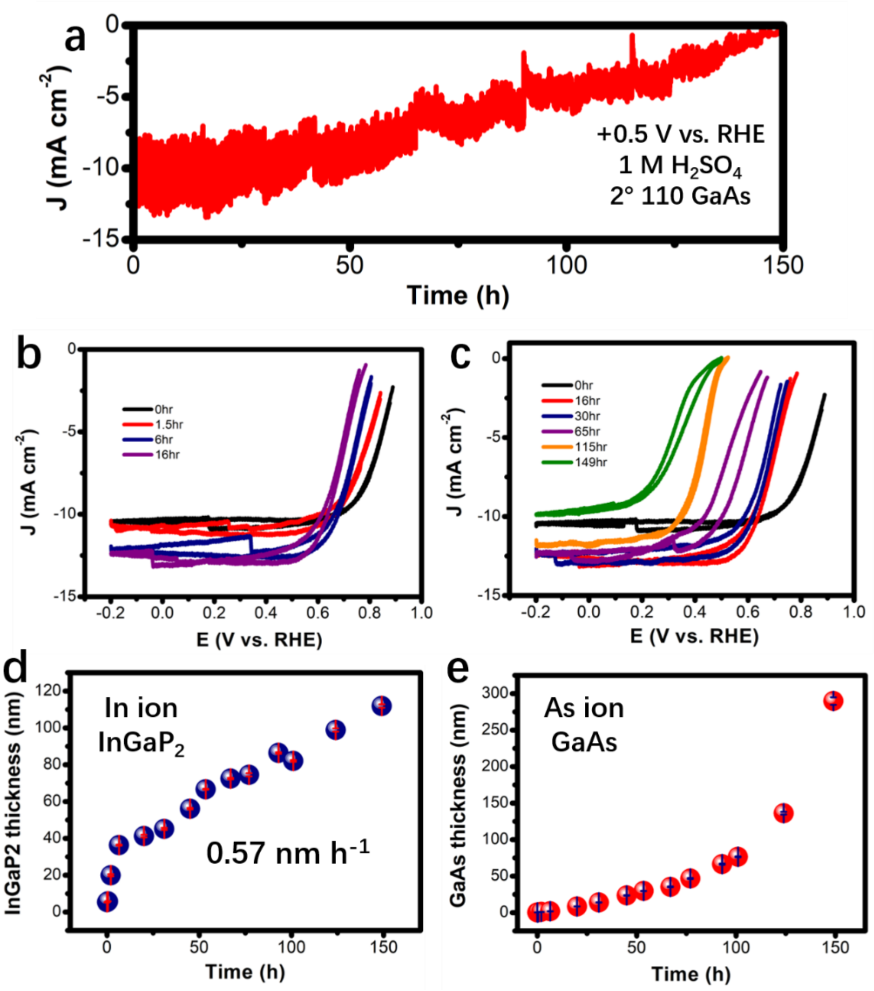

Figure S 5.2 (a) CA of a pn$^+$-InGaP$_2$/Pt photocathode in 1.0 M H_2SO_4(aq) held at +0.5 V vs. RHE under 1-sun illumination; the pn$^+$-InGaP$_2$ epilayer was grown on a p$^+$-GaAs (110) substrate by a 2° miscut. (b-c) Comparison of the J-E behavior of the pn$^+$-InGaP$_2$/Pt photocathode during the CA in (a) during (b) the first 16 h and (c) the whole 149 h. (d-e) Corrosion thicknesses of (d) InGaP$_2$ and (c) GaAs as a function of time, based on the concentrations of In and As ions dissolved in electrolyte measured by ICP-MS.

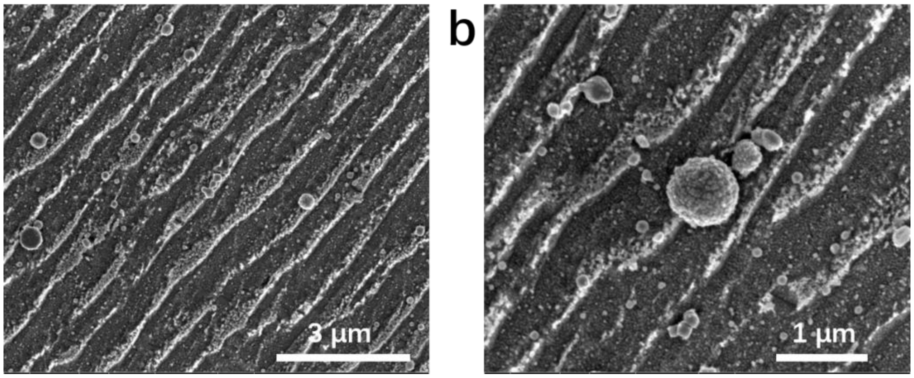

Figure S 5.3 SEM images of the pn$^+$-InGaP$_2$/Pt photocathode after test in Figure 1a in 1.0 M H_2SO_4(aq).

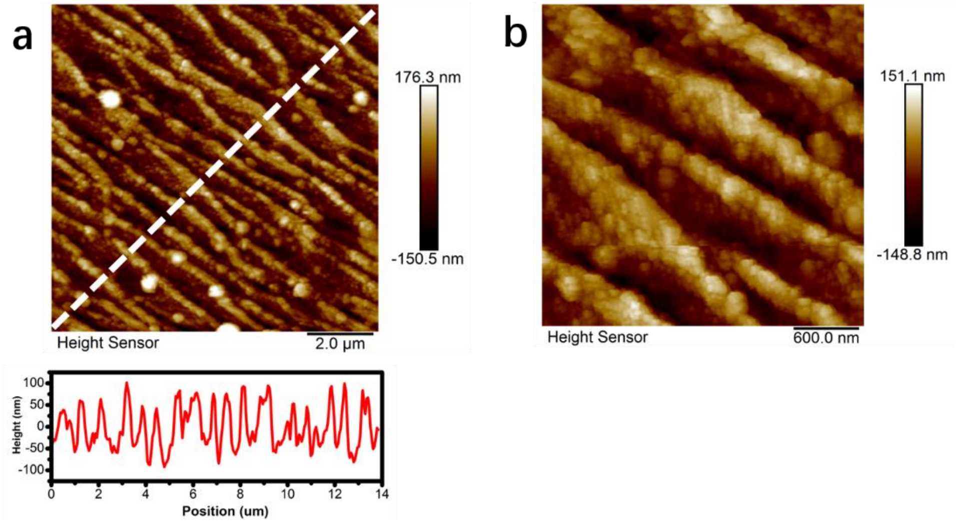

Figure S 5.4 AFM images of the pn$^+$-InGaP$_2$/Pt photocathode after test in Figure 1a in 1.0 M H_2SO_4(aq).

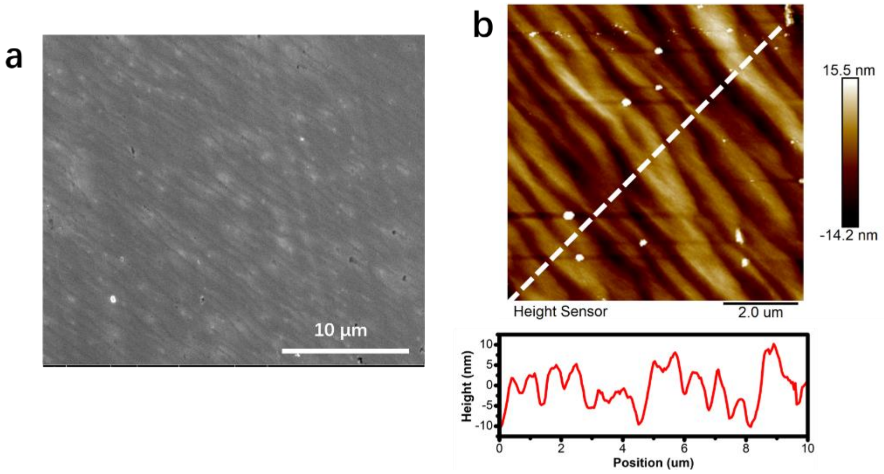

Figure S 5.5 (a) SEM image and (b) AFM image of an as-received pn$^+$-InGaP$_2$ sample grown on a p$^+$-GaAs (110) substrate by a 2° miscut.

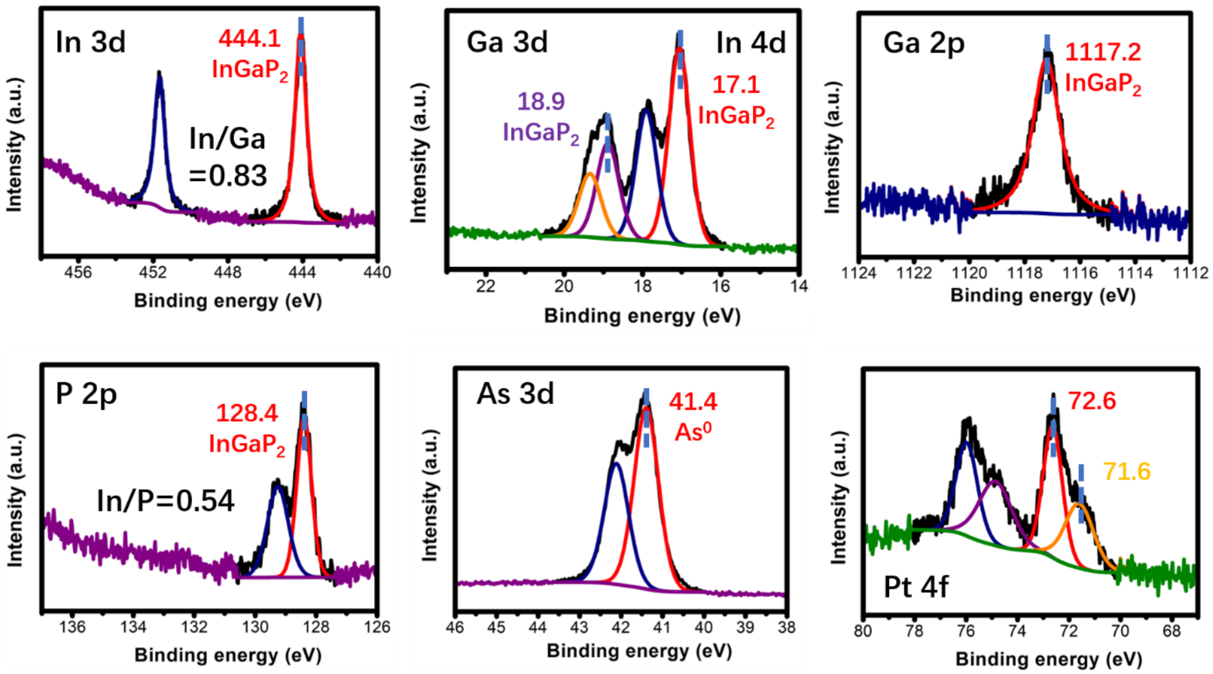

Figure S 5.6 XPS surface analyses of the pn$^+$-InGaP$_2$/Pt photocathode after the CA in Figure S 5.2 in 1.0 M H_2SO_4(aq). As^0 was observed indicating the anodic oxidation of underlying GaAs substrate.

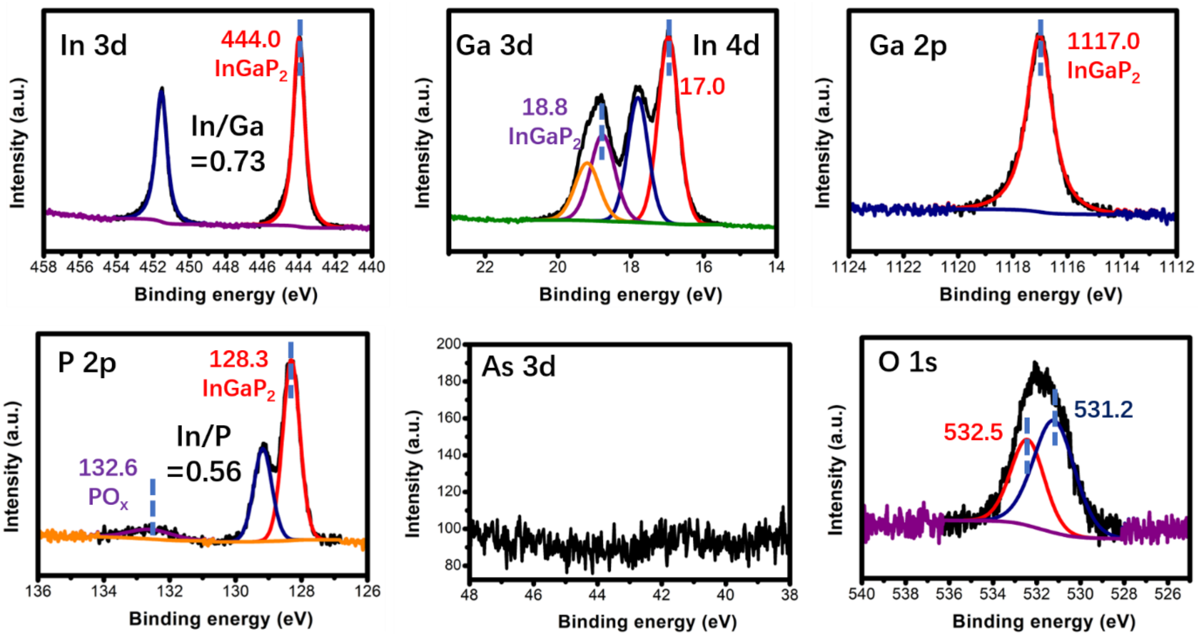

Figure S 5.7 XPS surface analyses of a pn$^+$-InGaP$_2$ sample without exposure to any electrochemical condition.

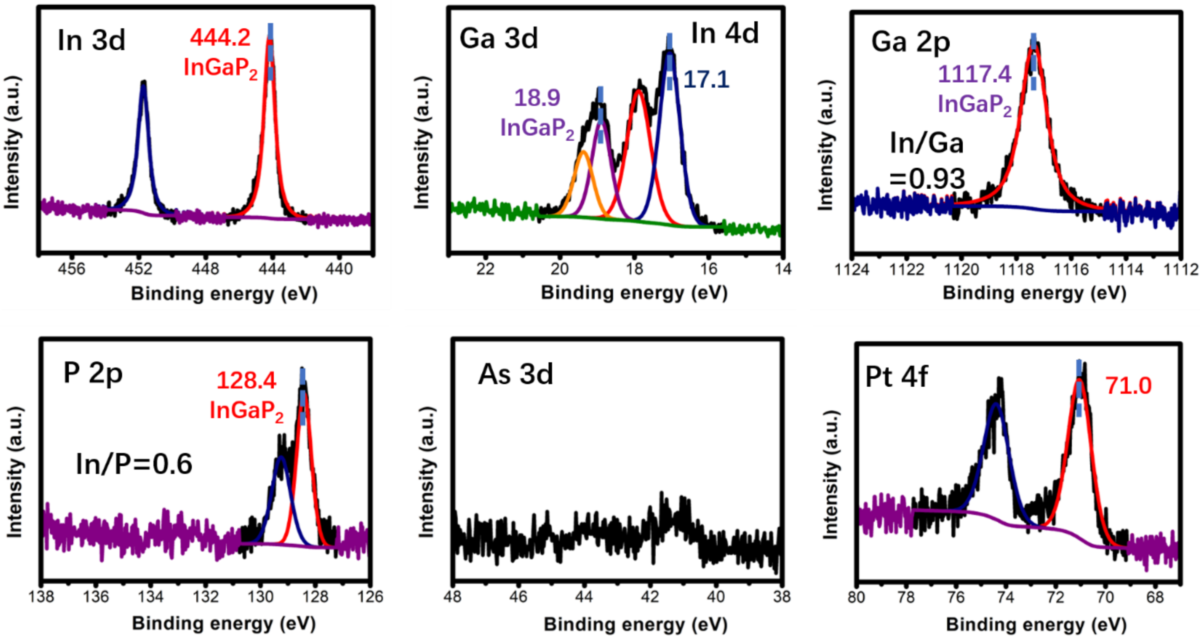

Figure S 5.8 XPS surface analyses of the pn$^+$-InGaP$_2$/Pt (GaAs 111B) photocathode after the CA in Figure 6 in 1.0 M KOH(aq) for 70 h.

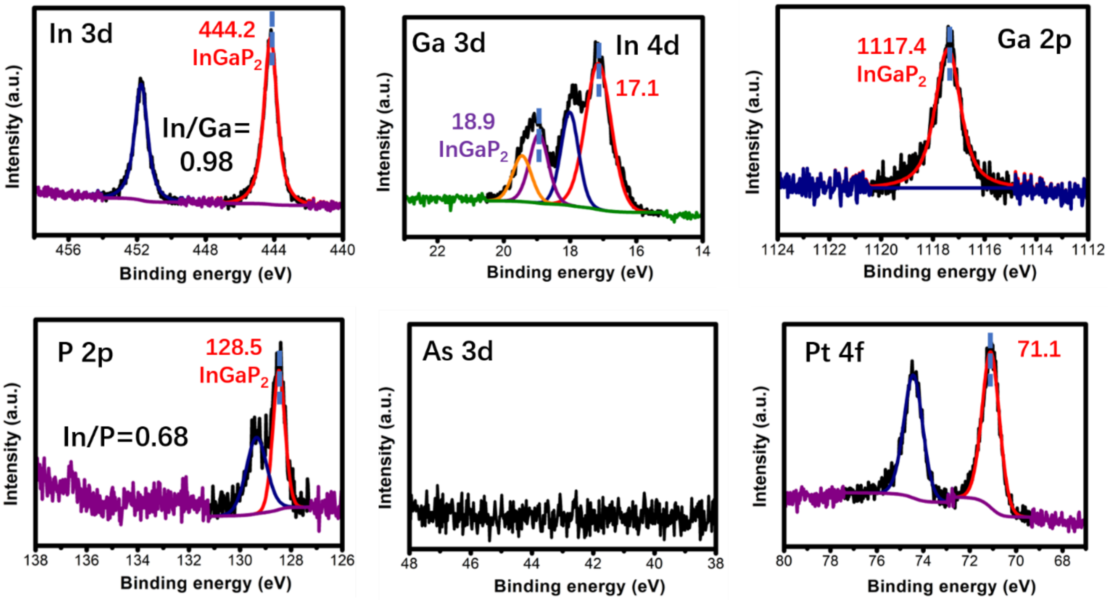

Figure S 5.9 XPS surface analyses of the pn$^+$-InGaP$_2$/Pt (GaAs 111B) photocathode after the CA in Figure 7 in 1.0 M KOH(aq) for 117 h.

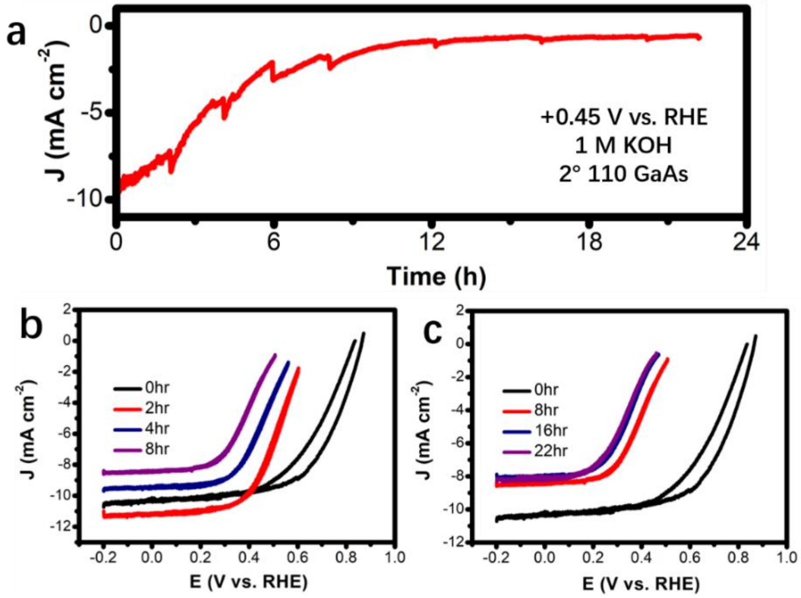

Figure S 5.10 (a) CA of a pn$^+$-InGaP$_2$/Pt photocathode in 1.0 M KOH(aq) held at +0.45 V vs. RHE under 1-sun illumination; the pn$^+$-InGaP$_2$ epilayer was grown on a p$^+$-GaAs (110) substrate by a 2° miscut. (b-c) Comparison of the J-E behavior of the pn$^+$-InGaP$_2$/Pt photocathode during the CA in (a) during (b) the first 8 h and (c) the whole 22 h.

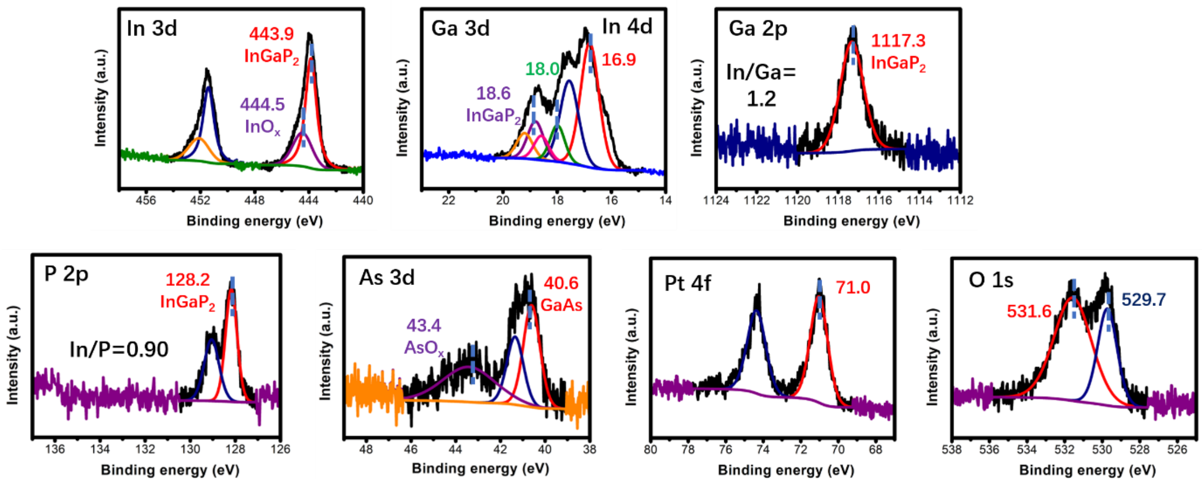

Figure S 5.11 XPS surface analyses of the pn$^+$-InGaP$_2$/Pt photocathode (GaAs 110) after the CA in Figure S 5.10 in 1.0 M KOH(aq) for 22 h.

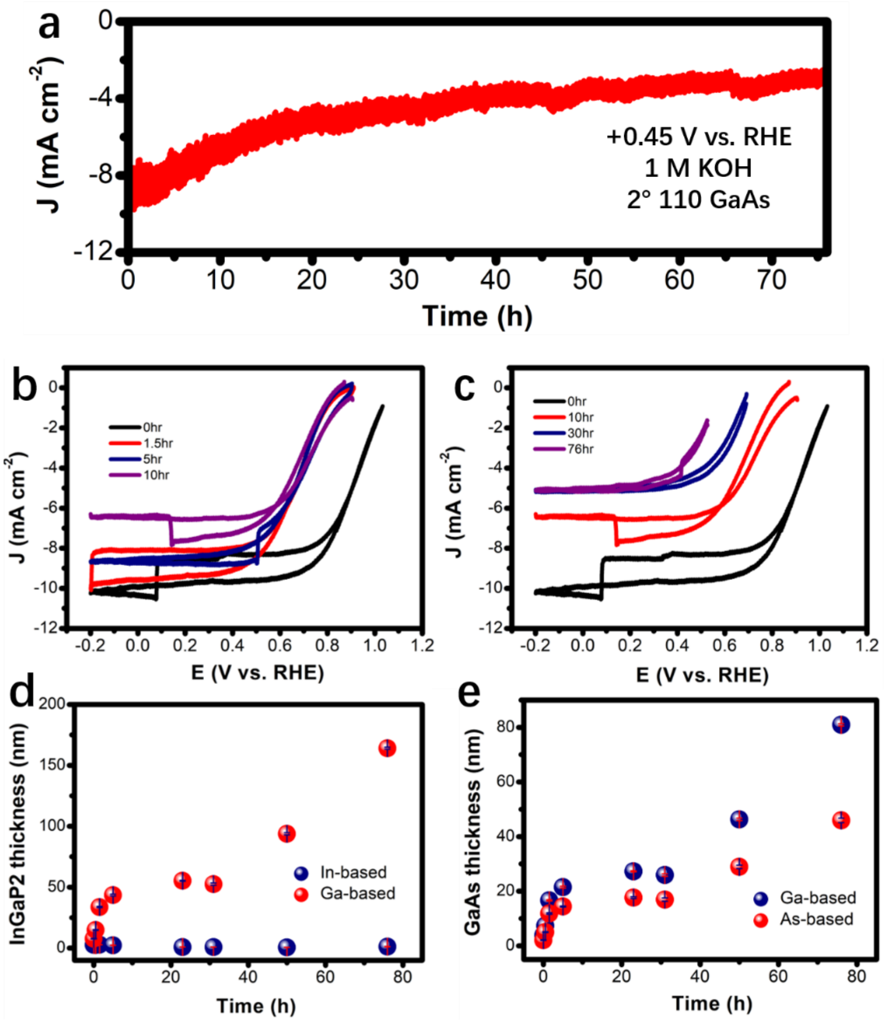

Figure S 5.12 (a) CA of a pn$^+$-InGaP$_2$/Pt photocathode in 1.0 M KOH(aq) held at +0.45 V vs. RHE under 1-sun illumination; the pn$^+$-InGaP$_2$ epilayer was grown on a p$^+$-GaAs (110) substrate by a 2° miscut. (b-c) Comparison of the J-E behavior of the pn$^+$-InGaP$_2$/Pt photocathode during the CA in (a) during (b) the first 10 h and (c) the whole 76 h. (d-e) Corrosion thicknesses of (d) InGaP$_2$ and (c) GaAs as a function of time, based on the concentrations of In, Ga and As ions dissolved in electrolyte measured by ICP-MS.

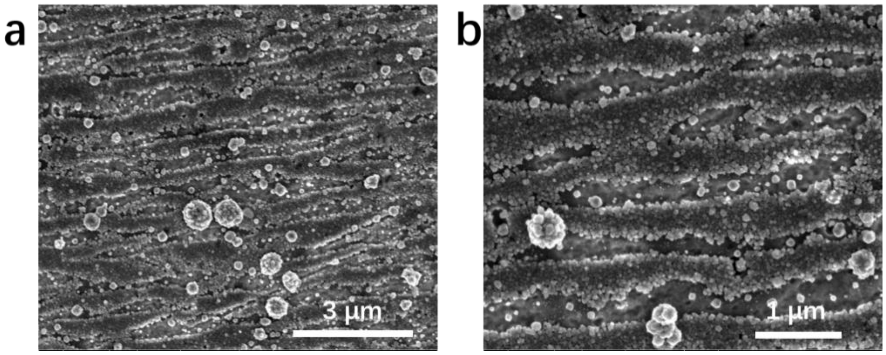

Figure S 5.13 SEM images of the pn$^+$-InGaP$_2$/Pt photocathode (GaAs 110) after test in Figure S 5.12 in 1.0 M KOH(aq).

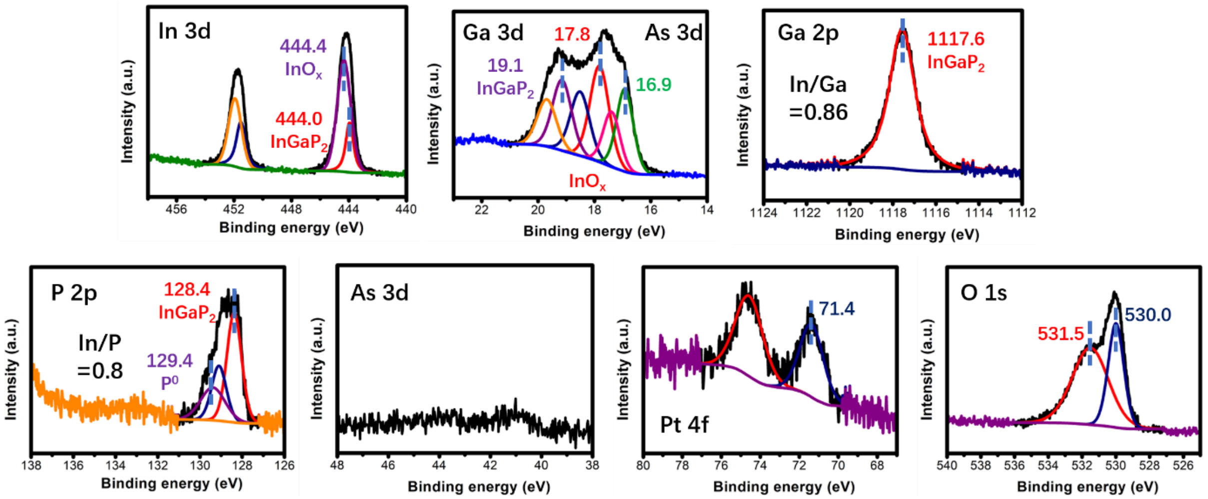

Figure S 5.14 XPS surface analyses of the pn$^+$-InGaP$_2$/Pt photocathode (GaAs 110) after the CA in Figure S 5.12 in 1.0 M KOH(aq) for 76 h. The results showed the formation of surficial InO$_x$ and P^0.

Chapter 6

6 ISOTOPICALLY SELECTIVE QUANTIFICATION BY UPLC-MS OF AQUEOUS AMMONIA AT SUBMICROMOLAR CONCENTRATIONS USING DANSYL CHLORIDE DERIVATIZATION

Reproduced with permission from:[104] Yu, W.; Lewis, N. S.; Gray, H. B.; Dalleska, N. F. Isotopically Selective Quantification by UPLC-MS of Aqueous Ammonia at Submicromolar Concentrations Using Dansyl Chloride Derivatization. *ACS Energy Letters* **2020**, 1532–1536. https://doi.org/10.1021/acsenergylett.0c00496.

6.1 Introduction

Ammonia (NH_3) is essential for food production,[6] and is commercially synthesized from nitrogen (N_2) and hydrogen (H_2) using the Haber-Bosch process.[105] Enormous amounts of ammonia are made every year in a reaction that requires high temperatures and pressures, with the Haber-Bosch accounting for ~1.6 % of total annual global energy consumption. Electrocatalysts are also being explored to convert in an environmentally friendly manner N_2 to NH_3 at ambient temperature and pressure.[108,215,216]

Conversion of N_2 to NH_3 involves 6-electron transfers compared with the more facile 2-electron hydrogen-evolution reaction (HER) that occurs in parallel with N_2 reduction.[217] Hence electrocatalysts for N_2 reduction to ammonia must be active and selective.[106] Several recent reports have described electrocatalysts that exhibit very high faradaic efficiencies for N_2 reduction.[216,218–220] Rigorous controls would insure that the detected NH_3 is produced by electrochemical reduction of N_2 rather than from ambient contamination sources. Increases in ammonia concentrations in electrolytes can be produced by corrosion/decomposition of materials in use, by ammonia impurities in ambient air or in purged N_2 gas (both $^{14}N_2$/$^{15}N_2$), and by other causes.[112,118,221–225] Therefore, special care has to be taken in experimental design to identify and exclude these contamination sources. Consequently ^{15}N labeling is an essential tool to verify the activities of putative electrocatalysts for N_2 reduction.[226,227]

Spectrophotometric/colorimetric techniques for ammonia detection include indophenol blue, salicylate, and Nessler reagent methods.[6] These spectrophotometric methods have disadvantages, including instability of derivatives, use of toxic chemicals, the interfering effect of metal ions/solvents, and the requirement of considerable bench time. Each of these factors presents major challenges to determining the ammonia concentration accurately and thus increases the chance of introducing additional analytical errors, especially at low concentrations. Recently, the use of ion chromatography (IC) to quantify ammonia concentrations has become increasingly popular in the field of N_2-electroreduction.[228,229] Although the IC method is powerful for accurately quantifying the total concentration of ammonia, challenges nevertheless persist in isotopically distinguishing $^{14}NH_3$ from $^{15}NH_3$. Even in an advanced, coupled ion chromatography-mass spectrometry (IC-MS) system, quantification of ammonia by evaluating the $^{14}NH_3/^{15}NH_3$ ratio is difficult because $^{15}NH_4^+$ and H_3O^+ share the same nominal m/z. For aqueous solutions, H_2O produces high background signals in MS spectra, precluding robust quantification of the $^{15}NH_3$ signal at the levels of interest. A frequency-selective nuclear magnetic resonance (NMR) technique has been reported to resolve $^{14}NH_3$ from $^{15}NH_3$ based on their distinctive chemical shifts.[118] However, analyzing NH_4^+ concentrations in the 5-10 μM range with a 600 MHz NMR spectrometer requires *acquisition* times from 12 to 22 min to produce acceptable signal-to-noise and up to 1 h to reach 1 μM with a 900 MHz NMR spectrometer.[118,119] Moreover, different solvents may alter the shapes of NMR peaks, which may introduce additional errors at low concentrations.

We report an analytical method that uses a dansyl chloride derivatization reaction to detect very low concentrations of ammonia. The ammonia derivatives were subsequently analyzed by ultrahigh performance liquid chromatography-mass spectrometry (UPLC-MS). The ammonia derivatization process is performed by simply mixing solutions of dansyl chloride and aqueous ammonium (NH_4^+) solution at optimal pH and room temperature (RT). The presence of ammonia and its heavy isotopologue can be distinguished and quantified by their MS peak areas at m/z=251.0854 (^{14}N) and m/z=252.0825 (^{15}N), respectively. The calibration curves are linear in the ammonia concentration range of 0.6-43.5 µM for both $^{14}NH_3$ and $^{15}NH_3$. As shown in Figure 6.1, using this analytical method, a high signal/noise (S/N) ratio of ~ 12 was achieved for a derivatized sample of only 0.6 µM $^{15}NH_3$ with a short elution time of ~3.1 min. Further, the method is demonstrated to allow monitoring of ambient ammonia ($^{14}NH_3$) in a sensitive fashion whereas the analysis of $^{15}NH_3$ is essentially immune to ambient contamination. This sensitive method for NH_3 analysis should allow more accurate determinations of faradaic efficiencies for electrochemical N_2 reduction and will facilitate large-scale screening and directed-evolution approaches to the development of efficient catalysts. Users have the option to easily tune the working range to higher concentrations by reducing the sample aliquot volume employed.

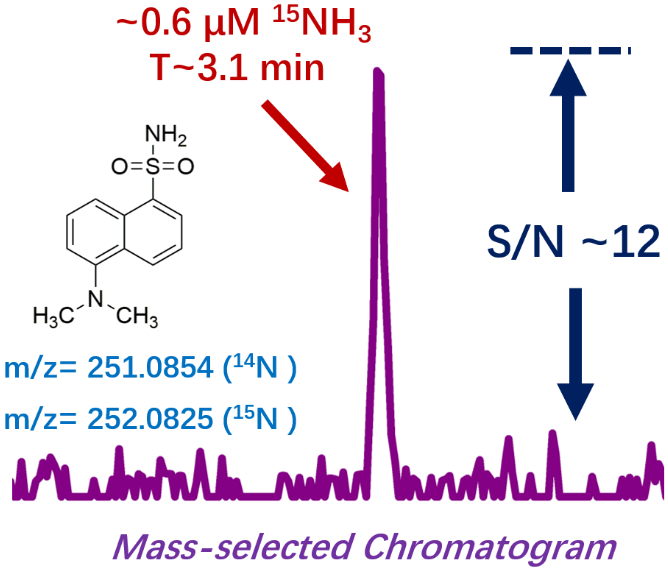

Figure 6.1. Representative mass-selected chromatogram for a 0.6-µM $^{15}NH_3$ sample derivatized by dansyl chloride, demonstrating a high S/N ratio of ~12 and a short elution time of ~3.1 min. The $^{14}N/^{15}N$-labelled ammonia derivatization products displayed distinct m/z of 251.0854 and 252.0825, respectively.

6.2 Results and discussion

Dansyl chloride is widely used in derivatization of amino acids for fluorescence and mass spectrometry analysis. The reaction of dansyl chloride with ammonia forms DNS-NH_2 (Equation 6.1). A solution of 50 mM H_2SO_4(aq) was used to dissolve NH_4Cl, and a stock solution of dansyl chloride (~290 μM) was prepared separately in acetonitrile. A relatively high concentration of dansyl chloride was used to consume all ammonia in the desired concentration range (0.6-43.5 μM). In addition, a side reaction of dansyl chloride with water was identified (Figure S 6.1). Notably, the hydrolysis product (DNS-OH) has a very similar molecular mass (m/z=252.0694) to DNS-$^{15}NH_2$ (m/z=252.0825).

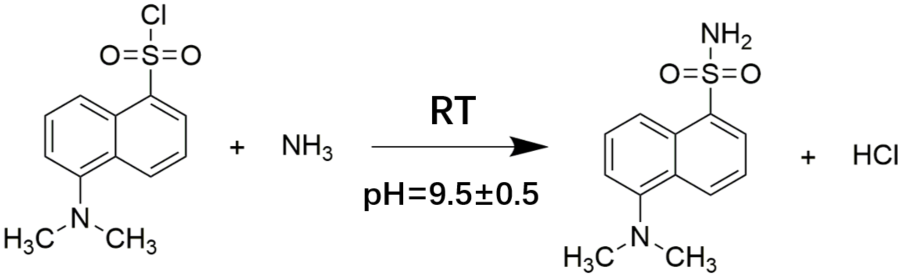

Equation 6.1 Derivatization reaction of dansyl chloride with ammonia forms DNS-NH_2; RT denotes room temperature

Despite their similar masses, the initial UPLC step separates the DNS-OH and DNS-NH_3 products by eluting them at substantially different times out from the column. As shown in Figure S 6.2a, the mass-selected chromatographs for DNS-OH and DNS-NH_3 displayed two distinct peaks (1.8 and 3.1 min, respectively). The peaks for DNS-NH_3 products labelled with ^{14}N or ^{15}N appeared at the same times in their respective mass-selective chromatographs (Figure S 6.2b). The subsequent MS step distinguished DNS-$^{14}NH_2$ from DNS-$^{15}NH_2$. As seen in Figure S 6.2c-d, samples derivatized with ^{14}N or ^{15}N exhibited distinctive MS peaks in the integrated mass spectra at ~3.1 min, allowing quantification using the respective MS peak areas. As expected, the integrated mass spectra at ~1.8 min displayed a distinctive peak at m/z=252.0694, which is attributable to DNS-OH (Figure

S 6.2e). Due to the UPLC separation, the presence of hydrolysis products did not influence the quantification of ^{14}N- or ^{15}N-derivatizations, based on their different elution times. Moreover, the more abundant hydrolysis product in source charge competition is thus avoided.

Two major factors were identified and optimized for the derivatization reaction conditions: pH and temperature (Figure S 6.3). Consistent with prior results, by adjusting the volume of added Na_2CO_3 stock solution (2 g/100 mL), the optimal pH value for the derivatization reaction was found to be ~9.5±0.5 (determined by pH test paper).[230] As shown in Figure S 6.3a, the optimal volume of the Na_2CO_3 stock solution was 0.3 mL, which produced the highest MS peak area for a given ammonia sample (~10 μM). Lower or higher pH values produced decreases in MS peak area, indicating that the derivatization reaction is governed by a pH equilibrium. Dansyl chloride and ammonia reacted readily at room temperature and required no heating. As shown in Figure S 6.3b, the MS peak areas for the same aqueous ammonia sample decreased by ~78 % after brief (10 min) heating at 70 °C. Clearly, the lack of a heating requirement simplified the derivatization procedures, but also indicated that these ammonia derivatives are heat-sensitive.

As shown in Figure 6.2, standard ammonia samples were prepared to establish respective calibration curves for DNS-$^{14}NH_2$ and DNS-$^{15}NH_2$, based on the synergy between the UPLC separation and the accurate mass resolution. The detected ^{14}N and ^{15}N concentrations were linear ($R^2 \geq 0.995$) for concentrations between 0.6 μM and >40 μM. The relatively large slopes for both calibration curves allowed for sensitive concentration determinations. The ^{14}N data had a higher intercept (53.69) than the ^{15}N data (-4.28), perhaps due to the presence of trace ammonia ($^{14}NH_3$) in the matrix solution of 50 mM H_2SO_4(aq). The concentration of "background" ammonia for these samples was ~1.5 μM based on the slope of the ^{14}N calibration curve.

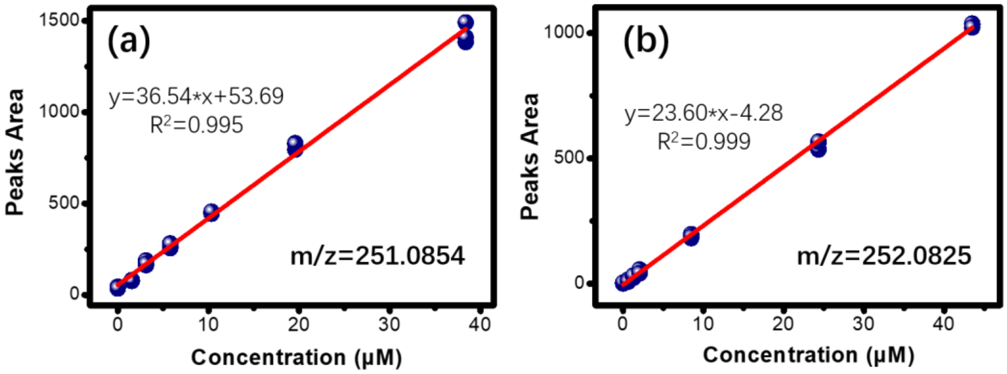

Figure 6.2 Calibration curves for derivatized DNS-NH_2 products labelled with (a) ^{14}N (m/z=251.0854) and (b) ^{15}N (m/z=252.0825). Injection volumes were 3 μL for all samples; triplicate measurements were made for each standard sample.

The stability of derivatized DNS-NH_2 was investigated by comparing MS peak areas between fresh and 14-day-old batches of standard ammonia samples. The samples were analyzed over the same run (Figure 6.3a and Figure S 6.4a). The ^{14}N- and ^{15}N-ammonia derivatives exhibited mutually similar MS peak-area responses between the fresh and old batches. Hence, the ^{14}N and ^{15}N calibration curves remained linear ($R^2 \geq 0.995$) for quantitative analysis even after 14 days (Table S 6.1). The stability of these ammonia derivatives over time strengthens the resulting measurement reliability and represents a substantial advantage relative to conventional colorimetric methods. As seen in Figure S 6.4b, the same batch of ^{15}N standard samples were measured over two different UPLC-MS runs between a period of 18 days. Again, mutually similar MS peak areas were obtained for the same samples and both runs yielded linear calibration curves ($R^2 > 0.997$). The slight differences in slope and intercept values for the same batch of standard samples measured over different runs can also arise from interday instrument variations. Furthermore, the signal/noise (S/N) ratios based on MS signals for the ^{15}N standard samples displayed almost linear relationships ($R^2 > 0.96$) over low concentrations (≤ 8.5 μM) for both the fresh and 14-day-old batch of samples (Figure S 6.4c). As seen, the S/N ratio for a 8.5-μM sample is determined to be >100, which is much higher than the S/N ratio (<10) for a 10-μM sample measured by NMR technique.[119] Moreover, the limit of quantification (LOQ) is determined to be ~0.5 μM at S/N=10 for the present method, which is also much lower compared with the optimized NMR method (5-10 μM).

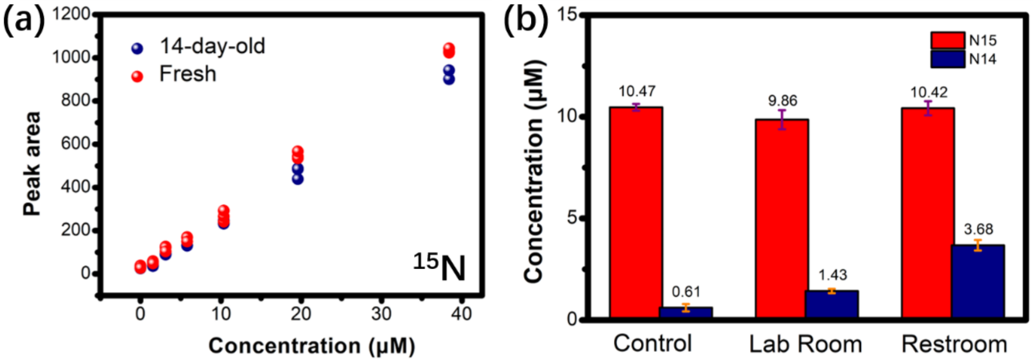

Figure 6.3 (a) Comparisons of measured MS peak areas between a 14-day-old batch and a fresh batch of standard samples for generation of DNS-$^{15}NH_2$ calibration curves (the samples were measured from the same UPLC-MS run); (b) application of the analytical method to assess the influence of ambient ammonia contamination in different environments

Five different replicate samples using the same ammonia solutions were prepared for UPLC-MS analyses (Figure S 6.5a). These five samples displayed very similar responses within the range of one standard deviation. No substantial differences were observed as a result of using different glass or plastic vials (Figure S 6.5b).

The analytical method was also applied to quantitatively measure the impact of ambient ammonia contamination. As shown in Figure 6.3b, leaving the vial containing a solution of ~10 µM $^{15}NH_4^+$ open in air for 6 hours led to measurable increases only in the $^{14}NH_3$ concentration (the concentration of $^{15}NH_3$ did not change from its original value). The contrast in changes of the $^{14}NH_3$ and $^{15}NH_3$ concentrations over time demonstrates the ability of the analytical method to quantitatively distinguish between ^{14}N- and ^{15}N-labelled ammonia and indicates that the $^{15}NH_3$-containing analyte data likely will be immune to interferences from contamination by ambient ammonia ($^{14}NH_3$). Compared with the control sample, the measured increase in $^{14}NH_3$ concentration from a normal wet-chemistry lab (0.82 µM) was only one fourth of that obtained from a restroom (3.06 µM). This difference is expected, as ambient ammonia concentrations are expected to be higher in restrooms.

Further optimization of sensitivity, limit-of-detection, and operational flexibility of the analytical method would be beneficial for very sensitive quantification of the properties of electrocatalysts for N_2 reduction. The present study focuses on detecting ammonia dissolved in acidic electrolytes (50 mM H_2SO_4), but the pH values of the derivatization reaction could be optimized for other electrolytes and variations in initial pH and different counter ions. The MS peak area increased proportionally from a low-concentration NH_4^+ sample (~0.6 μM) with increasing injection volumes (Figure S 6.6). When the injection volume is systematically increased, both the sensitivity and the limit-of-detection likely will be improved; moreover, both the dansyl chloride stock solution and the pH-tuning agent (Na_2CO_3 solution) with higher concentrations can be used so that the dilution effect from the original aqueous ammonia samples can be minimized in the resulting derivatization mixtures. Compared with other ammonia-analysis methods (NMR, IC, for example), the method has advantages in that: (1) it allows more sensitive determination of ammonia concentrations with lower limit-of-detection (LOD) using relatively inexpensive chemicals/materials, (2) it can be carried out rapidly using a widely available analytical instrument (LC-MS), and (3) it can detect ammonia at sub-μM concentrations with quantitative resolution of $^{14}NH_3$ and $^{15}NH_3$ concentrations.

6.3 Conclusion

In conclusion, a UPLC-MS analytical method for the sensitive, accurate determination of ammonia concentrations with isotopic selectivity was developed based on a dansyl chloride derivatization process. The ammonia derivatization reaction can be run at room temperature by simply mixing dansyl chloride and ammonia solutions at optimal pH. The reaction products exhibited stability over a period of 14 days, allowing repeated use of standard samples for generation of additional calibration curves. The capabilities of the method for analysis of sub-μM ammonia concentrations were demonstrated with isotopic selectivity. Hence, investigators in the N_2-reduction electrocatalysis community will be able to determine ammonia yields rapidly and accurately by this analytical method.

Acknowledgement

This work was supported by the NSF (CHE-1763429) and the Office of Science of the U.S. Department of Energy under Award Number DE-SC0004993. N.F.D. is grateful to the Linde Center for support. The Environmental Analysis Center is grateful for support from the Beckman Institute at Caltech. Dr. Fabai Wu and Prof. Victoria Orphan are thanked for providing the $^{15}NH_4Cl$ standard sample. Mr. Christopher Kenseth is thanked for assistance with UPLC-MS analysis. Dr. Yuanlong Huang is thanked for fruitful discussions.

6.4 Experimental

Materials: $NaCO_3$ (anhydrous powder, ≥99.5%, ACS grade, EM Science), $^{14}NH_4Cl$ (≥99.7%, ACS Reagent, Baker Analyzed), $^{15}NH_4Cl$ ($^{15}N \geq 99\%$, Cambridge Isotope Laboratories, Inc), sulfuric acid (1.0 N, laboratory reagent, VMR Chemical), acetonitrile (UPLC grade, Fischer Chemical), dansyl chloride (≥99.0%, for HPLC, Sigma Aldrich). High-purity deionized water (measured resistivity ≤ 18.2 MΩ cm at room temperature, by Milli-Q purification system) was used in all experiments.

UPLC-MS analysis: UPLC-MS analyses were performed on an Acquity I-Class UPLC coupled to a Xevo G2-S Quadrupole Time-of-Flight (QTof) mass spectrometer (both from Waters Corporation, Milford MA). 3 µL of the final derivatized solution was injected for separation on a Waters BEH C18 column (2.1 x 100 mm, 1.7 µm) with mobile phase flowing at 0.300 mL/min. Initial composition was 90 % water. At 0.25 minutes acetonitrile was increased linearly to 90 % at 3.25 minutes and maintained for 0.5 minutes. Acetonitrile was linearly decreased back to 10 % at 4.00 minutes and held for 0.2 minutes before the next run was started. Ionization was performed in a Waters atmospheric pressure ionization source operated in electrospray ionization mode. The capillary voltage was 3.0 kV, sampling cone 40 V, source temperature 120 °C, source offset 80 V, desolvation temperature 450 °C, cone gas flow 30 L/hr and desolvation gas flow 800 L/hr. The TOF was operated in resolution mode using the 120.0813 m/z fragment of leucine encephalin as a lock mass ion and data was recorded from 50 to 500 m/z.

Dansyl chloride derivatization: dansyl chloride derivatization processes were performed by preparing solution mixtures in 2 mL glass or plastic vials in the following order: 0.4 mL of ~290 µM dansyl chloride dissolved in acetonitrile; 0.3 mL of sodium carbonate stock solution (2 g/100 mL); and 0.4 mL of a NH_4Cl solution in 50 mM H_2SO_4(aq). The vials were capped and vortexed for 10 s before being loaded onto the autosampler plate for analysis. The derivatization conditions were extensively optimized; for example, the optimal pH value of the resulting mixtures was ~9.5±0.5, and no heating was required. The derivatization products (DNS-NH_2) were separated by reverse-phase chromatography using a binary water/acetonitrile solvent with a steady gradient. Each sample was measured three times consecutively. The concentration of the derivative was quantified by the MS peak area at specific mass positions (m/z=251.0854 for ^{14}N and z=252.0825 for ^{15}N). The mass windows were 0.01 m/z for this instrument. Data analysis was performed using Quanlynx software (Waters Corporation).

It is important to note that the product molecule containing ^{14}N from ammonia and one ^{13}C atom appears at m/z 252.0888, or 0.0063 m/z away from ^{15}N. Care must be taken that adequate mass resolution is maintained, especially if the concentration of ^{14}N ammonia is more than several times the ^{15}N concentration.

Measurement of ambient ammonia contamination: Ambient ammonia-trapping experiments were performed by leaving 0.4 mL of ^{15}N-labelled ammonium solutions (~10 μM) open for 6 h in vials placed in labs and/or restrooms. The derivatization procedures were then performed and the vials were capped and transferred for UPLC-MS analysis. During the course of ammonia-trapping experiments, a control sample was prepared by leaving the same volume of ^{15}N-labelled ammonia solution in place with the vial capped.

6.5 Supplementary figures and tables

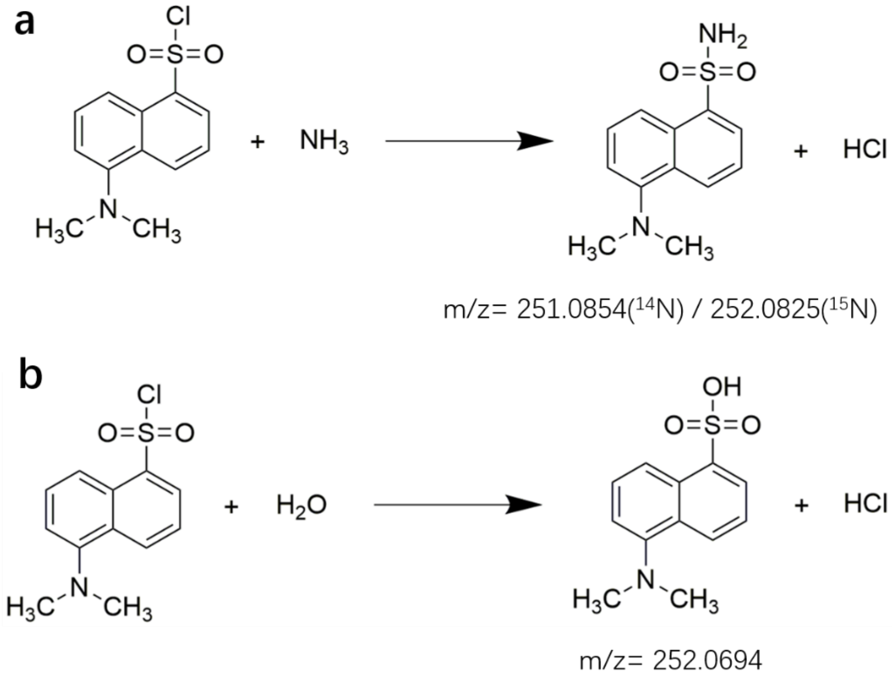

Figure S 6.1 Reactions of dansyl chloride molecules with (a) ammonia to form DNS-NH_2 and (b) water to form DNS-OH and a comparison in molecular masses between DNS-NH_2/DNS-OH

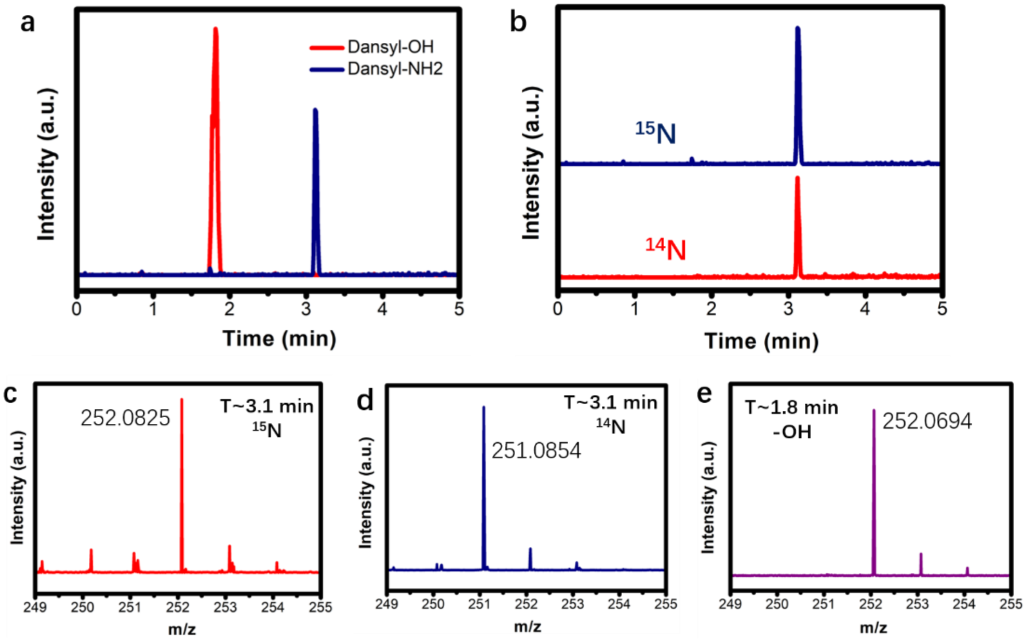

Figure S 6.2 (a) Comparison of mass-selected chromatographs for DNS-OH (red) and DNS-NH_2 (blue) products; (b) comparison of mass-selected chromatographs for DNS-NH_2 labelled with ^{14}N or ^{15}N, respectively; (c-e) comparison of representative time-integral mass spectra for (c) DNS-$^{15}NH_2$ (~3.1 min), (d) DNS-$^{14}NH_2$ (~3.1 min), and (e) DNS-OH (~1.8 min). The shown values in the panel (c-e) represent the exact mass values for the major peaks.

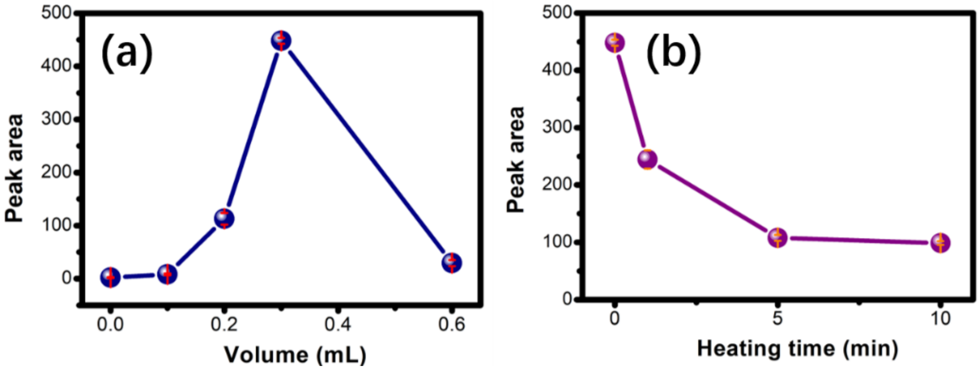

Figure S 6.3 Optimizing ammonia derivatization conditions. (a) comparison of MS peak area (at m/z=252.0825) for the same derivatized aqueous ammonia ($^{15}NH_4^+$) sample (~10 μM) vs different added volumes of $NaCO_3$(aq) stock solution (2g/100 mL), corrected by a volume factor; (b) comparison of the MS peak area vs different heating time (~70 °C) for the same aqueous ammonia sample in (a).

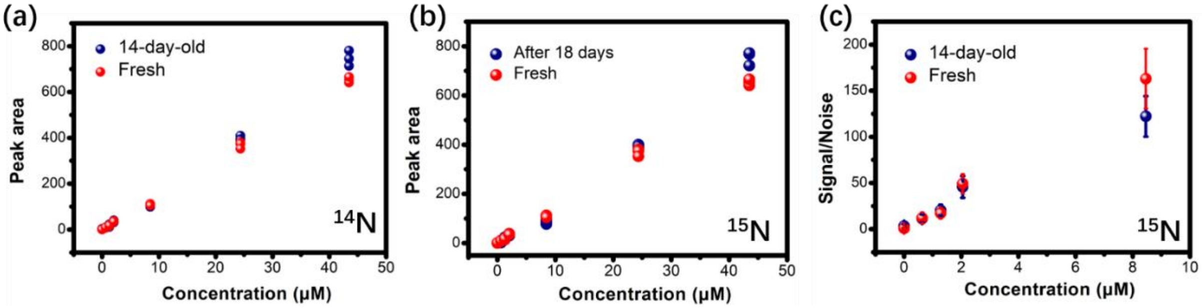

Figure S 6.4 (a) comparisons of measured MS peak areas between a 14-day-old batch and a fresh batch of standard samples for generation of DNS-$^{14}NH_2$ calibration curves (the samples were measured from the same UPLC-MS run); (b) comparison of MS peak area for the same batch of DNS-$^{15}NH_2$ standard samples measured as-prepared and after storage of 18 days. (c) signal/noise ratios based on the gained MS signals for the DNS-$^{15}NH_2$ standard samples in the low-concentration range of ≤ 8.5 μM.

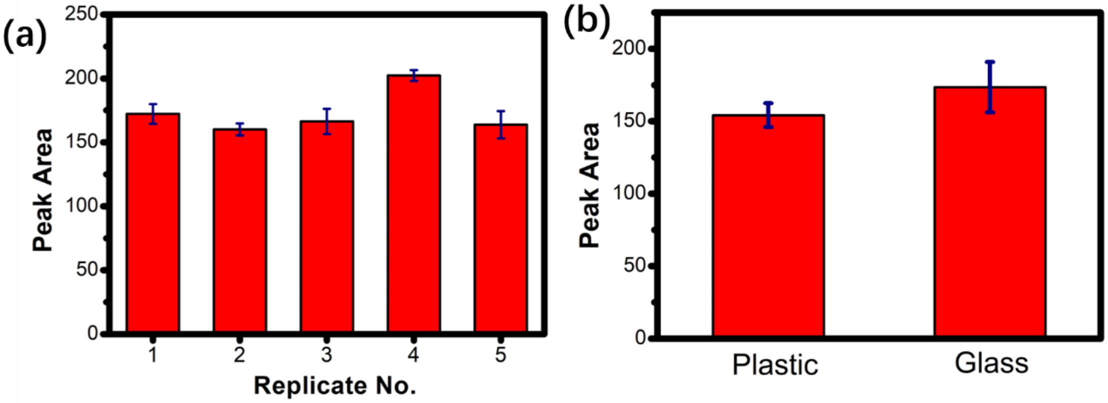

Figure S 6.5 (a) Comparison of MS peak areas for five different samples obtained from the same aqueous ammonia solutions; (b) comparison of the use of glass and plastic vials for sample preparation

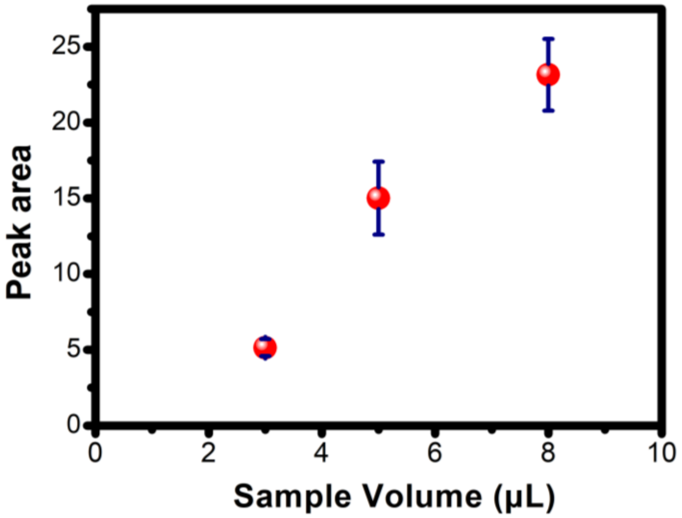

Figure S 6.6 Comparison of peak areas from a 0.6-µM ammonia sample as a function of the sample injection volume for UPLC-MS analysis.

Table S 6.1 Comparison of linear-fitting results between a 14-day-old batch and a fresh batch of standard samples for ^{14}N- or ^{15}N-ammonia calibration curves measured over the same UPLC-MS run.

Age	**Curve**	**Slope**	**Intercept**	**R^2**
14-day	^{14}N	23.5	10.1	0.996
14-day	^{15}N	17.1	-9.1	0.995
Fresh	^{14}N	26.3	19.7	0.997
Fresh	^{15}N	15.1	-2.1	0.998

Chapter 7

7 CATHODIC NH_4^+ LEACHING OF NITROGEN IMPURITIES IN COMO THIN-FILM ELECTRODES IN AQUEOUS ACIDIC SOLUTIONS

Reproduced with permission from:[116] Yu, W.; Buabthong, P.; Read, C. G.; Dalleska, N. F.; Lewis, N. S.; Lewerenz, H.-J.; Gray, H. B.; Brinkert, K. Cathodic NH_4^+ Leaching of Nitrogen Impurities in CoMo Thin-Film Electrodes in Aqueous Acidic Solutions. Sustainable Energy Fuels 2020, 4 (10), 5080–5087. https://doi.org/10.1039/D0SE00674B.

7.1 Abstract

Electrocatalytic reduction of dinitrogen (N_2) to ammonium (NH_4^+) in acidic aqueous solutions was investigated at ambient temperature and pressure using a cobalt-molybdenum (CoMo) thin-film electrode prepared by magnetron reactive sputtering. Increased concentrations of ammonium ions (NH_4^+) were consistently detected in the electrolyte using ion chromatography (IC) after constant-potential electrolysis at various potentials (≤-0.29 V *vs.* RHE). Using a newly developed analytical method based on ammonia derivatization, performing the experiments with $^{15}N_2$-labelled gas led however to the detection of increased $^{14}NH_4^+$ concentrations instead of $^{15}NH_4^+$. X-ray photoelectron spectroscopic (XPS) analysis of the electrode surface revealed the presence of Mo≡N and Mo-NH_x species. Several contamination sources were identified that led to substantial increases in the concentration of ammonium ions, including $^{15}NH_3$ impurities in $^{15}N_2$ gas. The observed ammonium concentrations can be consistently ascribed to leaching of nitrogen (^{14}N) impurities incorporated in the CoMo film during the sputtering process. Researchers in the field are therefore urged to adopt extended protocols to identify and eliminate sources of ammonia contamination and to very carefully monitor the ammonium concentrations in each experimental step.

7.2 Introduction

The discovery of ammonia (NH_3) synthesis, a milestone in the history of the chemical industry, has greatly enhanced global agriculture. Ammonia is the second-largest chemical produced worldwide, with 140 million tons manufactured annually via the Haber-Bosch process.[231] The process requires high-purity streams of $N_2(g)$ and $H_2(g)$, as well as high temperatures (400-500 °C) and high pressures (200-300 atm). Notably, ammonia synthesis consumes ~ 1% of the energy used on our planet.

Mild methods to break the N-N triple bond represent a major opportunity for catalyst development.[106,232–234] Electrochemically based nitrogen reduction could use renewable solar and wind electricity to drive reactions at ambient temperature and pressure,[107,219,234–237] thereby providing a sustainable technology for widespread production of ammonia for fertilizer and fuels.

Although the standard potential of reduction of dinitrogen to ammonia is similar to the standard potential of the hydrogen-evolution reaction (HER), the latter is kinetically favored:[215]

$$N_2(g) + 6H^+(aq) + 6e^- \rightarrow 2NH_3(aq) \qquad E° = +0.092\ \text{V}\ \textit{vs.}\ \text{RHE} \qquad (1)$$

$$2H^+(aq) + 2e^- \rightarrow H_2(g) \qquad E° = 0.00\ \text{V}\ \textit{vs.}\ \text{RHE} \qquad (2)$$

where RHE is the potential of the reversible hydrogen electrode. The high dissociation enthalpy (942 kJ mol^{-1}) of the N_2 triple bond and the required multiple proton-coupled electron transfer (PCET) steps lead to high overpotentials for direct conversion to NH_3. The high N_2 activation barrier compared to that of the HER, together with the low solubility of N_2 in H_2O, present major selectivity challenges for electrochemical N_2 reduction.

Among pure metals, Ru and Os are the best catalysts for gas-phase ammonia production from H_2 and N_2,[238] accomplishing the trade-off between a high nitrogen adsorption energy on the surface and a low activation energy for the dissociative step. In the quest for robust and active earth-abundant catalytic materials, mixed-metal systems such as the ternary metal nitride Co_3Mo_3N have shown promise for gas-phase ammonia production.[239,240] These catalysts are believed to fix nitrogen via the Mars-van Krevelen mechanism,[241,242] in which activated surface nitride participates in the reaction.[243] A theoretical analysis has indicated that MoN might catalyze electrochemical nitrogen reduction (NRR) under ambient conditions.[244] Although CoMo bimetallic nanoparticles exhibit similar gas-phase ammonia-production activities as those of Ru nanoparticles,[245] CoMo has not hitherto been explored extensively for electrochemical NRR under ambient conditions.

In addition to the considerations involving electrocatalyst materials, increasing emphasis has been placed on the design and execution of experiments for investigations of the electrochemical reduction of N_2 to NH_3.[112,118,222,226] Many contamination sources have been identified that can give rise to increased ammonia concentrations in electrolytes and thereby confound formulation of robust conclusions concerning the true efficacy of the electrocatalyst. Consequently, $^{15}N_2$ isotope-labelled electrochemical experiments are crucial to confirm the putative activity for electrochemical N_2 reduction.[222] In addition, analytical methods need to be user-friendly and enable isotope-selective quantification of µM concentrations of ammonia.[118,119]

Herein, we present a comprehensive investigation of the electrochemical activity of CoMo thin-film electrodes prepared by magnetron sputtering. To quantify $^{14}N/^{15}N$-labelled ammonium ions at µM concentration levels with isotope selectivity, we used an analytical method based on ammonia derivatization with dansyl chloride. Moreover, the electrode surfaces were characterized before and after electrochemical experiments using scanning-electron microscopy (SEM), atomic-force microscopy (AFM) and X-ray photoelectron spectroscopy (XPS) techniques. Despite the generally preserved surface morphology and evidence for the presence of $Mo{\equiv}N$ and $Mo\text{-}NH_x$ species on the electrode surface by XPS, we were not able to confirm electrocatalytic reduction of dinitrogen through $^{15}N_2$ labelling experiments. On the contrary, the observed increases in ammonium concentrations can be ascribed to leaching under cathodic conditions of nitrogen impurities from the sputtered CoMo thin-film. Based on the present results and identified $^{14}NH_4^+$ contamination sources, we conclude that additional protocols must be adopted before a robust claim can be sustained that NH_3 is a product of electrochemical N_2 reduction.[112,222,226]

7.3 Results and Discussion

Electrochemistry and ammonium yields (n^+-Si/Ti/CoMo electrodes) using $^{14}N_2$ gas. A CoMo thin-film was deposited using reactive magnetron sputtering onto a degenerately-doped n-type Si substrate that had been coated with a Ti adhesion layer. This deposition technique offers the advantage of close proximity and versatile composition-tuning between the two different elements. A pure Ar atmosphere (flow rate = 20 sccm and pressure = 5 mTorr) was used during the deposition process. Cross-sectional and high-resolution TEM images of the n^+-Si/Ti/CoMo electrode are shown in Figure S 7.1.

Initial electrochemical studies of CoMo electrodes revealed stable current densities for 1 h under a constant N_2(g) purge in a three-electrode cell with static electrolytes of 50 mM sulfuric acid, with either water or ethanol as solvent (Figure S 7.2). At a potential of -0.54 V *vs.* RHE, a cathodic current density of ~ 7.4 mA cm^{-2} was observed in aqueous H_2SO_4, whereas the cathodic current density in the ethanolic electrolyte was ~ 0.8 mA cm^{-2}. The much lower current density in the ethanolic electrolyte was due to suppression of the competing HER. As shown in Figure 7.1a, the highest ammonia production rate (0.19 ± 0.02 $nmol \cdot cm^{-2} \cdot s^{-1}$) was obseved in aqueous H_2SO_4 after 1 h, whereas the rate was slightly lower after 20 min of electrolysis (0.16 ± 0.01 $nmol \cdot cm^{-2} \cdot s^{-1}$). After 12 h at constant potential, the ammonium production rate decreased by about 80% to 0.03 ± 0.01 $nmol \cdot cm^{-2} \cdot s^{-1}$. Notably, the total ammonium yield after 12 h operation (1.3 ± 0.4 $\mu mol \cdot cm^{-2}$) was only ~2.3 times higher than the total yield after 1 h operation (0.69 ± 0.09 $\mu mol\ cm^{-2}$) (Figure 7.1c). Faradaic efficiencies in the aqueous system were ~ 0.6 ± 0.01% assuming that electrochemical NRR occurred. Owing to suppression of the HER, higher Faradaic efficiencies (FEs) were observed in the ethanolic electrolyte, with values of ~ 3.3 ± 0.3% after 20 min and ~ 1.3 ± 0.2% after 1 h of operation.

Ion chromatography (IC) was used to quantify the ammonium concentrations in the electrolytes after each experiment. Relative to colorimetric methods,[246] IC has substantially better accuracy and lower limits of detection (Figure S 7.3). To better quantify ammonium yields originating from the electrochemical process and to exclude ammonia contamination from various sources, control experiments were performed using the CoMo electrode, and the results were compared to those from analogue experiments using Co, Mo, NiMo, and FeMo films, respectively, deposited on the n^+-Si/Ti substrate (Table S 7.1). First, a background ammonium concentration of 1.1 µM was determined in the 50 mM H_2SO_4 electrolyte. After leaving the CoMo electrode in the electrolyte at the open-circuit potential (E_{oc} ~ 0.03 V *vs.* RHE) for 20 min, the detected ammonium concentrations ranged from 0.9-2.5 µM. After 12 h at E_{oc} in 50 mM H_2SO_4(aq), the background ammonia concentration produced by the n^+-Si/Ti/CoMo electrode doubled from 1.4 to 2.8 µM. Furthermore, a gas bubbler containing 50 mM H_2SO_4(aq) was used to remove potential ammonia impurities in the purged N_2 gas. After purging the electrochemical cell for > 60 min, no increase in ammonium concentration was observed, thereby confirming the absence of ammonia impurities originating from purging with Ar or N_2(g). A slightly higher ammonium concentration was observed (2.0-2.45 µM) when the solvent was switched from water to ethanol, suggesting that the background depended on the electrolyte system, consistent with the different solubility of ammonium in different solvents. Control experiments clearly must be performed so that correction for any background ammonium concentration can be made when quantifying the amount of ammonium produced by electrocatalysis.

Table 7.1 contains a comparison of various sputtered thin-film electrodes under potential control for 20 min at -0.54 V *vs.* RHE. The highest yields of ammonium were observed for CoMo electrodes in 50 mM H_2SO_4(aq). Switching electrolyte anions from SO_4^{2-} to Cl^- or ClO_4^- led to lower ammonium yields after 20 min under potential control. Under nominally identical conditions, elementary Co and Mo electrodes led to much lower ammonium yields, along with lower current densities, than were observed for CoMo. Morevoer, substituting Ni or Fe for Co also decreased the resulting ammonium yield (Table 7.1). The potential (*E*) dependence of the ammonium yields in aqueous H_2SO_4 was determined for a CoMo electrode over 20-min periods (Figure 7.1b). The highest yield (225 ± 20 nmol·cm^{-2}) was observed after 20 min for E = -1.29 V *vs.* RHE, whereas the yield decreased to 145 ± 30 nmol·cm^{-2} for E = -0.79 V and increased to 193 ± 12 nmol·cm^{-2} for E = -0.54 V, before decreasing again to 96 ± 30 nmol·cm^{-2} for E = -0.29 V.

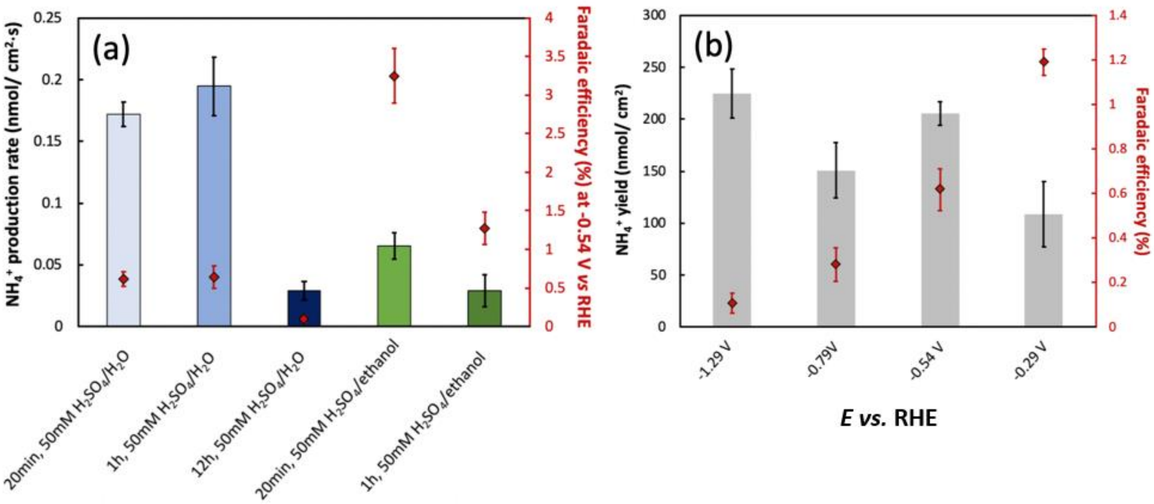

Figure 7.1 (a) NH_4^+-production rates in aqueous and ethanolic 50 mM H_2SO_4 as a function of electrolysis time. The secondary y-axis (data are filled diamonds) shows Faradaic efficiencies of the n^+-Si/Ti/CoMo electrodes for the respective electrochemical conditions, assuming that electrochemical NRR occurs. (b) NH_4^+-production yields of 20 min tests in aqueous 50 mM H_2SO_4 at different potentials. The NH_4^+-production yields and rates were corrected for background NH_4^+ values obtained with samples held under open-circuit conditions in the same electrolyte for the same time period (compare Table S 7.1). Unless indicated otherwise, the potential was -0.54 V *vs.* RHE. The error bars represent standard deviations from three independent electrochemical tests with fresh electrodes for each condition.

Table 7.1 Comparison of NH_4^+ yields after 20 min constant potential electrolyses with different electrodes. Calculated NH_4^+ yields were corrected against background NH_4^+ values obtained with the sample under open-circuit conditions in the same electrolyte for the same time period (Table S 7.1). The potential was -0.54 V *vs.* RHE, and the electrolyte was 50 mM aqueous H_2SO_4 (if not indicated otherwise).

Sample	**NH_4^+ yield (nmol cm^{-2})**	**c(NH_4^+) (μM cm^{-2})**	**J (mA cm^{-2})**	**FE (%)**
CoMo	193	9.6	7.36	0.63
CoMo, 50mM HCl	47	2.3	4.05	0.28
CoMo, 50mM $HClO_4$	4.8	0.2	4.17	0.03
Co	20	1.0	2.13	0.22
Mo	4	0.2	5.54	0.02
FeMo	0	0	4.29	0
NiMo	34	1.7	7.13	0.12

Surface morphology and topography. Atomic-force microscopy (AFM) and high-resolution scanning-electron microscopy (HRSEM) were used to probe changes in surface morphology of the CoMo electrode before and after electrochemical experiments, respectively. As evident from Figure 7.2a-c, an as-prepared CoMo thin-film exhibited a nano-particulate surface morphology that was largely preserved after the electrode was held for 1 to 12 h at -0.54 V *vs.* RHE. Based on the AFM images (Figure 7.2d-f), the initial surface roughness for an as-prepared CoMo thin-film was ~1 nm. After 1 h at -0.54 V *vs.* RHE, the electrode surface slightly roughened (roughness increased from 1 to 3 nm), and displayed higher film porosity with larger average particle size. Changes in CoMo surface morphology were even more evident after 12 h under potential control, with small particles (~3 nm) distributed among larger particles (~55 nm).

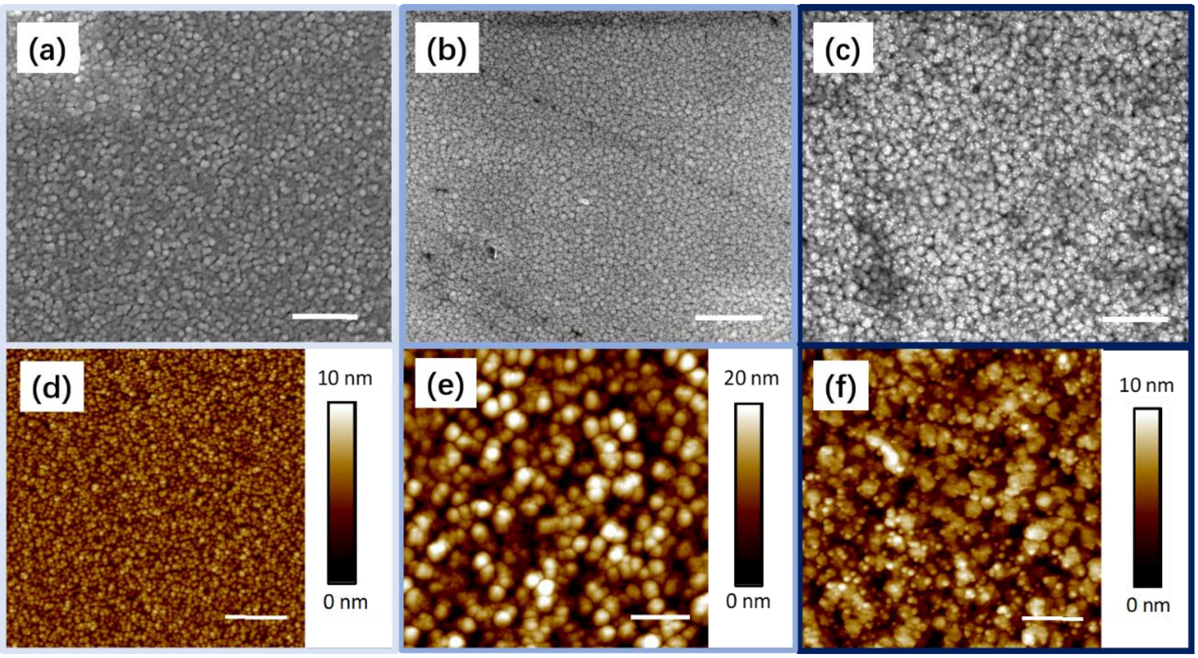

Figure 7.2 (a-c) HRSEM images of n^+-Si/Ti/CoMo surfaces: samples (a) before electrochemical testing; (b) after 1 h; and (c) after 12 h in aqueous 50 mM H_2SO_4 at E = -0.54 V *vs.* RHE (500 nm scale bars). (d-f) AFM images of samples (a)-(c), 200 nm scale bars.

Surface composition analysis by XPS. To assess compositional changes of the surface, X-ray photoelectron spectroscopy (XPS) was performed before electrochemical testing (Figure 7.3, top), as well as after applying E = -0.54 V *vs.* RHE to a CoMo electrode in aqueous electrolyte for 20 min (center) or 12 h (bottom). Peak assignments are based on previous reports and peak positions used in the analysis are listed in Table S 7.2.[247–249] Before electrochemical tests, the surface of an as-prepared CoMo thin-film was enriched in Mo^0 and Co^0 (combined with various oxide species). The dominant peak in the Co spectrum can be assigned to Co^0 with 13-22% surface oxides in the form of Co^{2+}, Co^{3+}, and Co-OH moieties, likely resulting from exposure to moisture and/or air (Figure 7.3a).[247–249] Based on the Mo 3d spectrum, $Mo^{2+/3+}$, $Mo^{3+/4+}$, and two Mo^{6+} species were present Figure 7.3b).[247–249]

Deconvolution of the N 1s spectrum was performed after accounting for partially overlapping Mo $3p^{3/2}$ features (Figure 7.3c). The N 1s spectrum of an as-prepared CoMo sample was partially obscured by a dominant Mo 3p peak attributable to MoO_3. After constant potential electrolysis at E

= -0.54 V *vs.* RHE for 20 min or 12 h, only Co^0 remained on the electrode surface (multiple CoO_x peaks disappeared, Figure 7.3 and Figure S 7.4). Moreover, the amount of surface MoO_x was substantially reduced and the surface Mo^0 coverage increased to ~ 66% of the total Mo signal. As seen in Figure 7.3b, the Mo^{6+} species (yellow) associated with surface MoO_3 disappeared and the Mo^{6+} peak (red) at lower binding energies remained, with the latter feature due to a Mo^{6+} nitride (Mo≡N). The Mo≡N signal first increased from 4% of the total Mo signal (as-prepared) to ~ 8% after 20-min under potential control and then to ~14% of the total Mo signal after 12 h under potential control. After electrochemical testing, removal of surface MoO_3 was apparent from the N 1s spectrum, as were distinctive features attributable to $Mo\text{-}NH_3^+$, $Mo\text{-}NH_2$ and Mo≡N species (high to low B.E., respectively).[247] After 10-min immersion at open circuit in 10 mM KOH(aq), the intensity of the $Mo\text{-}NH_2$ feature increased, along with disappearance of $Mo\text{-}NH_3^+$ on the electrode surface (Figure S 7.5). These findings suggest deprotonation of surface-adsorbed ammonium species in aqueous alkaline solutions. The collective XPS data confirm that adsorbed NH_x species were present on electrochemically evaluated CoMo electrode surfaces.

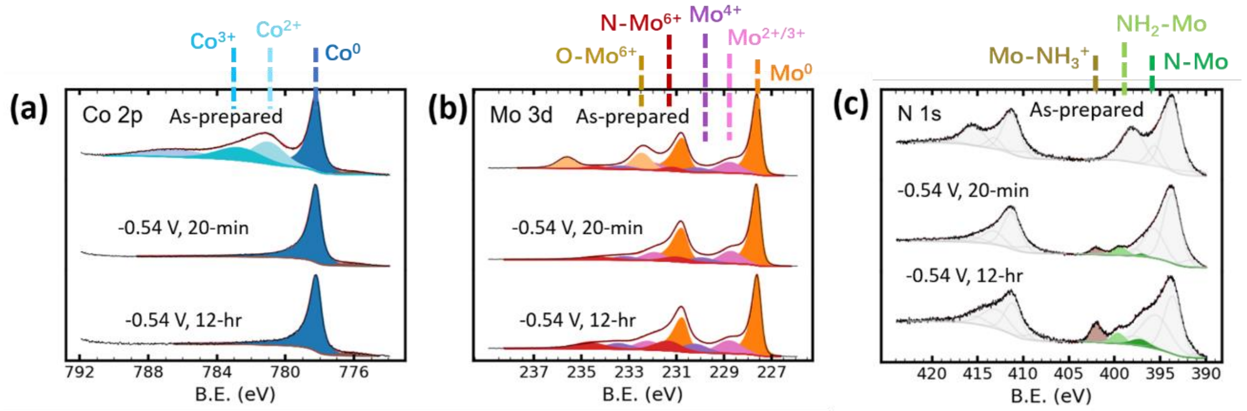

Figure 7.3 X-ray photoelectron spectra of the CoMo surface prior to electrocatalysis (top); after 20 min under potential control (center); and after 12 h (bottom) in aqueous 50 mM H_2SO_4 at a potential of -0.54 V *vs.* RHE. (a) Co 2p core levels; (b) Mo 3d core levels and (c) N 1s core levels. B.E. is the binding energy.

Electrochemical experiments with $^{15}N_2$. Experiments with $^{15}N_2$ gas were performed to determine definitively whether the detected ammonia was generated by electrochemical reduction of nitrogen catalysed by Co-Mo. The low-µM $^{15}NH_4^+$ concentrations were difficult to quantify with isotope-selectivity, either by NMR or by ion chromatography coupled mass spectrometry (IC-MS). This issue was addressed by using a new analytical method that allowed simultaneous quantification of $^{14}NH_4^+$ and $^{15}NH_4^+$ concentrations at sub-µM level.[104] In this procedure, dansyl chloride was used to derivatize ammonia at room temperature and optimal pH (Equation S 7.1), with the derivatized products subsequently analyzed by ultrahigh-performance liquid chromatography coupled mass spectrometry (UPLC-MS). The molecular derivates of $^{14}NH_4^+$/$^{15}NH_4^+$ ions were isotopically distinguished by their different masses and quantified based on their respective peak areas.

An acid trap was required to purify $^{15}N_2$ gas (Sigma Aldrich, No. 364584) before electrochemical experiments. After purging for 90 min, the gas-scrubber solution (~5 mL of 50 mM H_2SO_4(aq)) contained substantially increased concentrations of $^{14}NH_4^+$ (18.5 µM) and $^{15}NH_4^+$ ions (33 µM), indicating that $^{14}NH_3$ and $^{15}NH_3$ impurities were present in the $^{15}N_2$ gas (Figure 7.4).[225] An acid trap (Figure S 7.6) was thus required to first purify $^{15}N_2$ gas prior to any electrochemical experiments. Based on the results in Figure 7.1, isotope-labelled $^{15}N_2$ experiments were repeated for all potentials previously used with CoMo electrodes. To exclude contamination with ammonia, electrolyte samples were examined after three different experimental steps: (a) after the electrolyte was transferred into the cell; (b) after Ar and $^{15}N_2$ purging and before the electrode was placed in the cell for testing; and (c) after performing 20-min electrolyses. Table 7.2 provides a comparison of the $^{15}NH_4^+$ concentrations observed at different electrode potentials. Despite the presence of ammonia impurities in $^{15}N_2$ gas, no increases in $^{15}NH_4^+$ concentrations were observed in the setup with an acid trap for entry 1-5 after $^{15}N_2$ purging. Hence the $^{15}NH_3$ impurities were removed from $^{15}N_2$ gas prior to purging the electrolyte.

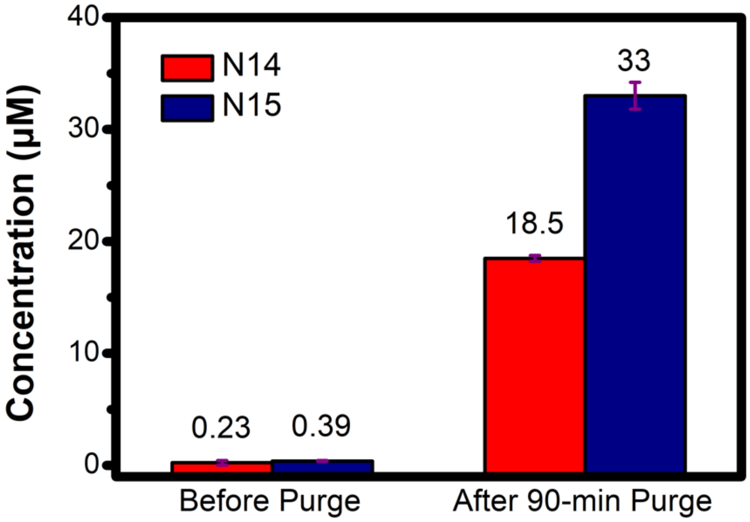

Figure 7.4 Comparison of $^{14}NH_4^+$/$^{15}NH_4^+$ concentrations in the gas scrubber solution (~5 mL of 50 mM H_2SO_4) before and after, respectively, purging $^{15}N_2$ gas for 90 min. Concentrations were determined by ammonia derivatization with dansyl chloride followed by UPLC-MS analysis.

Isotope-labelling experiments were repeated at different potentials and did not yield any detectable increases in the concentrations of $^{15}NH_4^+$. However, substantial increases in $^{14}NH_4^+$ concentrations were consistently observed for all conditions (Table 7.2). As shown in Figure 7.5 and Table S 7.3, normalized increases in $^{14}NH_4^+$ concentrations after electrolyses with $^{15}N_2$ were comparable to those obtained in electrolyses with $^{14}N_2$ gas. Within the same time period (20 min), $^{14}NH_4^+$ concentrations also increased as the electrode potential became more negative. This trend corresponds to higher cathodic current densities at more negative potentials, a large portion of which directly affects the HER (Figure S 7.7).

Table 7.2 Comparison of $^{15}NH_4^+$ concentrations obtained from experiments at three different steps for five electrochemical tests (20 min) at various potentials using $^{15}N_2$ gas. Concentrations were determined using dansylation followed by UPLC-MS analyses. Three UPLC-MS measurements were performed for each sample.

Entry	***E* (V *vs.* RHE)**	**Before purge[a] (μM)**	**After purge[b] (μM)**	**After 20 min at constant *E*[c] (μM)**
1	-0.29	0.49 ± 0.10	0.45 ± 0.06	0.65 ± 0.3
2	-0.54	0.74 ± 0.08	1.0 ± 0.3	1.0 ± 0.5
3	-0.54[d]	0.79 ± 0.02	0.79 ± 0.08	0.73 ± 0.08
4	-0.79	0.41 ± 0.09	1.1 ± 0.2	1.5 ± 0.6
5	-1.29	0.47 ± 0.1	0.49 ± 0.09	1.2 ± 0.7

[a] Electrolytes were sampled immediately after filling the cell; [b] electrolytes were sampled after Ar/$^{15}N_2$ purging with reference and counter electrodes in the cell; [c] electrolytes were sampled after putting electrodes into each cell and testing for 20 min; [d] electrolyses with E = -0.54 V *vs*. RHE were repeated twice.

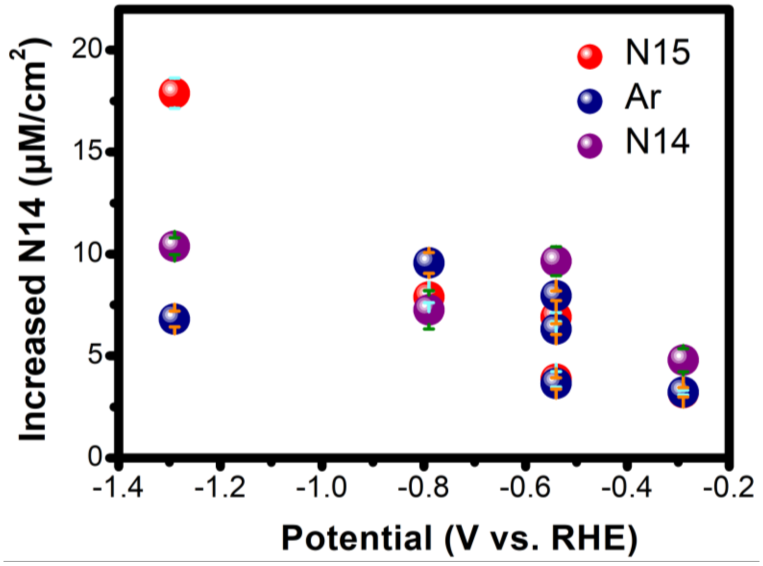

Figure 7.5 Comparison of increased $^{14}NH_4^+$ concentrations (normalized by electrode areas) for 20-min electrochemical experiments using CoMo electrodes at -0.54 V *vs.* RHE, purging with $^{15}N_2$/Ar/$^{14}N_2$ gases. The electrolytes obtained from Ar/$^{15}N_2$-purging experiments (red and blue) were analyzed by the dansyl chloride derivatization/UPLC-MS method; each error bar is based on three UPLC-MS measurements of the same sample. The $^{14}N_2$ data points (purple) are the same as those in Figure 1; each error bar is based on three independent experiments in which the electrolytes were analyzed by IC.

Ammonia contamination sources. Based on the present results, the increased ammonium concentrations detected after electrochemical experiments (Figure 7.1) likely do not originate from electrochemical reduction of N_2. Interestingly, compared to operation at E_{oc} (Table S 7.1), substantial ammonium concentrations were only observed for CoMo electrodes held under cathodic conditions. During electrochemical experiments, the epoxy and the CoMo thin-film were the only two components in direct contact with electrolyte. All electrodes were made using the same epoxy (Loctite 9460), so the effect of ammonia contamination from that potential source likely is limited, although most chemically resistant, two-component epoxies contain hardeners based on amines. The ammonia contamination from epoxy can be neglected for short-term experiments, but could impact the ammonia background concentration in electrolyses over longer time periods. We therefore conclude that increased amounts of $^{14}NH_4^+$ in the electrolyte were derived from the CoMo electrodes. Nitrogen impurities can be incorporated in CoMo thin-films during the sputtering process, even in an Ar atmosphere. Unlike the nitride-decomposition mechanism reported previously, nitrogen impurities likely originate from Ar flow gas, sputtering targets or the deposition chamber.[221,224,250]

To support the above claim, experiments were performed using CoMo electrodes under an Ar purge. Notably, increased amounts of $^{14}NH_4^+$ were consistently observed after 20-min electrolyses at four different potentials (Figure 7.5). Moreover, these increased $^{14}NH_4^+$ concentrations were comparable to those observed in electrolyses performed with $^{14}N_2/^{15}N_2$ (Table S 7.3). After various electrolyses under Ar purging, XPS analyses revealed Mo≡N and NH_x species at CoMo electrode surfaces similar to those evaluated under $^{14}N_2/^{15}N_2$ purging (Figure 7.6 and Figure S 7.8-9). These observations collectively indicate that the N species identified at these electrode surfaces were not derived from the purged N_2 gas. To exclude the formation of ammonia via reduction of nitrate (NO_3^-) or nitrite (NO_2^-) ions, the concentrations of both ions in the electrolyte at different experimental stages were measured using IC. Additional results with relevant discussion are available in the SI (Table S 7.4). μM-levels of NO_3^- ions were observed in all electrolyte samples, but NO_2^- was below the detection limit. Using chemiluminescence analysis, negligible NO(g) levels were found in the Ar and N_2^{14}(g) gas cylinders, whereas the NO_2(g) concentrations were lower than in the laboratory air. An additional experiment was performed by holding the CoMo electrode for 20 min at -0.54 V *vs.* RHE in 50 mM H_2SO_4(aq) that additionally contained 40.6 μM of pre-existing NO_3^- ions, with no gas purging. Of importance is that no decrease in nitrate concentration was observed after electrochemical experiment. Moreover, both cyclic voltammograms (CVs) and chronoamperometry at -0.54 V vs. RHE of CoMo electrode were measured in solutions of 50 mM H_2SO_4 containing substantial concentrations of nitrate ions (54, 104, and 170 μM). Upon addition of nitrate, neither differences in CVs nor increases in current density were observed (Figure S 7.10). Taken together, these data confirmed that electrochemical nitrate reduction at the CoMo surface was negligible.

Furthermore, prolonged storage (10 days) of sampled electrolytes in polypropylene vials (Thermo Scientific C4000-11) led to substantial increases in ammonium concentrations (Table S 7.5).

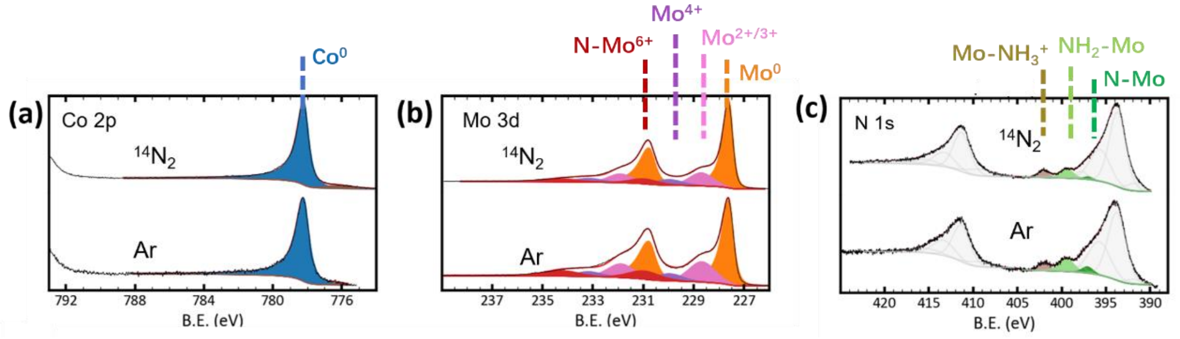

Figure 7.6 Comparison of X-ray photoelectron spectra of (a) Co 2p, (b) Mo 3d, and (c) N 1s for CoMo electrodes tested at -0.54 V *vs.* RHE for 20 min in 50 mM H_2SO_4(aq) under $^{14}N_2$ and Ar purging.

The increases in observed ammonium concentrations after various electrolyses were not dependent on the purge N_2 gas because the increases were produced from the electrode itself under cathodic conditions. The amounts of these incorporated nitrogen impurities depended on the deposited thin-film materials (Table 7.1). The highest amounts of N impurities were observed for the bimetallic (CoMo) system, consistent with favorable N adsorption/desorption energies in the gas phase.[238] The leaching kinetics of N impurities are likely regulated by anions in the electrolyte, as demonstrated by different ammonium concentrations observed after tests in 50 mM HCl/$HClO_4$(aq). The presence of self-containing N leaching is also supported by a series of previous observations: (a) the slightly higher porosity of the CoMo thin-film after electrochemical tests; (b) a non-linear increases in total ammonia yields over prolonged testing (12 h), likely due to a plateau effect of N leaching from the electrode; and (c) XPS evidence of surface Mo≡N and NH_x species after electrochemical experiments attributable to Mo-N groups originally present in the film. We therefore suggest that extra care should be taken during the electrode fabrication process to avoid incorporation of N impurities. As we have demonstrated, cathodic N leaching complicates analyses of ammonium ions in electrolytes. Moreover, a direct comparison of experiments under Ar/N_2 purging must be made before robustly establishing claims of electrochemical reduction of N_2 to NH_3. We note that another pre-reduction strategy has been used to remove N impurities in electrodes prior to N_2-reduction tests.[251]

7.4 Concluding Remarks

Extensive investigations employing $^{15}N_2$(g) as the potential reactant failed to confirm electrocatalytic activities of CoMo thin-film electrodes in aqueous and ethanolic H_2SO_4 for conversion of N_2 to NH_3. Simultaneous quantification of $^{14}NH_4^+$/$^{15}NH_4^+$ concentrations using a dansyl chloride derivatization/UPLC-MS method indicated that the increased ammonium concentrations observed after electrolyses were solely derived from $^{14}NH_4^+$ rather than $^{15}NH_4^+$. Based on these findings, we conclude that the additional ammonium ions originated from N impurities in CoMo thin-films, and that these impurities entered the electrolyte when the electrode was under cathodic conditions.

Our findings are in accord with those based on definitive work in other laboratories,[112,223,227] hence we close with a few take-home lessons for the nitrogen fixation/reduction community (Table 7.3): (1) perform extensive control experiments for more precise ammonia quantification; (2) identify and remove all possible ammonia contamination sources, especially $^{15}NH_3$ impurities in $^{15}N_2$ gas (as identified in our study); (3) carefully monitor ammonium concentrations during each experimental step; and (4) perform electrolyses using both pure $^{15}N_2$ (with gas bubbler) and Ar gas, and compare ammonium yields under both conditions to evaluate electrode activities.

Table 7.3 Ammonia contamination sources

Ammonia contamination source	**Recommended action**
Ambient ammonia contamination	Extensive control experiments
Various electrochemical test components (electrolyte/RE/CE/EC cell/epoxy, etc.)	Careful sampling of electrolyte during each experiment step
NH_3 in N_2 gas (both ^{14}N/^{15}N)	Use gas bubblers: confirm removal of NH_3 before/after purging
Plastic (polypropylene) analysis vials	Use glass vials; minimize sample storage time
N-based impurities in electrode materials	Compare results of N_2/Ar-purging experiments

Acknowledgments

K.B. acknowledges funding from the fellowship program of the German National Academy of Sciences - Leopoldina, grant LPDS 2016-06. Acknowledgment is made to the donors of The American Chemical Society Petroleum Research Fund for partial support of this research. Sample preparation and analyses were performed at the Joint Center for Artificial Photosynthesis, supported through the Office of Science of the U.S. Department of Energy under Award Number DE-SC0004993, which also provided support for N.S.L.. W.Y., P.B. and C.G.R. and K.B. acknowledge use of instrumentation in the Molecular Materials Research Center of the Beckman Institute at Caltech. N.F.D. is grateful to the Linde Center for support. The Environmental Analysis Center is supported by the Beckman Institute at Caltech. W.Y. and C.G.R. acknowledge the Resnick Sustainability Institute at Caltech for fellowship support. Dr. Fabai Wu and Prof. Victoria Orphan are acknowledged for providing the $^{15}NH_4Cl$ standard reagent for UPLC-MS analysis. Mr.

Christopher Kenseth is thanked for assistance with UPLC-MS analysis. Dr. Yuanlong Huang is acknowledged for assistance with chemiluminescence analysis. All authors would like to acknowledge the reviewers for their valuable comments in the first round.

7.5 Experimental

7.5.1 Electrode preparations

n-type Si wafers (111, As-doped, resistivity < 0.005 Ω · cm, 3” diameter) were obtained from Addison Inc. To remove the surface oxide, the Si substrate was etched for 1 min in a buffered HF etchant (6:1 volume ratio of 40% NH_4F(aq) to 49% HF(aq)). All solutions were made from ultrapure water and analytical grade chemicals having an organic impurity level < 50 ppb.

Sputtering using a high-vacuum magnetron-sputtering system (AJA International Inc.) was performed at a constant Ar flow of 20 sccm and a working pressure of 5 mTorr. The Ti adhesion layer was directly sputtered onto the freshly etched n^+-Si wafer substrate using direct-current (DC) mode at 60 W for 35 min. The substrates were maintained at room temperature during the sputtering process. The CoMo thin-film was then co-sputtered in radio frequency (RF) mode by simultaneously keeping the Co target at 150 W and the Mo target at 100 W, while under a constant Ar flow of 20 sccm for 1 h. FeMo and NiMo were deposited using an analogous procedure in which the sputtering power for Fe and Mo targets was the same as that for Co. Sputtering of the single-element Co and Mo thin films was performed with the target maintained for 1 h at 150 W and 100 W, respectively.

The wafer was cut into ~1.2 cm^2 pieces and ohmic contacts to the electrodes were formed by rubbing an In-Ga eutectic onto the unpolished back sides of the Si samples. Conductive Ag paste was applied to attach a Sn-plated Cu wire to the ohmic contact. The wire was threaded into a glass tube and the sample was encapsulated and sealed to the glass tube using black, chemically resistant epoxy (Loctite 9460).

7.5.2 Electrochemical nitrogen reduction in aqueous and non-aqueous electrolytes

Electrochemical experiments were performed using BioLogic SP-200 potentiostats (Biologic, Grenoble, France) controlled by standard EC-Lab software. The experiments were performed in a standard three-electrode potentiostatic arrangement in a sealable electrochemical cell. A Pt wire (ALS Co., Ltd) was used as the counter electrode and Ag/AgCl (3 M KCl, WPI Europe, DRIREF-5) was used as the reference electrode. No Pt deposits were observed by XPS on the catalyst (working electrode) surface after electrochemical testing. All potentials are referenced herein, unless otherwise specified, relative to the potential of the reversible hydrogen electrode (RHE). The electrolyte was 20 mL of 50 mM aqueous or ethanolic H_2SO_4. Prior to the measurements, the electrolyte was purged for 10 min with Ar (5.0 purity, flow rate 165 mL min^{-1}) under gentle stirring to remove O_2(g) from the electrolyte. To saturate the electrolyte with N_2 prior to electrochemical measurements, the electrolyte was purged for 15 min with 99.999% pure N_2 (flow rate 95 mL min^{-1}). Before entering the electrochemical (EC) cell, N_2 and Ar were directed through a gas bubbler that contained 50 mM H_2SO_4(aq).

Cyclic voltammetric and chronoamperometric measurements were performed on electrodes under a constant N_2 flow (95 mL min^{-1}). For isotope labelling experiments, the electrolyte was purged with $^{15}N_2$ instead of $^{14}N_2$ (Sigma-Aldrich, product no. 364584-5L) for 10 min prior to electrochemical tests. Before entering the electrochemical cell, the $^{15}N_2$ gas was directed through an acid-trap that contained 5 mL of 50 mM H_2SO_4(aq). Electrochemical tests were performed under a continuous $^{15}N_2$ purge. Three independent tests were carried out for each condition using freshly prepared electrodes to produce the error bars in Figure 7.1 in the main text. After sampling electrolyte in the cell at different stages of the experiment, the same amount of fresh electrolyte was added back into the cell to keep the total volume of electrolyte constant.

7.5.3 Determination of ammonium, nitrate and nitrite concentration by IC

Ammonium concentrations were determined using a Dionex (Sunnyvale CA, now Thermo) ICS 2000. The sample solutions were diluted to a certain ratio and loaded into a 5 μL sample loop by an AS40 autosampler. The sample was then injected onto a CS16 separator column (2 x 250 mm) that was protected by a CG16 guard column (2 x 50 mm). Isocratic methanesulfonic acid eluent at 20 mM and pumped at 0.25 mL min^{-1} was produced using an eluent generator cartridge based on methylsulfonic acid. Analytes were detected by suppressed conductivity detection using a Dionex CERS-500 2 mm suppressor operated in eluent recycle mode with an applied current of 15 mA. Concentrations were calculated using Chromeleon 6.8 software.

The concentration of hydrazine was determined below the detection limit in the electrolyte by the Watt and Chrisp method.[252]

7.5.4 $^{14}NH_4^+$/$^{15}NH_4^+$ derivatization with dansyl chloride and analysis by UPLC-MS

Detection of $^{14}NH_4^+$ and $^{15}NH_4^+$ as dansyl chloride derivation products was performed on an Acquity I-Class UPLC coupled to a Xevo G2-S Quadrupole Time-of-Flight (QTof) mass spectrometer (both from Waters Corporation).[104] Dansyl chloride derivatization was performed by preparing solution mixtures in the following order in 2 mL glass vials: 0.4 mL of ~ 290 µM dansyl chloride (Sigma Aldrich, ≥ 99.0%, for HPLC) was dissolved in acetonitrile (UPLC grade). Subsequently, 0.3 mL of sodium carbonate stock solution (2 g/100 mL) and 0.4 mL of collected electrolyte in 50 mM H_2SO_4(aq) were added to the vials. The vials were vortexed for 10 s before loading onto the autosampler plate for analysis. To achieve effective derivatization without heating the samples, the pH of the sample solution was adjusted between 9 and 10 using pH paper. The derivatization products (dansyl-ammonia adducts) in the sample solution were separated by reverse phase chromatography with a binary water/acetonitrile solvent and a steady gradient. The concentration was quantitatively determined by calculating the peak area at specific mass positions (m/z = 251.0854 a.u. for ^{14}N and z = 252.0825 a.u. for ^{15}N, resp.). Data analyses were performed using the Quanlynx software and each collected sample was measured three times for accurate concentration determination.

7.5.5 Materials characterization

Atomic-force microscopy (AFM) images were obtained on a Bruker Dimension Icon or a Mutimode 8 using Bruker ScanAsyst-Air probes (silicon tip, silicon nitride cantilever, spring constant: 0.4 N/m, frequency: 50-90 kHz), operating in the ScanAsyst mode. The scan sizes were 1 µm x 1 µm. Images were analyzed using the Nanoscope Analysis software (version 1.9).

For transmission-electron microscopy (TEM), samples of the films were prepared using a focused Ga-ion beam (FIB) on a FEI Nova-600 Nanolab FIB/FESEM. Pt and C protection layers were deposited before exposure of the sample to the FIB. High-resolution TEM (HRTEM) images were obtained using a Tecnai Polara (F30) TEM at an accelerating voltage of 300 keV.

Scanning-electron micrographs (SEMs) were obtained with a FEI Nova NanoSEM 450, at an accelerating voltage of 5.00 kV with a working distance of 5 mm and an in-lens secondary electron detector.

7.5.6 X-ray photoelectron spectroscopy

X-ray photoelectron spectroscopy (XPS) was performed using a Kratos Axis Ultra system with a base pressure of 1 x 10^{-9} torr in the analysis chamber. A monochromatic Al Kα source was used to irradiate the sample with X-rays (1486.7eV) at 450 W. A hemispherical analyzer oriented for detection along the sample surface normal was used for maximum depth sensitivity. High-resolution spectra were acquired at a resolution of 25 meV with a pass energy of 10 eV. The data were analyzed using CasaXPS computer software. First, the spectra were calibrated by referencing the C 1s peak position to 284.8 eV. Co 2p, Mo 3d, N 1s peaks were then fitted to multiple subspecies each having Gaussian-Lorentz peak shapes.

Peak assignments were based on previous reports.[247–249] The transmission function (T) of the analyzer was recorded automatically during the time of measurement. The relative sensitivity factors (RSF) of each element were provided by the instrument manufacturer, and the inelastic mean free path (IMFP) of photoelectrons at different kinetic energies was calculated using Quases imfptpp2m computer software.

Surface compositions of each element were calculated by comparing the area of the peaks for each element normalized by (RSF*T*IMFP).

XPS data were obtained ex-situ i.e., after a short sample transfer through air, which could potentially confound linking the surface composition and oxidation states found in UHV to the ones present during electrocatalysis.

7.5.7 Determination of $NO/NO_2(g)$ concentration in Ar and $^{14}N_2$ gases

Approximately 15 L of a gas sample was collected from an Ar/N_2 cylinder (ultra-high purity, Airgas) and stored in a Teflon bag before further analysis. A chemiluminescence $NO/NO_2/NO_X$ Analyzer (Teledyne Model T200) was used to measure the NO and NO_2 concentrations in the gas sample at a 200 cm^3 min^{-1} flow rate. The measurement had an uncertainty of 0.5 ppb. The concentration was recorded after ~ 15 min of equilibration between the gas, sampling line, and chemiluminescence chamber inside the instrument.

7.6 Supplementary figures and tables

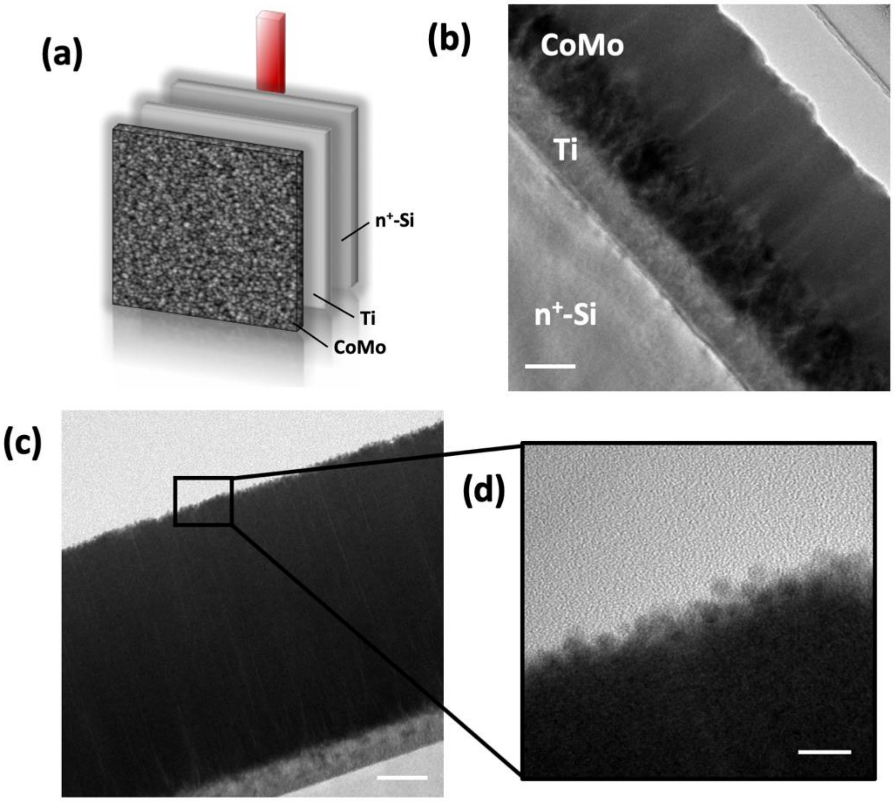

Figure S 7.1 **(a)** Scheme of the n$^+$-Si-Ti-CoMo electrode composition; **(b)** cross-section TEM image of the n$^+$-Si-Ti-CoMo electrode structure as-prepared; **(c)** HR-TEM image of the CoMo surface after 12 h testing at -0.54 V *vs.* RHE in 50 mM $H_2SO_{4(aq)}$ and **(d)** magnification of **(c)**. The scale bars are: **(b)** 100 nm; **(c)** 100 nm and **(d)** 10 nm.

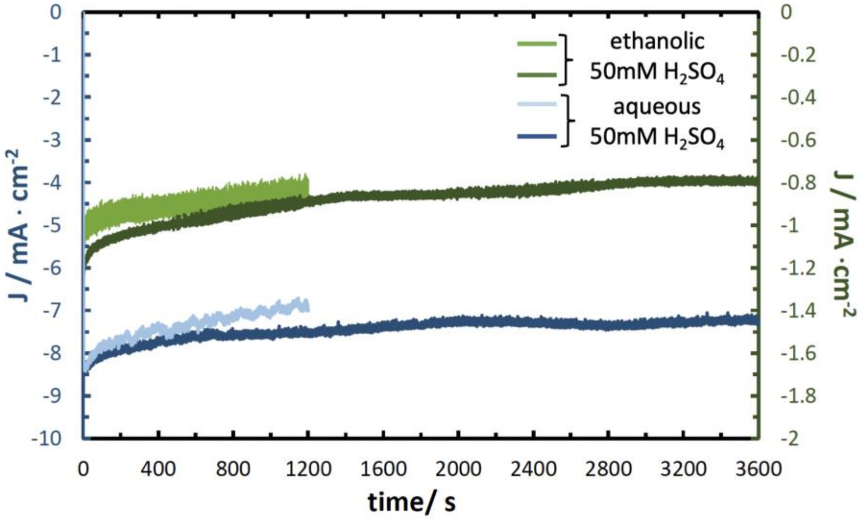

Figure S 7.2 Chronoamperometric (CA) measurements of an n^+-Si/Ti/CoMo electrode in aqueous 50 mM H_2SO_4 (blue) and 50 mM H_2SO_4 in ethanol (green).

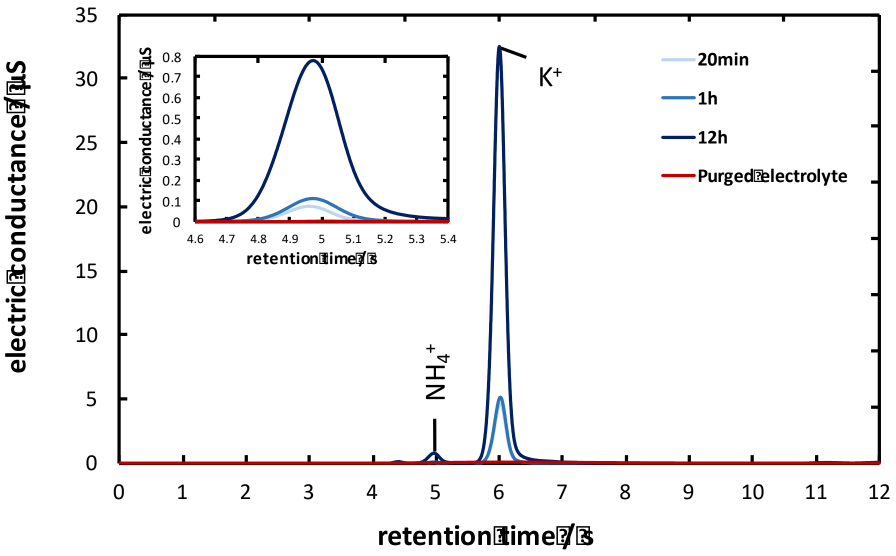

Figure S 7.3 Ion chromatogram of the electrolyte (red) and after 20 min (light blue), 1 h (cyan) and 12 h (dark blue) electrocatalysis of n^+-Si/Ti/CoMo electrode system in aqueous 50 mM H_2SO_4 at -0.54V *vs.* RHE. The inset shows the NH_4^+ chromatogram at a higher resolution. K^+ was introduced through the junction of Ag/AgCl (3 M KCl) reference electrode.

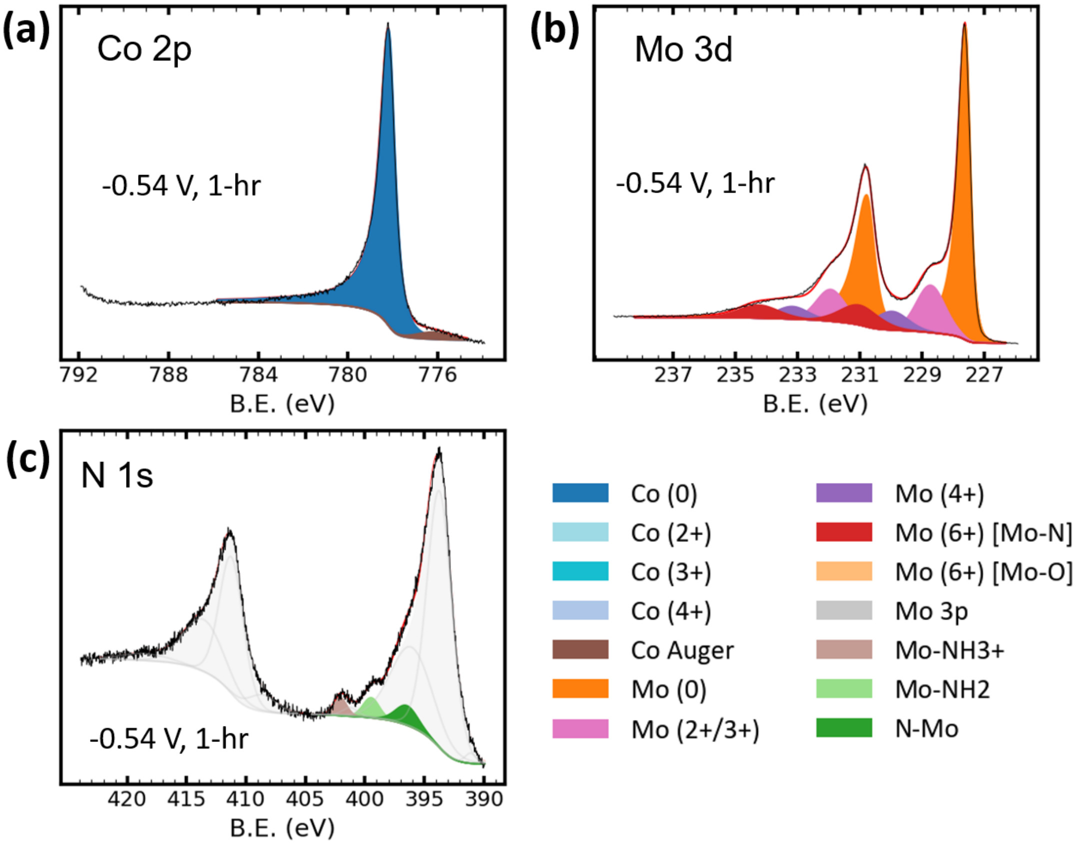

Figure S 7.4 X-ray photoelectron spectra of the n$^+$-Si/Ti/CoMo surface after 1 h of electrocatalysis in aqueous 50 mM H_2SO_4 electrolyte at -0.54V *vs* RHE. **(a)** Co 2p core levels; **(b)** Mo 3d core levels, and **(c)** N 1s core levels. Color coding is given in the legend; B.E is the binding energy.

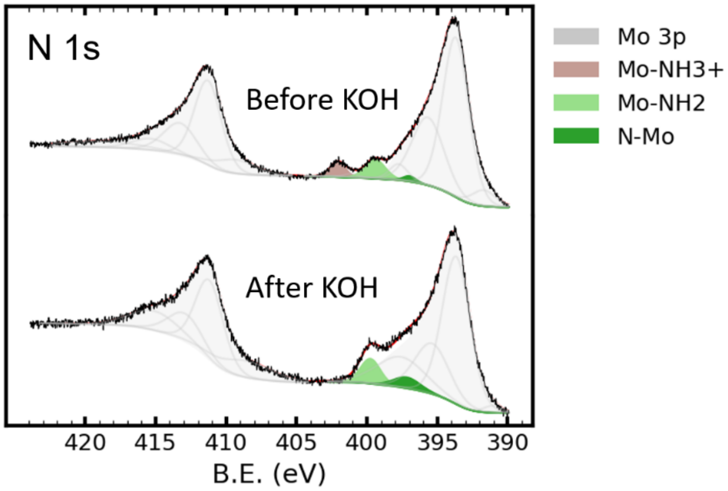

Figure S 7.5 N 1s core level X-ray photoelectron spectra of the CoMo surface after being held for 20 min at -0.54V *vs.* RHE in an aqueous 50 mM H_2SO_4 electrolyte (top) and after incubation of the electrode afterwards for 10 min in 10 mM KOH (bottom). Color coding is given in the legend; B.E is the binding energy.

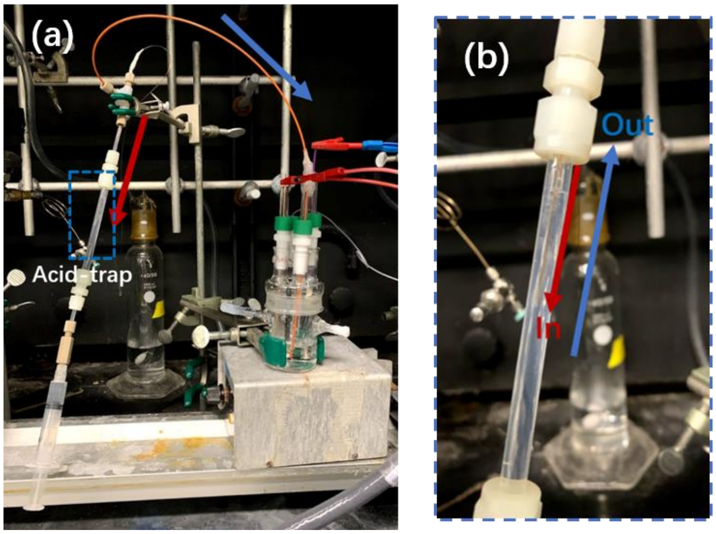

Figure S 7.6 **(a)** Photograph of our electrochemical experimental setup for purging with $^{15}N_2$ gas in the presence of an acid-trap **(b)**. The $^{15}N_2$ gas was directed through a plastic tube containing a solution of 50 mM H_2SO_4(aq) before going into the EC cell.

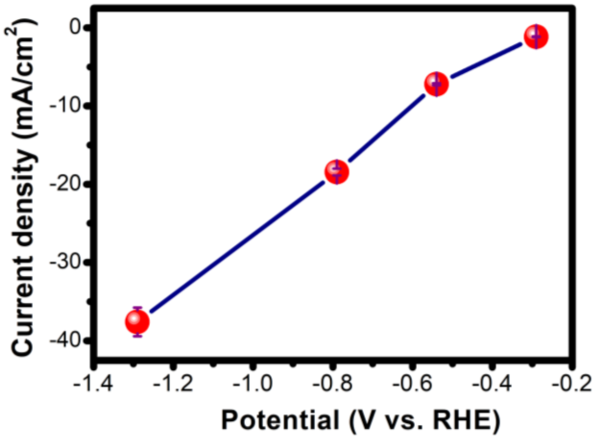

Figure S 7.7 Comparison of averaged current density of CoMo electrodes at different potentials under constant $^{15}N_2$ purging.

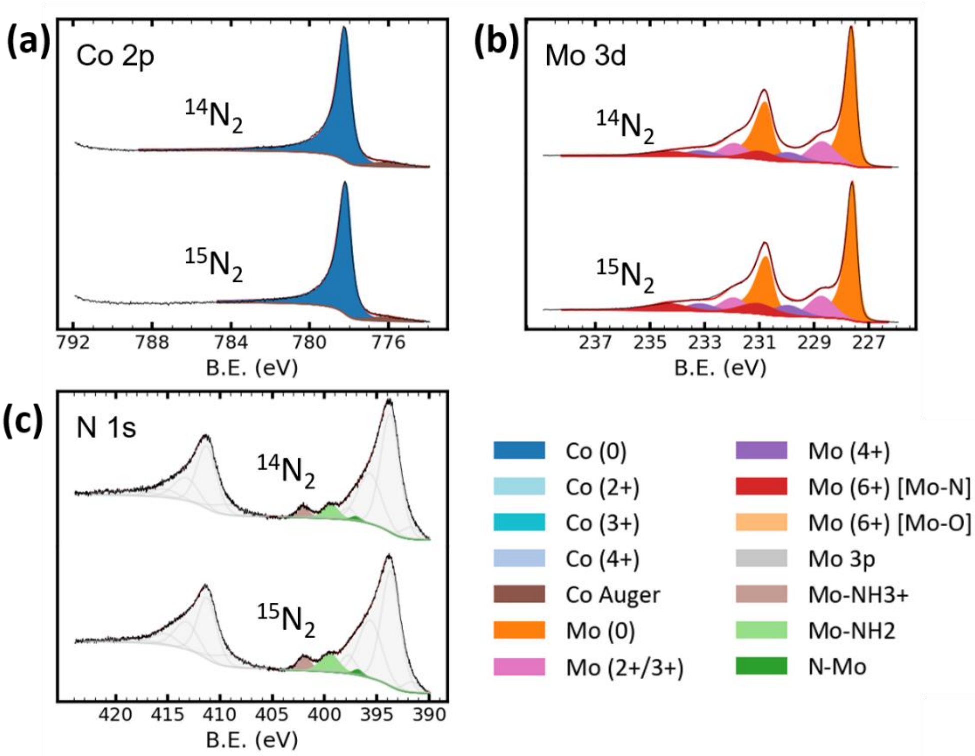

Figure S 7.8 X-ray photoelectron spectra of the n$^+$-Si/Ti/CoMo surface after 20 min of electrocatalysis in aqueous 50 mM H_2SO_4 electrolyte at -0.54 V *vs.* RHE under $^{14}N_2$ purging (top) and $^{15}N_2$ purging (bottom). **(a)** Co 2p core levels, **(b)** Mo 3d core levels, and **(c)** N 1s core levels. Color coding is given in the legend; B.E. is the binding energy.

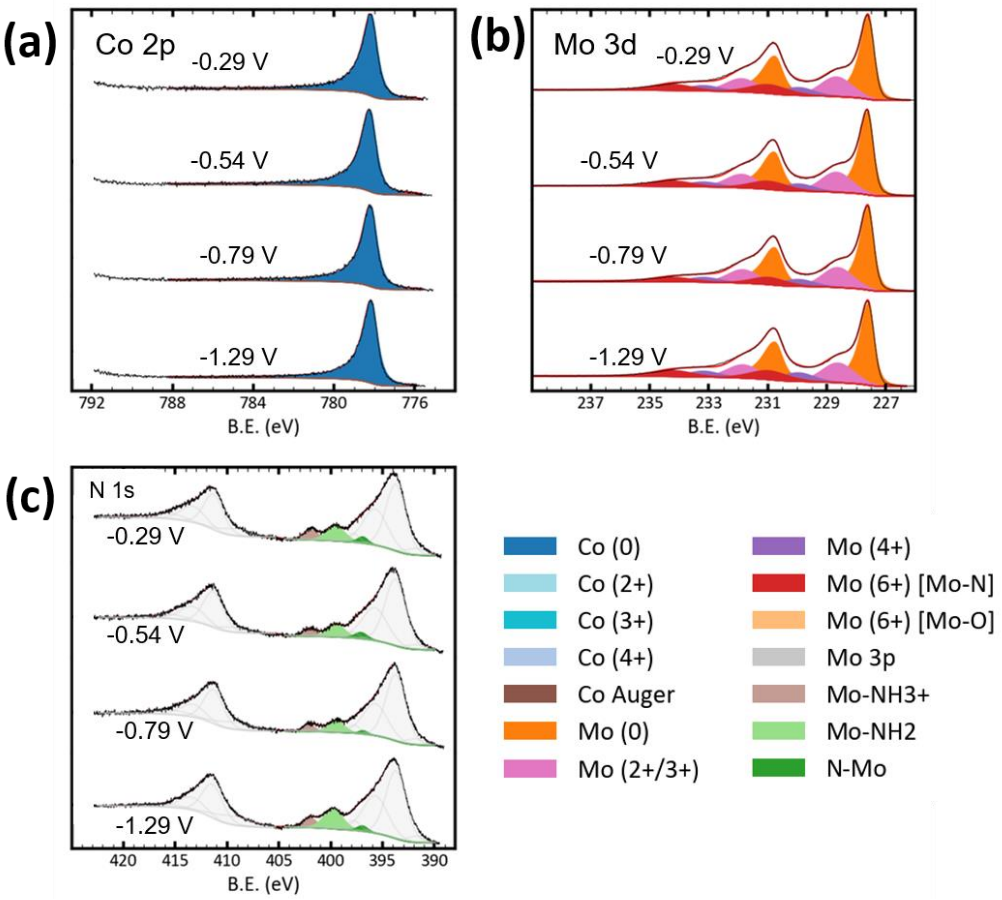

Figure S 7.9 X-ray photoelectron spectra of the n^+-Si/Ti/CoMo surface after 20 min of electrocatalysis in aqueous 50 mM H_2SO_4 electrolyte at four different potentials vs. RHE. **(a)** Co 2p core levels, **(b)** Mo 3d core levels, and **(c)** N 1s core levels. Color coding is given in the legend; B.E. is the binding energy.

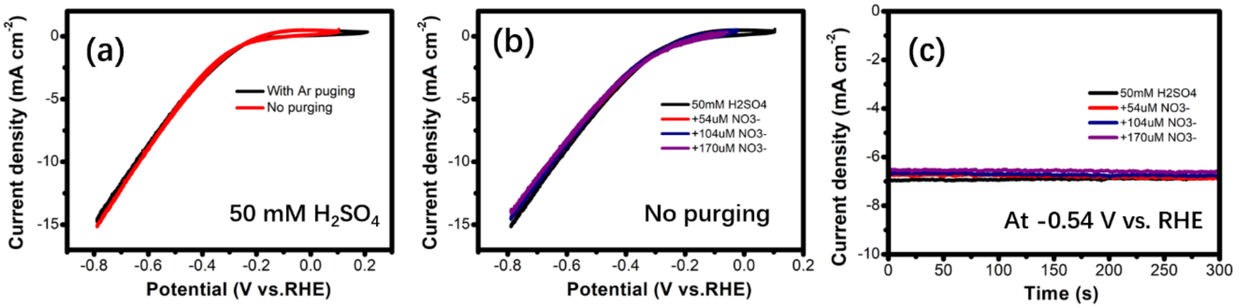

Figure S 7.10 (a) Comparison of cyclic voltammograms (CVs) obtained at the CoMo electrode tested in 50 mM H_2SO_4(aq) with Ar(g) purging and without purging. (b) Comparison of CVs (CoMo electrode) tested in 50 mM H_2SO_4(aq) without purging in the presence of different concentrations (0, 54, 104, 170 μM) of nitrate ions (scan rate: 20 mV s^{-1}). (c) Comparison of chronoamperometry (CA) at the CoMo electrode held at -0.54 V vs. RHE in 50 mM H_2SO_4(aq) without purging in the presence of different concentrations (0, 54, 104, 170 μM) of nitrate ions.

Table S 7.1 Measured NH_4^+ concentrations by IC obtained from various control experiments. The NH_4^+-production yield in Table 7.1 (main text) is corrected against these background NH_4^+ values under corresponding conditions. The total volume of electrolyte is 20 mL.

Control Experiment	**t [min]**	**c(NH_4^+) [µM]**	**Total amount [nmol]**
50 mM H_2SO_4		1.1	22
CoMo at E_{oc}	20	1.4	28
CoMo at E_{oc}	60	2.6	52
CoMo at E_{oc}	720	2.8	56
NiMo at E_{oc}	20	1.4	28
FeMo at E_{oc}	20	1.7	34
Co at E_{oc}	20	1.0	20
Mo at E_{oc}	20	2.5	50
CoMo at E_{oc} in 50 mM HCl	20	1.9	38
CoMo at E_{oc} in 50 mM $HClO_4$	20	2.3	46
50 mM H_2SO_4, Ar/N_2 Purge	20	0.8	16
50 mM H_2SO_4, Ar/N_2 Purge	60	0.7	14
50 mM H_2SO_4/Ethanol, Ar/N_2 Purge	20	2.0	40
Pt wire in 50 mM H_2SO_4	20	0.9	18
Pt wire in 50 mM H_2SO_4/Ethanol	20	2.5	50

Table S 7.2 Summary of the peak positions in the XPS analysis.[247–249]

Species	**Binding energy [eV]**
Co^0	778.2
Co^{2+}	781
Co^{3+}	782.7
Co-OH	786.5
$Mo^{2+/3+}$	228.7-228.8
$Mo^{3+/4+}$	230.2
Mo^{6+}	231.2-232.5
$Mo^{d+}(2 < d < 4)$	229.97
Mo-N	397.2
$NH_{ad}/NH_{2,ad}$	399.4
$NH3_{,ad}^{+}$	402.1

Table S 7.3 Comparison of electrode area-normalized increases in $^{14}NH_4^+$ ion concentration determined by the dansyl chloride derivatization/UPLC-MS method, after electrochemical tests using CoMo electrodes under various potential and gas-purging ($^{15}N_2$/Ar) conditions. The values correspond to the data points shown in Figure 7.5 in main text.

Entry	**E [V *vs.* RHE]**	**Purged gas[a]**	**Increased c($^{14}NH_4^+$) [μM · cm^{-2}]**
1	-0.29	$^{15}N_2$	3.2±0.1
2	-0.54	$^{15}N_2$	3.9±0.4
3	-0.54	$^{15}N_2$	6.9±0.2
4	-0.79	$^{15}N_2$	7.9±0.3
5	-1.29	$^{15}N_2$	17.9±0.7
6	-0.29	Ar	3.2±0.2
7	-0.54	Ar	3.7±0.03
8	-0.54	Ar	6.3±0.3
9	-0.54	Ar	7.9±0.2
10	-0.79	Ar	9.6±0.5
11	-1.29	Ar	6.8±0.4

[a] All purged gases were first passed through a gas bubbler of 50 mM H_2SO_4(aq).

Table S 7.4 Comparison of nitrate (NO_3^-) concentration measured by IC in the electrolyte samples collected at different experiment stages for four independent experiments.

Entry[a]	**Gas**	**c(NO_3^-) before purge [μM]**	**c(NO_3^-) after purge [μM]**	**c(NO_3^-) after EC**[b] **[μM]**	**$^{14}NH_4^+$ yield [μM]**
1	^{15}N	14.2	12.6	17.1	9.8
2	^{15}N	10.9	5.3	18.8	3.2
3	Ar	21.5	10.7	18.1	6.3
4	Ar	18.9	4.9	16.4	7

[a] All electrochemical experiments were performed at -0.54 V *vs.* RHE. The electrolyte volume was 20 mL. The concentrations of nitrite ions were below the detection limit for all electrolyte samples.

[b] EC represents electrochemical experiments

The 50 mM sulfuric acid stock solution had low concentrations (1.8 μM) of nitrate ions, which increased to >10 μM after transferring to the electrochemical cell possibly due to the additional contaminants in the cell. After 10-min of purging of both $^{15}N_2$ and Ar gas, the nitrate concentrations consistently decreased in four independent tests. This behavior indicated that continuous purging of $^{15}N_2$/Ar might have removed volatile HNO_3 species from the solution, instead of introducing additional NO_3^- into the electrolyte. In comparison, only a slight increase (6.9 μM) in the concentration of nitrate ions was observed in a small volume (5 mL) of 50 mM H_2SO_4(aq) electrolyte that contained 56.6 μM of pre-existing nitrate ions after purging with $^{14}N_2$ gas for 20 min. Furthermore, we used a chemiluminescence analyzer to measure the NO(g) and NO_2(g) concentrations in both Ar and $^{14}N_2$ gas cylinders (ultra-high purity, Airgas). The concentrations of NO(g) in both the Ar and $^{14}N_2$ cylinders was measured as 0 ppb, whereas ~ 1.3 and 3.1 ppb of NO_2(g), respectively, were detected. As a reference, the concentrations of NO(g) and NO_2(g) in the laboratory air were 0 and 4.8 ppb, respectively. The results showed that both $^{14}N_2$(g) and Ar gases were free of NO(g) and contained lower levels of NO_2(g) than the laboratory air.

After 20-min electrochemical experiments with electrodes introduced into electrolyte, increased concentrations of nitrate ions were found in all electrolyte samples. However, we did not find a direct correlation between these increased nitrate concentrations and the ammonium ($^{14}NH_4^+$) yields.

To exclude active nitrate reduction by the CoMo electrode, we performed an additional electrochemical experiment in which a CoMo electrode was held at -0.54 V vs. RHE in 50 mM H_2SO_4(aq) that additionally contained 40.6 μM of pre-existing nitrate ions (volume=20 mL). The electrochemical experiment was performed without any gas purging to avoid the effects of: (1) HNO_3 removal by purging; and (2) introduction of additional nitrate impurities. After electrochemical experiments, the nitrate concentration slightly increased to 41.9 μM after 20 min of testing, while the ammonium concentration increased from negligible amounts to 3.8 μM (measured by IC). These observations exclude substantial nitrate reduction at the CoMo electrode, which would have reduced the nitrate concentration during production of ammonia.

Collectively, these results show that μM-level nitrate ions were present in the electrolyte (although their concentration can vary at different experimental stages). We however conclude that it is unlikely that these nitrate ions led to the ammonia that was consistently observed in our study.

Table S 7.5 Contamination effect of the plastic polypropylene vials (Thermo Scientific C4000-11) for IC analysis found for 6 different samples, showing consistent increases of ammonium concentration over prolonged storage (10 days).

Sample No.	Initial results [µM]	After 10 days [µM]	Increase [µM]
1	0.3	6.4	6.1
2	5.2	10.3	5.1
3	49.8	65.3	15.5
4	0.4	3.4	3.0
5	0.4	3.8	3.4
6	2.4	6.0	3.6

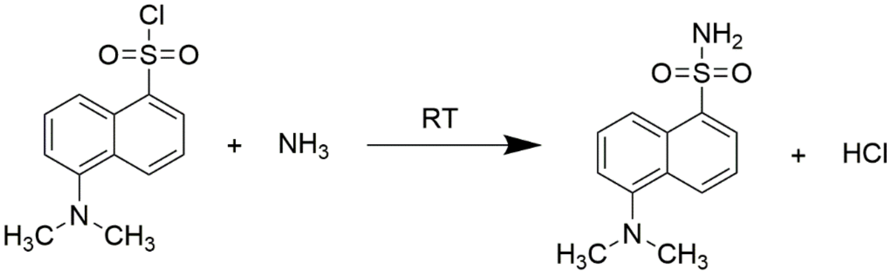

Equation S 7.1 The derivatization reaction of dansyl chloride with ammonia used for UPLC-MS analysis. RT is room temperature.

Chapter 8

8 CONCLUDING REMARKS

The works presented in this thesis has pointed out several important considerations when evaluating the stability of semiconductor photoelectrodes for solar fuel generation. For long, the instability of photoelectrodes was attributed to the dissolution of light-absorbing semiconductors in corrosive acidic and alkaline electrolytes. However, our results revealed that many factors beyond electrode dissolution can be responsible for the apparently unstable PEC performance of photoelectrodes.

Catalytic kinetics: In the first study of p-InP, we found drastic differences in stability between etched and platinized p-InP photoelectrodes. Bare p-InP electrodes suffered from rapid cathodic photocorrosion forming In^0 metal at surface, leading to decreasing J over short periods. The plated In^0 metal decreased both E_{oc} and J_{sc} by altering junction property and blocking incident light, respectively. Importantly, we discovered the onset E of such photocorrosion shifted positively compared with its thermodynamic E of -0.31 V vs. RHE, due to the generation of photovoltage inherent in illuminated p-InP electrode. This photovoltage effect convoluted a direct analysis of the thermodynamics of corrosion chemistry occurring at its front surface. In the presence of Pt, we discovered that such corrosion pathways were completely mitigated at both pH 0 and pH 14, whereas no In^0 was detected by XPS at electrode surface after prolonged PEC testing. This difference was attributed to a much lowered E_{surf} due to a fast kinetics of Pt, as well as the thermodynamic preference of the HER (E_{fuel}=0 V vs. RHE) over the cathodic corrosion of InP (E_{corro}=-0.31 V vs. RHE). As a result, the position of E_{surf} under a photo-stationary state relative to E_{fuel} and E_{corro}, defines the long-term corrosion chemistry at semiconductor surface. When E_{surf} moves in response to changes in catalytic kinetics, the thermodynamic coordinate (E, pH) of the electrode in the Pourbaix diagram also shifts correspondingly. Our results were consistent with the theoretical framework proposed by Gerischer of understanding the photoelectrode stability, where p-InP is ascribed to a “quasi-stable” semiconductor photocathode. In addition, we found this principle of kinetic stabilization also well applied to both p-$InGaP_2$ and pn^+-$InGaP_2$ photocathodes for the HER.

Surface stoichiometry: While p-InP/Pt electrodes exhibited no cathodic corrosion at both pH 0 and pH 14, another important finding is that substantial degradation in the J-E behavior occurred only in alkaline electrolyte. Such degradation corresponded to the formation of a surficial InO_x layer resulting in an In-rich surface. Based on the unified defect model proposed by Spicer, an In-rich surface led to surface states below the conduction band by 0.4 eV, thus limiting the PEC performance of the resulting p-InP/InO_x/Pt electrode. In comparison, a slow and continuous leaching of In^{3+} ions was observed for the same p-InP/Pt electrode at pH 0, indicating a higher solubility of InO_x in acidic solutions. Such a slow dissolution turned out to be somewhat beneficial as it resulted in a "self-cleaning" behavior continuously removing the detrimental surface states. Similar surface changes also occurred for p-$InGaP_2$/Pt photocathodes.

For p-GaAs, we identified a self-limiting galvanic corrosion in the presence of Pt catalyst, forming an non-stoichiometric and As^0-rich surface. After the rapid surface conversion, the resulting p-GaAs/Pt electrode exhibited a complete loss in photoactivity as well as a shunting type behavior. Comparatively, bare p-GaAs photoelectrodes preserved nearly stoichiometric surface after prolonged testing of the HER. Such a loss in photoactivity was again attributed to the presence of mid-gap surface states above the valence band of p-GaAs by 0.5 eV, induced by an As-rich surface.

Both of these examples emphasized the significant impact of altered surface stoichiometry towards the PEC behaviors of photoelectrodes. Non-stoichiometric surfaces can create additional surface states modifying the change separation property, as manifested in the measured J-E curve.

Physical stability vs. Electrochemical stability: For the p-InP/Pt system, we showed that a dissolving electrode at pH 0 yielded a stable J-t profile, whereas an insoluble electrode passivated with an InO_x surface exhibited unstable J-E behavior. For p-GaAs/Pt electrodes, we also showed that GaAs remained physically robust with little dissolution under cathodic E despite the substantial changes in the J-E behaviors. Therefore, the physical stability and electrochemical stability of a photoelectrode need to be evaluated separately. Contrary to the conventional view that dissolution is responsible for the electrode instability, we emphasize that more attention needs to be paid to correlating the surface changes with the evolution of the J-E behavior over time.

Structural integrity: Besides the corrosion chemistry of light-absorbing layers outlined above, the robustness of the supporting substrates is equally significant for maintaining a stable PEC performance under corrosive electrolytes. By ICP-MS and XPS, we revealed that the p^+-GaAs substrates, on which the pn^+-InGaP layers were grown, are also prone to anodic corrosion under positive operating E close to the maximum power point. Upon substantial removal of GaAs from substrate, severe cracking and delamination of the top $InGaP_2$ layers occurred, thus damaging the structural integrity of the whole photoelectrode. The occurrence of GaAs corrosion suggested the presence of structural defects within the upper epi-layers that allowed penetration of electrolytes. Such GaAs corrosion can be largely, but not completely, mitigated by holding electrode at more negative E. However, for a practical solar water-splitting cell, the operating E at the photocathode side is expected much positive to the RHE potential. Therefore, it is important to improve the process of material fabrication to eliminate such structural defects and minimize the substrate/electrolyte contact.

Outlook: Based on the mechanistic insights from this thesis, future strategies of stabilizing photoelectrodes can be rationally designed. For both InP and $InGaP_2$, it will be beneficial to develop surface protection or passivation scheme to inhibit their slow but continuous dissolution in acidic solution. It will be ideal that such protection or passivation strategies can be versatile such that they can also inhibit the formation of InO_x at electrode interface in basic media. Overall such a protection layer should minimize the direct contact between the light absorber and electrolyte, to slow down any interfacial reaction dictated by the Pourbaix predictions.

TiO_2 thin film is a promising starting point for such developments considering its Pourbaix stability across a wide range of E and pH, whereas more attention needs to be paid to optimize both the inter-layer adhesion and charge transport property at semiconductor/TiO_2 interface.[48,253–258] Further, it will be useful to systematically examine and compare the properties of TiO_2 thin-films deposited using different techniques and under various conditions, for use as protection layer of photocathode. Moreover, the electronic properties of TiO_2 thin-film can be tailored by both cationic and anionic (N or S) doping, offering additional space of improvement. Another promising route is to leverage controllable inter-layer diffusion between the semiconductor and TiO_2 layer to strengthen their inter-layer bonding, whereas a systematic TEM imaging may be needed.

For p-GaAs, a judicious choice of HER catalysts to avoid unfavorable interfacial reaction is the key to maintain electrode photoactivity. However, the PEC performance of p-GaAs electrode remains poor with nearly negligible photovoltage. Further works can be done by employing a multi-layered pn^+-GaAs homojunction, together with necessary electronically passivation and protection layers, to achieve high energy-conversion efficiency for the HER. For pn^+-$InGaP_2$ system, further efforts should be devoted to minimizing the structural defects by improving the material fabrication process, while identifying the microscopic origins of the above structural defects. It is speculated that the emergence of these defects may be correlated with the deposition environment and condition.

Besides, future works need to be done in establishing the dark stability of various III-V semiconductors, both with or without the HER catalysts. Restoring the original stoichiometric surface by leaving the electrode in the dark at E_{oc} for short periods may be potentially useful for healing the electronic character at photoelectrode interface. This can lead to the development of semiconductor photoelectrodes that are functionally stable by adapting to the natural day/night cycle.

9 APPENDIX

9.1 Fabrication of dual-working-electrode (DWE) of p-InP

A p-InP wafer was first attached to a Cu tape on a glass slide using Ag paint, before encapsulating its surrounding with epoxy. After Pt deposition over p-InP by either evaporation or electrodeposition, an Au thin-film was subsequently evaporated on top of the electrode. The deposited Au layer extended along epoxy, allowing its connection with another wire for making front contact. After the wire was firmly attached onto the Au layer, another layer of epoxy was applied for insulation. The detailed structure of p-InP DWE is presented in Figure 9.1a-b.

Dual-working electrode (DWE) was tested in a custom 3D-printed cell with a glass window (Figure 9.1c), under continuous H_2(g) purging and 1-sun illumination (100 mW cm^{-2}). Under varied back-contact potential (V_b), the front-contact potential (V_f) of the DWE was measured at open-circuit using the potential probe (S3) from a counter electrode of a BioLogic potentiostat.

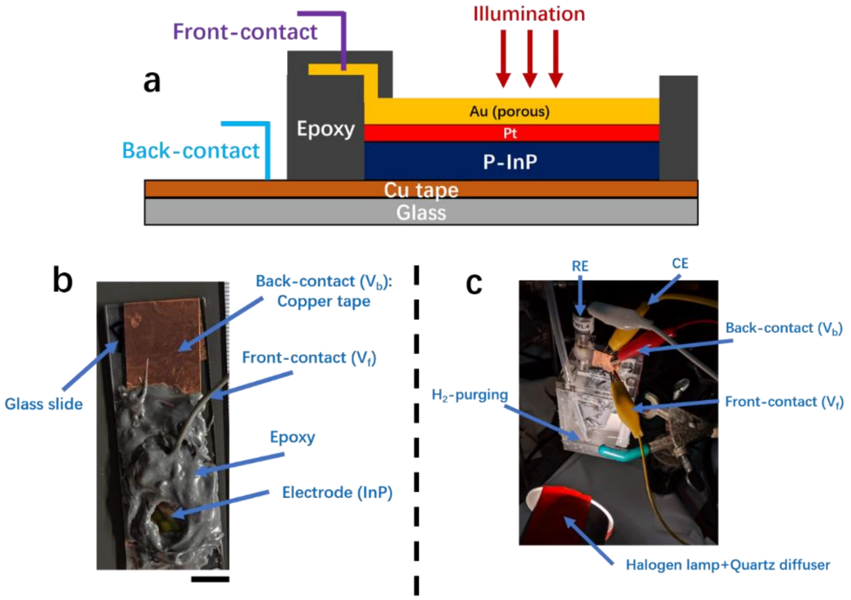

Figure 9.1 (a) Schematic illustration of a p-InP dual-working electrode (DWE) and (b) an image of an as-prepared p-InP/Pt/Au DWE. Scale bar: 1 cm. (c) Experimental setup of four-electrode measurement of a DWE under H_2(g) purging and 1-sun illumination.

9.2 DWE photoelectrochemistry of p-InP photocathodes

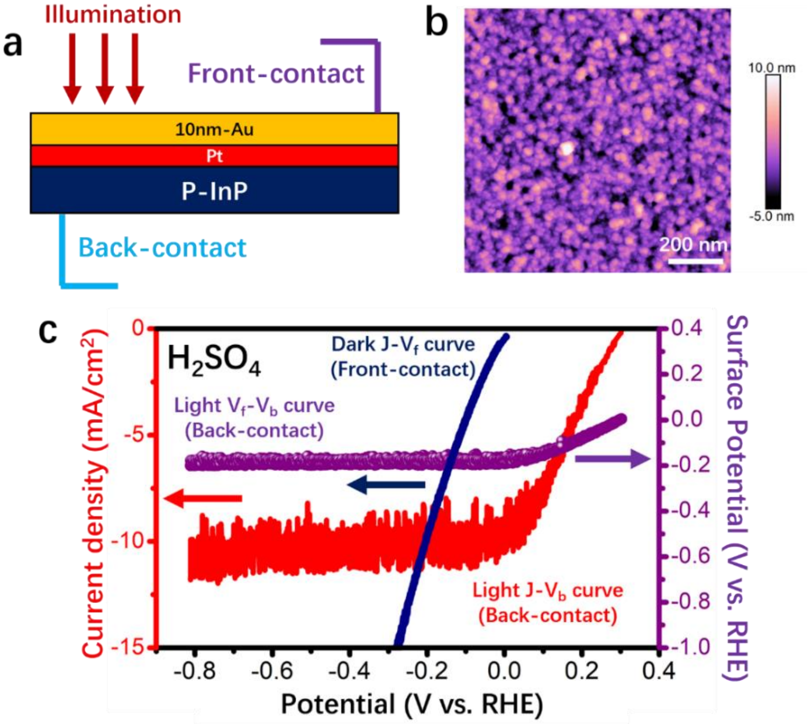

Figure 9.2 (a) Cross-sectional structure of an illuminated p-InP/3-nm Pt/10-nm Au (p-InP/3Pt/10Au) DWE with both back contact and front contact. (b) AFM image of a 10-nm Au thin-film prepared by e-beam evaporation, exhibiting nanoparticulate and porous morphology (R_q=1.9 nm). (c) Comparison of current density vs. back-contact potential curve (J-V_b, red) and front-contact vs. back-contact potential curve (V_f-V_b, purple) under illumination, and the current density vs. front-contact potential curve (J-V_f, blue) in the dark for the DWE shown in (a) measured in 1.0 M H_2SO_4(aq); the results of the same electrode tested in 1.0 M KOH (aq) is shown in Figure 9.3. Scan rate: 50 mV s^{-1}.

To distinguish between back-contact potential (V_b) and front-surface potential (V_f), a dual-working-electrode (DWE) was fabricated by evaporating a thin (~10 nm) Au layer over p-InP/Pt (or etched p-InP) electrode, for making front contact (Figure 9.2a).[77,259] Consistent with the previous studies, e-beam evaporated Au thin-film displayed an interconnected nanoparticulate morphology with a R_q of 1.9 nm Figure 9.2b). The porous morphology of the Au film allows electrolyte to penetrate through and reach the underlying Pt layer for performing the HER.

Under 1-sun illumination, the V_f of the p-InP/3-nm Pt/10-nm Au (p-InP/3Pt/10Au) DWE saturated at ~-0.17 V vs. RHE under J_{sc}=-10.5±0.2 mA cm^{-2} in H_2SO_4, and ~-0.23 V vs. RHE under J_{sc}=-11.7±0.2 mA cm^{-2} in KOH, even when V_b reached as negative as -0.9 V vs. RHE (Figure 9.3c and Figure 9.3). These results confirmed that the surface potential of the DWE is only a function of current density, instead of applied back-contact potential. The results obtained under potentiostatic conditions at different applied V_b were consistent with those of voltammetric measurements (Figure 9.4e-f).

Experiments of p-InP electrodes with electrodeposited Pt particles produced similar results, whereas the V_f also pinned at ~-0.12 V vs. RHE in H_2SO_4 and ~-0.23 V vs. RHE in KOH under similar J_{sc} (Figure 9.5). A comparison of the results of different DWEs was shown in Table 9.1.

When the p-InP/3Pt/10Au DWE was left at open circuit, its V_f remained ~0 V vs. RHE regardless of illumination (Figure 9.4a-b), suggesting equilibration with the RHE by the surficial Pt. Directly varying the V_f of p-InP/3Pt/10Au via front contact in the dark yielded J-V_f curves matching the HER behavior of Pt electrode (Figure 9.4c-d).

Measurement of V_f at the surface of an etched p-InP electrode was complicated by the considerable HER activities of Au. As shown in Figure 9.6, the p-InP/14Au DWE produced a V_f of ~-0.3 V vs. RHE under J_{sc}=-8.1±0.3 mA cm^{-2} in H_2SO_4, and ~-0.47 V vs. RHE under J_{sc}=-7.5±0.3 mA cm^{-2} in KOH. The measured V_f of the p-InP/14Au DWE were substantially more negative than those of the p-InP/3Pt/10Au DWE under the same conditions. These results confirmed that the presence of Pt caused a lower η under similar J_{sc}.

Altogether these results supported the conclusion that the surface potential (V_f) of p-InP photocathodes primarily depended on the catalytic kinetics at electrode surface.

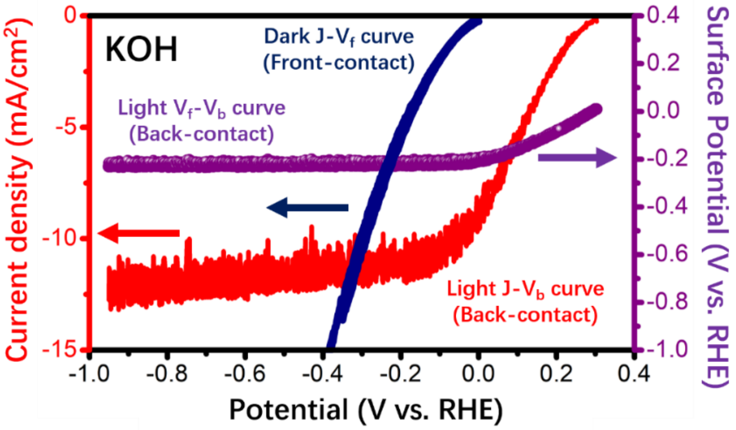

Figure 9.3 Comparison of the current density vs. back-contact potential (J-V$_b$, red) curve and front-contact vs. back-contact potential (V$_f$-V$_b$, purple) curve under illumination, and the measured current density vs. front-contact potential (J-V$_f$, blue) curve in the dark for the same DWE in Figure 9.2 in contact with 1.0 M KOH (aq).

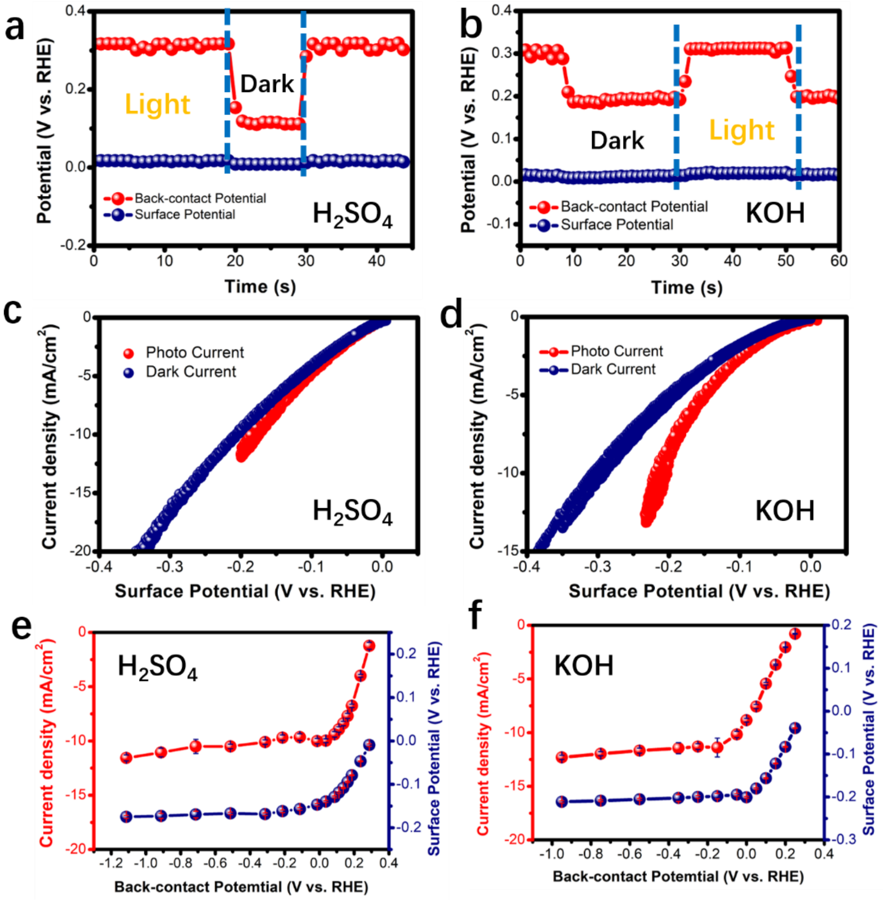

Figure 9.4 (a-b) Comparison of open-circuit potentials at back-contact and front-contact under dark and illumination for the DWE shown in Figure 9.2a in (a) 1.0 M H_2SO_4(aq) and (b) 1.0 M KOH(aq). (c-d) Comparison of the measured J-V_f curves from controlling either V_b under illumination (denoted as “photo current”) or V_f in the dark (denoted as “dark current”) in in (c) 1.0 M H_2SO_4(aq) and (d) 1.0 M KOH(aq). (e-f) Comparison of measured surface potentials (blue) and current densities (red) under potentiostatic conditions (held for 60 s) at each applied potential of V_b in (e) 1.0 M H_2SO_4(aq) and (f) 1.0 M KOH(aq).

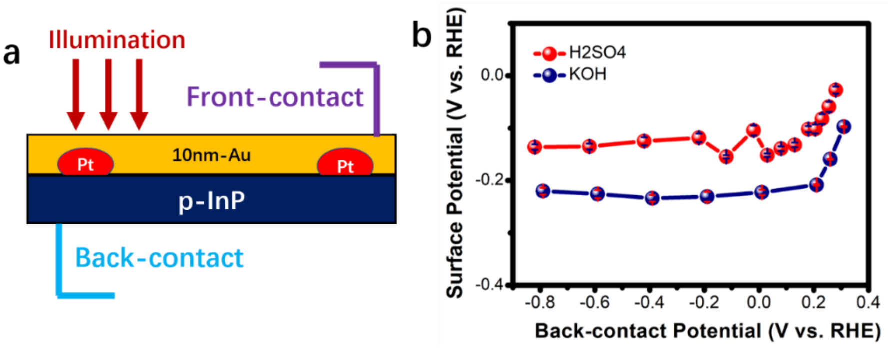

Figure 9.5 (a) Schematic illustration of a DWE of p-InP with electrodeposited Pt particles. (b) Comparison of measured V_f of the DWE in (a) under varied V_b in 1.0 M H_2SO_4(aq) and 1.0 M KOH(aq) under 1-sun illumination.

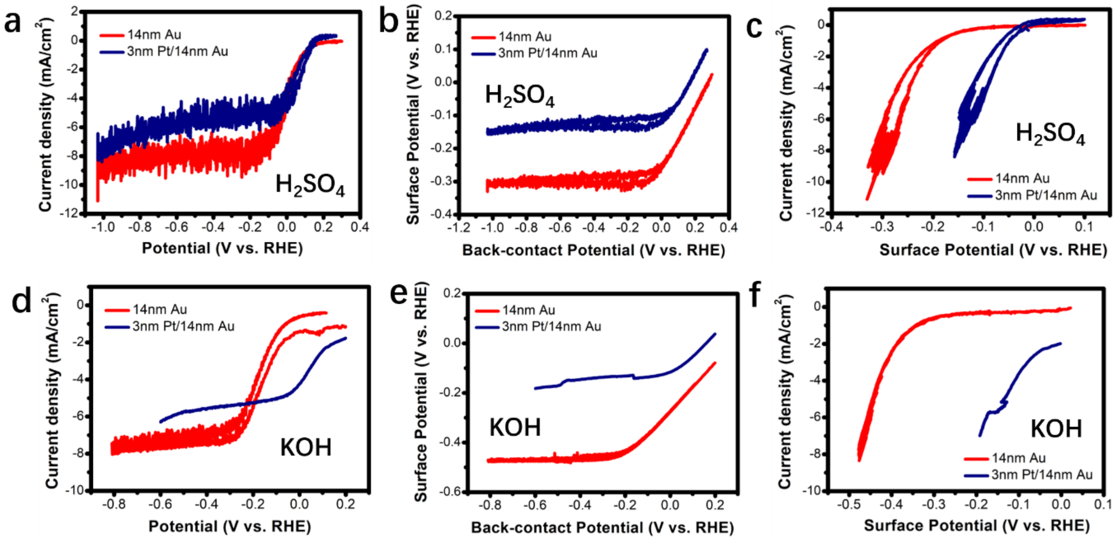

Figure 9.6 Comparison of (a,d) J-V_b curves, (b,e) V_f-V_b curves and (c,f) J-V_f curves (V_f at open-circuit) for the p-InP/3Pt/14Au (blue) and p-InP/14Au (red) DWE in contact with (a-c) 1.0 M H_2SO_4(aq) and (d-f) 1.0 M KOH(aq) under 1-sun illumination. Scan rate: 50 mV s^{-1}.

Table 9.1 Summary of measured V_f under J_{sc} for different p-InP DWE

Electrolyte	**Electrode**[a]	**J_{sc} (mA cm^{-2})**[b]	**V_f (V vs. RHE)**
H_2SO_4	Ed-Pt/10Au[c]	-13.1±0.2	-0.12±0.008
	3Pt/10Au	-10.5±0.2	-0.17±0.003
	14Au	-8.1±0.3	-0.3±0.005
	3Pt/14Au	-5.8±0.3	-0.13±0.003
KOH	Ed-Pt/10Au	-13.7±0.2	-0.23±0.006
	3Pt/10Au	-11.7±0.2	-0.23±0.008
	14Au	-7.5±0.3	-0.47±0.003
	3Pt/14Au	-6.0±0.05	-0.17±0.001

[a] Number in the column represents the thickness (nm) of evaporated Pt or Au film; [b] J_{sc} represents the light-limited current density as measured at V_b =-0.4/-0.5 V vs. RHE; [c] Ed means electrodeposition.

BIBLIOGRAPHY

(1) Lewis, N. S.; Nocera, D. G. Powering the Planet: Chemical Challenges in Solar Energy Utilization. *Proceedings of the National Academy of Sciences* **2006**, *103* (43), 15729–15735.

(2) Davis, S. J.; Lewis, N. S.; Shaner, M.; Aggarwal, S.; Arent, D.; Azevedo, I. L.; Benson, S. M.; Bradley, T.; Brouwer, J.; Chiang, Y.-M.; Clack, C. T. M.; Cohen, A.; Doig, S.; Edmonds, J.; Fennell, P.; Field, C. B.; Hannegan, B.; Hodge, B.-M.; Hoffert, M. I.; Ingersoll, E.; Jaramillo, P.; Lackner, K. S.; Mach, K. J.; Mastrandrea, M.; Ogden, J.; Peterson, P. F.; Sanchez, D. L.; Sperling, D.; Stagner, J.; Trancik, J. E.; Yang, C.-J.; Caldeira, K. Net-Zero Emissions Energy Systems. *Science* **2018**, *360* (6396), eaas9793. https://doi.org/10.1126/science.aas9793.

(3) Shaner, M. R.; Davis, S. J.; Lewis, N. S.; Caldeira, K. Geophysical Constraints on the Reliability of Solar and Wind Power in the United States. *Energy Environ. Sci.* **2018**, *11* (4), 914–925. https://doi.org/10.1039/C7EE03029K.

(4) Dowling, J. A.; Rinaldi, K. Z.; Ruggles, T. H.; Davis, S. J.; Yuan, M.; Tong, F.; Lewis, N. S.; Caldeira, K. Role of Long-Duration Energy Storage in Variable Renewable Electricity Systems. *Joule* **2020**, *4* (9), 1907–1928. https://doi.org/10.1016/j.joule.2020.07.007.

(5) Gray, H. B. Powering the Planet with Solar Fuel. *Nature Chem* **2009**, *1* (1), 7–7. https://doi.org/10.1038/nchem.141.

(6) Cui, X.; Tang, C.; Zhang, Q. A Review of Electrocatalytic Reduction of Dinitrogen to Ammonia under Ambient Conditions. *Advanced Energy Materials* **2018**, *8* (22), 1800369. https://doi.org/10.1002/aenm.201800369.

(7) Ertl, G.; Thiele, N. XPS Studies with Ammonia Synthesis Catalysts. *Applications of Surface Science* **1979**, *3* (1), 99–112. https://doi.org/10.1016/0378-5963(79)90064-3.

(8) Seh, Z. W.; Kibsgaard, J.; Dickens, C. F.; Chorkendorff, I.; Nørskov, J. K.; Jaramillo, T. F. Combining Theory and Experiment in Electrocatalysis: Insights into Materials Design. *Science* **2017**, *355* (6321), eaad4998. https://doi.org/10.1126/science.aad4998.

(9) Shaner, M. R.; Atwater, H. A.; Lewis, N. S.; McFarland, E. W. A Comparative Technoeconomic Analysis of Renewable Hydrogen Production Using Solar Energy. *Energy Environ. Sci.* **2016**, *9* (7), 2354–2371. https://doi.org/10.1039/C5EE02573G.

(10) McKone, J. R.; Lewis, N. S.; Gray, H. B. Will Solar-Driven Water-Splitting Devices See the Light of Day? *Chemistry of Materials* **2014**, *26* (1), 407–414. https://doi.org/10.1021/cm4021518.

(11) Callejas, J. F.; Read, C. G.; Roske, C. W.; Lewis, N. S.; Schaak, R. E. Synthesis, Characterization, and Properties of Metal Phosphide Catalysts for the Hydrogen-Evolution Reaction. *Chem. Mater.* **2016**, *28* (17), 6017–6044. https://doi.org/10.1021/acs.chemmater.6b02148.

(12) Ager, J. W.; Shaner, M. R.; Walczak, K. A.; Sharp, I. D.; Ardo, S. Experimental Demonstrations of Spontaneous, Solar-Driven Photoelectrochemical Water Splitting. *Energy & Environmental Science* **2015**, *8* (10), 2811–2824. https://doi.org/10.1039/C5EE00457H.

(13) Popczun, E. J.; McKone, J. R.; Read, C. G.; Biacchi, A. J.; Wiltrout, A. M.; Lewis, N. S.; Schaak, R.

E. Nanostructured Nickel Phosphide as an Electrocatalyst for the Hydrogen Evolution Reaction. *Journal of the American Chemical Society* **2013**, *135* (25), 9267–9270. https://doi.org/10.1021/ja403440e.

(14) Read, C. G.; Callejas, J. F.; Holder, C. F.; Schaak, R. E. General Strategy for the Synthesis of Transition Metal Phosphide Films for Electrocatalytic Hydrogen and Oxygen Evolution. *ACS applied materials & interfaces* **2016**, *8* (20), 12798–12803. https://doi.org/10.1021/acsami.6b02352.

(15) Carim, A. I.; Saadi, F. H.; Soriaga, M. P.; Lewis, N. S. Electrocatalysis of the Hydrogen-Evolution Reaction by Electrodeposited Amorphous Cobalt Selenide Films. *J. Mater. Chem. A* **2014**, *2* (34), 13835–13839. https://doi.org/10.1039/C4TA02611J.

(16) Jaramillo, T. F.; Jorgensen, K. P.; Bonde, J.; Nielsen, J. H.; Horch, S.; Chorkendorff, I. Identification of Active Edge Sites for Electrochemical H_2 Evolution from MoS_2 Nanocatalysts. *Science* **2007**, *317* (5834), 100–102. https://doi.org/10.1126/science.1141483.

(17) Morales-Guio, C. G.; Stern, L.-A.; Hu, X. Nanostructured Hydrotreating Catalysts for Electrochemical Hydrogen Evolution. *Chemical Society Reviews* **2014**, *43* (18), 6555–6569. https://doi.org/10.1039/C3CS60468C.

(18) Hunter, B. M.; Gray, H. B.; Müller, A. M. Earth-Abundant Heterogeneous Water Oxidation Catalysts. *Chem. Rev.* **2016**, *116* (22), 14120–14136. https://doi.org/10.1021/acs.chemrev.6b00398.

(19) Burke, M. S.; Zou, S.; Enman, L. J.; Kellon, J. E.; Gabor, C. A.; Pledger, E.; Boettcher, S. W. Revised Oxygen Evolution Reaction Activity Trends for First-Row Transition-Metal (Oxy)Hydroxides in Alkaline Media. *J Phys Chem Lett* **2015**, *6* (18), 3737–3742. https://doi.org/10.1021/acs.jpclett.5b01650.

(20) Burke, M. S.; Kast, M. G.; Trotochaud, L.; Smith, A. M.; Boettcher, S. W. Cobalt–Iron (Oxy)Hydroxide Oxygen Evolution Electrocatalysts: The Role of Structure and Composition on Activity, Stability, and Mechanism. *J. Am. Chem. Soc.* **2015**, *137* (10), 3638–3648. https://doi.org/10.1021/jacs.5b00281.

(21) Dette, C.; Hurst, M. R.; Deng, J.; Nellist, M. R.; Boettcher, S. W. Structural Evolution of Metal (Oxy)Hydroxide Nanosheets during the Oxygen Evolution Reaction. *ACS Applied Materials & Interfaces* **2019**, *11* (6), 5590–5594. https://doi.org/10.1021/acsami.8b02796.

(22) Trotochaud, L.; Young, S. L.; Ranney, J. K.; Boettcher, S. W. Nickel-Iron Oxyhydroxide Oxygen-Evolution Electrocatalysts: The Role of Intentional and Incidental Iron Incorporation. *J Am Chem Soc* **2014**, *136* (18), 6744–6753. https://doi.org/10.1021/ja502379c.

(23) Trotochaud, L.; Boettcher, S. W. Precise Oxygen Evolution Catalysts: Status and Opportunities. *Scripta Materialia* **2014**, *74*, 25–32. https://doi.org/10.1016/j.scriptamat.2013.07.019.

(24) Hunter, B. M.; Winkler, J. R.; Gray, H. B. Iron Is the Active Site in Nickel/Iron Water Oxidation Electrocatalysts. *Molecules* **2018**, *23* (4). https://doi.org/10.3390/molecules23040903.

(25) Hunter, B. M.; Thompson, N. B.; Müller, A. M.; Rossman, G. R.; Hill, M. G.; Winkler, J. R.; Gray, H. B. Trapping an Iron(VI) Water-Splitting Intermediate in Nonaqueous Media. *Joule* **2018**, *2* (4), 747–763. https://doi.org/10.1016/j.joule.2018.01.008.

(26) King, L. A.; Hubert, M. A.; Capuano, C.; Manco, J.; Danilovic, N.; Valle, E.; Hellstern, T. R.; Ayers, K.; Jaramillo, T. F. A Non-Precious Metal Hydrogen Catalyst in a Commercial Polymer Electrolyte

Membrane Electrolyser. *Nat. Nanotechnol.* **2019**, *14* (11), 1071–1074. https://doi.org/10.1038/s41565-019-0550-7.

(27) Giesbrecht, P. K.; Müller, A. M.; Read, C. G.; Holdcroft, S.; Lewis, N. S.; Freund, M. S. Vapor-Fed Electrolysis of Water Using Earth-Abundant Catalysts in Nafion or in Bipolar Nafion/Poly(Benzimidazolium) Membranes. *Sustainable Energy Fuels* **2019**, *3* (12), 3611–3626. https://doi.org/10.1039/C9SE00672A.

(28) Oener, S. Z.; Foster, M. J.; Boettcher, S. W. Accelerating Water Dissociation in Bipolar Membranes and for Electrocatalysis. *Science* **2020**, *369* (6507), 1099–1103. https://doi.org/10.1126/science.aaz1487.

(29) McKone, J. R.; Sadtler, B. F.; Werlang, C. A.; Lewis, N. S.; Gray, H. B. Ni–Mo Nanopowders for Efficient Electrochemical Hydrogen Evolution. *ACS Catalysis* **2013**, *3* (2), 166–169. https://doi.org/10.1021/cs300691m.

(30) McKone, J. R.; Warren, E. L.; Bierman, M. J.; Boettcher, S. W.; Brunschwig, B. S.; Lewis, N. S.; Gray, H. B. Evaluation of Pt, Ni, and Ni–Mo Electrocatalysts for Hydrogen Evolution on Crystalline Si Electrodes. *Energy & Environmental Science* **2011**, *4* (9), 3573. https://doi.org/10.1039/c1ee01488a.

(31) Zhang, Y.; Gao, L.; Hensen, E. J. M.; Hofmann, J. P. Evaluating the Stability of Co_2 P Electrocatalysts in the Hydrogen Evolution Reaction for Both Acidic and Alkaline Electrolytes. *ACS Energy Lett.* **2018**, *3* (6), 1360–1365. https://doi.org/10.1021/acsenergylett.8b00514.

(32) Moreno-Hernandez, I. A.; MacFarland, C. A.; Read, C. G.; Papadantonakis, K. M.; Brunschwig, B. S.; Lewis, N. S. Crystalline Nickel Manganese Antimonate as a Stable Water-Oxidation Catalyst in Aqueous 1.0 M H_2SO_4. *Energy Environ. Sci.* **2017**, *10* (10), 2103–2108. https://doi.org/10.1039/C7EE01486D.

(33) Fujishima, A.; Honda, K. Photolysis-Decomposition of Water at the Surface of an Irradiated Semiconductor. *nature* **1972**, *238* (5385), 37–38.

(34) Kamat, P. V. A Conversation with Akira Fujishima. *ACS Energy Lett.* **2017**, *2* (7), 1586–1587. https://doi.org/10.1021/acsenergylett.7b00483.

(35) Wrighton, M. S.; Wolczanski, P. T.; Ellis, A. B. Photoelectrolysis of Water by Irradiation of Platinized N-Type Semiconducting Metal Oxides. *Journal of Solid State Chemistry* **1977**, *22* (1), 17–29. https://doi.org/10.1016/0022-4596(77)90185-2.

(36) Khaselev, O.; Turner, J. A. A Monolithic Photovoltaic-Photoelectrochemical Device for Hydrogen Production via Water Splitting. *Science* **1998**, *280* (5362), 425.

(37) Wang, H.; Deutsch, T.; Welch, A.; Turner, J. A. The Stability of Illuminated P-GaInP2 Semiconductor Photoelectrode. *International Journal of Hydrogen Energy* **2012**, *37* (19), 14009–14014. https://doi.org/10.1016/j.ijhydene.2012.07.052.

(38) Wang, H.; Turner, J. A. Photoelectrochemical Reduction of Nitrates at the Illuminated P-$GaInP_2$ Photoelectrode. *Energy Environ. Sci.* **2013**, *6* (6), 1802–1805. https://doi.org/10.1039/C3EE40745D.

(39) Khaselev, O.; Turner, J. A. Electrochemical Stability of P-$GaInP_2$ in Aqueous Electrolytes Toward Photoelectrochemical Water Splitting. *Journal of The Electrochemical Society* **1998**, *145* (10), 3335–3339. https://doi.org/10.1149/1.1838808.

(40) May, M. M.; Lewerenz, H.-J.; Lackner, D.; Dimroth, F.; Hannappel, T. Efficient Direct Solar-to-Hydrogen Conversion by in Situ Interface Transformation of a Tandem Structure. *Nature Communications* **2015**, *6*, 8286. https://doi.org/10.1038/ncomms9286 https://www.nature.com/articles/ncomms9286#supplementary-information.

(41) Cheng, W.-H.; Richter, M. H.; May, M. M.; Ohlmann, J.; Lackner, D.; Dimroth, F.; Hannappel, T.; Atwater, H. A.; Lewerenz, H.-J. Monolithic Photoelectrochemical Device for Direct Water Splitting with 19% Efficiency. *ACS Energy Letters* **2018**, *3* (8), 1795–1800. https://doi.org/10.1021/acsenergylett.8b00920.

(42) Reece, S. Y.; Hamel, J. A.; Sung, K.; Jarvi, T. D.; Esswein, A. J.; Pijpers, J. J. H.; Nocera, D. G. Wireless Solar Water Splitting Using Silicon-Based Semiconductors and Earth-Abundant Catalysts. *Science* **2011**, *334* (6056), 645–648. https://doi.org/10.1126/science.1209816.

(43) Licht, S.; Wang, B.; Mukerji, S.; Soga, T.; Umeno, M.; Tributsch, H. Efficient Solar Water Splitting, Exemplified by RuO_2 -Catalyzed AlGaAs/Si Photoelectrolysis. *J. Phys. Chem. B* **2000**, *104* (38), 8920–8924. https://doi.org/10.1021/jp002083b.

(44) Hu, S.; Xiang, C.; Haussener, S.; Berger, A. D.; Lewis, N. S. An Analysis of the Optimal Band Gaps of Light Absorbers in Integrated Tandem Photoelectrochemical Water-Splitting Systems. *Energy & Environmental Science* **2013**, *6* (10), 2984–2993. https://doi.org/10.1039/C3EE40453F.

(45) Chen, Y.; Hu, S.; Xiang, C.; Lewis, N. S. A Sensitivity Analysis to Assess the Relative Importance of Improvements in Electrocatalysts, Light Absorbers, and System Geometry on the Efficiency of Solar-Fuels Generators. *Energy Environ. Sci.* **2015**, *8* (3), 876–886. https://doi.org/10.1039/C4EE02314E.

(46) Hu, S.; Shaner, M. R.; Beardslee, J. A.; Lichterman, M.; Brunschwig, B. S.; Lewis, N. S. Amorphous TiO<Sub>2</Sub> Coatings Stabilize Si, GaAs, and GaP Photoanodes for Efficient Water Oxidation. *Science* **2014**, *344* (6187), 1005.

(47) Fu, H. J.; Moreno-Hernandez, I. A.; Buabthong, P.; Papadantonakis, K. M.; Brunschwig, B. S.; Lewis, N. S. Enhanced Stability of Silicon for Photoelectrochemical Water Oxidation through Self-Healing Enabled by an Alkaline Protective Electrolyte. *Energy Environ. Sci.* **2020**, *13* (11), 4132–4141. https://doi.org/10.1039/D0EE02250K.

(48) Bae, D.; Shayestehaminzadeh, S.; Thorsteinsson, E. B.; Pedersen, T.; Hansen, O.; Seger, B.; Vesborg, P. C. K.; Ólafsson, S.; Chorkendorff, I. Protection of Si Photocathode Using TiO_2 Deposited by High Power Impulse Magnetron Sputtering for H_2 Evolution in Alkaline Media. *Solar Energy Materials and Solar Cells* **2016**, *144*, 758–765. https://doi.org/10.1016/j.solmat.2015.10.020.

(49) Sun, K.; McDowell, M. T.; Nielander, A. C.; Hu, S.; Shaner, M. R.; Yang, F.; Brunschwig, B. S.; Lewis, N. S. Stable Solar-Driven Water Oxidation to O_2(g) by Ni-Oxide-Coated Silicon Photoanodes. *The Journal of Physical Chemistry Letters* **2015**, *6* (4), 592–598. https://doi.org/10.1021/jz5026195.

(50) Sun, K.; Saadi, F. H.; Lichterman, M. F.; Hale, W. G.; Wang, H.-P.; Zhou, X.; Plymale, N. T.; Omelchenko, S. T.; He, J.-H.; Papadantonakis, K. M.; Brunschwig, B. S.; Lewis, N. S. Stable Solar-Driven Oxidation of Water by Semiconducting Photoanodes Protected by Transparent Catalytic Nickel Oxide Films. *Proceedings of the National Academy of Sciences* **2015**, *112* (12), 3612.

(51) Zhou, X.; Liu, R.; Sun, K.; Friedrich, D.; McDowell, M. T.; Yang, F.; Omelchenko, S. T.; Saadi, F. H.; Nielander, A. C.; Yalamanchili, S.; Papadantonakis, K. M.; Brunschwig, B. S.; Lewis, N. S.

Interface Engineering of the Photoelectrochemical Performance of Ni-Oxide-Coated n-Si Photoanodes by Atomic-Layer Deposition of Ultrathin Films of Cobalt Oxide. *Energy & Environmental Science* **2015**, *8* (9), 2644–2649. https://doi.org/10.1039/C5EE01687H.

(52) Zhou, X.; Liu, R.; Sun, K.; Papadantonakis, K. M.; Brunschwig, B. S.; Lewis, N. S. 570 MV Photovoltage, Stabilized n-Si/CoOx Heterojunction Photoanodes Fabricated Using Atomic Layer Deposition. *Energy & Environmental Science* **2016**, *9* (3), 892–897. https://doi.org/10.1039/C5EE03655K.

(53) Lichterman, M. F.; Sun, K.; Hu, S.; Zhou, X.; McDowell, M. T.; Shaner, M. R.; Richter, M. H.; Crumlin, E. J.; Carim, A. I.; Saadi, F. H.; Brunschwig, B. S.; Lewis, N. S. Protection of Inorganic Semiconductors for Sustained, Efficient Photoelectrochemical Water Oxidation. *Catalysis Today* **2016**, *262*, 11–23. https://doi.org/10.1016/j.cattod.2015.08.017.

(54) Masuda, T.; Tomasulo, S.; Lang, J. R.; Lee, M. L. Comparison of Single Junction AlGaInP and GaInP Solar Cells Grown by Molecular Beam Epitaxy. *Journal of Applied Physics* **2015**, *117* (9), 094504. https://doi.org/10.1063/1.4914046.

(55) Fan, S.; Yu, Z. J.; Hool, R. D.; Dhingra, P.; Weigand, W.; Kim, M.; Ratta, E. D.; Li, B. D.; Sun, Y.; Holman, Z. C.; Lee, M. L. Current-Matched III–V/Si Epitaxial Tandem Solar Cells with 25.0% Efficiency. *Cell Reports Physical Science* **2020**, *1* (9), 100208. https://doi.org/10.1016/j.xcrp.2020.100208.

(56) Lee, M. H.; Takei, K.; Zhang, J.; Kapadia, R.; Zheng, M.; Chen, Y.-Z.; Nah, J.; Matthews, T. S.; Chueh, Y.-L.; Ager, J. W.; Javey, A. P-Type InP Nanopillar Photocathodes for Efficient Solar-Driven Hydrogen Production. *Angewandte Chemie International Edition* **2012**, *51* (43), 10760–10764. https://doi.org/10.1002/anie.201203174.

(57) Hu, S.; Chi, C.-Y.; Fountaine, K. T.; Yao, M.; Atwater, H. A.; Dapkus, P. D.; Lewis, N. S.; Zhou, C. Optical, Electrical, and Solar Energy-Conversion Properties of Gallium Arsenide Nanowire-Array Photoanodes. *Energy & Environmental Science* **2013**, *6* (6), 1879. https://doi.org/10.1039/c3ee40243f.

(58) Lim, H.; Young, J. L.; Geisz, J. F.; Friedman, D. J.; Deutsch, T. G.; Yoon, J. High Performance III-V Photoelectrodes for Solar Water Splitting via Synergistically Tailored Structure and Stoichiometry. *Nature Communications* **2019**, *10* (1). https://doi.org/10.1038/s41467-019-11351-1.

(59) Sun, K.; Kuang, Y.; Verlage, E.; Brunschwig, B. S.; Tu, C. W.; Lewis, N. S. Sputtered NiOx Films for Stabilization of P+n-InP Photoanodes for Solar-Driven Water Oxidation. *Advanced Energy Materials* **2015**, *5* (11), 1402276. https://doi.org/10.1002/aenm.201402276.

(60) Buabthong, P.; Ifkovits, Z. P.; Kempler, P. A.; Chen, Y.; Nunez, P. D.; Brunschwig, B. S.; Papadantonakis, K. M.; Lewis, N. S. Failure Modes of Protection Layers Produced by Atomic Layer Deposition of Amorphous TiO $_2$ on GaAs Anodes. *Energy & Environmental Science* **2020**. https://doi.org/10.1039/D0EE02032J.

(61) Verlage, E.; Hu, S.; Liu, R.; Jones, R. J. R.; Sun, K.; Xiang, C.; Lewis, N. S.; Atwater, H. A. A Monolithically Integrated, Intrinsically Safe, 10% Efficient, Solar-Driven Water-Splitting System Based on Active, Stable Earth-Abundant Electrocatalysts in Conjunction with Tandem III-V Light Absorbers Protected by Amorphous TiO2 Films. *Energy & Environmental Science* **2015**, *8* (11), 3166–3172. https://doi.org/10.1039/C5EE01786F.

(62) Lichterman, M. F.; Carim, A. I.; McDowell, M. T.; Hu, S.; Gray, H. B.; Brunschwig, B. S.; Lewis, N. S. Stabilization of N-Cadmium Telluride Photoanodes for Water Oxidation to O_2(g) in Aqueous Alkaline Electrolytes Using Amorphous TiO_2 Films Formed by Atomic-Layer Deposition. *Energy Environ. Sci.* **2014**, *7* (10), 3334–3337. https://doi.org/10.1039/c4ee01914h.

(63) Heller, A.; Vadimsky, R. G. Efficient Solar to Chemical Conversion: 12% Efficient Photoassisted Electrolysis in the [p-Type InP(Ru)]/HCl-KCl/Pt(Rh) Cell. *Physical Review Letters* **1981**, *46* (17), 1153–1156.

(64) Heller, A.; Miller, B.; Thiel, F. A. 11.5% Solar Conversion Efficiency in the Photocathodically Protected P-InP/V3+-V2+-HCI/C Semiconductor Liquid Junction Cell. *Applied Physics Letters* **1981**, *38* (4), 282–284. https://doi.org/10.1063/1.92307.

(65) Heller, A.; Miller, B.; Lewerenz, H. J.; Bachmann, K. J. An Efficient Photocathode for Semiconductor Liquid Junction Cells: 9.4% Solar Conversion Efficiency with p-InP/VCl3-VCl2-HCl/C. *Journal of the American Chemical Society* **1980**, *102* (21), 6555–6556. https://doi.org/10.1021/ja00541a029.

(66) Aharon-Shalom, E.; Heller, A. Efficient p - InP (Rh - H Alloy) and p - InP (Re - H Alloy) Hydrogen Evolving Photocathodes. *Journal of The Electrochemical Society* **1982**, *129* (12), 2865–2866. https://doi.org/10.1149/1.2123695.

(67) Gu, J.; Aguiar, J. A.; Ferrere, S.; Steirer, K. X.; Yan, Y.; Xiao, C.; Young, J. L.; Al-Jassim, M.; Neale, N. R.; Turner, J. A. A Graded Catalytic–Protective Layer for an Efficient and Stable Water-Splitting Photocathode. *Nature Energy* **2017**, *2*, 16192. https://doi.org/10.1038/nenergy.2016.192 https://www.nature.com/articles/nenergy2016192#supplementary-information.

(68) Gu, J.; Yan, Y.; Young, J. L.; Steirer, K. X.; Neale, N. R.; Turner, J. A. Water Reduction by a P-GaInP2 Photoelectrode Stabilized by an Amorphous TiO2 Coating and a Molecular Cobalt Catalyst. *Nature materials* **2015**, *15*, 456. https://doi.org/10.1038/nmat4511 https://www.nature.com/articles/nmat4511#supplementary-information.

(69) Britto, R. J.; Benck, J. D.; Young, J. L.; Hahn, C.; Deutsch, T. G.; Jaramillo, T. F. Molybdenum Disulfide as a Protection Layer and Catalyst for Gallium Indium Phosphide Solar Water Splitting Photocathodes. *The journal of physical chemistry letters* **2016**, *7* (11), 2044–2049. https://doi.org/10.1021/acs.jpclett.6b00563.

(70) Britto, R. J.; Young, J. L.; Yang, Y.; Steiner, M. A.; LaFehr, D. T.; Friedman, D. J.; Beard, M.; Deutsch, T. G.; Jaramillo, T. F. Interfacial Engineering of Gallium Indium Phosphide Photoelectrodes for Hydrogen Evolution with Precious Metal and Non-Precious Metal Based Catalysts. *Journal of Materials Chemistry A* **2019**, *7* (28), 16821–16832. https://doi.org/10.1039/C9TA05247J.

(71) Gerischer, H. Electrolytic Decomposition and Photodecomposition of Compound Semiconductors in Contact with Electrolytes. *Journal of Vacuum Science and Technology* **1978**, *15* (4), 1422–1428. https://doi.org/10.1116/1.569800.

(72) Paracchino, A.; Laporte, V.; Sivula, K.; Grätzel, M.; Thimsen, E. Highly Active Oxide Photocathode for Photoelectrochemical Water Reduction. *Nature Mater* **2011**, *10* (6), 456–461. https://doi.org/10.1038/nmat3017.

(73) Chen, S.; Wang, L.-W. Thermodynamic Oxidation and Reduction Potentials of Photocatalytic

Semiconductors in Aqueous Solution. *Chemistry of Materials* **2012**, *24* (18), 3659–3666. https://doi.org/10.1021/cm302533s.

(74) Boettcher, S. W.; Warren, E. L.; Putnam, M. C.; Santori, E. A.; Turner-Evans, D.; Kelzenberg, M. D.; Walter, M. G.; McKone, J. R.; Brunschwig, B. S.; Atwater, H. A.; Lewis, N. S. Photoelectrochemical Hydrogen Evolution Using Si Microwire Arrays. *J Am Chem Soc* **2011**, *133* (5), 1216–1219. https://doi.org/10.1021/ja108801m.

(75) Nellist, M. R.; Laskowski, F. A.; Lin, F.; Mills, T. J.; Boettcher, S. W. Semiconductor-Electrocatalyst Interfaces: Theory, Experiment, and Applications in Photoelectrochemical Water Splitting. *Acc Chem Res* **2016**, *49* (4), 733–740. https://doi.org/10.1021/acs.accounts.6b00001.

(76) Laskowski, F. A. L.; Nellist, M. R.; Venkatkarthick, R.; Boettcher, S. W. Junction Behavior of N-Si Photoanodes Protected by Thin Ni Elucidated from Dual Working Electrode Photoelectrochemistry. *Energy & Environmental Science* **2017**, *10* (2), 570–579. https://doi.org/10.1039/C6EE03505A.

(77) Lin, F.; Boettcher, S. W. Adaptive Semiconductor/Electrocatalyst Junctions in Water-Splitting Photoanodes. *Nat Mater* **2014**, *13* (1), 81–86. https://doi.org/10.1038/nmat3811.

(78) Spurgeon, J. M.; Velazquez, J. M.; McDowell, M. T. Improving O_2 Production of WO_3 Photoanodes with IrO_2 in Acidic Aqueous Electrolyte. *Phys. Chem. Chem. Phys.* **2014**, *16* (8), 3623. https://doi.org/10.1039/c3cp55527e.

(79) Kelzenberg, M. D.; Boettcher, S. W.; Petykiewicz, J. A.; Turner-Evans, D. B.; Putnam, M. C.; Warren, E. L.; Spurgeon, J. M.; Briggs, R. M.; Lewis, N. S.; Atwater, H. A. Enhanced Absorption and Carrier Collection in Si Wire Arrays for Photovoltaic Applications. *Nature Mater* **2010**, *9* (3), 239–244. https://doi.org/10.1038/nmat2635.

(80) Zhu, J.; Hsu, C.-M.; Yu, Z.; Fan, S.; Cui, Y. Nanodome Solar Cells with Efficient Light Management and Self-Cleaning. *Nano Lett.* **2010**, *10* (6), 1979–1984. https://doi.org/10.1021/nl9034237.

(81) Wang, K. X.; Yu, Z.; Liu, V.; Cui, Y.; Fan, S. Absorption Enhancement in Ultrathin Crystalline Silicon Solar Cells with Antireflection and Light-Trapping Nanocone Gratings. *Nano Lett.* **2012**, *12* (3), 1616–1619. https://doi.org/10.1021/nl204550q.

(82) Kempler, P. A.; Richter, M. H.; Cheng, W.-H.; Brunschwig, B. S.; Lewis, N. S. Si Microwire-Array Photocathodes Decorated with Cu Allow CO_2 Reduction with Minimal Parasitic Absorption of Sunlight. *ACS Energy Lett.* **2020**, *5* (8), 2528–2534. https://doi.org/10.1021/acsenergylett.0c01334.

(83) Zhu, K.; Ma, D.; Boettcher, S. W. Energy Spotlight: Advances in Solar Cells and Solar Fuels. *ACS Energy Lett.* **2020**, *5* (8), 2739–2741. https://doi.org/10.1021/acsenergylett.0c01622.

(84) Roske, C. W.; Popczun, E. J.; Seger, B.; Read, C. G.; Pedersen, T.; Hansen, O.; Vesborg, P. C.; Brunschwig, B. S.; Schaak, R. E.; Chorkendorff, I.; Gray, H. B.; Lewis, N. S. Comparison of the Performance of CoP-Coated and Pt-Coated Radial Junction n(+)p-Silicon Microwire-Array Photocathodes for the Sunlight-Driven Reduction of Water to H_2(g). *J Phys Chem Lett* **2015**, *6* (9), 1679–1683. https://doi.org/10.1021/acs.jpclett.5b00495.

(85) Kempler, P. A.; Gonzalez, M. A.; Papadantonakis, K. M.; Lewis, N. S. Hydrogen Evolution with Minimal Parasitic Light Absorption by Dense Co–P Catalyst Films on Structured p-Si Photocathodes. *ACS Energy Letters* **2018**, 612–617. https://doi.org/10.1021/acsenergylett.8b00034.

(86) Shaner, M. R.; McKone, J. R.; Gray, H. B.; Lewis, N. S. Functional Integration of Ni–Mo

Electrocatalysts with Si Microwire Array Photocathodes to Simultaneously Achieve High Fill Factors and Light-Limited Photocurrent Densities for Solar-Driven Hydrogen Evolution. *Energy & Environmental Science* **2015**, *8* (10), 2977–2984. https://doi.org/10.1039/C5EE01076D.

(87) Lewerenz, H. J. Surface Scientific Aspects in Semiconductor Electrochemistry. *Chem. Soc. Rev.* **1997**, *26* (4), 239. https://doi.org/10.1039/cs9972600239.

(88) Menezes, S.; Lewerenz, H.-J.; Bachmann, K. J. Efficient and Stable Solar Cell by Interfacial Film Formation. *Nature* **1983**, *305* (5935), 615–616. https://doi.org/10.1038/305615a0.

(89) Doscher, H.; Supplie, O.; May, M. M.; Sippel, P.; Heine, C.; Munoz, A. G.; Eichberger, R.; Lewerenz, H. J.; Hannappel, T. Epitaxial III-V Films and Surfaces for Photoelectrocatalysis. *Chemphyschem* **2012**, *13* (12), 2899–2909. https://doi.org/10.1002/cphc.201200390.

(90) Klahr, B.; Gimenez, S.; Fabregat-Santiago, F.; Hamann, T.; Bisquert, J. Water Oxidation at Hematite Photoelectrodes: The Role of Surface States. *J. Am. Chem. Soc.* **2012**, *134* (9), 4294–4302. https://doi.org/10.1021/ja210755h.

(91) Du, C.; Zhang, M.; Jang, J.-W.; Liu, Y.; Liu, G.-Y.; Wang, D. Observation and Alteration of Surface States of Hematite Photoelectrodes. *J. Phys. Chem. C* **2014**, *118* (30), 17054–17059. https://doi.org/10.1021/jp5006346.

(92) Zandi, O.; Hamann, T. W. Enhanced Water Splitting Efficiency Through Selective Surface State Removal. *J. Phys. Chem. Lett.* **2014**, *5* (9), 1522–1526. https://doi.org/10.1021/jz500535a.

(93) Cabán-Acevedo, M.; Papadantonakis, K. M.; Brunschwig, B. S.; Lewis, N. S. Surface Passivation and Positive Band-Edge Shift of p-Si(111) Surfaces Functionalized with Mixed Methyl/Trifluoromethylphenylacetylene Overlayers. *J. Phys. Chem. C* **2020**, *124* (30), 16338–16349. https://doi.org/10.1021/acs.jpcc.0c02017.

(94) Boucher, D. G.; Kearney, K.; Ertekin, E.; Rose, M. J. Tuning P-Si(111) Photovoltage via Molecule|Semiconductor Electronic Coupling. *J. Am. Chem. Soc.* **2021**, *143* (6), 2567–2580. https://doi.org/10.1021/jacs.0c12075.

(95) Haick, H.; Hurley, P. T.; Hochbaum, A. I.; Yang, P.; Lewis, N. S. Electrical Characteristics and Chemical Stability of Non-Oxidized, Methyl-Terminated Silicon Nanowires. *J. Am. Chem. Soc.* **2006**, *128* (28), 8990–8991. https://doi.org/10.1021/ja056785w.

(96) Boucher, D. G.; Speller, J. R.; Han, R.; Osterloh, F. E.; Rose, M. J. Decoupling Effects of Surface Recombination and Barrier Height on P-Si(111) Photovoltage in Semiconductor|Liquid Junctions via Molecular Dipoles and Metal Oxides. *ACS Appl. Energy Mater.* **2019**, *2* (1), 66–79. https://doi.org/10.1021/acsaem.8b01563.

(97) Wong, K. T.; Lewis, N. S. What a Difference a Bond Makes: The Structural, Chemical, and Physical Properties of Methyl-Terminated Si(111) Surfaces. *Acc. Chem. Res.* **2014**, *47* (10), 3037–3044. https://doi.org/10.1021/ar500207y.

(98) Lee, D.; Wang, W.; Zhou, C.; Tong, X.; Liu, M.; Galli, G.; Choi, K.-S. The Impact of Surface Composition on the Interfacial Energetics and Photoelectrochemical Properties of BiVO4. *Nat Energy* **2021**. https://doi.org/10.1038/s41560-021-00777-x.

(99) Spicer, W. E.; Lindau, I.; Skeath, P.; Su, C. Y. Unified Defect Model and Beyond. *Journal of Vacuum Science and Technology* **1980**, *17* (5), 1019–1027. https://doi.org/10.1116/1.570583.

(100) Menezes, S.; Lewerenz, H. -J.; Betz, G.; Bachmann, K. J.; Kötz, R. Heterojunction by Photoelectrochemical Surface Transformation: N : CuInSe2 / p - CuISe3Se0. *J. Electrochem. Soc.* **1984**, *131* (12), 3030–3031. https://doi.org/10.1149/1.2115465.

(101) Lewerenz, H. J.; Schulte, K. H. Combined Photoelectrochemical Conditioning and Surface Analysis of InP Photocathodes. *Electrochimica Acta* **2002**, *47* (16), 2639–2651. https://doi.org/10.1016/S0013-4686(02)00125-1.

(102) Schulte, K. H.; Lewerenz, H. J. Combined Photoelectrochemical Conditioning and Photoelectron Spectroscopy Analysis of InP Photocathodes. I. The Modification Procedure. *Electrochimica Acta* **2002**, *47* (16), 2633–2638. https://doi.org/10.1016/S0013-4686(02)00124-X.

(103) Moreno-Hernandez, I. A.; Brunschwig, B. S.; Lewis, N. S. Tin Oxide as a Protective Heterojunction with Silicon for Efficient Photoelectrochemical Water Oxidation in Strongly Acidic or Alkaline Electrolytes. *Adv. Energy Mater.* **2018**, *8* (24), 1801155. https://doi.org/10.1002/aenm.201801155.

(104) Yu, W.; Lewis, N. S.; Gray, H. B.; Dalleska, N. F. Isotopically Selective Quantification by UPLC-MS of Aqueous Ammonia at Submicromolar Concentrations Using Dansyl Chloride Derivatization. *ACS Energy Letters* **2020**, 1532–1536. https://doi.org/10.1021/acsenergylett.0c00496.

(105) Ertl, G. Reactions at Surfaces: From Atoms to Complexity (Nobel Lecture). *Angewandte Chemie International Edition* **2008**, *47* (19), 3524–3535. https://doi.org/10.1002/anie.200800480.

(106) Singh, A. R.; Rohr, B. A.; Schwalbe, J. A.; Cargnello, M.; Chan, K.; Jaramillo, T. F.; Chorkendorff, I.; Nørskov, J. K. Electrochemical Ammonia Synthesis—The Selectivity Challenge. *ACS Catalysis* **2017**, *7* (1), 706–709. https://doi.org/10.1021/acscatal.6b03035.

(107) McEnaney, J. M.; Singh, A. R.; Schwalbe, J. A.; Kibsgaard, J.; Lin, J. C.; Cargnello, M.; Jaramillo, T. F.; Nørskov, J. K. Ammonia Synthesis from N_2 and H_2O Using a Lithium Cycling Electrification Strategy at Atmospheric Pressure. *Energy & Environmental Science* **2017**, *10* (7), 1621–1630. https://doi.org/10.1039/C7EE01126A.

(108) Lazouski, N.; Schiffer, Z. J.; Williams, K.; Manthiram, K. Understanding Continuous Lithium-Mediated Electrochemical Nitrogen Reduction. *Joule* **2019**, *3* (4), 1127–1139. https://doi.org/10.1016/j.joule.2019.02.003.

(109) Lazouski, N.; Chung, M.; Williams, K.; Gala, M. L.; Manthiram, K. Non-Aqueous Gas Diffusion Electrodes for Rapid Ammonia Synthesis from Nitrogen and Water-Splitting-Derived Hydrogen. *Nat Catal* **2020**, *3* (5), 463–469. https://doi.org/10.1038/s41929-020-0455-8.

(110) Andersen, S. Z.; Statt, M. J.; Bukas, V. J.; Shapel, S. G.; Pedersen, J. B.; Krempl, K.; Saccoccio, M.; Chakraborty, D.; Kibsgaard, J.; Vesborg, P. C. K.; Nørskov, J.; Chorkendorff, I. Increasing Stability, Efficiency, and Fundamental Understanding of Lithium-Mediated Electrochemical Nitrogen Reduction. *Energy Environ. Sci.* **2020**, *13* (11), 4291–4300. https://doi.org/10.1039/D0EE02246B.

(111) Li, Y.; Li, Y.; Sun, Y.; Butz, B.; Yan, K.; Koh, A. L.; Zhao, J.; Pei, A.; Cui, Y. Revealing Nanoscale Passivation and Corrosion Mechanisms of Reactive Battery Materials in Gas Environments. *Nano Lett.* **2017**, *17* (8), 5171–5178. https://doi.org/10.1021/acs.nanolett.7b02630.

(112) Andersen, S. Z.; Čolić, V.; Yang, S.; Schwalbe, J. A.; Nielander, A. C.; McEnaney, J. M.; Enemark-Rasmussen, K.; Baker, J. G.; Singh, A. R.; Rohr, B. A.; Statt, M. J.; Blair, S. J.; Mezzavilla, S.; Kibsgaard, J.; Vesborg, P. C. K.; Cargnello, M.; Bent, S. F.; Jaramillo, T. F.; Stephens, I. E. L.; Nørskov, J. K.; Chorkendorff, I. A Rigorous Electrochemical Ammonia Synthesis Protocol with

Quantitative Isotope Measurements. *Nature* **2019**, *570* (7762), 504–508. https://doi.org/10.1038/s41586-019-1260-x.

(113) Tang, C.; Qiao, S.-Z. How to Explore Ambient Electrocatalytic Nitrogen Reduction Reliably and Insightfully. *Chem. Soc. Rev.* **2019**, *48* (12), 3166–3180. https://doi.org/10.1039/C9CS00280D.

(114) Liu, H.; Guijarro, N.; Luo, J. The Pitfalls in Electrocatalytic Nitrogen Reduction for Ammonia Synthesis. *Journal of Energy Chemistry* **2021**, S2095495621000759. https://doi.org/10.1016/j.jechem.2021.01.039.

(115) Choi, J.; Suryanto, B. H. R.; Wang, D.; Du, H.-L.; Hodgetts, R. Y.; Ferrero Vallana, F. M.; MacFarlane, D. R.; Simonov, A. N. Identification and Elimination of False Positives in Electrochemical Nitrogen Reduction Studies. *Nat Commun* **2020**, *11* (1), 5546. https://doi.org/10.1038/s41467-020-19130-z.

(116) Yu, W.; Buabthong, P.; Read, C. G.; Dalleska, N. F.; Lewis, N. S.; Lewerenz, H.-J.; Gray, H. B.; Brinkert, K. Cathodic NH_4^+ Leaching of Nitrogen Impurities in CoMo Thin-Film Electrodes in Aqueous Acidic Solutions. *Sustainable Energy Fuels* **2020**, *4* (10), 5080–5087. https://doi.org/10.1039/D0SE00674B.

(117) Choi, J.; Du, H.-L.; Nguyen, C. K.; Suryanto, B. H. R.; Simonov, A. N.; MacFarlane, D. R. Electroreduction of Nitrates, Nitrites, and Gaseous Nitrogen Oxides: A Potential Source of Ammonia in Dinitrogen Reduction Studies. *ACS Energy Lett.* **2020**, *5* (6), 2095–2097. https://doi.org/10.1021/acsenergylett.0c00924.

(118) Nielander, A. C.; McEnaney, J. M.; Schwalbe, J. A.; Baker, J. G.; Blair, S. J.; Wang, L.; Pelton, J. G.; Andersen, S. Z.; Enemark-Rasmussen, K.; Čolić, V.; Yang, S.; Bent, S. F.; Cargnello, M.; Kibsgaard, J.; Vesborg, P. C. K.; Chorkendorff, I.; Jaramillo, T. F. A Versatile Method for Ammonia Detection in a Range of Relevant Electrolytes via Direct Nuclear Magnetic Resonance Techniques. *ACS Catalysis* **2019**, *9* (7), 5797–5802. https://doi.org/10.1021/acscatal.9b00358.

(119) Hodgetts, R. Y.; Kiryutin, A. S.; Nichols, P.; Du, H.-L.; Bakker, J. M.; Macfarlane, D. R.; Simonov, A. N. Refining Universal Procedures for Ammonium Quantification via Rapid ^{1}H NMR Analysis for Dinitrogen Reduction Studies. *ACS Energy Letters* **2020**, 736–741. https://doi.org/10.1021/acsenergylett.9b02812.

(120) Tembhurne, S.; Nandjou, F.; Haussener, S. A Thermally Synergistic Photo-Electrochemical Hydrogen Generator Operating under Concentrated Solar Irradiation. *Nat Energy* **2019**, *4* (5), 399–407. https://doi.org/10.1038/s41560-019-0373-7.

(121) Licht, S. Over 18% Solar Energy Conversion to Generation of Hydrogen Fuel; Theory and Experiment for Efficient Solar Water Splitting. *International Journal of Hydrogen Energy* **2001**, *26* (7), 653–659. https://doi.org/10.1016/S0360-3199(00)00133-6.

(122) Ben-Naim, M.; Britto, R. J.; Aldridge, C. W.; Mow, R.; Steiner, M. A.; Nielander, A. C.; King, L. A.; Friedman, D. J.; Deutsch, T. G.; Young, J. L.; Jaramillo, T. F. Addressing the Stability Gap in Photoelectrochemistry: Molybdenum Disulfide Protective Catalysts for Tandem III–V Unassisted Solar Water Splitting. *ACS Energy Letters* **2020**, *5* (8), 2631–2640. https://doi.org/10.1021/acsenergylett.0c01132.

(123) Singh, M. R.; Papadantonakis, K.; Xiang, C.; Lewis, N. S. An Electrochemical Engineering Assessment of the Operational Conditions and Constraints for Solar-Driven Water-Splitting Systems

at near-Neutral PH. *Energy & Environmental Science* **2015**, *8* (9), 2760–2767. https://doi.org/10.1039/C5EE01721A.

(124) Jin, J.; Walczak, K.; Singh, M. R.; Karp, C.; Lewis, N. S.; Xiang, C. An Experimental and Modeling/Simulation-Based Evaluation of the Efficiency and Operational Performance Characteristics of an Integrated, Membrane-Free, Neutral PH Solar-Driven Water-Splitting System. *Energy Environ. Sci.* **2014**, *7* (10), 3371–3380. https://doi.org/10.1039/C4EE01824A.

(125) Pourbaix, M. Atlas of Electrochemical Equilibria in Aqueous Solutions. *Atlas of electrochemical equilibria in aqueous solutions* **1974**.

(126) Jain, A.; Ong, S. P.; Hautier, G.; Chen, W.; Richards, W. D.; Dacek, S.; Cholia, S.; Gunter, D.; Skinner, D.; Ceder, G.; Persson, K. A. Commentary: The Materials Project: A Materials Genome Approach to Accelerating Materials Innovation. *APL Materials* **2013**, *1* (1), 011002. https://doi.org/10.1063/1.4812323.

(127) Persson, K. A.; Waldwick, B.; Lazic, P.; Ceder, G. Prediction of Solid-Aqueous Equilibria: Scheme to Combine First-Principles Calculations of Solids with Experimental Aqueous States. *Physical Review B* **2012**, *85* (23). https://doi.org/10.1103/PhysRevB.85.235438.

(128) Singh, A. K.; Zhou, L.; Shinde, A.; Suram, S. K.; Montoya, J. H.; Winston, D.; Gregoire, J. M.; Persson, K. A. Electrochemical Stability of Metastable Materials. *Chemistry of Materials* **2017**, *29* (23), 10159–10167. https://doi.org/10.1021/acs.chemmater.7b03980.

(129) Geisz, J. F.; Steiner, M. A.; Jain, N.; Schulte, K. L.; France, R. M.; McMahon, W. E.; Perl, E. E.; Friedman, D. J. Building a Six-Junction Inverted Metamorphic Concentrator Solar Cell. *IEEE J. Photovoltaics* **2018**, *8* (2), 626–632. https://doi.org/10.1109/JPHOTOV.2017.2778567.

(130) Young, J. L.; Steiner, M. A.; Döscher, H.; France, R. M.; Turner, J. A.; Deutsch, T. G. Direct Solar-to-Hydrogen Conversion via Inverted Metamorphic Multi-Junction Semiconductor Architectures. *Nature Energy* **2017**, *2*, 17028. https://doi.org/10.1038/nenergy.2017.28 https://www.nature.com/articles/nenergy201728#supplementary-information.

(131) Heller, A.; Aharon-Shalom, E.; Bonner, W. A.; Miller, B. Hydrogen-Evolving Semiconductor Photocathodes: Nature of the Junction and Function of the Platinum Group Metal Catalyst. *Journal of the American Chemical Society* **1982**, *104* (25), 6942–6948. https://doi.org/10.1021/ja00389a010.

(132) Lee, M. H.; Takei, K.; Zhang, J.; Kapadia, R.; Zheng, M.; Chen, Y.-Z.; Nah, J.; Matthews, T. S.; Chueh, Y.-L.; Ager, J. W.; Javey, A. P-Type InP Nanopillar Photocathodes for Efficient Solar-Driven Hydrogen Production. *Angewandte Chemie* **2012**, *124* (43), 10918–10922. https://doi.org/10.1002/ange.201203174.

(133) Hettick, M.; Zheng, M.; Lin, Y.; Sutter-Fella, C. M.; Ager, J. W.; Javey, A. Nonepitaxial Thin-Film InP for Scalable and Efficient Photocathodes. *J Phys Chem Lett* **2015**, *6* (12), 2177–2182. https://doi.org/10.1021/acs.jpclett.5b00744.

(134) Lin, Y.; Kapadia, R.; Yang, J.; Zheng, M.; Chen, K.; Hettick, M.; Yin, X.; Battaglia, C.; Sharp, I. D.; Ager, J. W.; Javey, A. Role of TiO_2 Surface Passivation on Improving the Performance of p-InP Photocathodes. *J. Phys. Chem. C* **2015**, *119* (5), 2308–2313. https://doi.org/10.1021/jp5107313.

(135) Gao, L.; Cui, Y.; Vervuurt, R. H. J.; van Dam, D.; van Veldhoven, R. P. J.; Hofmann, J. P.; Bol, A. A.; Haverkort, J. E. M.; Notten, P. H. L.; Bakkers, E. P. A. M.; Hensen, E. J. M. High-Efficiency InP-Based Photocathode for Hydrogen Production by Interface Energetics Design and Photon

Management. *Advanced Functional Materials* **2016**, *26* (5), 679–686. https://doi.org/10.1002/adfm.201503575.

(136) Bogdanoff, P.; Friebe, P.; Alonso-Vante, N. A New Inlet System for Differential Electrochemical Mass Spectroscopy Applied to the Photocorrosion of P-InP(111) Single Crystals. *J. Electrochem. Soc.* **1998**, *145* (2), 576–582. https://doi.org/10.1149/1.1838306.

(137) Goryachev, A.; Gao, L.; van Veldhoven, R. P. J.; Haverkort, J. E. M.; Hofmann, J. P.; Hensen, E. J. M. On the Origin of the Photocurrent of Electrochemically Passivated P-InP(100) Photoelectrodes. *Phys Chem Chem Phys* **2018**, *20* (20), 14242–14250. https://doi.org/10.1039/c8cp00894a.

(138) Detweiler, Z. M.; Wulfsberg, S. M.; Frith, M. G.; Bocarsly, A. B.; Bernasek, S. L. The Oxidation and Surface Speciation of Indium and Indium Oxides Exposed to Atmospheric Oxidants. *Surface Science* **2016**, *648*, 188–195. https://doi.org/10.1016/j.susc.2015.10.026.

(139) Kościelniak, P.; Mazur, J.; Henek, J.; Kwoka, M.; Pawela, Ł.; Szuber, J. XPS and AFM Studies of Surface Chemistry and Morphology of In_2O_3 Ultrathin Films Deposited by Rheotaxial Growth and Vacuum Oxidation. *Thin Solid Films* **2011**, *520* (3), 927–931. https://doi.org/10.1016/j.tsf.2011.04.184.

(140) Bayón, R.; Maffiotte, C.; Herrero, J. Chemical Bath Deposition of Indium Hydroxy Sulphide Thin Films: Process and XPS Characterization. *Thin Solid Films* **1999**, *353* (1–2), 100–107. https://doi.org/10.1016/S0040-6090(99)00381-8.

(141) Ishida, T.; Kobayashi, H.; Nakato, Y. Structures and Properties of Electron-beam-evaporated Indium Tin Oxide Films as Studied by X-ray Photoelectron Spectroscopy and Work-function Measurements. *Journal of Applied Physics* **1993**, *73* (9), 4344–4350. https://doi.org/10.1063/1.352818.

(142) Barr, T. L.; Ying Li Liu. An X-Ray Photoelectron Spectroscopy Study of the Valence Band Structure of Indium Oxides. *Journal of Physics and Chemistry of Solids* **1989**, *50* (7), 657–664. https://doi.org/10.1016/0022-3697(89)90001-2.

(143) White, J. L.; Bocarsly, A. B. Enhanced Carbon Dioxide Reduction Activity on Indium-Based Nanoparticles. *J. Electrochem. Soc.* **2016**, *163* (6), H410–H416. https://doi.org/10.1149/2.0681606jes.

(144) McCrory, C. C. L.; Jung, S.; Ferrer, I. M.; Chatman, S. M.; Peters, J. C.; Jaramillo, T. F. Benchmarking Hydrogen Evolving Reaction and Oxygen Evolving Reaction Electrocatalysts for Solar Water Splitting Devices. *Journal of the American Chemical Society* **2015**, *137* (13), 4347–4357. https://doi.org/10.1021/ja510442p.

(145) Saadi, F. H.; Carim, A. I.; Verlage, E.; Hemminger, J. C.; Lewis, N. S.; Soriaga, M. P. CoP as an Acid-Stable Active Electrocatalyst for the Hydrogen-Evolution Reaction: Electrochemical Synthesis, Interfacial Characterization and Performance Evaluation. *The Journal of Physical Chemistry C* **2014**, *118* (50), 29294–29300. https://doi.org/10.1021/jp5054452.

(146) Bard, A. J.; Wrighton, M. S. Thermodynamic Potential for the Anodic Dissolution of N-Type Semiconductors: A Crucial Factor Controlling Durability and Efficiency in Photoelectrochemical Cells and an Important Criterion in the Selection of New Electrode/Electrolyte Systems. *Journal of The Electrochemical Society* **1977**, *124* (11), 1706–1710. https://doi.org/10.1149/1.2133140.

(147) May, M. M.; Lewerenz, H.-J.; Hannappel, T. Optical in Situ Study of InP(100) Surface Chemistry: Dissociative Adsorption of Water and Oxygen. *The Journal of Physical Chemistry C* **2014**, *118* (33),

19032–19041. https://doi.org/10.1021/jp502955m.

(148) Spicer, W. E. The Advanced Unified Defect Model for Schottky Barrier Formation. *Journal of Vacuum Science & Technology B: Microelectronics and Nanometer Structures* **1988**, *6* (4), 1245. https://doi.org/10.1116/1.584244.

(149) Spicer, W. E.; Lindau, I.; Skeath, P.; Su, C. Y.; Chye, P. Unified Mechanism for Schottky-Barrier Formation and III-V Oxide Interface States. *Phys. Rev. Lett.* **1980**, *44* (6), 420–423. https://doi.org/10.1103/PhysRevLett.44.420.

(150) Liu, K.; Yu, J. C.-C.; Dong, H.; Wu, J. C. S.; Hoffmann, M. R. Degradation and Mineralization of Carbamazepine Using an Electro-Fenton Reaction Catalyzed by Magnetite Nanoparticles Fixed on an Electrocatalytic Carbon Fiber Textile Cathode. *Environmental Science & Technology* **2018**, *52* (21), 12667–12674. https://doi.org/10.1021/acs.est.8b03916.

(151) Corson, E. R.; Creel, E. B.; Kim, Y.; Urban, J. J.; Kostecki, R.; McCloskey, B. D. A Temperature-Controlled Photoelectrochemical Cell for Quantitative Product Analysis. *Review of Scientific Instruments* **2018**, *89* (5), 055112. https://doi.org/10.1063/1.5024802.

(152) Moreno-Hernandez, I. A.; Yalamanchili, S.; Fu, H. J.; Atwater, H. A.; Brunschwig, B. S.; Lewis, N. S. Conformal SnO $_x$ Heterojunction Coatings for Stabilized Photoelectrochemical Water Oxidation Using Arrays of Silicon Microcones. *J. Mater. Chem. A* **2020**, *8* (18), 9292–9301. https://doi.org/10.1039/D0TA01144D.

(153) Hu, T.; Li, H.; Liang, Z.; Du, N.; Hou, W. Facile Synthesis of Indium Hydroxide Nanosheet/Bismuth Molybdate Hierarchical Microsphere Heterojunction with Enhanced Photocatalytic Performance. *Journal of Colloid and Interface Science* **2019**, *545*, 301–310. https://doi.org/10.1016/j.jcis.2019.03.040.

(154) Zhu, W.; Zhai, J.; Sun, Z.; Jiang, L. Ammonia Responsive Surface Wettability Switched on Indium Hydroxide Films with Micro- and Nanostructures. *J. Phys. Chem. C* **2008**, *112* (22), 8338–8342. https://doi.org/10.1021/jp800661h.

(155) Detweiler, Z. M.; White, J. L.; Bernasek, S. L.; Bocarsly, A. B. Anodized Indium Metal Electrodes for Enhanced Carbon Dioxide Reduction in Aqueous Electrolyte. *Langmuir* **2014**, *30* (25), 7593–7600. https://doi.org/10.1021/la501245p.

(156) Shinde, D. V.; Ahn, D. Y.; Jadhav, V. V.; Lee, D. Y.; Shrestha, N. K.; Lee, J. K.; Lee, H. Y.; Mane, R. S.; Han, S.-H. A Coordination Chemistry Approach for Shape Controlled Synthesis of Indium Oxide Nanostructures and Their Photoelectrochemical Properties. *J. Mater. Chem. A* **2014**, *2* (15), 5490–5498. https://doi.org/10.1039/C3TA15407F.

(157) Hoch, L. B.; He, L.; Qiao, Q.; Liao, K.; Reyes, L. M.; Zhu, Y.; Ozin, G. A. Effect of Precursor Selection on the Photocatalytic Performance of Indium Oxide Nanomaterials for Gas-Phase CO_2 Reduction. *Chem. Mater.* **2016**, *28* (12), 4160–4168. https://doi.org/10.1021/acs.chemmater.6b00301.

(158) Hofmann, A.; Streubel, P.; Meisel, A. XPS Investigation of Oxide Films on InP(100). *Surf. Interface Anal.* **1988**, *12* (5), 315–319. https://doi.org/10.1002/sia.740120508.

(159) Glorieux, B.; Berjoan, R.; Matecki, M.; Kammouni, A.; Perarnau, D. XPS Analyses of Lanthanides Phosphates. *Applied Surface Science* **2007**, *253* (6), 3349–3359. https://doi.org/10.1016/j.apsusc.2006.07.027.

(160) Virieux, H.; Le Troedec, M.; Cros-Gagneux, A.; Ojo, W.-S.; Delpech, F.; Nayral, C.; Martinez, H.; Chaudret, B. InP/ZnS Nanocrystals: Coupling NMR and XPS for Fine Surface and Interface Description. *J. Am. Chem. Soc.* **2012**, *134* (48), 19701–19708. https://doi.org/10.1021/ja307124m.

(161) Jean, S.-T.; Her, Y.-C. Growth Mechanism and Cathodoluminescence Properties of Indium Hydroxide Nanocubes Synthesized from a Simple Aqueous Solution. *CrystEngComm* **2011**, *13* (7), 2324. https://doi.org/10.1039/c0ce00480d.

(162) Lewis, N. S. Developing a Scalable Artificial Photosynthesis Technology through Nanomaterials by Design. *Nature Nanotechnology* **2016**, *11*, 1010. https://doi.org/10.1038/nnano.2016.194.

(163) Walter, M. G.; Warren, E. L.; McKone, J. R.; Boettcher, S. W.; Mi, Q.; Santori, E. A.; Lewis, N. S. Solar Water Splitting Cells. *Chemical Reviews* **2010**, *110* (11), 6446–6473.

(164) Bae, D.; Seger, B.; Vesborg, P. C.; Hansen, O.; Chorkendorff, I. Strategies for Stable Water Splitting via Protected Photoelectrodes. *Chem Soc Rev* **2017**, *46* (7), 1933–1954. https://doi.org/10.1039/c6cs00918b.

(165) Hu, S.; Lewis, N. S.; Ager, J. W.; Yang, J.; McKone, J. R.; Strandwitz, N. C. Thin-Film Materials for the Protection of Semiconducting Photoelectrodes in Solar-Fuel Generators. *The Journal of Physical Chemistry C* **2015**, *119* (43), 24201–24228. https://doi.org/10.1021/acs.jpcc.5b05976.

(166) Sun, K.; Moreno-Hernandez, I. A.; Schmidt, W. C.; Zhou, X.; Crompton, J. C.; Liu, R.; Saadi, F. H.; Chen, Y.; Papadantonakis, K. M.; Lewis, N. S. A Comparison of the Chemical, Optical and Electrocatalytic Properties of Water-Oxidation Catalysts for Use in Integrated Solar-Fuel Generators. *Energy & Environmental Science* **2017**, *10* (4), 987–1002. https://doi.org/10.1039/C6EE03563A.

(167) Lebedev, M. V.; Calvet, W.; Mayer, T.; Jaegermann, W. Photoelectrochemical Processes at N-GaAs(100)/Aqueous HCl Electrolyte Interface: A Synchrotron Photoemission Spectroscopy Study of Emersed Electrodes. *The Journal of Physical Chemistry C* **2014**, *118* (24), 12774–12781. https://doi.org/10.1021/jp500564c.

(168) Huang, Y.; Luo, J.; Ivey, D. G. Steady-State and Impedance Study of n-GaAs in H_2SO_4 Solution: Mechanism Analysis. *Thin Solid Films* **2006**, *496* (2), 724–734. https://doi.org/10.1016/j.tsf.2005.09.003.

(169) Huang, Y.; Luo, J.; Ivey, D. G. Comparative Study of GaAs Corrosion in H_2SO_4 and $NH_3{\cdot}H_2O$ Solutions by Electrochemical Methods and Surface Analysis. *Materials Chemistry and Physics* **2005**, *93* (2–3), 429–442. https://doi.org/10.1016/j.matchemphys.2005.03.049.

(170) Alqaradawi, S. Y.; Aljaber, A. S.; Khader, M. M. Activation and Stabilization of Gallium Arsenide Anode in an Aqueous Photoelectrochemical Cell. *Thin Solid Films* **2003**, *444* (1–2), 282–289. https://doi.org/10.1016/S0040-6090(03)01104-0.

(171) Kraft, A.; Heckner, K.-H. Neutron Activation Analysis of the Dissolution Ofn-GaAs in 1M KOH. *Journal of Radioanalytical and Nuclear Chemistry Articles* **1994**, *182* (2), 257–265. https://doi.org/10.1007/BF02037501.

(172) Zhang, J.; Lai, J.; Wang, W.; Huang, P.; Jia, J.; Han, L.; Tian, Z.-W.; Tian, Z.-Q.; Zhan, D. Etching Kinetics of III–V Semiconductors Coupled with Surface Passivation Investigated by Scanning Electrochemical Microscopy. *The Journal of Physical Chemistry C* **2017**, *121* (18), 9944–9952. https://doi.org/10.1021/acs.jpcc.7b01868.

(173) Zhang, J.; Zhang, L.; Wang, W.; Han, L.; Jia, J.-C.; Tian, Z.-W.; Tian, Z.-Q.; Zhan, D. Contact Electrification Induced Interfacial Reactions and Direct Electrochemical Nanoimprint Lithography in N-Type Gallium Arsenate Wafer. *Chemical Science* **2017**, *8* (3), 2407–2412. https://doi.org/10.1039/C6SC04091H.

(174) Lai, J.; Yuan, D.; Huang, P.; Zhang, J.; Su, J.-J.; Tian, Z.-W.; Zhan, D. Kinetic Investigation on the Photoetching Reaction of N-Type GaAs by Scanning Electrochemical Microscopy. *The Journal of Physical Chemistry C* **2016**, *120* (30), 16446–16452. https://doi.org/10.1021/acs.jpcc.6b04646.

(175) Zhang, J.; Zhang, L.; Han, L.; Tian, Z.-W.; Tian, Z.-Q.; Zhan, D. Electrochemical Nanoimprint Lithography: When Nanoimprint Lithography Meets Metal Assisted Chemical Etching. *Nanoscale* **2017**, *9* (22), 7476–7482. https://doi.org/10.1039/C7NR01777D.

(176) Chang, K. C.; Heller, A.; Schwartz, B.; Menezes, S.; Miller, B. Stable Semiconductor Liquid Junction Cell with 9 Percent Solar-to-Electrical Conversion Efficiency. *Science* **1977**, *196* (4294), 1097–1099. https://doi.org/10.1126/science.196.4294.1097.

(177) Tufts, B. J.; Abrahams, I. L.; Santangelo, P. G.; Ryba, G. N.; Casagrande, L. G.; Lewis, N. S. Chemical Modification of N-GaAs Electrodes with Os3+ Gives a 15% Efficient Solar Cell. *Nature* **1987**, *326* (6116), 861–863. https://doi.org/10.1038/326861a0.

(178) Yang, F.; Nielander, A. C.; Grimm, R. L.; Lewis, N. S. Photoelectrochemical Behavior of N-Type GaAs(100) Electrodes Coated by a Single Layer of Graphene. *The Journal of Physical Chemistry C* **2016**, *120* (13), 6989–6995. https://doi.org/10.1021/acs.jpcc.6b00232.

(179) Fan, F. R. F.; Bard, A. J. Semiconductor Electrodes. 24. Behavior of Photoelectrochemical Cells Based on p-Type Gallium Arsenide in Aqueous Solutions. *Journal of the American Chemical Society* **1980**, *102* (11), 3677–3683. https://doi.org/10.1021/ja00531a002.

(180) Young, J. L.; Steirer, K. X.; Dzara, M. J.; Turner, J. A.; Deutsch, T. G. Remarkable Stability of Unmodified GaAs Photocathodes during Hydrogen Evolution in Acidic Electrolyte. *Journal of Materials Chemistry A* **2016**, *4* (8), 2831–2836. https://doi.org/10.1039/c5ta07648j.

(181) Traub, M. C.; Biteen, J. S.; Michalak, D. J.; Webb, L. J.; Brunschwig, B. S.; Lewis, N. S. High-Resolution X-Ray Photoelectron Spectroscopy of Chlorine-Terminated GaAs(111)A Surfaces. *The Journal of Physical Chemistry B* **2006**, *110* (32), 15641–15644. https://doi.org/10.1021/jp061623n.

(182) Lunt, S. R.; Ryba, G. N.; Santangelo, P. G.; Lewis, N. S. Chemical Studies of the Passivation of GaAs Surface Recombination Using Sulfides and Thiols. *Journal of Applied Physics* **1991**, *70* (12), 7449–7467. https://doi.org/10.1063/1.349741.

(183) Traub, M. C.; Biteen, J. S.; Michalak, D. J.; Webb, L. J.; Brunschwig, B. S.; Lewis, N. S. Phosphine Functionalization of GaAs(111)A Surfaces. *The Journal of Physical Chemistry C* **2008**, *112* (47), 18467–18473. https://doi.org/10.1021/jp803992h.

(184) Kempler, P. A.; Ifkovits, Z. P.; Yu, W.; Carim, A. I.; Lewis, N. S. Optical and Electrochemical Effects of H_2 and O_2 Bubbles at Upward-Facing Si Photoelectrodes. *Energy Environ. Sci.* **2021**, *14* (1), 414–423. https://doi.org/10.1039/D0EE02796K.

(185) Kempler, P. A.; Coridan, R. H.; Lewis, N. S. Effects of Bubbles on the Electrochemical Behavior of Hydrogen-Evolving Si Microwire Arrays Oriented against Gravity. *Energy Environ. Sci.* **2020**, *13* (6), 1808–1817. https://doi.org/10.1039/D0EE00356E.

(186) Choi, K.; Kim, K.; Moon, I. K.; Oh, I.; Oh, J. Evaluation of Electroless Pt Deposition and Electron Beam Pt Evaporation on P-GaAs as a Photocathode for Hydrogen Evolution. *ACS Applied Energy Materials* **2019**, *2* (1), 770–776. https://doi.org/10.1021/acsaem.8b01838.

(187) Lee, Y. H.; Kim, J.; Oh, J. Wafer-Scale Ultrathin, Single-Crystal Si and GaAs Photocathodes for Photoelectrochemical Hydrogen Production. *ACS Applied Materials & Interfaces* **2018**, *10* (39), 33230–33237. https://doi.org/10.1021/acsami.8b10943.

(188) Choi, K.; Kim, K.; Moon, I. K.; Bang, J.; Oh, J. Subwavelength Photocathodes *via* Metal-Assisted Chemical Etching of GaAs for Solar Hydrogen Generation. *Nanoscale* **2019**, *11* (32), 15367–15373. https://doi.org/10.1039/C9NR03870A.

(189) Kwon, K. C.; Choi, S.; Hong, K.; Moon, C. W.; Shim, Y.-S.; Kim, D. H.; Kim, T.; Sohn, W.; Jeon, J.-M.; Lee, C.-H.; Nam, K. T.; Han, S.; Kim, S. Y.; Jang, H. W. Wafer-Scale Transferable Molybdenum Disulfide Thin-Film Catalysts for Photoelectrochemical Hydrogen Production. *Energy & Environmental Science* **2016**, *9* (7), 2240–2248. https://doi.org/10.1039/C6EE00144K.

(190) Ou, S.-L.; Wuu, D.-S.; Fu, Y.-C.; Liu, S.-P.; Horng, R.-H.; Liu, L.; Feng, Z.-C. Growth and Etching Characteristics of Gallium Oxide Thin Films by Pulsed Laser Deposition. *Materials Chemistry and Physics* **2012**, *133* (2–3), 700–705. https://doi.org/10.1016/j.matchemphys.2012.01.060.

(191) Guo, D. Y.; Wu, Z. P.; An, Y. H.; Li, P. G.; Wang, P. C.; Chu, X. L.; Guo, X. C.; Zhi, Y. S.; Lei, M.; Li, L. H.; Tang, W. H. Unipolar Resistive Switching Behavior of Amorphous Gallium Oxide Thin Films for Nonvolatile Memory Applications. *Appl. Phys. Lett.* **2015**, *106* (4), 042105. https://doi.org/10.1063/1.4907174.

(192) Kempler, P. A.; Fu, H. J.; Ifkovits, Z. P.; Papadantonakis, K. M.; Lewis, N. S. Spontaneous Formation of >90% Optically Transmissive, Electrochemically Active CoP Films for Photoelectrochemical Hydrogen Evolution. *The Journal of Physical Chemistry Letters* **2020**, *11* (1), 14–20. https://doi.org/10.1021/acs.jpclett.9b02926.

(193) Erné, B. H.; Ozanam, F.; Chazalviel, J.-N. The Mechanism of Hydrogen Gas Evolution on GaAs Cathodes Elucidated by In Situ Infrared Spectroscopy. *The Journal of Physical Chemistry B* **1999**, *103* (15), 2948–2962. https://doi.org/10.1021/jp984765t.

(194) Erné, B. H.; Ozanam, F.; Chazalviel, J.-N. Dynamics of Hydrogen Adsorption on GaAs Electrodes. *Physical Review Letters* **1998**, *80* (19), 4337–4340. https://doi.org/10.1103/PhysRevLett.80.4337.

(195) Ostermayer, F. W.; Kohl, P. A. Photoelectrochemical Etching of *p* -GaAs. *Applied Physics Letters* **1981**, *39* (1), 76–78. https://doi.org/10.1063/1.92522.

(196) Kornblum, L.; Fenning, D. P.; Faucher, J.; Hwang, J.; Boni, A.; Han, M. G.; Morales-Acosta, M. D.; Zhu, Y.; Altman, E. I.; Lee, M. L.; Ahn, C. H.; Walker, F. J.; Shao-Horn, Y. Solar Hydrogen Production Using Epitaxial $SrTiO_3$ on a GaAs Photovoltaic. *Energy Environ. Sci.* **2017**, *10* (1), 377–382. https://doi.org/10.1039/C6EE03170F.

(197) Wu, Y.; Chan, M. K. Y.; Ceder, G. Prediction of Semiconductor Band Edge Positions in Aqueous Environments from First Principles. *Phys. Rev. B* **2011**, *83* (23), 235301. https://doi.org/10.1103/PhysRevB.83.235301.

(198) Laflere, W. H.; Cardon, F.; Gomes, W. P. On the Differential Capacitance of the N- and p-Type Gallium Arsenide Electrode. *Surface Science* **1974**, *44* (2), 541–552. https://doi.org/10.1016/0039-6028(74)90136-8.

(199) Mandler, D.; Bard, A. J. Hole Injection and Etching Studies of Gallium Arsenide Using the Scanning Electrochemical Microscope. *Langmuir* **1990**, *6* (9), 1489–1494. https://doi.org/10.1021/la00099a010.

(200) Smith, W. A.; Sharp, I. D.; Strandwitz, N. C.; Bisquert, J. Interfacial Band-Edge Energetics for Solar Fuels Production. *Energy & Environmental Science* **2015**, *8* (10), 2851–2862. https://doi.org/10.1039/C5EE01822F.

(201) Allongue, P.; Blonkowski, S.; Souteyrand, E. Experimental Investigation of Charge Transfer at the Semiconductor/Electrolyte Junction. *Electrochimica Acta* **1992**, *37* (5), 781–797. https://doi.org/10.1016/0013-4686(92)85032-G.

(202) Li, X. Metal Assisted Chemical Etching for High Aspect Ratio Nanostructures: A Review of Characteristics and Applications in Photovoltaics. *Current Opinion in Solid State and Materials Science* **2012**, *16* (2), 71–81. https://doi.org/10.1016/j.cossms.2011.11.002.

(203) Li, X.; Bohn, P. W. Metal-Assisted Chemical Etching in HF/H_2O_2 Produces Porous Silicon. *Appl. Phys. Lett.* **2000**, *77* (16), 2572–2574. https://doi.org/10.1063/1.1319191.

(204) Huang, Z.; Geyer, N.; Werner, P.; de Boor, J.; Gösele, U. Metal-Assisted Chemical Etching of Silicon: A Review: In Memory of Prof. Ulrich Gösele. *Adv. Mater.* **2011**, *23* (2), 285–308. https://doi.org/10.1002/adma.201001784.

(205) Xiang, C.; Weber, A. Z.; Ardo, S.; Berger, A.; Chen, Y.; Coridan, R.; Fountaine, K. T.; Haussener, S.; Hu, S.; Liu, R.; Lewis, N. S.; Modestino, M. A.; Shaner, M. M.; Singh, M. R.; Stevens, J. C.; Sun, K.; Walczak, K. Modeling, Simulation, and Implementation of Solar-Driven Water-Splitting Devices. *Angewandte Chemie International Edition* **2016**, *55* (42), 12974–12988. https://doi.org/10.1002/anie.201510463.

(206) Spitler, M. T.; Modestino, M. A.; Deutsch, T. G.; Xiang, C. X.; Durrant, J. R.; Esposito, D. V.; Haussener, S.; Maldonado, S.; Sharp, I. D.; Parkinson, B. A.; Ginley, D. S.; Houle, F. A.; Hannappel, T.; Neale, N. R.; Nocera, D. G.; McIntyre, P. C. Practical Challenges in the Development of Photoelectrochemical Solar Fuels Production. *Sustainable Energy & Fuels* **2020**, *4* (3), 985–995. https://doi.org/10.1039/C9SE00869A.

(207) Wu, J.; Li, Y.; Kubota, J.; Domen, K.; Aagesen, M.; Ward, T.; Sanchez, A.; Beanland, R.; Zhang, Y.; Tang, M.; Hatch, S.; Seeds, A.; Liu, H. Wafer-Scale Fabrication of Self-Catalyzed 1.7 EV GaAsP Core–Shell Nanowire Photocathode on Silicon Substrates. *Nano Letters* **2014**, *14* (4), 2013–2018. https://doi.org/10.1021/nl500170m.

(208) Steiner, M. A.; France, R. M.; Buencuerpo, J.; Geisz, J. F.; Nielsen, M. P.; Pusch, A.; Olavarria, W. J.; Young, M.; Ekins-Daukes, N. J. High Efficiency Inverted GaAs and GaInP/GaAs Solar Cells With Strain-Balanced GaInAs/GaAsP Quantum Wells. *Advanced Energy Materials* **2020**, 2002874. https://doi.org/10.1002/aenm.202002874.

(209) Steiner, M. A.; Barraugh, C. D.; Aldridge, C. W.; Alvarez, I. B.; Friedman, D. J.; Ekins-Daukes, N. J.; Deutsch, T. G.; Young, J. L. Photoelectrochemical Water Splitting Using Strain-Balanced Multiple Quantum Well Photovoltaic Cells. *Sustainable Energy & Fuels* **2019**, *3* (10), 2837–2844. https://doi.org/10.1039/C9SE00276F.

(210) Hwang, S.; Young, J. L.; Mow, R.; Laursen, A. B.; Li, M.; Yang, H.; Batson, P. E.; Greenblatt, M.; Steiner, M. A.; Friedman, D.; Deutsch, T. G.; Garfunkel, E.; Dismukes, G. C. Highly Efficient and

Durable III–V Semiconductor-Catalyst Photocathodes *via* a Transparent Protection Layer. *Sustainable Energy & Fuels* **2020**, *4* (3), 1437–1442. https://doi.org/10.1039/C9SE01264H.

(211) Lancaster, M.; Mow, R.; Liu, J.; Cheek, Q.; MacInnes, M. M.; Al-Jassim, M. M.; Deutsch, T. G.; Young, J. L.; Maldonado, S. Protection of $GaInP_2$ Photocathodes by Direct Photoelectrodeposition of MoS_x Thin Films. *ACS Appl Mater Interfaces* **2019**, *11* (28), 25115–25122. https://doi.org/10.1021/acsami.9b03742.

(212) Bard, A. J.; Parsons, R.; Jordan, J. *Standard Potentials in Aqueous Solution*; CRC press, 1985; Vol. 6.

(213) Chen, Y.; Sun, K.; Audesirk, H.; Xiang, C.; Lewis, N. S. A Quantitative Analysis of the Efficiency of Solar-Driven Water-Splitting Device Designs Based on Tandem Photoabsorbers Patterned with Islands of Metallic Electrocatalysts. *Energy & Environmental Science* **2015**, *8* (6), 1736–1747. https://doi.org/10.1039/C5EE00311C.

(214) Moon, C.; Seger, B.; Kjærgaard Vesborg, P. C.; Hansen, O.; Chorkendorff, I. Wireless Photoelectrochemical Water Splitting Using Triple-Junction Solar Cell Protected by TiO_2. *Cell Reports Physical Science* **2021**, *2* (2), 100340. https://doi.org/10.1016/j.xcrp.2021.100340.

(215) Deng, J.; Iñiguez, J. A.; Liu, C. Electrocatalytic Nitrogen Reduction at Low Temperature. *Joule* **2018**, *2* (5), 846–856. https://doi.org/10.1016/j.joule.2018.04.014.

(216) Zhou, F.; Azofra, L. M.; Ali, M.; Kar, M.; Simonov, A. N.; McDonnell-Worth, C.; Sun, C.; Zhang, X.; MacFarlane, D. R. Electro-Synthesis of Ammonia from Nitrogen at Ambient Temperature and Pressure in Ionic Liquids. *Energy & Environmental Science* **2017**, *10* (12), 2516–2520. https://doi.org/10.1039/C7EE02716H.

(217) Lu, S.; Lee, D. H.; Liu, C. Modeling of Electrocatalytic Dinitrogen Reduction on Microstructured Electrodes. *Small Methods* **2019**, *3* (6), 1800332. https://doi.org/10.1002/smtd.201800332.

(218) Yu, X.; Han, P.; Wei, Z.; Huang, L.; Gu, Z.; Peng, S.; Ma, J.; Zheng, G. Boron-Doped Graphene for Electrocatalytic N_2 Reduction. *Joule* **2018**, *2* (8), 1610–1622. https://doi.org/10.1016/j.joule.2018.06.007.

(219) Suryanto, B. H. R.; Wang, D.; Azofra, L. M.; Harb, M.; Cavallo, L.; Jalili, R.; Mitchell, D. R. G.; Chatti, M.; MacFarlane, D. R. MoS_2 Polymorphic Engineering Enhances Selectivity in the Electrochemical Reduction of Nitrogen to Ammonia. *ACS Energy Lett.* **2019**, *4* (2), 430–435. https://doi.org/10.1021/acsenergylett.8b02257.

(220) Xiong, W.; Guo, Z.; Zhao, S.; Wang, Q.; Xu, Q.; Wang, X. Facile, Cost-Effective Plasma Synthesis of Self-Supportive FeS_x on Fe Foam for Efficient Electrochemical Reduction of N_2 under Ambient Conditions. *Journal of Materials Chemistry A* **2019**, *7* (34), 19977–19983. https://doi.org/10.1039/C9TA07790A.

(221) Hu, B.; Hu, M.; Seefeldt, L.; Liu, T. L. Electrochemical Dinitrogen Reduction to Ammonia by Mo_2N: Catalysis or Decomposition? *ACS Energy Letters* **2019**, *4* (5), 1053–1054. https://doi.org/10.1021/acsenergylett.9b00648.

(222) MacLaughlin, C. Role for Standardization in Electrocatalytic Ammonia Synthesis: A Conversation with Leo Liu, Lauren Greenlee, and Douglas MacFarlane. *ACS Energy Letters* **2019**, *4* (6), 1432–1436. https://doi.org/10.1021/acsenergylett.9b01123.

(223) Greenlee, L. F.; Renner, J. N.; Foster, S. L. The Use of Controls for Consistent and Accurate Measurements of Electrocatalytic Ammonia Synthesis from Dinitrogen. *ACS Catalysis* **2018**, *8* (9), 7820–7827. https://doi.org/10.1021/acscatal.8b02120.

(224) Du, H.-L.; Gengenbach, T. R.; Hodgetts, R.; MacFarlane, D. R.; Simonov, A. N. Critical Assessment of the Electrocatalytic Activity of Vanadium and Niobium Nitrides toward Dinitrogen Reduction to Ammonia. *ACS Sustainable Chemistry & Engineering* **2019**, *7* (7), 6839–6850. https://doi.org/10.1021/acssuschemeng.8b06163.

(225) Dabundo, R.; Lehmann, M. F.; Treibergs, L.; Tobias, C. R.; Altabet, M. A.; Moisander, P. H.; Granger, J. The Contamination of Commercial 15N2 Gas Stocks with 15N–Labeled Nitrate and Ammonium and Consequences for Nitrogen Fixation Measurements. *PLoS ONE* **2014**, *9* (10), e110335. https://doi.org/10.1371/journal.pone.0110335.

(226) Kibsgaard, J.; Nørskov, J. K.; Chorkendorff, I. The Difficulty of Proving Electrochemical Ammonia Synthesis. *ACS Energy Letters* **2019**, *4* (12), 2986–2988. https://doi.org/10.1021/acsenergylett.9b02286.

(227) Suryanto, B. H. R.; Du, H.-L.; Wang, D.; Chen, J.; Simonov, A. N.; MacFarlane, D. R. Challenges and Prospects in the Catalysis of Electroreduction of Nitrogen to Ammonia. *Nature Catalysis* **2019**, *2* (4), 290–296. https://doi.org/10.1038/s41929-019-0252-4.

(228) Xue, Z.-H.; Zhang, S.-N.; Lin, Y.-X.; Su, H.; Zhai, G.-Y.; Han, J.-T.; Yu, Q.-Y.; Li, X.-H.; Antonietti, M.; Chen, J.-S. Electrochemical Reduction of N_2 into NH_3 by Donor–Acceptor Couples of Ni and Au Nanoparticles with a 67.8% Faradaic Efficiency. *Journal of the American Chemical Society* **2019**, *141* (38), 14976–14980. https://doi.org/10.1021/jacs.9b07963.

(229) Lin, Y.-X.; Zhang, S.-N.; Xue, Z.-H.; Zhang, J.-J.; Su, H.; Zhao, T.-J.; Zhai, G.-Y.; Li, X.-H.; Antonietti, M.; Chen, J.-S. Boosting Selective Nitrogen Reduction to Ammonia on Electron-Deficient Copper Nanoparticles. *Nature Communications* **2019**, *10* (1). https://doi.org/10.1038/s41467-019-12312-4.

(230) Bravo, M.; Eran, H.; Zhang, F. X.; McKenna, C. E. A Rapid, Sensitive High-Performance Liquid Chromatography Analysis of Ammonia and Methylamine for Nitrogenase Assays. *Analytical Biochemistry* **1988**, *175* (2), 482–491. https://doi.org/10.1016/0003-2697(88)90572-6.

(231) Wang, L.; Xia, M.; Wang, H.; Huang, K.; Qian, C.; Maravelias, C. T.; Ozin, G. A. Greening Ammonia toward the Solar Ammonia Refinery. *Joule* **2018**, *2* (6), 1055–1074. https://doi.org/10.1016/j.joule.2018.04.017.

(232) Anderson, J. S.; Rittle, J.; Peters, J. C. Catalytic Conversion of Nitrogen to Ammonia by an Iron Model Complex. *Nature* **2013**, *501* (7465), 84–87. https://doi.org/10.1038/nature12435.

(233) Chalkley, M. J.; Del Castillo, T. J.; Matson, B. D.; Peters, J. C. Fe-Mediated Nitrogen Fixation with a Metallocene Mediator: Exploring PKa Effects and Demonstrating Electrocatalysis. *Journal of the American Chemical Society* **2018**, *140* (19), 6122–6129. https://doi.org/10.1021/jacs.8b02335.

(234) van der Ham, C. J. M.; Koper, M. T. M.; Hetterscheid, D. G. H. Challenges in Reduction of Dinitrogen by Proton and Electron Transfer. *Chemical Society Reviews* **2014**, *43* (15), 5183–5191. https://doi.org/10.1039/C4CS00085D.

(235) Wang, M.; Liu, S.; Qian, T.; Liu, J.; Zhou, J.; Ji, H.; Xiong, J.; Zhong, J.; Yan, C. Over 56.55% Faradaic Efficiency of Ambient Ammonia Synthesis Enabled by Positively Shifting the Reaction

Potential. *Nature Communications* **2019**, *10* (1). https://doi.org/10.1038/s41467-018-08120-x.

(236) Singh, A. R.; Rohr, B. A.; Statt, M. J.; Schwalbe, J. A.; Cargnello, M.; Nørskov, J. K. Strategies toward Selective Electrochemical Ammonia Synthesis. *ACS Catalysis* **2019**, *9* (9), 8316–8324. https://doi.org/10.1021/acscatal.9b02245.

(237) Xue, X.; Chen, R.; Yan, C.; Zhao, P.; Hu, Y.; Zhang, W.; Yang, S.; Jin, Z. Review on Photocatalytic and Electrocatalytic Artificial Nitrogen Fixation for Ammonia Synthesis at Mild Conditions: Advances, Challenges and Perspectives. *Nano Research* **2019**, *12* (6), 1229–1249. https://doi.org/10.1007/s12274-018-2268-5.

(238) Jacobsen, C. J. H.; Dahl, S.; Clausen, B. S.; Bahn, S.; Logadottir, A.; Nørskov, J. K. Catalyst Design by Interpolation in the Periodic Table: Bimetallic Ammonia Synthesis Catalysts. *Journal of the American Chemical Society* **2001**, *123* (34), 8404–8405. https://doi.org/10.1021/ja010963d.

(239) Jacobsen, C. J. H. Novel Class of Ammonia Synthesis Catalysts. *Chemical Communications* **2000**, No. 12, 1057–1058. https://doi.org/10.1039/b002930k.

(240) Kojima, R.; Aika, K. Cobalt Molybdenum Bimetallic Nitride Catalysts for Ammonia Synthesis. *Chemistry Letters* **2000**, *29* (5), 514–515. https://doi.org/10.1246/cl.2000.514.

(241) Zeinalipour-Yazdi, C. D.; Hargreaves, J. S. J.; Catlow, C. R. A. Nitrogen Activation in a Mars–van Krevelen Mechanism for Ammonia Synthesis on Co_3Mo_3N. *The Journal of Physical Chemistry C* **2015**, *119* (51), 28368–28376. https://doi.org/10.1021/acs.jpcc.5b06811.

(242) Zeinalipour-Yazdi, C. D.; Hargreaves, J. S. J.; Catlow, C. R. A. Low-T Mechanisms of Ammonia Synthesis on Co_3Mo_3N. *J. Phys. Chem. C* **2018**, *122* (11), 6078–6082. https://doi.org/10.1021/acs.jpcc.7b12364.

(243) McPherson, I. J.; Sudmeier, T.; Fellowes, J.; Tsang, S. C. E. Materials for Electrochemical Ammonia Synthesis. *Dalton Transactions* **2019**, *48* (5), 1562–1568. https://doi.org/10.1039/C8DT04019B.

(244) Howalt, J. G.; Vegge, T. Electrochemical Ammonia Production on Molybdenum Nitride Nanoclusters. *Physical Chemistry Chemical Physics* **2013**, *15* (48), 20957. https://doi.org/10.1039/c3cp53160k.

(245) Tsuji, Y.; Ogasawara, K.; Kitano, M.; Kishida, K.; Abe, H.; Niwa, Y.; Yokoyama, T.; Hara, M.; Hosono, H. Control of Nitrogen Activation Ability by Co-Mo Bimetallic Nanoparticle Catalysts Prepared via Sodium Naphthalenide-Reduction. *Journal of Catalysis* **2018**, *364*, 31–39. https://doi.org/10.1016/j.jcat.2018.04.029.

(246) Bolleter, W. T.; Bushman, C. J.; Tidwell, P. W. Spectrophotometric Determination of Ammonia as Indophenol. *Analytical Chemistry* **1961**, *33* (4), 592–594. https://doi.org/10.1021/ac60172a034.

(247) Cao, B.; Veith, G. M.; Neuefeind, J. C.; Adzic, R. R.; Khalifah, P. G. Mixed Close-Packed Cobalt Molybdenum Nitrides as Non-Noble Metal Electrocatalysts for the Hydrogen Evolution Reaction. *Journal of the American Chemical Society* **2013**, *135* (51), 19186–19192. https://doi.org/10.1021/ja4081056.

(248) Podila, S.; Zaman, S. F.; Driss, H.; Alhamed, Y. A.; Al-Zahrani, A. A.; Petrov, L. A. Hydrogen Production by Ammonia Decomposition Using High Surface Area Mo_2N and Co_3Mo_3N Catalysts. *Catal. Sci. Technol.* **2016**, *6* (5), 1496–1506. https://doi.org/10.1039/C5CY00871A.

(249) Fu, X.; Su, H.; Yin, W.; Huang, Y.; Gu, X. Bimetallic Molybdenum Nitride Co_3Mo_3N: A New

Promising Catalyst for CO_2 Reforming of Methane. *Catal. Sci. Technol.* **2017**, *7* (8), 1671–1678. https://doi.org/10.1039/C6CY02428A.

(250) Shipman, M. A.; Symes, M. D. Recent Progress towards the Electrosynthesis of Ammonia from Sustainable Resources. *Catalysis Today* **2017**, *286*, 57–68. https://doi.org/10.1016/j.cattod.2016.05.008.

(251) Liu, H.; Zhang, Y.; Luo, J. The Removal of Inevitable NO Species in Catalysts and the Selection of Appropriate Membrane for Measuring Electrocatalytic Ammonia Synthesis Accurately. *Journal of Energy Chemistry* **2020**, *49*, 51–58. https://doi.org/10.1016/j.jechem.2020.01.029.

(252) Watt, G. W.; Chrisp, J. D. Spectrophotometric Method for Determination of Hydrazine. *Analytical Chemistry* **1952**, *24* (12), 2006–2008. https://doi.org/10.1021/ac60072a044.

(253) Seger, B.; Herbst, K.; Pedersen, T.; Abrams, B.; Vesborg, P. C. K.; Hansen, O.; Chorkendorff, I. Mo_3S_4 Clusters as an Effective H_2 Evolution Catalyst on Protected Si Photocathodes. *J. Electrochem. Soc.* **2014**, *161* (12), H722–H724. https://doi.org/10.1149/2.0161412jes.

(254) Mei, B.; Pedersen, T.; Malacrida, P.; Bae, D.; Frydendal, R.; Hansen, O.; Vesborg, P. C. K.; Seger, B.; Chorkendorff, I. Crystalline TiO_2: A Generic and Effective Electron-Conducting Protection Layer for Photoanodes and -Cathodes. *J. Phys. Chem. C* **2015**, *119* (27), 15019–15027. https://doi.org/10.1021/acs.jpcc.5b04407.

(255) Seger, B.; Tilley, S. D.; Pedersen, T.; Vesborg, P. C. K.; Hansen, O.; Grätzel, M.; Chorkendorff, I. Silicon Protected with Atomic Layer Deposited TiO_2: Conducting versus Tunnelling through TiO_2. *J. Mater. Chem. A* **2013**, *1* (47), 15089. https://doi.org/10.1039/c3ta12309j.

(256) Seger, B.; Tilley, D. S.; Pedersen, T.; Vesborg, P. C. K.; Hansen, O.; Grätzel, M.; Chorkendorff, I. Silicon Protected with Atomic Layer Deposited TiO_2: Durability Studies of Photocathodic H_2 Evolution. *RSC Adv.* **2013**, *3* (48), 25902. https://doi.org/10.1039/c3ra45966g.

(257) Malizia, M.; Seger, B.; Chorkendorff, I.; Vesborg, P. C. K. Formation of a p–n Heterojunction on GaP Photocathodes for H_2 Production Providing an Open-Circuit Voltage of 710 MV. *J. Mater. Chem. A* **2014**, *2* (19), 6847–6853. https://doi.org/10.1039/C4TA00752B.

(258) Seger, B.; Pedersen, T.; Laursen, A. B.; Vesborg, P. C. K.; Hansen, O.; Chorkendorff, I. Using TiO_2 as a Conductive Protective Layer for Photocathodic H_2 Evolution. *J. Am. Chem. Soc.* **2013**, *135* (3), 1057–1064. https://doi.org/10.1021/ja309523t.

(259) Boettcher, S. W.; Strandwitz, N. C.; Schierhorn, M.; Lock, N.; Lonergan, M. C.; Stucky, G. D. Tunable Electronic Interfaces between Bulk Semiconductors and Ligand-Stabilized Nanoparticle Assemblies. *Nature Materials* **2007**, *6* (8), 592–596. https://doi.org/10.1038/nmat1943.